THE ANALYSIS OF POLAR CLOUDS FROM AVHRR SATELLITE DATA USING PATTERN RECOGNITION TECHNIQUES

The Analysis of Polar Clouds
from AVHRR Satellite Data
Using Pattern Recognition Techniques

National Aeronautics and Space Administration
Grant NAG5-1117

Final Report

William L. Smith, Director
The Cooperative Institute for Meteorological Satellite Studies (CIMSS)
Principal Investigator

Elizabeth Ebert, Research Associate
Department of Meteorology
Co-Investigator

Space Science and Engineering Center
at the University of Wisconsin-Madison
1225 West Dayton Street
Madison, Wisconsin 53706
(608) 262-0544

May 1990

TABLE OF CONTENTS

Summary

The cloud cover in a set of summertime and wintertime AVHRR data from the Arctic and Antarctic regions was analyzed using a pattern recognition algorithm. The data were collected by the NOAA-7 satellite on 6-13 January and 1-7 July 1984 between 60° and 90° north and south latitude in 5 spectral channels, at the Global Area Coverage (GAC) resolution of approximately 4 km. This data embodied a Polar Cloud Pilot Data Set which was analyzed by a number of research groups as part of a polar cloud algorithm intercomparison study. This study was intended to determine whether the additional information contained in the AVHRR channels (beyond the standard visible and infrared bands on geostationary satellites) could be effectively utilized in cloud algorithms to resolve some of the cloud detection problems caused by low visible and thermal contrasts in the polar regions.

The analysis described here makes use of a pattern recognition algorithm which estimates the surface and cloud classification, cloud fraction, and surface and cloudy visible (channel 1) albedo and infrared (channel 4) brightness temperatures on a 2.5°x2.5° latitude-longitude grid. In each grid box several spectral and textural features were computed from the calibrated pixel values in the multispectral imagery, then used to classify the region into one of eighteen surface and/or cloud types using the maximum likelihood decision rule. A slightly different version of the algorithm was used for each season and hemisphere because of differences in categories and because of the lack of visible imagery during winter. The details of the classification algorithm are given in Ebert (1987a, 1987b, 1990).

The classification of the scene is used to specify the optimal AVHRR channel for separating clear and cloudy pixels using a hybrid histogram-spatial coherence method. This method estimates values for cloud fraction, clear and cloudy albedos and brightness temperatures in each grid box. The choice of a class-dependent AVHRR channel allows for better separation of clear and cloudy pixels than does a global choice of a visible and/or infrared threshold. The

classification also prevents erroneous estimates of large fractional cloudiness in areas of cloud-free snow and sea ice. The hybrid histogram-spatial coherence technique and the advantages of first classifying a scene in the polar regions are detailed in Ebert (1989), which is also reproduced in the appendix of this report.

The complete Polar Cloud Pilot Data Set has been analyzed and the results are presented and discussed in the next part of this report. The graphs were prepared with the assistance of a SSEC programmer, Mr. Frank LaFontaine. In April 1989 a magnetic tape containing the analyzed surface and cloud type, cloud fraction, clear and cloudy visible albedo and infrared brightness temperature in each 2.5°x2.5° box in every image, along with daily and weekly summary statistics, was forwarded to Professor E. Raschke at the University of Cologne for intercomparison with the analyses of other groups. The results may be obtained from Prof. Raschke at his new address at the GKSS, Hamburg. The results from the Arctic winter and Antarctic summer and winter analyses were presented at the IAMAP Symposium for Remote Sensing in the Polar Regions in Reading, England, in August 1989. A paper based on this presentation has been accepted for publication in the International Journal of Remote Sensing, and the final manuscript is reprinted in the appendix.

Analysis of the Polar Cloud Pilot Data Set

The data set contains 365 AVHRR images, or an average of 13 images per day. Each image was analyzed individually, then the analyses were combined into daily mosaics of classification and cloud fraction. These will be described in the following section for each season and hemisphere. The next section presents the weekly statistics of total, low and high cloud fraction. The fractional area and frequency of each surface and cloud type are given in the third section and compared to climatological values where possible. The last section examines the values of the surface and cloudy albedos and brightness temperatures for each of the surface and cloud classes.

Reference maps of the Arctic and Antarctic are given in Figs. 1 and 2.

1. Daily analyses

This section describes in detail the nature and evolution of the cloud cover over each 7-day period. Daily mosaics of surface and cloud type were constructed by simply choosing, in each grid box, the classification which occurred most frequently during the day. The cloud fraction mosaics depict the daily mean total cloud fraction for the day. Thus it is possible that a region which has a clear classification in the mosaic may have a mean cloud fraction which is greater than zero if some cloud cover has been analyzed there during the day. Smoothing in the contouring routine may also produce this effect.

Each mosaic has a "hole" immediately surrounding the pole where the imagery was not analyzed because of excessive distortion due to the earth's curvature. Also, some of the region between 90°E and 90°W (including the dateline) was not analyzed because the Pilot Data Set only included images which contained data in the hemisphere between 90°W and 90°E (including the Greenwich meridian).

References are made to the synoptic weather during each period. (Charts for these days are not shown here, but may be found in the publications of ECMWF, 1984, and the Free University of Berlin, 1984.) The goal is to relate the analyzed cloud cover to that which would be expected for various synoptic situations.

a. Arctic summer

Figures 3-9 show the automated classification and cloud fraction analyses for the Arctic during 1-7 July 1984 (days 183-189). The key to the surface and cloud types in the Arctic summer algorithm is given below:

1. Land without snow
2. Land with snow
3. Open water
4. Unbroken sea ice
5. Broken sea ice
6. Ice sheet
7. Mixed surface types
8. Cs/As over land/water
9. Ci/Cc/Ac over land/water
10. St over land/water
11. Sc over land/water
12. Cu over land/water
13. Cs/As over snow/ice
14. Ci/Cc/Ac over snow/ice
15. St over snow/ice
16. Sc over snow/ice
17. Cu over snow/ice
18. High cloud over low cloud

The standard meteorological abbreviations for cloud types are used (WMO, 1956). We assume that the low cloud types (classes 10, 11, 12, 15, 16, 17) consist of liquid water droplets, while the high cloud types (calsses 8, 9, 13, 14) are composed of ice crystals. Thus a mid-level cloud would be classified as either low or high, depending on its phase. Class 17, "cumulus over snow/ice," includes isolated low clouds of small horizontal extent (i.e., much smaller than the grid square) since convective clouds over snow and ice are not common. "High clouds over low clouds" will frequently be abbreviated in the following sections as "layered clouds." The classification skill for the Arctic summer training data was 84.6% (Ebert 1987b), and the root-mean-square (RMS) error in the cloud fraction was 0.18 when verified against a manual nephanalysis of the training imagery (Ebert 1989).

Starting in the western part of the analyses, northwestern Canada showed significant cloud cover in the early part of the period associated with a decaying cyclone. These were replaced by high clouds in the latter part of the period. The Beaufort Sea had large amounts of low and layered clouds throughout most of the period, with clear patches of unbroken and broken sea ice on days 183 and 185-187. In the Canadian Archipelago layered clouds predominated, although there was a tendency for cirrus clouds to be found over Baffin Island. Baffin Bay had moderate amounts of stratus cloud until day 186 when high pressure moved in and significant clearing took place to reveal the broken sea ice cover. Moderate amounts of low, high, and layered clouds were analyzed over Greenland during the entire week. Clearer areas were found along the central eastern and western coasts on days 187-188. Stratus clouds covered the Greenland and Norwegian Seas, with fractional amounts generally exceeding 80%. Layered clouds on days 188-189 were related to a trough connecting low pressure centers south of Iceland and northwest of Novaya Zemlya. This also produced large amounts of layered cloudiness in the Barents Sea and over Scandinavia, which was under low pressure during the entire week. Mainly clear conditions characterized Svalbard during the first two days of the period. Novaya Zemlya and the Kara Sea displayed moderate amounts of stratus and layered cloud cover. The analysis of "stratus over land/water" (class 10) on days 183-185 is erroneous, as the Kara Sea was nearly 100% ice-covered at that time. Siberia, particularly the eastern sector, remained mostly cloud-free during the week, with only small amounts of cumulus, stratocumulus, and cirrus clouds.

b. Arctic winter

Mosaics of classification and total cloud fraction for the Arctic during 6-12 January 1984 are shown in Figs. 10-16. The classification key for Arctic winter is:

1. Land without snow
2. Land with snow
3. Open water and thin ice
4. Unbroken sea ice
5. Broken sea ice
6. Ice sheet
7. Mixed surface types
8. Cs/As over land/water
9. Ci/Cc/Ac over land/water
10. St over land/water
11. Sc over land/water
12. Cu over land/water
13. Cs/As over snow/ice
14. Ci/Cc/Ac over snow/ice
15. St over ice sheet
16. Sc over snow/ice
17. Inversion St over snow/ice
18. High cloud over low cloud

Class 15, "stratus over ice sheet," designates a flat, fairly featureless cloud which occurred over Greenland. Class 17, "inversion stratus over snow/ice," refers to stratus clouds which are warmer than the underlying snow and ice surface. The Arctic winter algorithm had a classification skill of 71.9% and a RMS cloud fraction error of 0.24 on the training data (Ebert 1987a, 1990).

Again starting in the west, high pressure over much of the Beaufort Sea during the week suppressed cloud cover, allowing only small amounts of stratus, stratocumulus, and layered clouds. On days 9-11 much of the clear area was classified as "broken sea ice" (class 5), when actually the sea ice cover was unbroken (class 4); the misclassification was probably the result of warm air advection. This illustrates one of the problems caused by the lack of visible data combined with relatively low spatial resolution. Stratus and layered clouds covered most of northwestern Canada until the last day of the period, while the Canadian Archipelago experienced primarily clear conditions. The frequent analysis of "ice sheet" (class 6) over Baffin and Ellesmere Islands reflects the cold textureless wintertime snow cover and should properly be labeled as "land with snow" (class 2) (although Ellesmere Island does have permanent ice cover at its higher elevations). Baffin Bay and Davis Strait also remained primarily clear throughout the period. Northern Greenland was cloud free through day 9, after which a large shield of high clouds developed in the easterly flow and propagated slowly eastward.

The conditions in southern Greenland, northern Europe, and the adjacent Greenland, Norwegian, and Barents Seas were dominated by the development and propagation of three cyclones. The first brought significant cloud cover with rain and snow to Sweden and Finland on days 7 and 8, while cumulus clouds filled the Norwegian Sea in the cold air behind the front. At this time a second cyclone was developing to the southeast of Greenland. As is intensified during days 8-10 the Greenland and Norwegian Seas were filled with layered and high clouds. The line of maximum cloud fraction along the occluded front can be seen in Figs. 14b and 15b. By day 12 the low pressure center was decaying over Svalbard and the cloud cover was diminishing in the Norwegian and Barents Seas. The third cyclone moved into western Norway on day 12, bringing with it large amounts of layered and high clouds.

The northwestern Soviet Union contained moderate amounts of cumulus and cirrus cloud cover early in the period, shifting to primarily stratiform cloudiness later on. Stratiform and high clouds over Novaya Zemlya and the Kara Sea on days 6 and 7 gave way to clear conditions during the next three days. Southwesterly flow ahead of the second cyclone led to significant high cloudiness on days 11 and 12. As in the summertime analysis, the stratiform clouds over the Kara Sea were misclassified as "stratus over land/water" (class 10) when in fact the surface was ice-covered. Sparse stratus and stratocumulus cloudiness was analyzed in the Laptev Sea, as well as in the central Arctic. However, the Arctic winter algorithm has difficulty detecting low clouds over sea ice at night (Table 3.12 of Ebert (1987a) indicates that "inversion stratus over snow/ice" was misclassified as clear 54% of the time) so the actual low cloud amounts in the central Arctic are probably much higher. In Siberia, cirrus and stratus clouds were present in large quantities between 60°E and 100°E during the entire period, probably as the result of moist air advection from the west. Further to the east clearer conditions prevailed.

c. Antarctic summer

Figures 17-23 show the cloud analyses for the Antarctic on 6-12 January 1984. The analyses are frequently incomplete near the northern edges because the satellite crossed 60°S in the early morning hours when part of the image was still dark. Since the Antarctic summer algorithm relies on data in the visible channels, the affected pixels were discarded. The classes used in the Antarctic summer algorithm are:

1. Ice haze
2. Land with snow
3. Open water
4. Unbroken sea ice
5. Broken sea ice
6. Ice sheet
7. Mixed surface types
8. Cs/As over land/water
9. Ci/Cc/Ac over land/water
10. St over land/water
11. Sc over land/water
12. Cu over land/water
13. Cs/As over snow/ice
14. Ci/Cc/Ac over snow/ice
15. St over snow/ice
16. Sc over snow/ice
17. Cu over snow/ice
18. High cloud over low cloud

Class 1 differs from the Arctic summer algorithm. A cloud type characteristic of low level ice crystal haze had a tenuous appearance in the visible imagery, a small signal in channel 3, and a slightly warmer brightness temperature than the surface in channel 4. The classification skill for the Antarctic summer algorithm was 85.1% when tested on the training data (Ebert 1987a, 1990).

In general, Antarctica was characterized by quite small fractional cloud cover over the interior of the continent, moderate amounts near the coasts, and nearly overcast conditions in the surrounding ocean. Cyclones developing and propagating eastward in the Southern Ocean near 60°S tended to have large amounts of low and layered clouds in their centers and eastern flanks. Examples of this are seen at 10°W on day 6 (see Fig. 3b of Ebert, 1990, for the sea level pressure chart for this day), 30°W on day 10, and especially 110°E on day 11, where the central pressure of 957 mb and the strong upper level support indicated a mature cyclone. The Weddell Sea and Ronne Ice Shelf were persistently covered by extensive stratus and layered cloud cover. The region just to the west of the Antarctic Peninsula was less cloudy. This is unusual from a climatic point of view, but the easterly air flow over the peninsula between days 6 and 10 may have caused downslope subsidence warming which suppressed the cloud cover.

Western Antarctica had varying amounts of low clouds during the week, with stratus as the dominant type. Layered clouds occurred close to the coast and near the base of the Antarctic Peninsula. Clouds occurred frequently over East Antarctica as well, but their horizontal extent was typically small so the total cloud fraction was often less than 20%. Low cloud types were the most common except in regions where the upper tropospheric circulation brought moister air from the north to form cirrus clouds (for example, at 45°E on day 8 and at 140°E on day 11).

d. Antarctic winter

The Antarctic classification and cloud fraction mosaics for 1-7 July 1984 (days 183-189) are shown in Figs. 24-30. Again, the analysis is incomplete near 60°S, this time because of solar radiation contaminating some of the channel 3 radiances. Since the wintertime algorithm requires purely thermal radiances, the affected pixels were discarded. The classification key for the Antarctic winter algorithm is given below:

1. Polar stratospheric cloud
2. Land with snow
3. Open water and thin ice
4. Unbroken sea ice
5. Broken sea ice
6. Ice sheet
7. Mixed surface types

10. St over land/water
11. Sc over land/water
12. Cu over land/water
13. Cs/As over snow/ice
14. Ci/Cc/Ac over snow/ice
15. St over snow/ice
16. Sc over snow/ice

8. Cs/As over land/water
9. Ci/Cc/Ac over land/water
17. Inversion St over snow/ice
18. High cloud over low cloud

The Antarctic winter algorithm had a classification skill of 78.4% on the training data (Ebert 1987a, 1990).

The significant feature in this set of imagery was the large 2-lobed polar stratospheric cloud over East Antarctica during the entire week. The brightness temperatures in the center of the lobes reached as low as 179 K, a full 19 degrees colder than the surface temperature recorded at nearby Vostok station. The calibration error of the AVHRR channel 4 sensor probably does not exceed a few degrees (see Appendix A of Ebert, 1990), so one plausible explanation for the very cold temperatures is the presence of an optically thick cloud at high altitude. The boundaries of this cloud are not sharp in the imagery–the sharp boundaries seen in the cloud fraction analysis are an artifact of the algorithm's temperature differentiation between "polar stratospheric cloud" (class 1), "cirrostratus over snow/ice" (class 13), and "ice sheet" (class 6), which all look qualitatively similar. The distinction between areas of "polar stratospheric cloud" and "cirrostratus over snow/ice" is in fact rather arbitrary and perhaps need not be made.

Cloud amounts were generally small over the rest of the continental interior, with inversion stratus being the dominant type. Even so, the true fractional coverage of inversion stratus may be greater because the Antarctic winter algorithm has difficulty detecting this cloud type over snow and ice at night (Table 3.15 of Ebert (1987a) indicates that 38% of class 17 training samples were misclassified as clear). Layered cloudiness occurred in greater amounts near the coastlines and in the vicinity of cyclones. Good examples of this are found near 120°W on days 184-188 and near 90°E throughout the period, where a strong ridge at 120°E blocked the movement of cyclones around the periphery of the continent. Stratus, stratocumulus, and layered clouds were analyzed in the Bellingshausen and Amundsen Seas and between 0° and 60°E. Cloud-free unbroken sea ice was analyzed in the northern Weddell Sea, while small amounts of stratus and occasional cirrus clouds were found closer to the Ronne Ice Shelf. The Weddell Sea constituted an outflow region for cold, dry continental air.

The automated analyses have not been independently verified against surface observations except for the first day of each analysis period (Ebert 1989, 1990). Such a validation encounters significant problems and uncertainties with regard to spatial and temporal resolution, not to mention the extreme sparsity of surface observations at the highest latitudes. However, the analyses described above show a high degree of coherence from day to day, as would be expected for naturally evolving and propagating systems. Also, the analyzed cloud types and amounts are consistent with the synoptic weather situations given by the ECMWF and Free University of Berlin charts. These two factors give credence to the algorithm and its results.

2. Weekly analyses

The mosaics of weekly mean total, low, and high cloud cover were averaged from all of the analyses during each week. The standard deviation of the total cloud fraction is a measure of the temporal variability, where low values correspond to persistent conditions. The mean low and high cloud fractions give a rough idea of the vertical distribution of cloud cover. The low cloud types include stratus, inversion stratus, stratocumulus, cumulus, ice haze, and the low cloud portion of class 18, "high cloud over low cloud." The high cloud types were cirrus/cirrocumulus/altocumulus (classes 9 and 14), cirrostratus/altostratus (classes 8 and 13), polar stratospheric cloud, and the high cloud portion of "high cloud over low cloud." No corrections for cloud overlap have been made to account for low clouds hidden from the view of the satellite, so the low cloud fraction analyzed for class 18 is likely to significantly underestimate the true low cloud amount.

For comparison, the high latitude climatologies of Huschke (1969) and Schwerdtfeger (1970) are shown in Fig. 31. These are based on relatively few surface observations and reconnaissance flights and may not be extremely reliable. (There is some feeling in the polar community that the Huschke summertime cloud amounts may be too high (Curry and Herman 1985, McGuffie et al. 1988).) However, they do convey a general sense of the annual cycle of cloudiness in the Arctic and Antarctic. The cloud fraction in the Arctic is much smaller in winter than in summer, and the Canadian Arctic tends to be less cloudy than the other regions. The Antarctic has a less pronounced annual cycle, but a greater contrast between the extensive cloudiness over the ocean and clearer conditions inland.

a. Arctic summer

Figures 32 a and b show the mean and standard deviation of total cloud fraction for the week of 1-7 July 1984. Figures 32 c and d separate the total cloud fraction into its low and high cloud components. The clearest regions were over land in Siberia and in the Canadian Archipelago, while the maximum cloud cover during the week was found over the Norwegian and Barents Seas. The greatest persistence was found here, with standard deviations below 20%. The greatest variability occurred in northern Canada in the vicinity of the decaying cyclone, and in the eastern Arctic. Low clouds occurred much more frequently than high clouds everywhere except in northwestern Canada where cirrus and layered clouds predominated. Large amounts of low cloudiness are typical of the summertime Arctic (Vowinckel and Orvig 1970). However, the analyzed total cloud fraction was everywhere smaller than the Huschke (1969) climatological values for July.

b. Arctic winter

The weekly mosaics for the Arctic during 6-12 January 1984 are shown in Fig. 33. Overall, the total cloud cover was less than in the summer case, being below 20% over much of the Canadian and Siberian Arctic. These amounts are far less than the climatological amounts of

Huschke (1969), partly due to an underestimation of stratus amounts as discussed in Section 1b. The cloudiest regions occurred over northwestern Canada, which had persistent layered clouds, and in northwestern Siberia. Vigorous synoptic activity led to high overall variability in the total cloud fraction, with standard deviations exceeding 40% in much of the Arctic. In contrast to the summer case, analyzed high cloud amounts were greater than low cloud amounts everywhere but in the Siberian Arctic. However, this should be interpreted with caution because the satellite cannot detect low clouds beneath a higher cloud layer. Also, many mid-level clouds of ice phase were grouped with high clouds in winter, while summertime mid-level clouds were more likely to be composed of liquid water and grouped with low clouds.

c. Antarctic summer

Figure 34 shows the weekly mosaics for the Antarctic on 6-12 January 1984. The total cloud fraction resembled the daily mosaics in that the continental interior was mostly cloud-free while the Southern Ocean had large fractional cloud amounts. This resembles the climatological field in January (Fig. 31b). The minimum standard deviation was less than 10% in the Weddell Sea, which was characterized by persistent stratus and layered clouds. The greatest variability occurred near the coasts of the continent where synoptic cyclones had a strong influence on the cloud conditions. Low cloud fractions were greater than high cloud fractions in all regions of the Antarctic except along the coast at 150°E. This is partially a result of warmer summertime temperatures favoring water phase clouds, as discussed above.

d. Antarctic winter

The weekly Antarctic mosaics for the week of 1-7 July 1984 are given in Fig. 35. The two-lobed polar stratospheric cloud and the clear regions on the Antarctic Plateau and in the Weddell Sea are markedly evident on the mean total cloud fraction map. The variabilities were also quite low in these regions, with standard deviations ranging between 10% and 20%. Large standard deviations were analyzed at the edges of the polar stratospheric cloud where slight shifts in position and temperature caused a shift in the analyzed sharp cloud boundary (refer to Section 1d). Except for the Weddell Sea, the oceanic regions showed moderate mean cloudiness with a standard deviation of approximately 30%, reflecting the evolution and motion of clouds during the 7-day period. This is somewhat smaller than the climatological cloud fraction in July given by Schwerdtfeger (1970) and may again be related to difficulties in analyzing low clouds over sea ice at night. Bearing in mind this shortcoming, low clouds and high clouds were present in roughly equal proportions in the Bellingshausen and Amundsen Seas and between 0° and 60°E. Low clouds were more common in the southern Weddell Sea, while high cloud predominated at the tip of the Antarctic Peninsula, in the ocean east of 60°E, and of course in the locations of the polar stratospheric cloud.

3. Surface and cloud type statistics

Figures 36-39 show the fractional area statistics of two surface types and five cloud types for each analysis period. In this analysis the layered clouds (class 18) have been assumed to contain Ci/Cc/Ac in the upper layer and stratus in the lower layer. The fractional area covered by each surface or cloud type is a quantitative measure of the prevalence of that type. The trends in the curves are a result of synoptic evolution during the week.

The mean frequency indicates the fraction of grid boxes which were classified as each surface and cloud type, and indicates how often that type occurred during the given period. Table 1 gives values of frequency for the four analysis periods. One can compare this to similar statistics computed by Hahn et al. (1982, 1984). Their cloud frequency represents the fraction of all ship and ground observations reporting each cloud type over a span of twelve years. Their values for ocean and land were area weighted by give zonal mean values; these are summarized in Table 2, and will be referred to as the "observed climatological frequencies" in the following discussion. The comparison is inexact because the two quantities differ with respect to cloud views (from space versus from the surface), spatial extent (60°-90°N versus 60°-80°N, also 2.5°x2.5° grid boxes versus point observations[1]), temporal domain (specific 7-day periods versus seasonal means), and cloud categories (compare Tables 1 and 2). Nevertheless, such a comparison is instructive because it indicates departures of the analyzed polar cloud fields of 6-12 January and 1-7 July from climatology.

a. Arctic summer

The mean cloud fraction in the Arctic for the week of 1-7 July 1984 was 0.56, with only small daily departures from this value. This is in contrast to Huschke's (1969) climatological value of 0.80 in July (however, his analysis does not include land regions). The area of clear land and water was much greater than that for clear snow and ice, first because the sea ice extent was nearing its summertime minimum, and also because the cloud-free conditions in Siberia had a large influence on the mean value. The frequency of grid boxes analyzed as cloud-free was 0.15, compared to the observed climatological value of 0.05 between 60°and 80°N. Stratus was by far the most extensive cloud type analyzed, and was diagnosed in 61% of the grid boxes. This was very close to the observed climatological frequency of 0.60 for combined stratus, stratocumulus, and nimbostratus. The fractional area covered by cumulus clouds was less than 1%. High stratiform clouds were less common than broken high clouds. Their combined frequency of 0.39 was on the same order as the observed climatological frequency of 0.45.

b. Arctic winter

The analyzed total cloud fraction of 0.37 in the Arctic was much smaller in the winter period than in the summer period, and smaller than the Huschke (1969) January climatological cloud fraction of 0.50. The large amount of clouds created by the passage of cyclones over Europe and Western Siberia was offset by the large clear regions in the central Arctic and Canadian

---

[1] The Hahn et al. (1982, 1984) statistics are also biased by the locations of the surface stations and shipping lanes.

Archipelago. The area of clear snow and ice was much greater than in summer, due partly to the seasonal increase in sea ice extent, but more importantly to the significant reduction in stratus cloud cover. As the total amount of high cloudiness increased in the Barents and Chukchi Seas, the area of clear snow and ice decreased (Fig. 37). The mean frequency of high clouds (0.21) was less than the mean frequency of low clouds (0.28), but their mean fractional coverage was greater (0.23 as opposed to 0.15), at least when viewed from above. The analyzed high cloud frequency was significantly lower than the observed climatological frequency of Ci/Cs/Cc/As/Ac of 0.56. The analyzed frequency for stratus and stratocumulus of 0.23 was also much lower than the observed stratiform frequency of 0.47, but some low clouds were undoubtedly missed by the classification algorithm. The week of 6-12 January 1984 may have been less cloudy than occurs climatologically.

c. Antarctic summer

The mean cloud fraction analyzed in the Antarctic region for the week of 6-12 January 1984 was 0.45, a balance between the very cloudy conditions in the Southern Ocean and the sparse cloudiness in the interior. The cloud cover was composed primarily of stratus and cirrus clouds, with cirrostratus and cumulus clouds occurring only rarely. There were only four grid boxes analyzed as clear ocean, for a frequency of 0.0001. The observed climatological frequency of clear sky is 0.01 between 60°S and 70°S. The analyzed frequency of 0.60 for combined stratus and stratocumulus cloudiness was comparable to the observed climatological frequency of 0.64 for combined St/Sc and Ns clouds in the Antarctic. However, the computed cirrus frequency of 0.18 was much smaller than the observed climatological value of 0.48. This may partially explain why the total cloud fraction was lower than has been climatologically observed (refer to Fig. 31b).

d. Antarctic winter

The Antarctic mean cloud fraction of 0.38 during 1-7 July 1984 comprised roughly equal amounts of cirrus, stratus, and polar stratospheric cloud, with much smaller quantities of cirrostratus, stratocumulus, and cumulus. The true amount of stratus cover may have been underestimated. In spite of that, stratus was the most commonly analyzed cloud type, with a frequency of 0.43. The data used by Hahn et al. (1982) did not contain enough cloud observations over the Southern Ocean to derive reliable cloud frequencies. They did, however, obtain enough clear observations to derive an observed climatological clear-sky frequency of 0.25 between 60°S and 90°S. The analyzed clear-sky frequency of 0.23 compares closely to this value. The cumulus frequency of 0.001 was the lowest of the cloud types.

4. Surface and cloudy albedos and brightness temperatures

In this section we examine the values of channel 1 (0.6 μm) albedo and channel 4 (11 μm) brightness temperature for the clear and cloudy portions of each of the eighteen surface and cloud classes (denoted α_S, T_S, α_C, and T_C, respectively). These were derived using the hybrid histogram-spatial coherence method.

The measured visible reflectances were normalized by the cosine of the solar zenith angle, but no other corrections for atmospheric effects were made. The term "cloudy" is used instead of "cloud" because the effects of the underlying surface on the measured albedo and brightness temperature, namely multiple reflections in channel 1 and upwelling longwave radiation in channel 4, have not been removed. Thus a semi-transparent cloud appears brighter and colder over a snow surface than over a land surface. This is seen in the results to be presented here, although there may also be morphological differences between clouds over land and clouds over snow. In principle it is possible to derive cloud optical properties from the satellite measured albedos and brightness temperatures given appropriate microphysical models (Kriebel et al. 1989), and to use these to estimate cloud temperature and surface radiative fluxes. (In fact, that was one of the original reasons for classifying cloud types when this study was begun.) In practice, however, small errors in analyzed cloud fraction and surface and cloudy albedos and brightness temperatures, combined with deviations of the true cloud microphysical properties from the idealized models, led to large errors in the cloud optical properties and unreasonable values and spatial variations in cloud temperatures and surface fluxes. These difficulties are certainly greater in the polar regions than elsewhere because a high proportion of clouds are semi-transparent and because multiple reflections are prevalent.

The means and standard deviations of surface and cloudy albedos and brightness temperatures are presented in both tabular and graphical form for each of the four analysis periods.

a. Arctic summer

Table 3 and Fig. 40 show the mean and standard deviation of α_s, T_S, α_c, and T_C for 1-7 July 1984. Open water had the darkest surface, with α_s=0.05, and clear land had an albedo of α_s=0.09. The albedo of unbroken sea ice, much of which was in a state of melting, was 0.49, equal to the 0.6 μm spectral albedo of an Arctic early season melt pond measured by Grenfell and Maykut (1977). Clear snow was the brightest surface in the imagery, with α_s between 0.61 and 0.65 (classes 2, 6, 17). The mean surface albedo for class 18 had an intermediate value of 0.34 and a large standard deviation because layered clouds were analyzed over many different surface types. The albedos for clouds occurring over snow and ice were much higher than those for clouds over land and water. The cumulus cloudiness over snow and ice had the highest mean albedo of 0.70.

Channel 1 separated surface and clouds quite well in classes 1-12. The channel 4 brightness temperature was effective for separating classes 8, 9, 11, 12, 13, and 18. (Classes 15-18 used channel 3 as the class-optimal channel but channel 3 radiances are not shown here.) The land had the warmest temperatures, at T_S=285-290 K (classes 1, 2, 12). The brightness temperature of water was approximately 277 K (classes 3, 5). The mean measured brightness temperature of sea ice was 271.3 K, close to the melting point of sea ice of 271.2 K (Untersteiner 1961). Clouds over snow and ice tended to have colder brightness temperatures and smaller variabilities than those over land and water. The exception was "Cs/As over land/water," which had a mean T_C of 243.8 K, but with a large variability. The brightness temperatures of the more tenuous cirrus clouds were 10-20° greater than that of cirrostratus. Cumulus clouds over land and water had a mean value of T_C=272.6 K. These cloud appeared to have small horizontal and vertical dimensions and were most frequently found over Siberia.

b. Arctic winter

The means and standard deviations of surface and cloudy channel 4 brightness temperatures are given in Table 4 and Fig. 41. Because of the high level of noise in channel 3 and the near redundancy of channel 5 with channel 4, the class-optimal channel was chosen as channel 4 for all classes.

All occurrences of cloud-free land were diagnosed as being snow-covered with a mean brightness temperature of 270.9 K. Open water and thin ice was only slightly warmer at T_S=272.3 K. The surface brightness temperature analyzed for classes 8-12 had high standard deviations because they included both the relatively warm Norwegian Sea and the cold land of Canada and Siberia (cloud over land/water included cloud overlying snow-covered land in this analysis). Similarly the surface temperatures for classes 13-17 had high variabilities because they represent both sea ice (T_S=233-247 K) and ice sheet (T_S=225 K). The unbroken sea ice statistics include some misclassified cases of inversion stratus, and may be slightly too warm. The low standard deviations of T_S and T_C computed for class 17 may have resulted from the algorithm correctly analyzing the "obvious" cases while failing to recognize the less obvious stratus cases. The differences between surface and cloudy brightness temperatures in classes 8-12 were generally sufficient to enable them to be distinguished using channel 4. This was less true for classes 13-18, and was undoubtedly a large source of error in estimating the fractional cloudiness over snow and ice in the wintertime Arctic.

c. Antarctic summer

Means and standard deviations of α_S, T_S, α_C, and T_C for the Antarctic during 6-12 January 1984 are given in Table 5 and Fig. 42. Most of the comments made for the Arctic summer case apply qualitatively to the Antarctic summer results. The snow albedo was slightly brighter in the Antarctic (α_S=0.62-0.70), as was the mean sea ice albedo (α_S=0.60) because surface melting is much less pronounced in the southern polar region. The mean surface albedo of α_S=0.10 for class 18 is certainly erroneous because layered clouds were analyzed over all surface types.[2] Channel 1 effectively separated clouds from land and water, but was quite useless for distinguishing clouds from snow and ice over Antarctica. In fact, some of the cloudy albedos were actually lower than the snow albedos. This can happen when the cloud itself is less reflective than the surface, and also if some of the shadowed pixels are included in the analysis as was the case for ice haze.

The water temperature in the Antarctic (T_S=272 K) was much colder than in the Arctic were warm currents influence the temperature of the Norwegian Sea. The brightness temperature of snow and ice ranged from 240.4 K (class 1) on the high plateau to 268.3 K for unbroken sea ice. The surface elevation strongly influences the snow and cloud temperatures. This is why brightness temperatures for low cloud classes (15, 16, 17), which were diagnosed over all parts of the continent, were colder than those for the high cloud classes (13, 14), which were diagnosed close to the coast. The standard deviation for T_S for classes 13-17 was also high. T_S for class 18 was too high for the reasons explained in Section 4a, and probably led to the overestimation of layered cloud fraction in West Antarctica. The high cloud brightness temperatures over land a water (classes 8, 9) were slightly warmer than the low cloud brightness temperatures because they were much more tenuous.

---

[2] After first analyzing the grid boxes closest to 60°S and building a class characteristic value of α_S appropriate for the ocean surface, when the algorithm encountered layered clouds over snow and ice it "forced" α_S to be close to the class characteristic value. The specific details of this method are described in Ebert (1989). This obvious defect is being corrected in an updated version of the algorithm.

d. Antarctic winter

Table 6 and Fig. 43 show the means and standard deviations of T_S and T_C for the week of 1-7 July 1984 in the Antarctic. Because the ocean surface was covered with sea ice in most of the domain, there were few incidences of open water and this ice (class 3) or clouds over land/water (classes 8-12). The mean brightness temperature of open water and thin ice in cloud-free conditions was 267.6 K, while beneath clouds it tended to be warmer by a few degrees. This is physically reasonable if the radiative loss at the surface under clear skies led to rapid cooling and refreezing. As in the Antarctic summer, the surface temperature beneath clouds of classes 13-17 had a large range and variability due to the effects of surface elevation. The brightness temperature of the ice sheet ranged between 212 K and 229 K (classes 1, 6, 13). The cloudy brightness temperatures for clouds over land and water were 20-35° greater than those for corresponding cloud types over snow and ice. The coldest clouds were polar stratospheric cloud (T_C=199 K) and cirrostratus over snow and ice (T_C=203 K). As discussed earlier, the distinction between these two cloud types may not be meaningful. Using channel 4 alone it was possible to separate cloud from surface in most classes except 15 and 17, which designate stratus over snow and ice.

References

Curry, J.A. and G.F. Herman, 1985: Relationships between large-scale heat and moisture budgets and the occurrence of Arctic stratus clouds. *Mon. Wea. Rev.*, **113**, 1441-1457.

Ebert, E.E., 1987a: Classification and analysis of surface and clouds at high latitudes from AVHRR multispectral satellite data. Ph.D. Thesis, University of Wisconsin-Madison.

Ebert, E.E., 1987b: A pattern recognition algorithm for distinguishing surface and cloud types in the polar regions. *J. Clim. Appl. Meteor.*, **26**, 1412-1427.

Ebert, E.E., 1989: Analysis of polar clouds from satellite imagery using pattern recognition with a statistical cloud analysis scheme. *J. Appl. Meteor.*, **28**, 382-399.

Ebert, E.E., 1990: Pattern recognition analysis of polar cloud during summer and winter. *Int. J. Remote Sensing*, in press.

European Centre for Medium Range Forecasting, 1984: Daily global analyses. July-September 1984.

Free University of Berlin, 1984: Berliner Wetterkarte, *Meteorologische Abhandlungen, Serie B*, **43**, No.33-6.

Grenfell, T.C. and G.A. Maykut, 1977: The optical properties of ice and snow in the Arctic Basin. *J. Glaciol.*, **18**, 445-463.

Hahn, C.J., S.G. Warren, J. London, R.M. Chervin and R. Jenne, 1982: Atlas of simultaneous occurrence of different cloud types over the ocean. NCAR Tech. Note NCAR/TN-201+STR, 212 pp.

Hahn, C.J., S.G. Warren, J. London, R.M. Chervin and R. Jenne, 1984: Atlas of simultaneous occurrence of different cloud types over land. NCAR Tech. Note NCAR/TN-241-STR.

Huschke, R.E., 1969: Arctic cloud statistics from "air-calibrated" surface weather observations. The RAND Corporation, RM-6173-PR, Santa Monica, Calif., 79 pp.

Kriebel, K.T., R.W. Saunders and G. Gesell, 1989: Determination of cloud optical properties from fully cloudy AVHRR pixel radiances. *Bietr. Phys. Atmosph.*

McGuffie, K., R.G. Barry, A. Schweiger, D.A. Robinson and J. Newell, 1988: Intercomparison of satellite-derived cloud analyses for the Arctic Ocean in spring and summer. *Int. J. Remote Sensing*, **9**, 447-467.

Schwerdtfeger, W., 1970: The climate of the Antarctic. *Climates of the Polar Regions*, S. Orvig, Ed., World Survey of Climatology, **14**, Elsevier, Amsterdam, 370 pp.

Untersteiner, N., 1961: On the mass and heat budget of Arctic sea ice. *Arch. Meteor. Geophys. Bioklim.*, **A12**, 151-182.

Vowinckel, E. and S. Orvig, 1970: The climate of the North Polar Basin. *Climates of the Polar Regions*, S. Orvig, Ed., World Survey of Climatology, **14** (Elsevier, Amsterdam).

WMO, 1956: *International Cloud Atlas* (WMO, Geneva).

	60° - 90° N 1-7 July 1984 Arctic summer	60° - 90° N 6-12 January 1984 Arctic winter	60° - 90° S 6-12 January 1984 Antarctic summer	60° - 90° S 1-7 July 1984 Antarctic winter
Frequency (clear land/water)	0.08[a]	0.04[h]	0.00[l]	0.00[l]
Frequency (clear snow/ice)	0.07[b]	0.44[i]	0.22[m]	0.23[m]
Frequency (Cs/As)	0.02[c]	0.05[c]	0.01[c]	0.04[c]
Frequency (Ci/Cc/Ac)	0.37[d]	0.16[d]	0.18[d]	0.16[d]
Frequency (St)	0.61[e]	0.14[j]	0.47[e]	0.43[j]
Frequency (Sc)	0.11[f]	0.09[f]	0.13[n]	0.04[f]
Frequency (Cu)	0.02[g]	0.05[k]	0.13[g]	0.00[k]
Frequency (PSC)				0.18[o]
Frequency (all clouds)	0.85	0.52	0.74	0.77

[a] Classes 1, 2, 3, 7
[b] Classes 4, 5, 6
[c] Classes 8, 13
[d] Classes 9, 14, 18
[e] Classes 10, 15, 18
[f] Classes 12, 17
[g] Classes 12, 17
[h] Classes 1, 2, 3
[i] Classes 4, 5, 6, 7
[j] Classes 10, 15, 17, 18
[k] Class 12
[l] Class 3
[m] Classes 2, 4, 5, 6, 7
[n] Classes 1, 11, 16
[o] Class 1

Table 1. Frequencies of surface and cloud types.

	60° - 80° N JJA	60° - 80° N DJF	60° - 90° S DJF	60° - 90° S JJA
Frequency (clear sky)	0.05 (0.03 / 0.07)	0.19 (0.08 / 0.29)	0.08 (0.01* / 0.15)	0.25 (0.08* / 0.42)
Frequency (sky obsc. by fog)	0.06 (0.09 / 0.03)	0.01 (0.01 / 0.00)	0.04 (0.07* / 0.01)	0.02 (0.03* / 0.00)
Frequency (Ci/Cs/Cc)	0.45 (0.44 / 0.45)	0.38 (0.35 / 0.40)	0.48 (0.38* / 0.58)	– (– / 0.37)
Frequency (As/Ac)	0.49 (0.53 / 0.45)	0.33 (0.35 / 0.31)	0.45 (0.52* / 0.37)	– (– / 0.21)
Frequency (Ns)	0.13 (0.14 / 0.12)	0.20 (0.24 / 0.16)	0.18 (0.20* / 0.16)	– (– / 0.10)
Frequency (St/Sc)	0.56 (0.62 / 0.50)	0.34 (0.47 / 0.23)	0.58 (0.74* / 0.42)	– (– / 0.13)
Frequency (Cu)	0.09 (0.10 / 0.09)	0.07 (0.13 / 0.01)	0.05 (0.08* / 0.02)	– (– / 0.01)
Frequency (Cb)	0.08 (0.08 / 0.08)	0.10 (0.19 / 0.02)	0.02 (0.03* / 0.01)	– (– / 0.00)
Frequency (Ci/Cs/Cc/As/Ac) †	0.69 (0.71 / 0.68)	0.56 (0.54 / 0.51)	0.75 (0.70 / 0.81)	– (– / –)
Frequency (St/Sc/Ns) §	0.60 (0.67 / 0.55)	0.47 (0.61 / 0.34)	0.64 (0.79 / 0.50)	– (– / –)

* Frequencies given for 60°S - 70°S

† Frequency (Ci/Cs/Cc/As/Ac) = Frequency (Ci/Cs/Cc) + Frequency (As/Ac) - Frequency (As/Ac) * Probabilty (As/Ac ⇒ Ci/Cs/Cc)

§ Frequency (St/Sc/Ns) = Frequency (Ns) + Frequency (St/Sc) - Frequency (St/Sc) * Probabilty (St/Sc ⇒ Ns)

Table 2. Seasonally and zonally averaged frequencies of cloud types based on data from Hahn et al. (1982, 1984). The quantity outside the parentheses is the area weighted frequency; the quantites inside the parentheses are the frequencies over ocean and over land.

Class	Number of Observations	Class-optimal Channel	Surface Ch. 1 Albedo α_s	Cloudy Ch. 1 Albedo α_c	Surface Ch. 4 Brightness Temperature (K) T_s	Cloudy Ch. 4 Brightness Temperature (K) T_s
1. Land	1016	1	0.09 (0.02)		285.5 (5.4)	
2. Snow on land[1]	1158	1	0.11 (0.05)	0.61 (0.08)	285.4 (4.9)	270.5 (9.8)
3. Open water	7	1	0.05 (0.02)		277.8 (1.7)	
4. Unbroken sea ice	1720	1	0.49 (0.07)		271.3 (2.4)	
5. Broken sea ice[2]	645	1	0.08 (0.04)	0.44 (0.07)	276.4 (2.4)	269.2 (2.8)
6. Ice sheet	125	1	0.63 (0.05)		259.3 (6.2)	
7. Mixed surface types[3]	766	2	0.07 (0.04)	0.47 (0.11)	277.9 (3.2)	270.8 (3.2)
8. Cs/As over land/water	230	4	0.10 (0.02)	0.54 (0.09)	280.2 (4.8)	243.8 (11.3)
9. Ci/Cc/Ac over land/water	2178	4	0.09 (0.02)	0.35 (0.10)	285.7 (6.9)	267.0 (8.8)
10. St over land/water	4529	1	0.09 (0.03)	0.42 (0.09)	278.7 (5.9)	269.0 (5.1)
11. Sc over land/water	850	1	0.09 (0.02)	0.36 (0.10)	283.4 (5.3)	268.3 (5.3)
12. Cu over land/water	467	1	0.10 (0.02)	0.26 (0.05)	290.2 (5.4)	272.6 (6.4)
13. Cs/As over snow/ice	394	4	0.50 (0.06)	0.60 (0.04)	265.5 (3.3)	248.9 (6.2)
14. Ci/Cc/Ac over snow/ice	1615	4	0.49 (0.14)	0.57 (0.11)	269.7 (2.7)	258.0 (4.3)
15. St over snow/ice	7752	3	0.52 (0.10)	0.57 (0.08)	269.1 (3.5)	263.1 (4.4)
16. Sc over snow/ice	3023	3	0.47 (0.09)	0.56 (0.07)	268.0 (4.3)	260.3 (4.6)
17. Cu over snow/ice	178	3	0.65 (0.07)	0.70 (0.06)	267.0 (3.4)	258.9 (4.4)
18. High cloud over low cloud	9806	3,4	0.34 (0.17)	0.54 (0.14)	273.4 (5.0)	255.3 (7.5)

Table 3. Means (standard deviations) of surface and cloudy albedos and brightness temperatures for the Arctic during 1-7 July 1984.

---

[1] "Surface" refers to land, "Cloud" refers to snow.

[2] "Surface" refers to open water, "Cloud" refers to sea ice.

[3] "Surface" refers to warmer, darker surface, "Cloud" to colder, brighter surface.

	Class	Number of Observations	Class-optimal Channel	Surface Ch. 4 Brightness Temperature (K) T_s	Cloudy Ch. 4 Brightness Temperature (K) T_c
1.	Land	0	4		
2.	Snow on land	1119	4	270.9 (3.5)	
3.	Open water and thin ice	267	4	272.3 (2.4)	
4.	Unbroken sea ice	9202	4	233.7 (7.0)	
5.	Broken sea ice[1]	2557	4	270.0 (0.4)	243.2 (4.2)
6.	Ice sheet	1529	4	225.0 (5.6)	
7.	Mixed surface types[2]	2230	4	260.9 (5.1)	237.2 (7.6)
8.	Cs/As over land/water	298	4	261.3 (3.2)	227.3 (6.1)
9.	Ci/Cc/Ac over land/water	2897	4	261.1 (4.7)	245.4 (5.5)
10.	St over land/water	2010	4	260.4 (3.7)	246.9 (6.9)
11.	Sc over land/water	272	4	265.1 (7.5)	243.6 (4.6)
12.	Cu over land/water	1680	4	267.4 (7.1)	250.2 (3.1)
13.	Cs/As over snow/ice	1622	4	232.7 (6.9)	227.0 (4.7)
14.	Ci/Cc/Ac over snow/ice	374	4	246.5 (9.9)	231.4 (8.7)
15.	St over ice sheet	551	4	236.9 (6.3)	221.3 (5.9)
16.	Sc over snow/ice	2937	4	241.3 (4.6)	231.3 (3.6)
17.	Inversion St over snow/ice	3003	4	232.4 (1.3)	242.5 (3.7)
18.	High cloud over low cloud	2390	4	248.6 (9.7)	235.0 (7.4)

Table 4. Means (standard deviations) of surface and cloudy brightness temperatures for the Arctic during 6-12 January 1984.

---

[1] "Surface" refers to open water, "Cloud" refers to sea ice.

[2] "Surface" refers to warmer surface, "Cloud" to colder surface.

Class	Number of Observations	Class-optimal Channel	Surface Ch. 1 Albedo α_s	Cloudy Ch. 1 Albedo α_c	Surface Ch. 4 Brightness Temperature (K) T_s	Cloudy Ch. 4 Brightness Temperature (K) T_s
1. Ice haze	1148	3	0.67 (0.04)	0.62 (0.05)	240.4 (5.4)	241.9 (5.8)
2. Snow on land[1]	134	1	0.09 (0.02)	0.67 (0.04)	267.4 (3.9)	252.0 (3.8)
3. Open water	4	1	0.05 (0.01)		272.3 (0.4)	
4. Unbroken sea ice	30	1	0.60 (0.12)		268.3 (1.6)	
5. Broken sea ice[2]	0	1				
6. Ice sheet	5562	1	0.68 (0.05)		243.3 (9.0)	
7. Mixed surface types[3]	130	1	0.06 (0.02)	0.70 (0.05)	272.1 (1.2)	264.8 (4.4)
8. Cs/As over land/water	27	4	0.09 (0.01)	0.62 (0.07)	273.2 (2.1)	262.8 (6.9)
9. Ci/Cc/Ac over land/water	35	4	0.07 (0.02)	0.55 (0.18)	271.8 (0.8)	262.8 (5.6)
10. St over land/water	1469	1	0.08 (0.02)	0.53 (0.10)	272.0 (1.3)	257.3 (5.9)
11. Sc over land/water	557	1	0.08 (0.02)	0.44 (0.10)	272.0 (0.9)	256.1 (4.8)
12. Cu over land/water	29	1	0.06 (0.02)	0.45 (0.13)	272.6 (0.6)	260.9 (4.4)
13. Cs/As over snow/ice	124	4	0.70 (0.07)	0.66 (0.09)	251.1 (5.5)	235.3 (7.2)
14. Ci/Cc/Ac over snow/ice	1129	4	0.68 (0.05)	0.64 (0.06)	255.1 (5.8)	241.9 (4.0)
15. St over snow/ice	7700	3	0.62 (0.07)	0.66 (0.06)	246.6 (6.5)	251.0 (6.7)
16. Sc over snow/ice	1772	3	0.63 (0.08)	0.69 (0.06)	249.2 (5.3)	254.6 (6.6)
17. Cu over snow/ice	3494	3	0.67 (0.05)	0.74 (0.06)	245.2 (7.4)	252.7 (8.5)
18. High cloud over low cloud	3550	3,4	0.10 (0.02)	0.63 (0.13)	271.6 (0.9)	252.2 (9.1)

Table 5. Means (standard deviations) of surface and cloudy albedos and brightness temperatures for the Antarctic during 6-12 January 1984.

---

[1] "Surface" refers to land, "Cloud" refers to snow.

[2] "Surface" refers to open water, "Cloud" refers to sea ice.

[3] "Surface" refers to warmer, darker surface, "Cloud" to colder, brighter surface.

	Class	Number of Observations	Class-optimal Channel	Surface Ch. 4 Brightness Temperature (K) T_s		Cloudy Ch. 4 Brightness Temperature (K) T_c	
1.	Polar stratospheric cloud	6687	4	211.8	(3.6)	199.0	(6.4)
2.	Snow on land	18	4	244.5	(5.3)		
3.	Open water and thin ice	74	4	267.6	(1.9)		
4.	Unbroken sea ice	2444	4	242.7	(5.9)		
5.	Broken sea ice[1]	53	4	268.0	(2.1)	249.2	(3.2)
6.	Ice sheet	5698	4	220.0	(8.2)		
7.	Mixed surface types[2]	267	4	258.1	(7.7)	238.7	(6.4)
8.	Cs/As over land/water	3	4	267.1	(0.6)	237.8	(2.9)
9.	Ci/Cc/Ac over land/water	41	4	270.0	(2.1)	244.6	(5.4)
10.	St over land/water	56	4	268.1	(2.0)	253.5	(4.3)
11.	Sc over land/water	606	4	269.8	(1.9)	260.5	(4.2)
12.	Cu over land/water	55	4	271.5	(1.4)	251.8	(6.3)
13.	Cs/As over snow/ice	1456	4	228.8	(10.8)	202.8	(7.8)
14.	Ci/Cc/Ac over snow/ice	2898	4	241.9	(7.6)	224.9	(4.6)
15.	St over snow/ice	6191	4	246.8	(4.9)	234.9	(5.7)
16.	Sc over snow/ice	795	4	254.4	(7.5)	238.8	(4.2)
17.	Inversion St over snow/ice	6906	4	223.4	(9.4)	244.6	(4.2)
18.	High cloud over low cloud	3052	4	266.8	(0.9)	237.8	(12.7)

Table 6. Means (standard deviations) of surface and cloudy brightness temperatures for the Antarctic during 1-7 July 1984.

---

[1] "Surface" refers to open water, "Cloud" refers to sea ice.

[2] "Surface" refers to warmer surface, "Cloud" to colder surface.

Figure Captions

Fig. 1. The north polar region.

Fig. 2. The south polar region, including some manned research stations.

Figs. 3-9. (a) Automated classification and (b) cloud fraction analyses for the Arctic during 1-7 July 1984. Refer to p. 4 for a key to the surface and cloud types for the Arctic summer algorithm.

Figs. 10-16. (a) Automated classification and (b) cloud fraction analyses for the Arctic during 6-12 January 1984. Refer to p. 5 for a key to the surface and cloud types for the Arctic winter algorithm.

Figs. 17-23. (a) Automated classification and (b) cloud fraction analyses for the Antarctic during 6-12 January 1984. Refer to p. 7 for a key to the surface and cloud types for the Antarctic summer algorithm.

Figs. 24-30. (a) Automated classification and (b) cloud fraction analyses for the Antarctic during 1-7 July 1984. Refer to p. 9 for a key to the surface and cloud types for the Antarctic winter algorithm.

Fig. 31. Annual variation of cloud fraction with region in (a) the Arctic (Huschke 1969), and (b) the Antarctic (from the climatic tables of Schwerdtfeger 1970).

Fig. 32. (a) Mean total cloud fraction, (b) standard deviation of total cloud fraction, (c)

mean low cloud fraction, and (d) mean high cloud fraction for the Arctic during 1-7 July 1984.

Fig. 33. As in Fig. 32, for the Arctic during 6-12 January 1984.

Fig. 34. As in Fig. 32, for the Antarctic during 6-12 January 1984.

Fig. 35. As in Fig. 32, for the Antarctic during 1-7 January 1984.

Fig. 36. Fractional area covered by each surface and cloud type during the week of 1-7 July 1984 in the Arctic.

Fig. 37. Fractional area covered by each surface and cloud type during the week of 6-12 January 1984 in the Arctic.

Fig. 38. Fractional area covered by each surface and cloud type during the week of 6-12 January 1984 in the Antarctic.

Fig. 39. Fractional area covered by each surface and cloud type during the week of 1-7 July 1984 in the Antarctic.

Fig. 40. Mean and standard deviation of channel 1 albedo and channel 4 brightness temperatures for the Arctic during 1-7 July 1984. Closed circles denote the surface values, open circles denote the cloud values, and error bars indicate one standard deviation on each side of the mean. For the interpretation of "cloud" in classes 2, 5, and 7, refer to the footnote in Table 3.

Fig. 41. Mean and standard deviation of channel 4 brightness temperatures for the Arctic during 6-12 January 1984. For the interpretation of "cloud" in classes 5 and 7, refer to the footnote in Table 4.

Fig. 42. Mean and standard deviation of channel 1 albedo and channel 4 brightness temperatures for the Antarctic during 6-12 January 1984. For the interpretation of "cloud" in classes 2, 5, and 7, refer to the footnote in Table 5.

Fig. 43. Mean and standard deviation of channel 4 brightness temperatures for the Antarctic during 1-7 July 1984. For the interpretation of "cloud" in classes 5 and 7, refer to the footnote in Table 6.

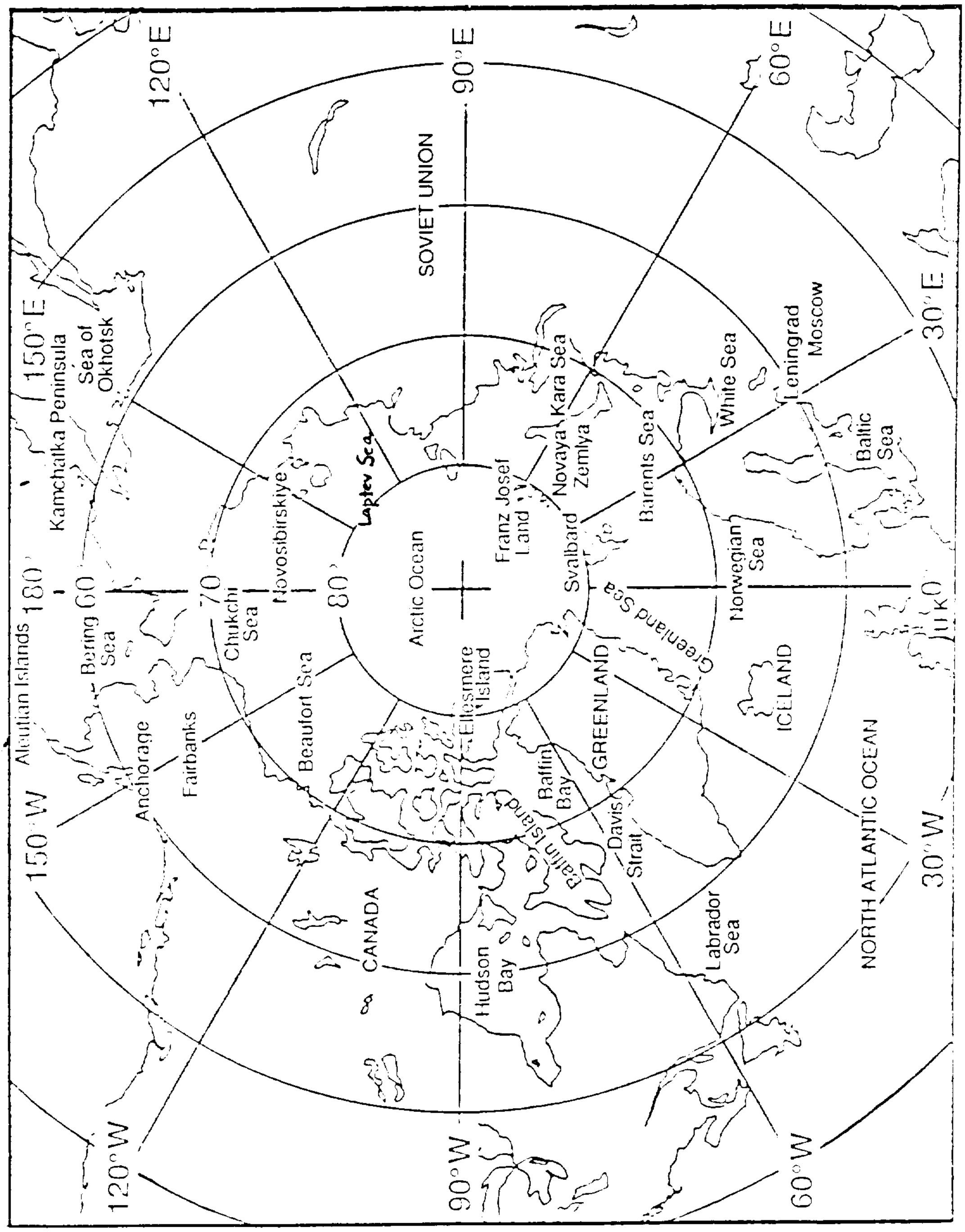

Figure 1. The north polar region.

ORIGINAL PAGE IS
OF POOR QUALITY

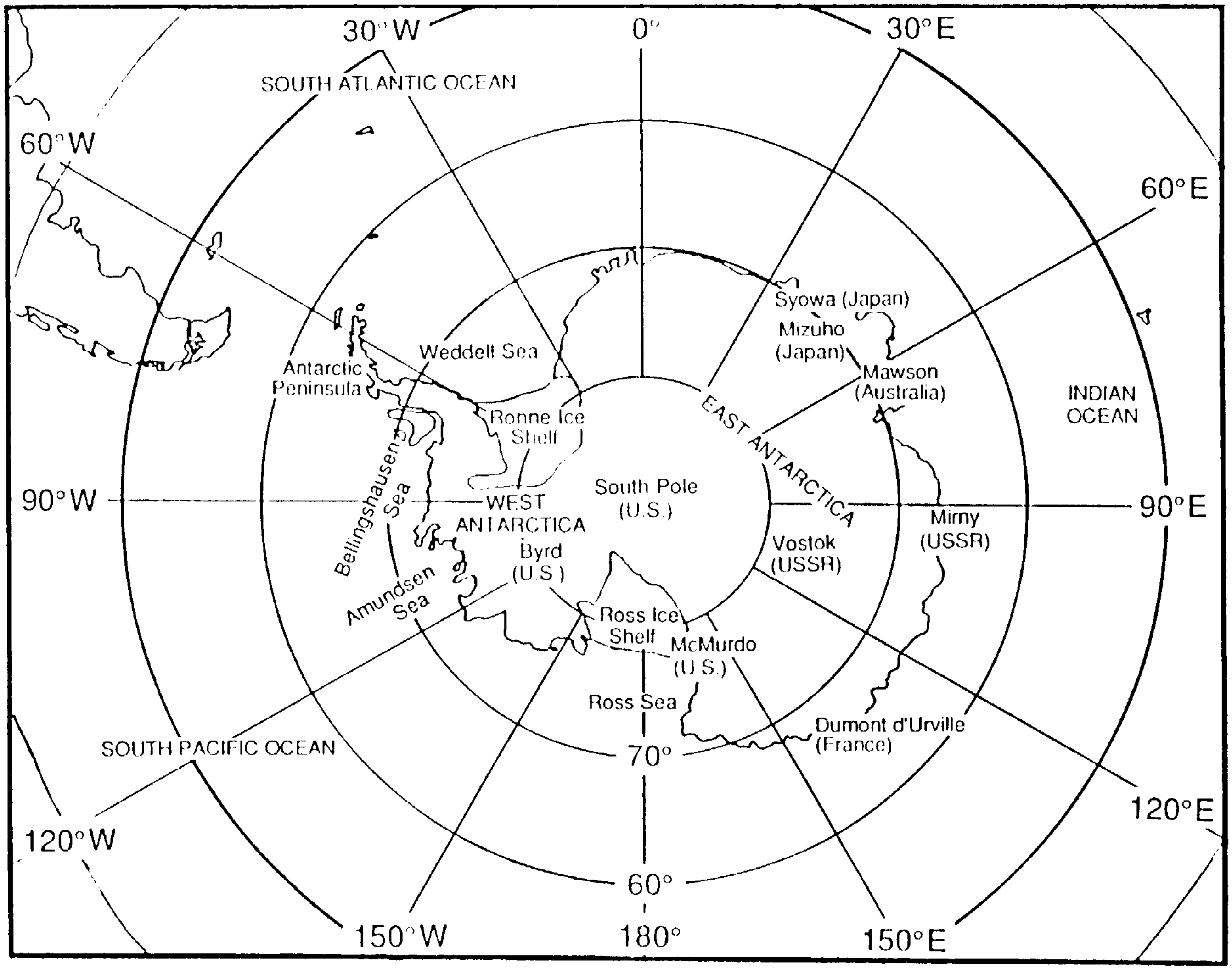

Figure 2. The south polar region, including some manned research stations.

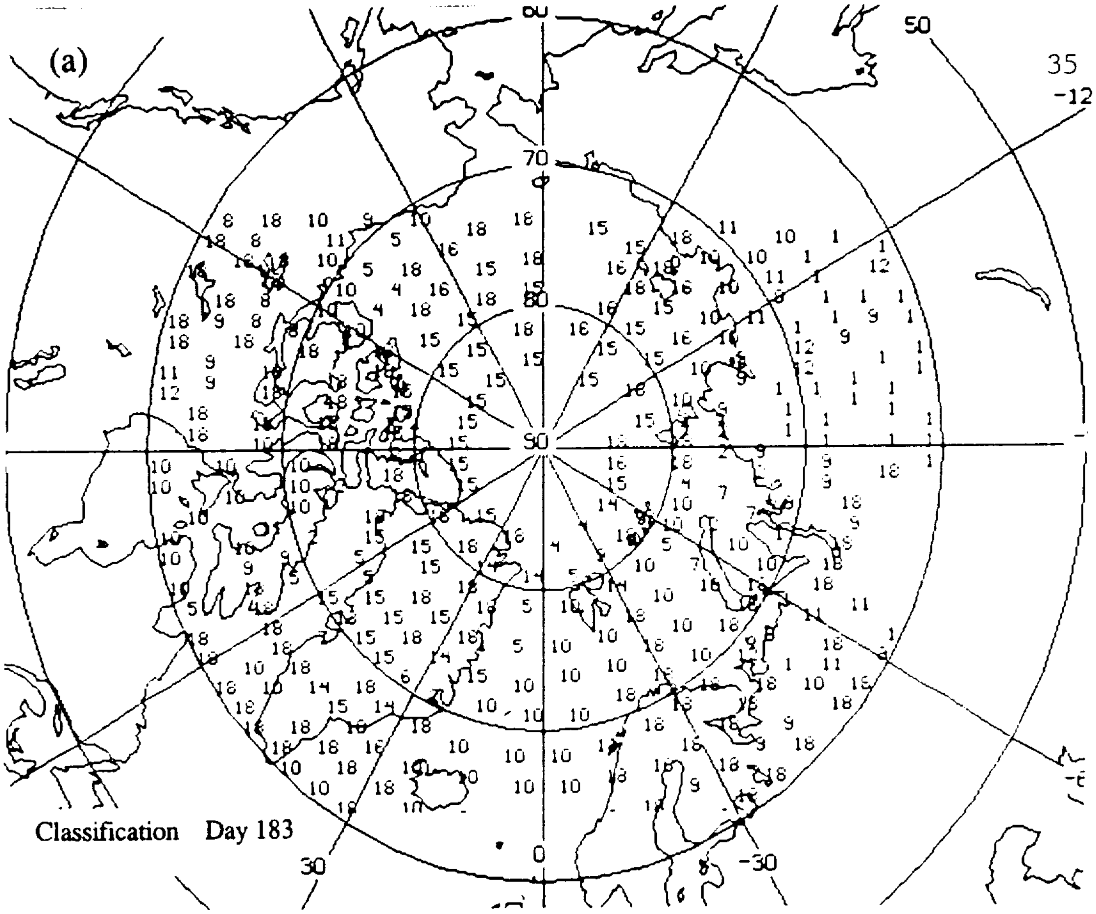

Classification Day 183

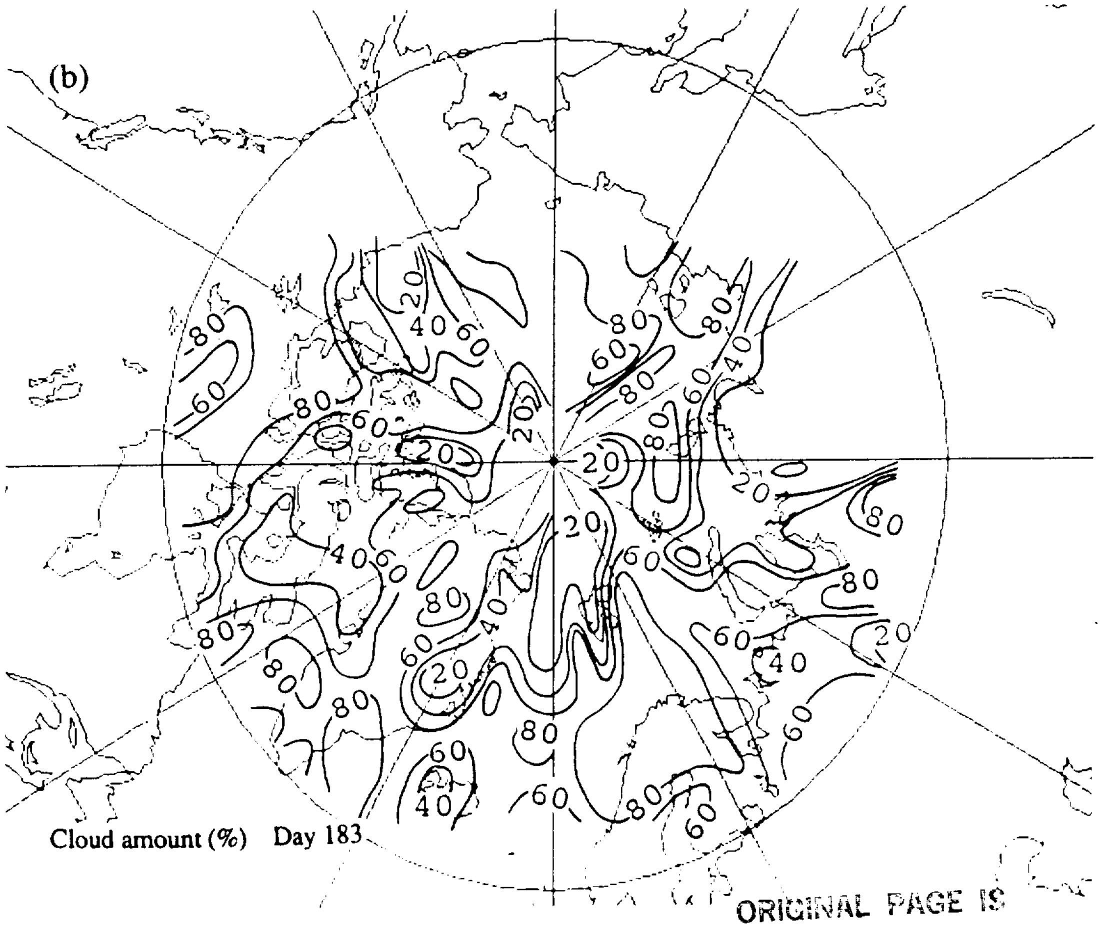

Cloud amount (%) Day 183

Figure 3

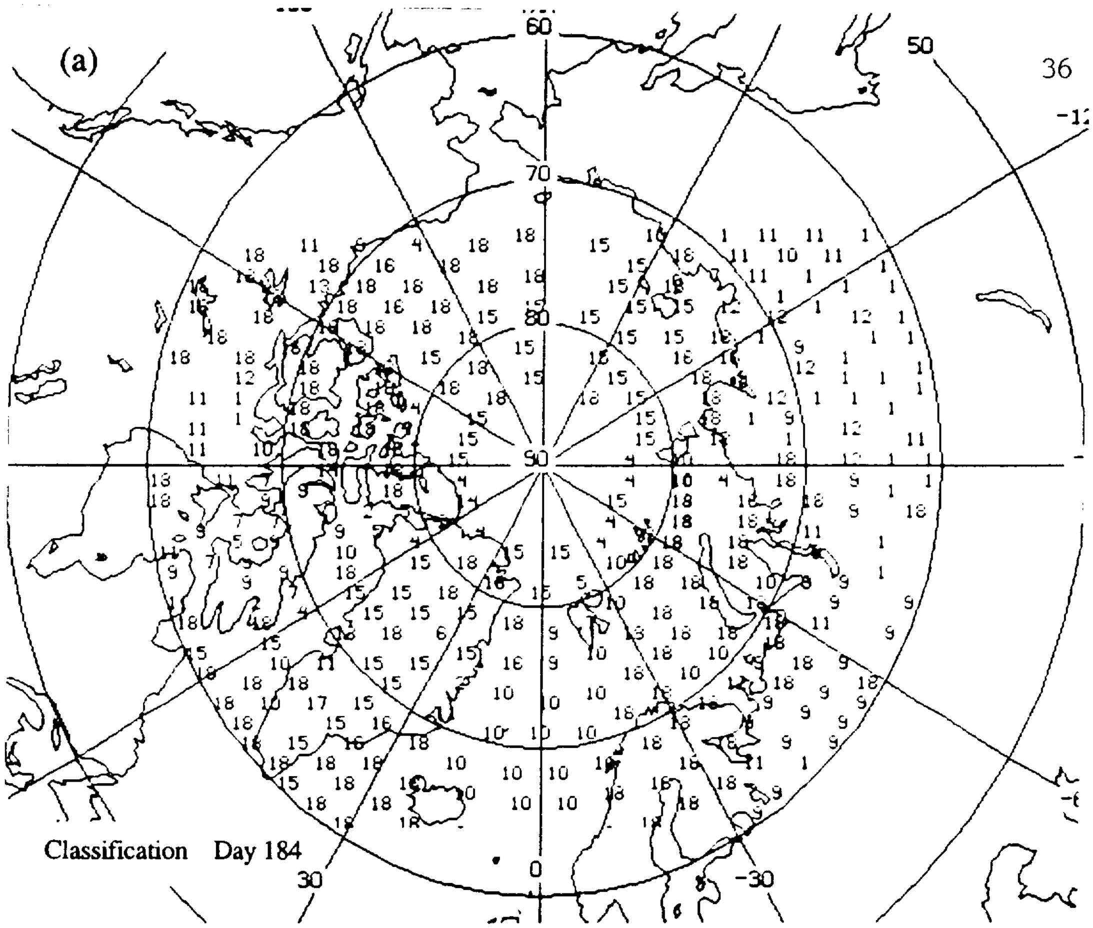

Classification Day 184

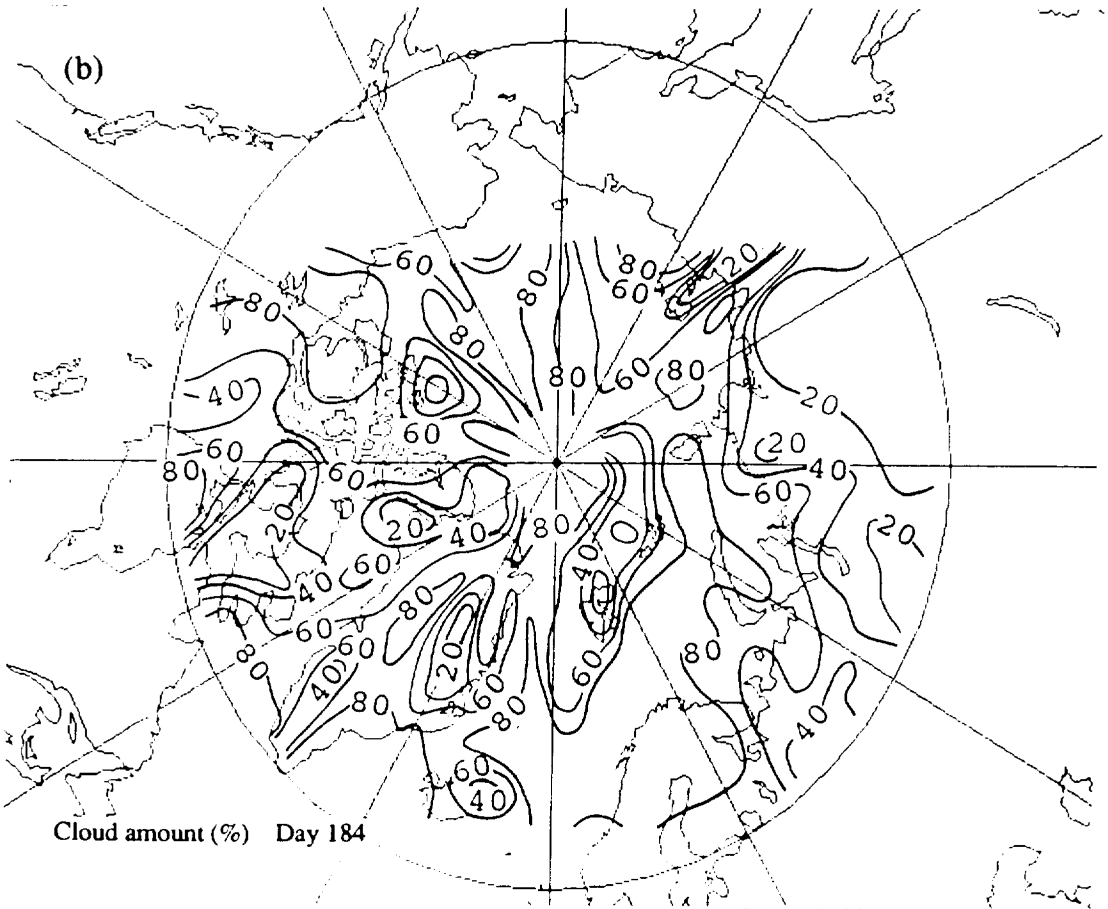

Cloud amount (%) Day 184

Figure 4

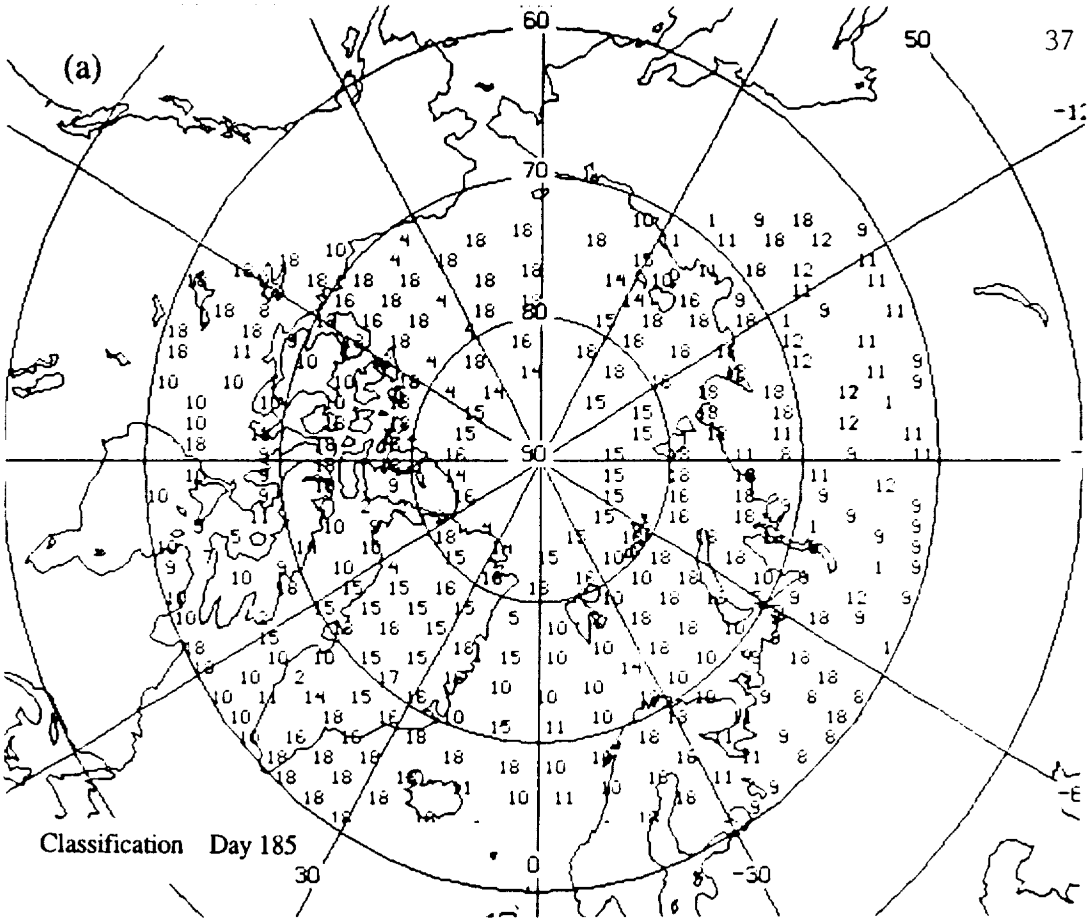

Classification Day 185

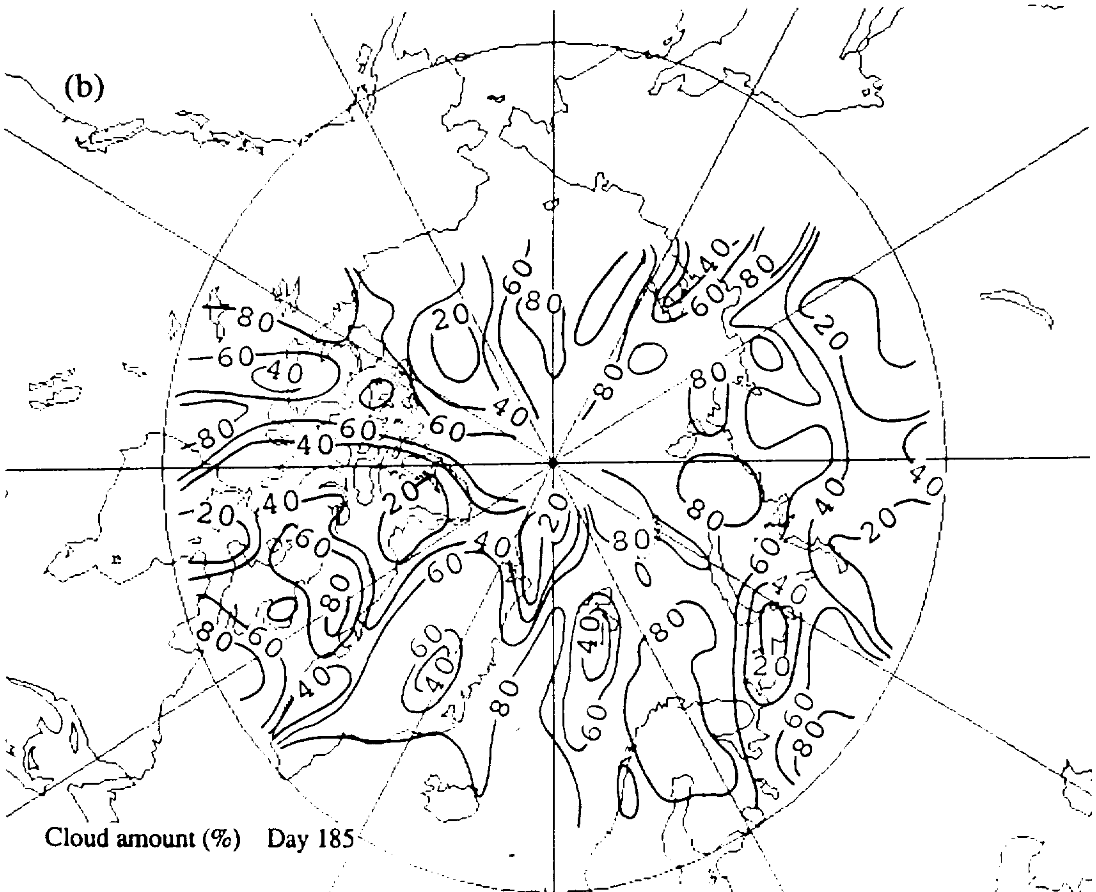

Cloud amount (%) Day 185

Figure 5

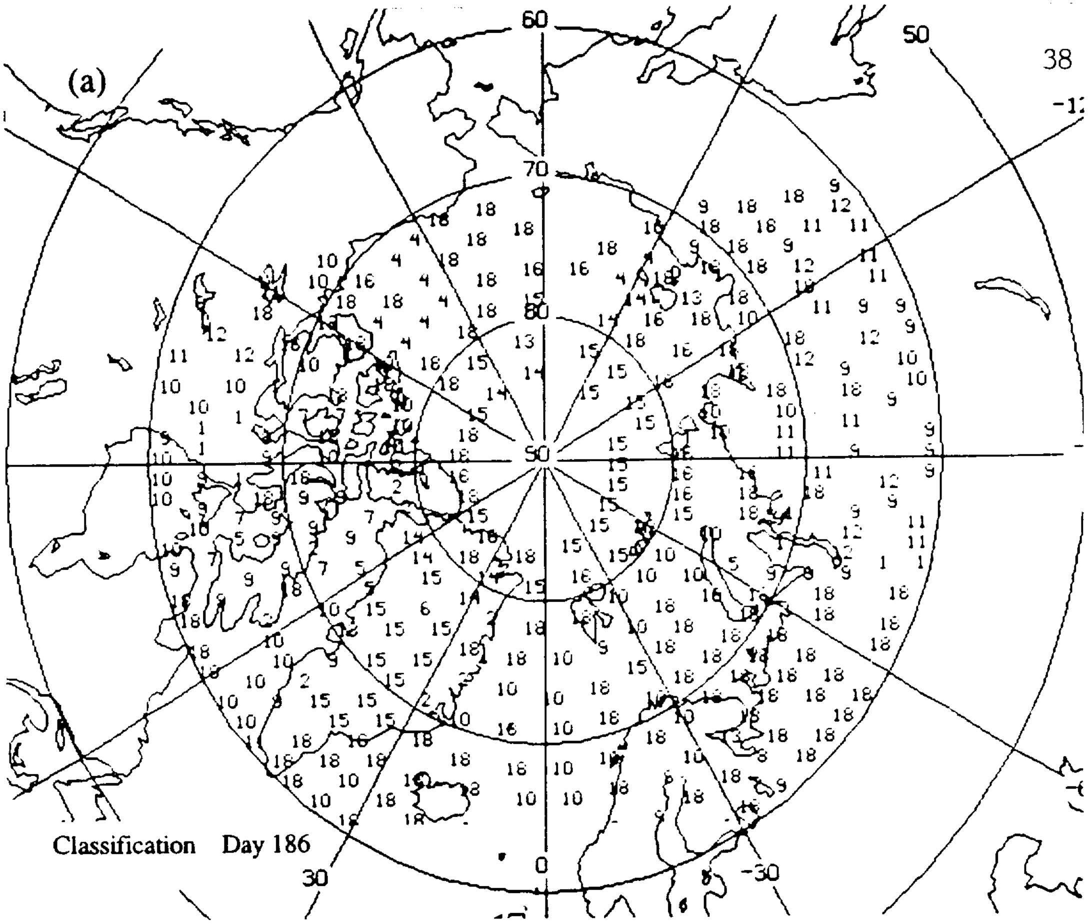

Classification Day 186

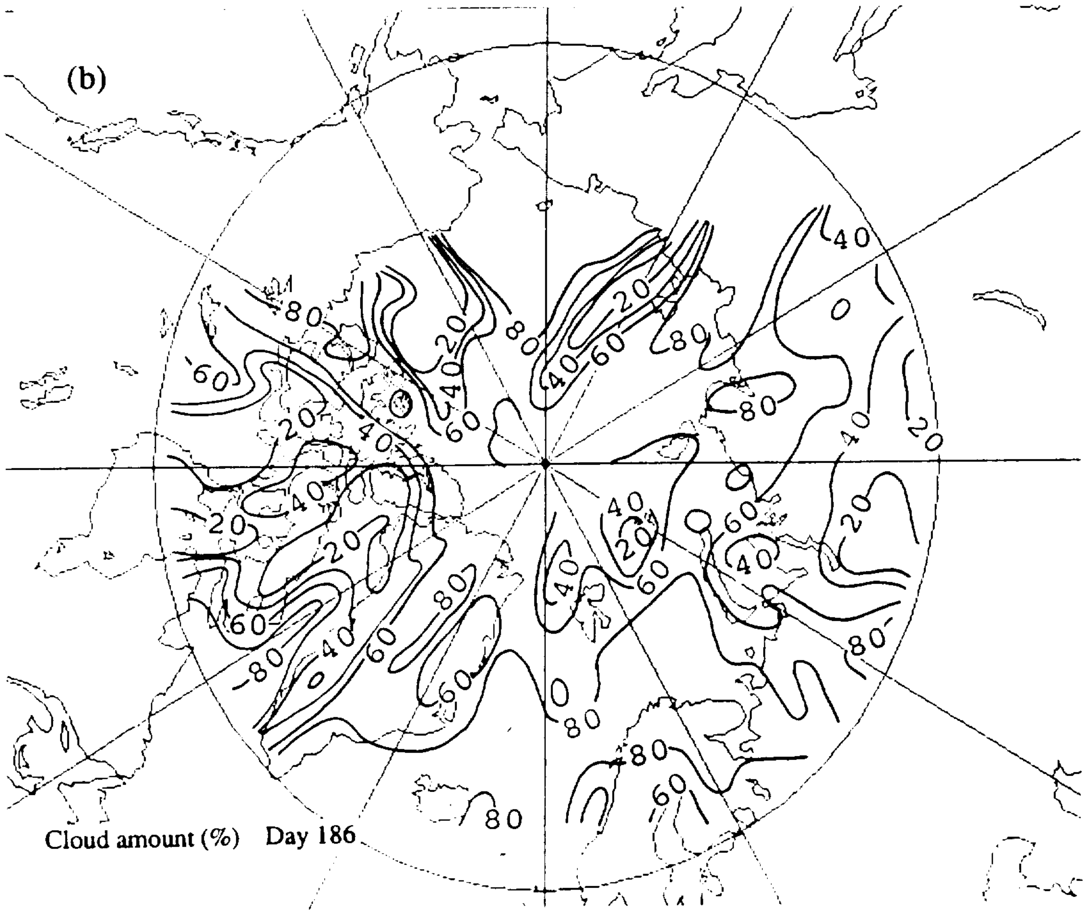

Cloud amount (%) Day 186

Figure 6

ORIGINAL PAGE IS
OF POOR QUALITY

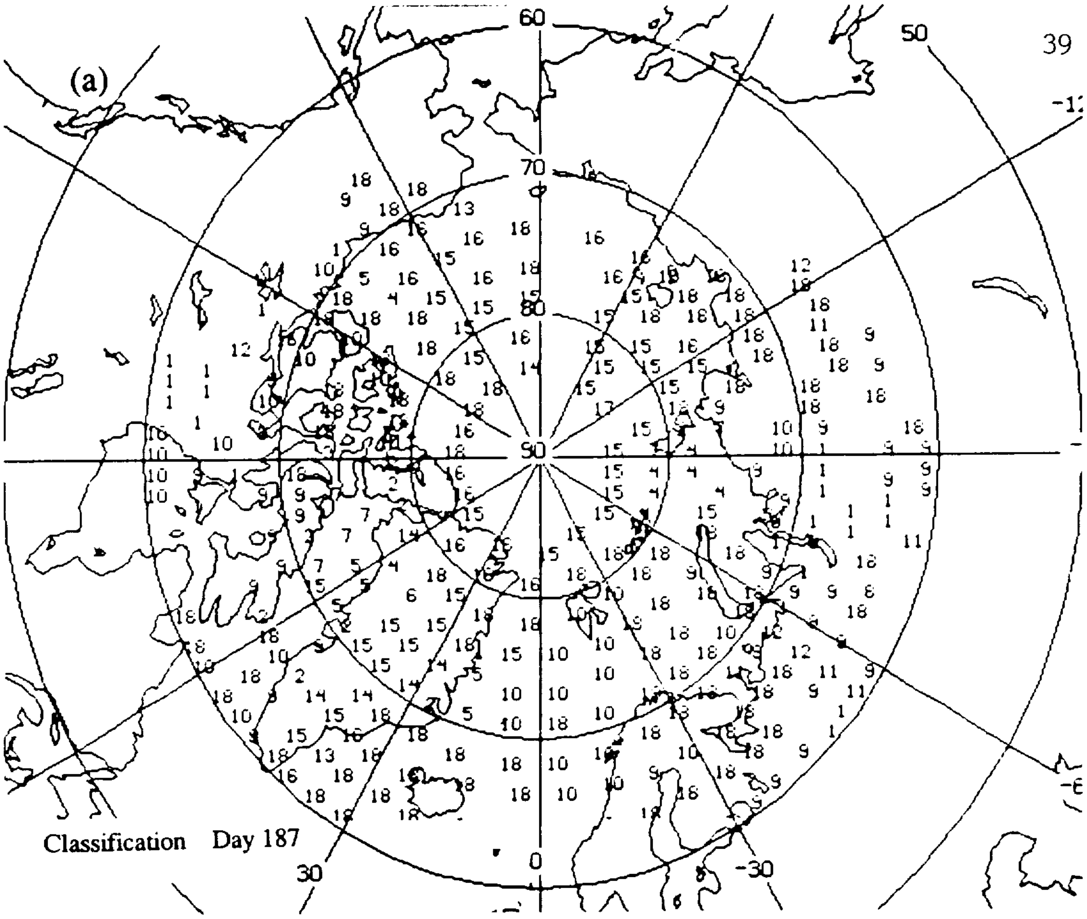

Classification Day 187

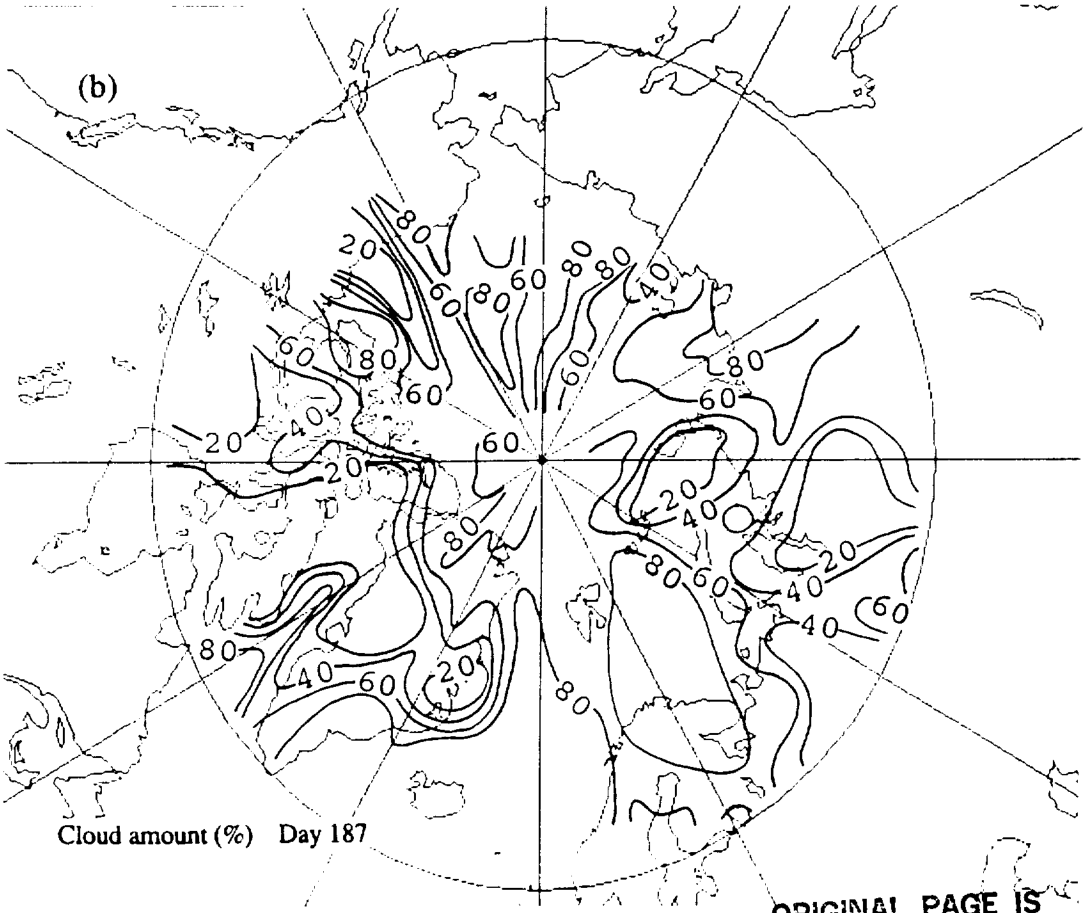

Cloud amount (%) Day 187

Figure 7

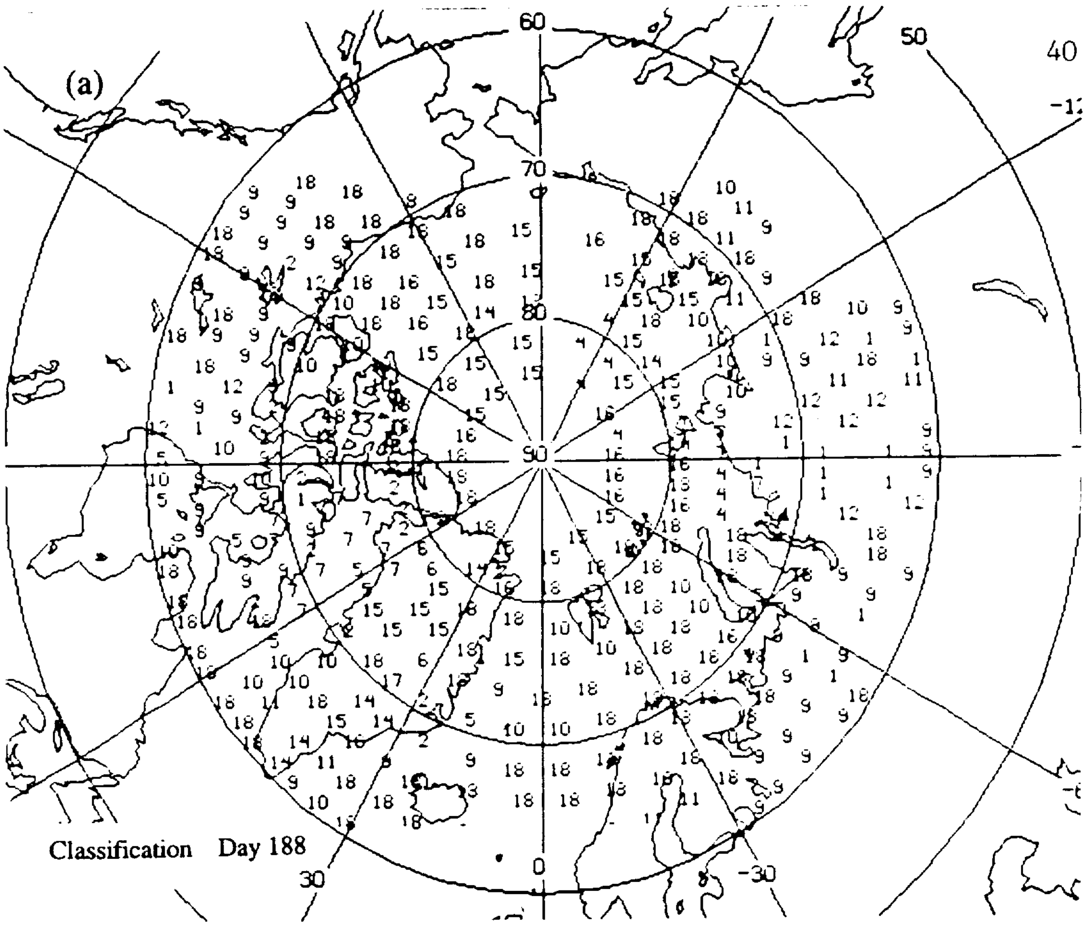

Classification Day 188

Cloud amount (%) Day 188

Figure 8

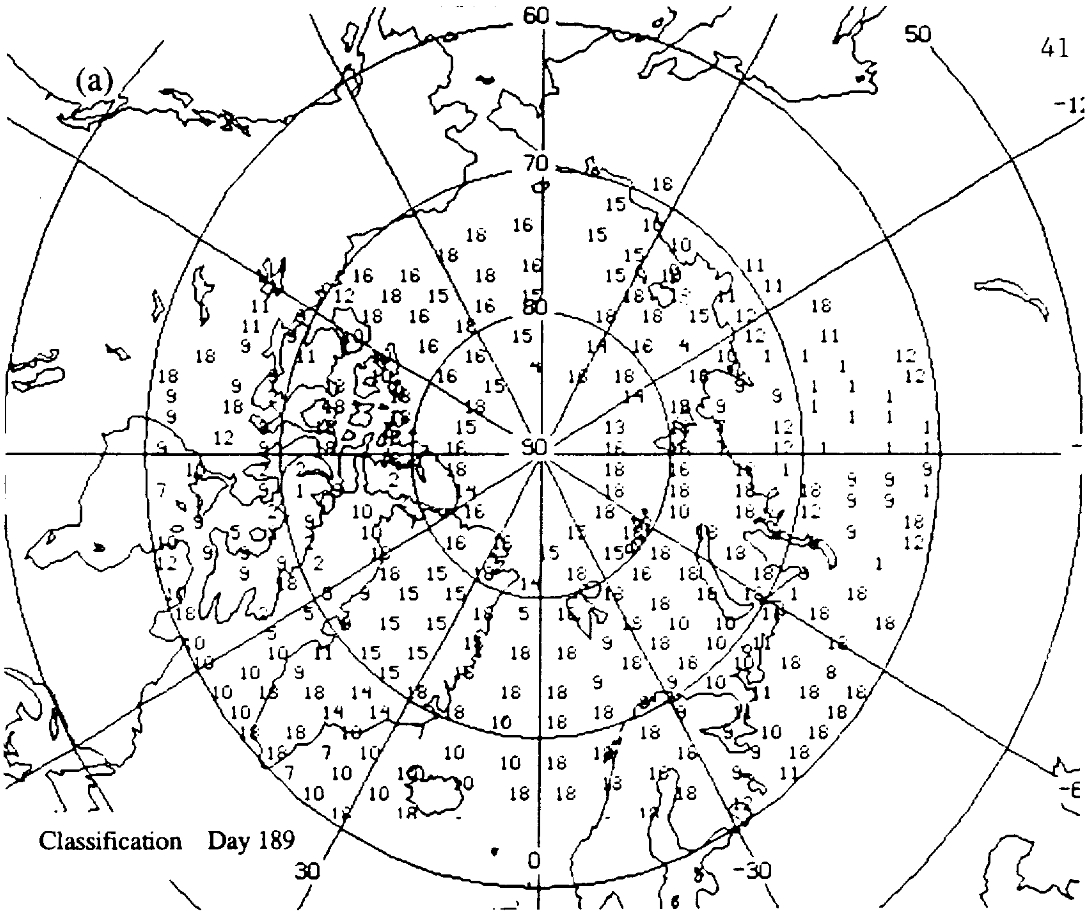

Classification Day 189

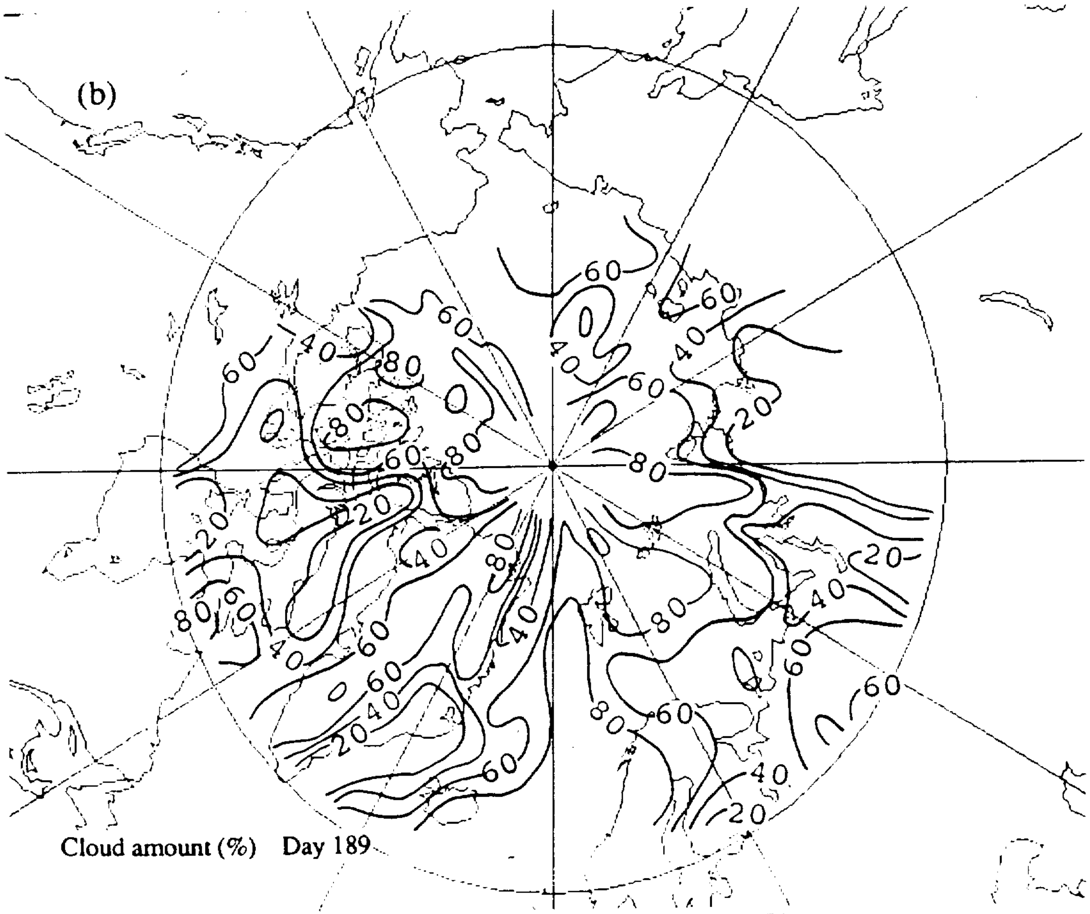

Cloud amount (%) Day 189

Figure 9

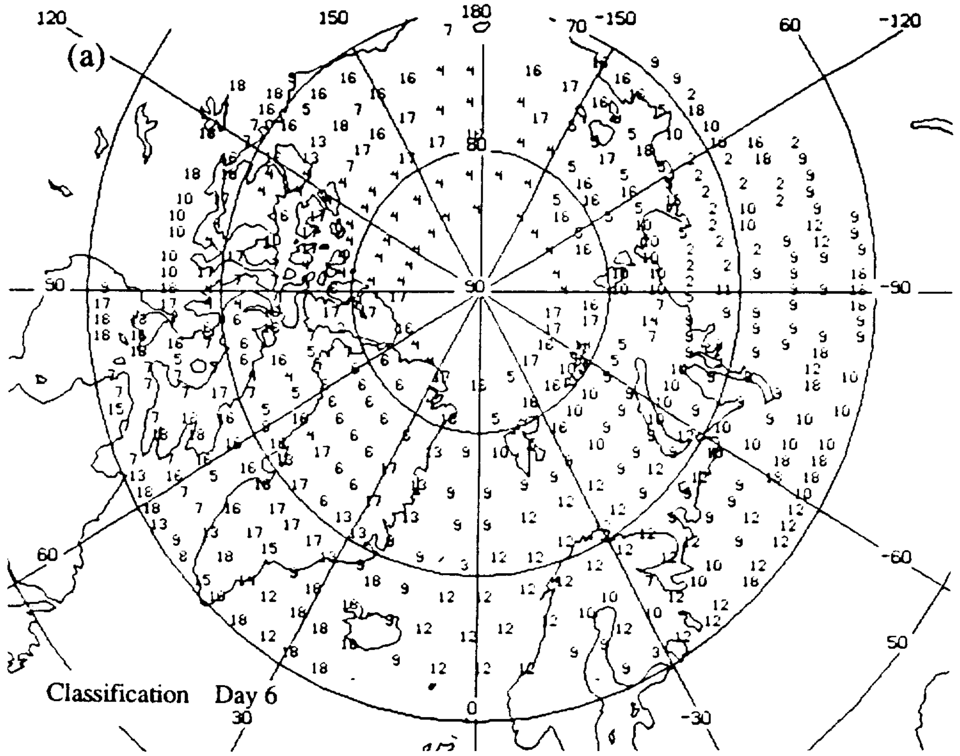

Classification Day 6

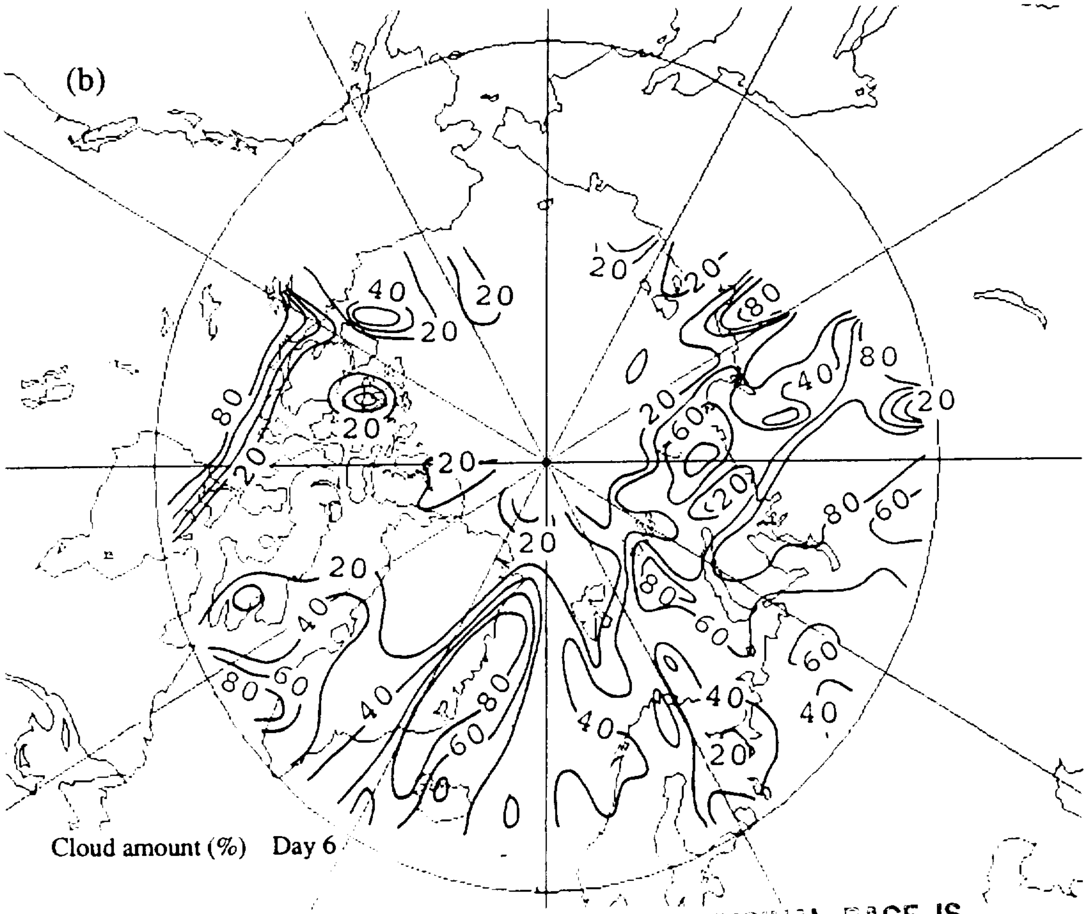

Cloud amount (%) Day 6

Figure 10

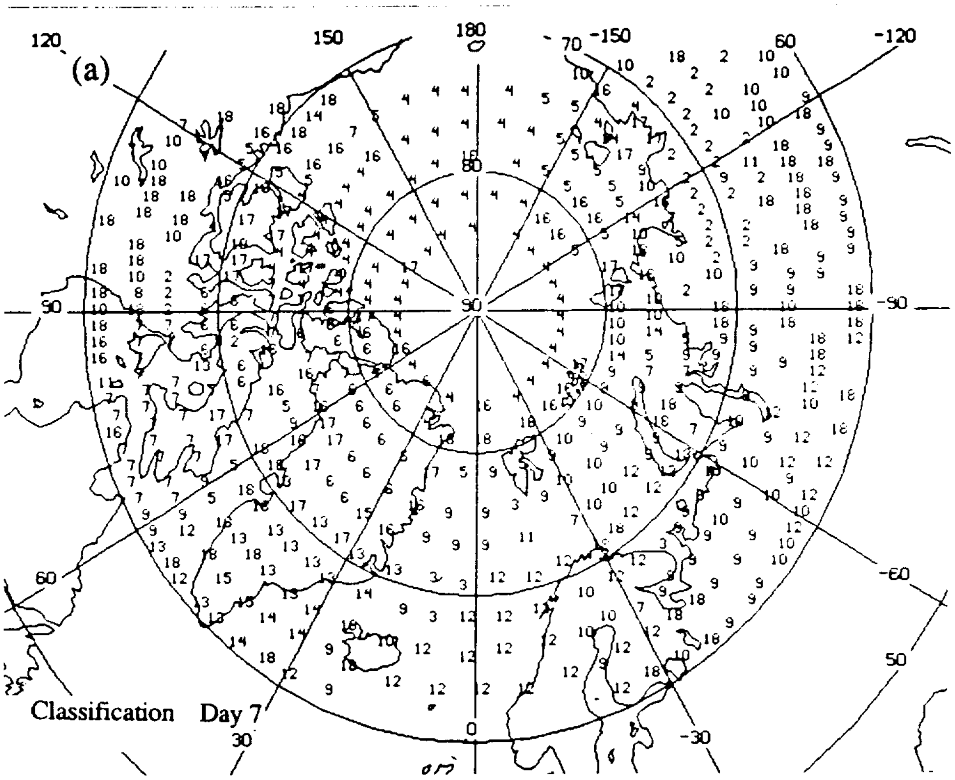
(a)
120
150
180
-150
-120
90
-90
60
-60
50
30
0
-30
80
70
Classification Day 7

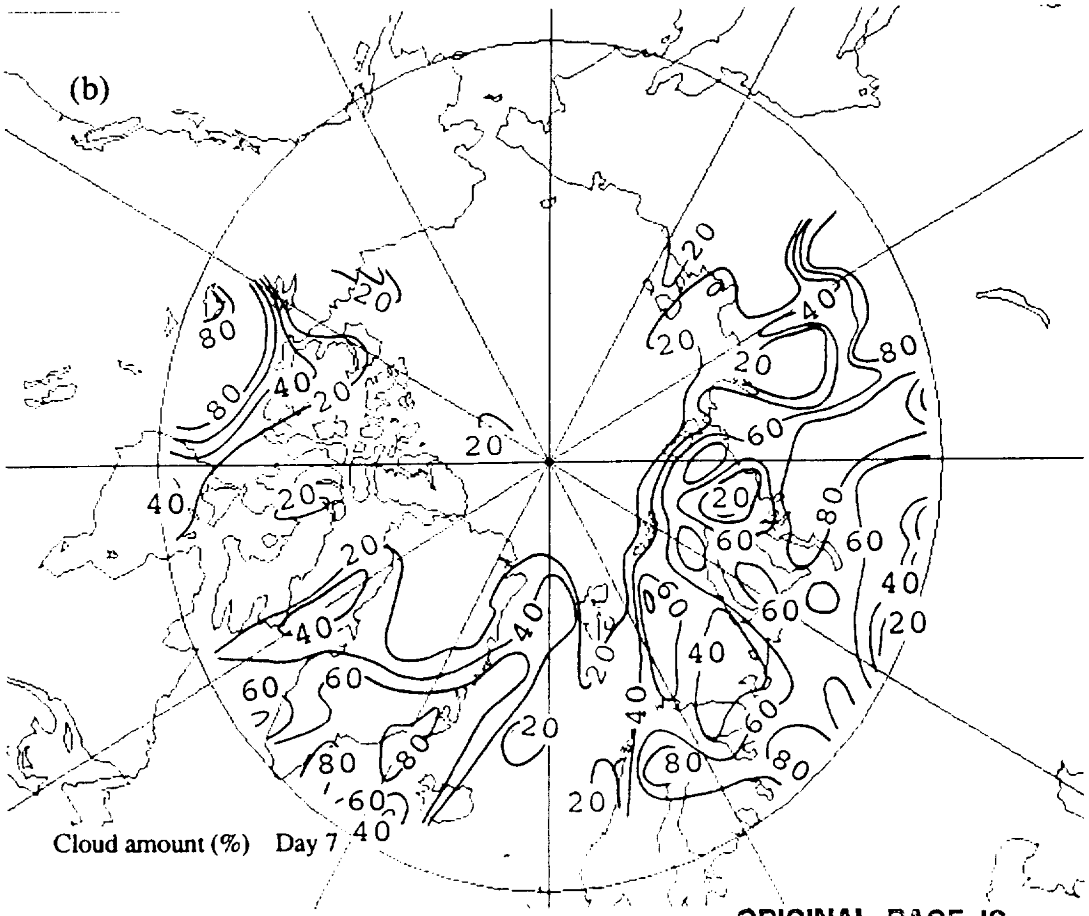
(b)
20
40
60
80
Cloud amount (%) Day 7

Figure 11

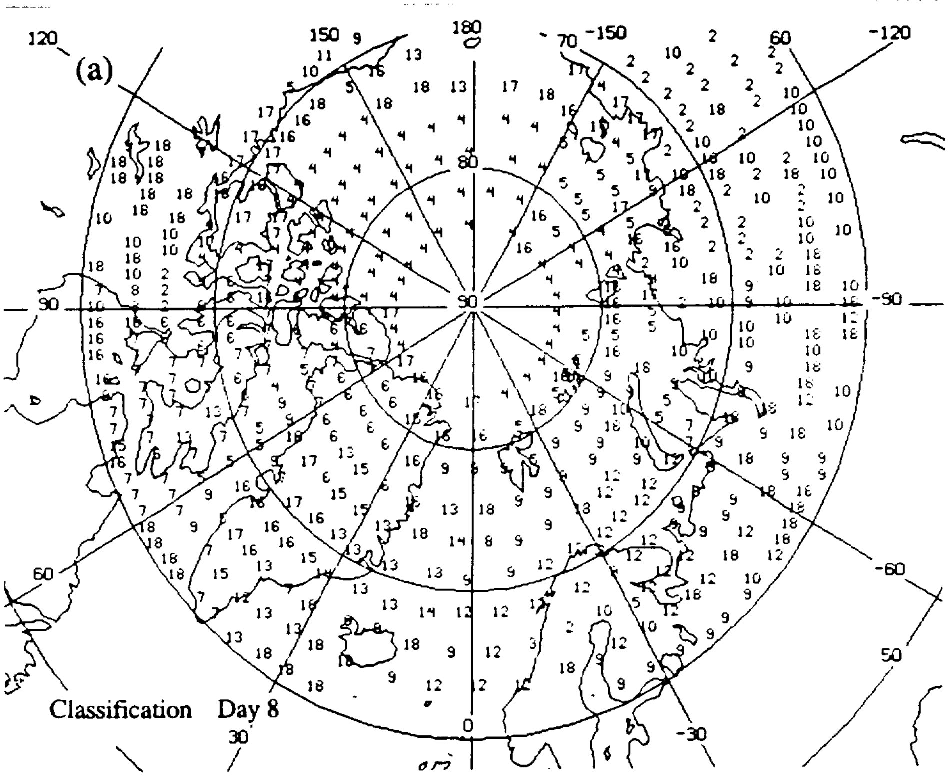

Classification Day 8

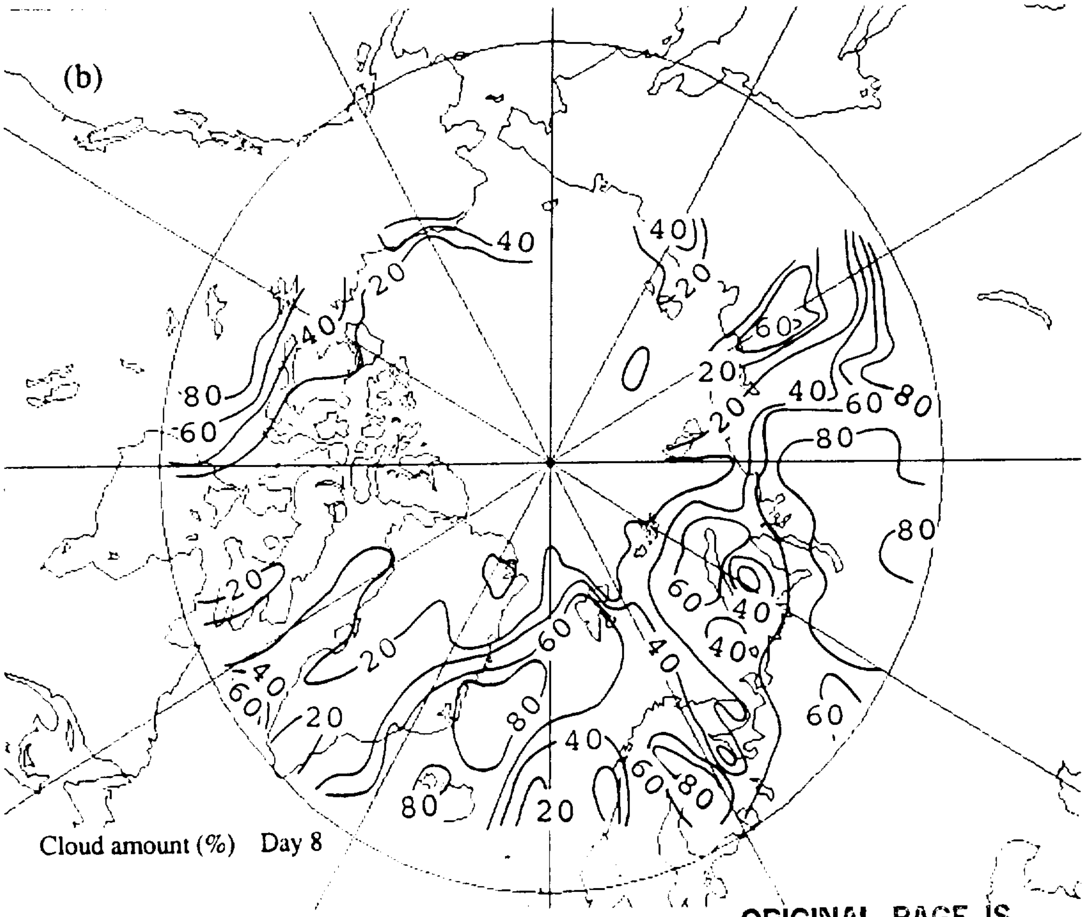

Cloud amount (%) Day 8

Figure 12

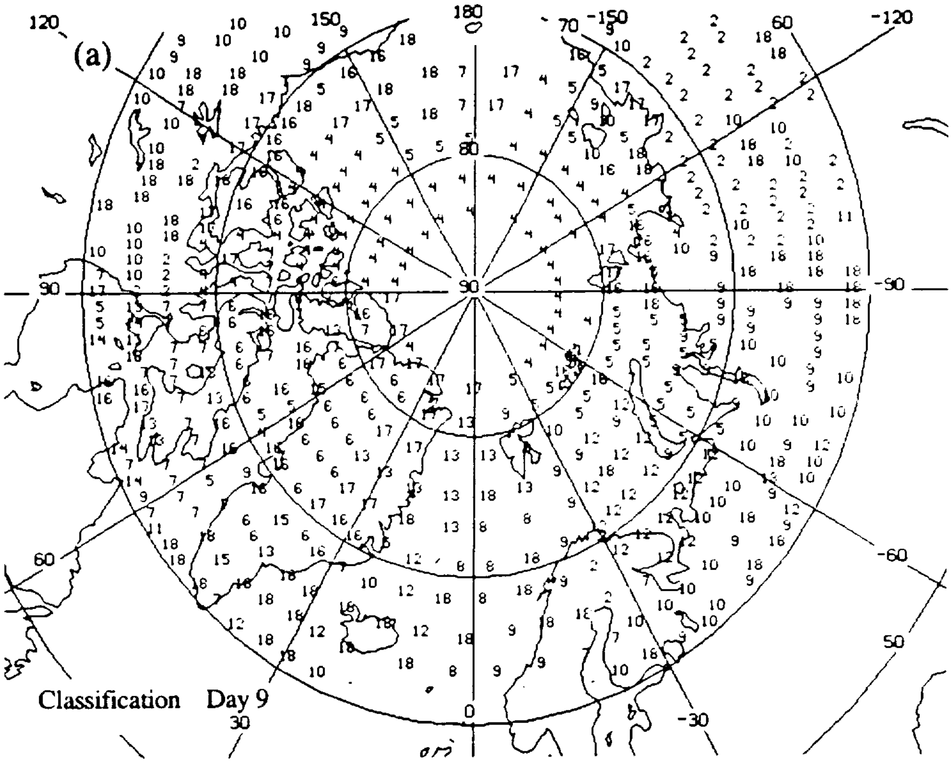

Classification Day 9

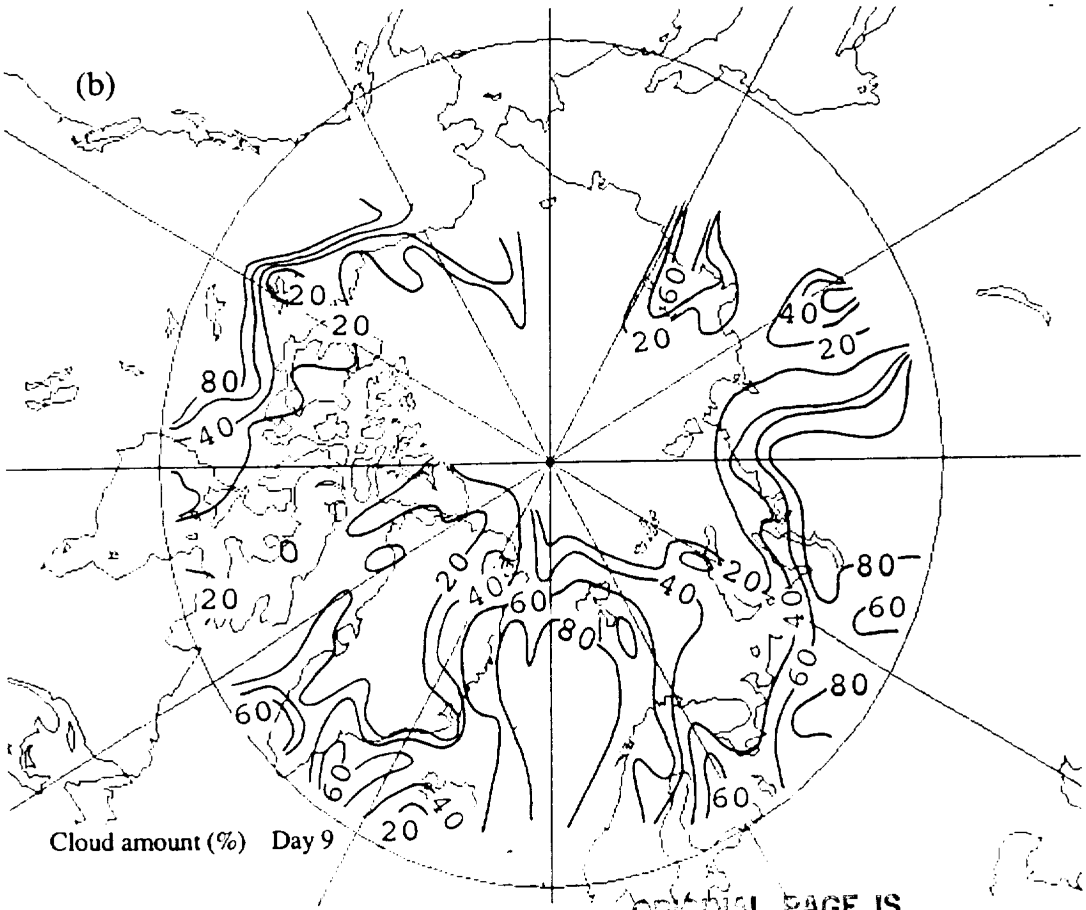

Cloud amount (%) Day 9

Figure 13

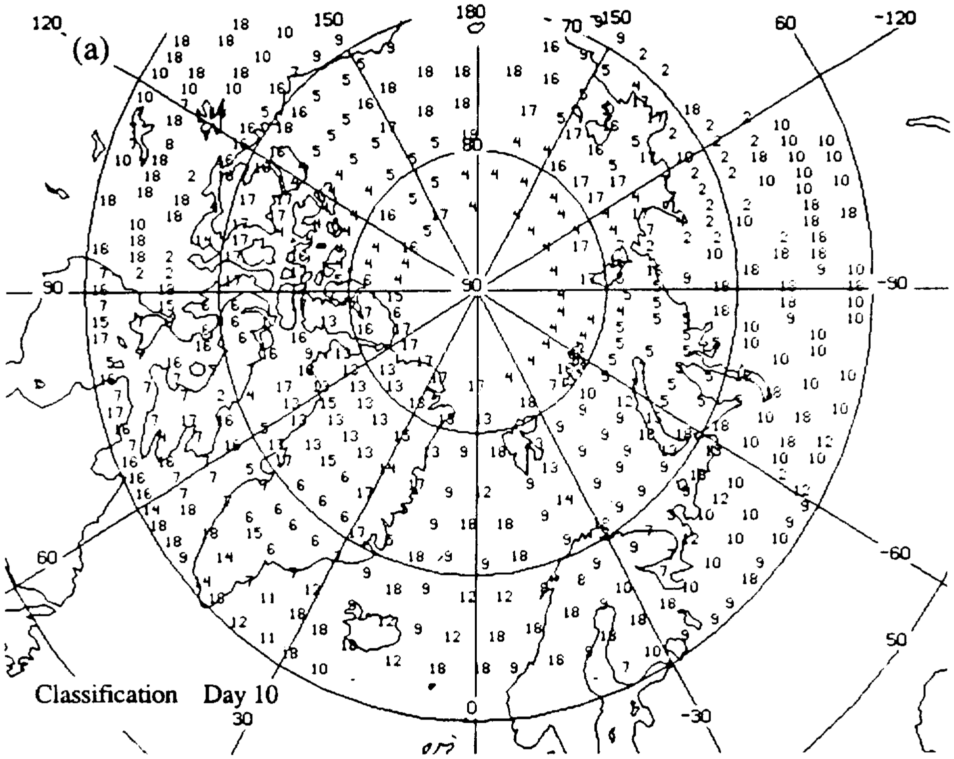

Classification Day 10

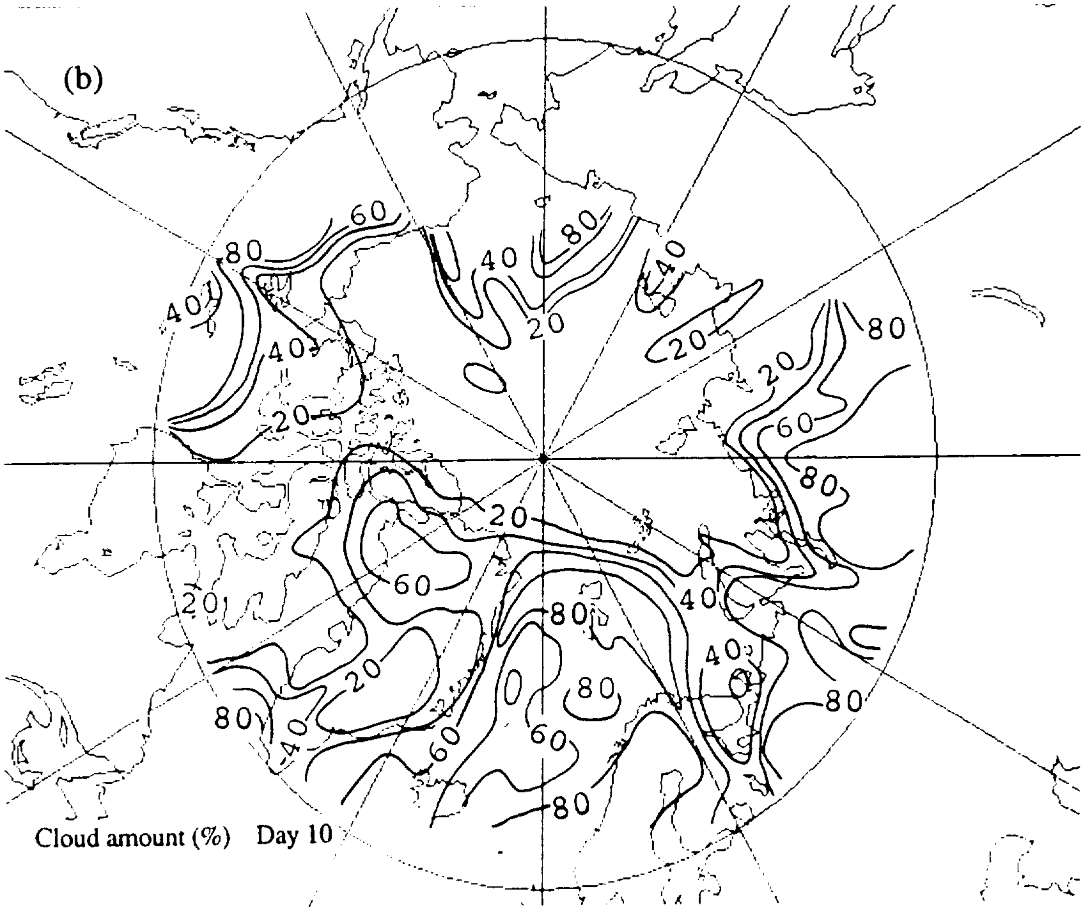

Cloud amount (%) Day 10

Figure 14

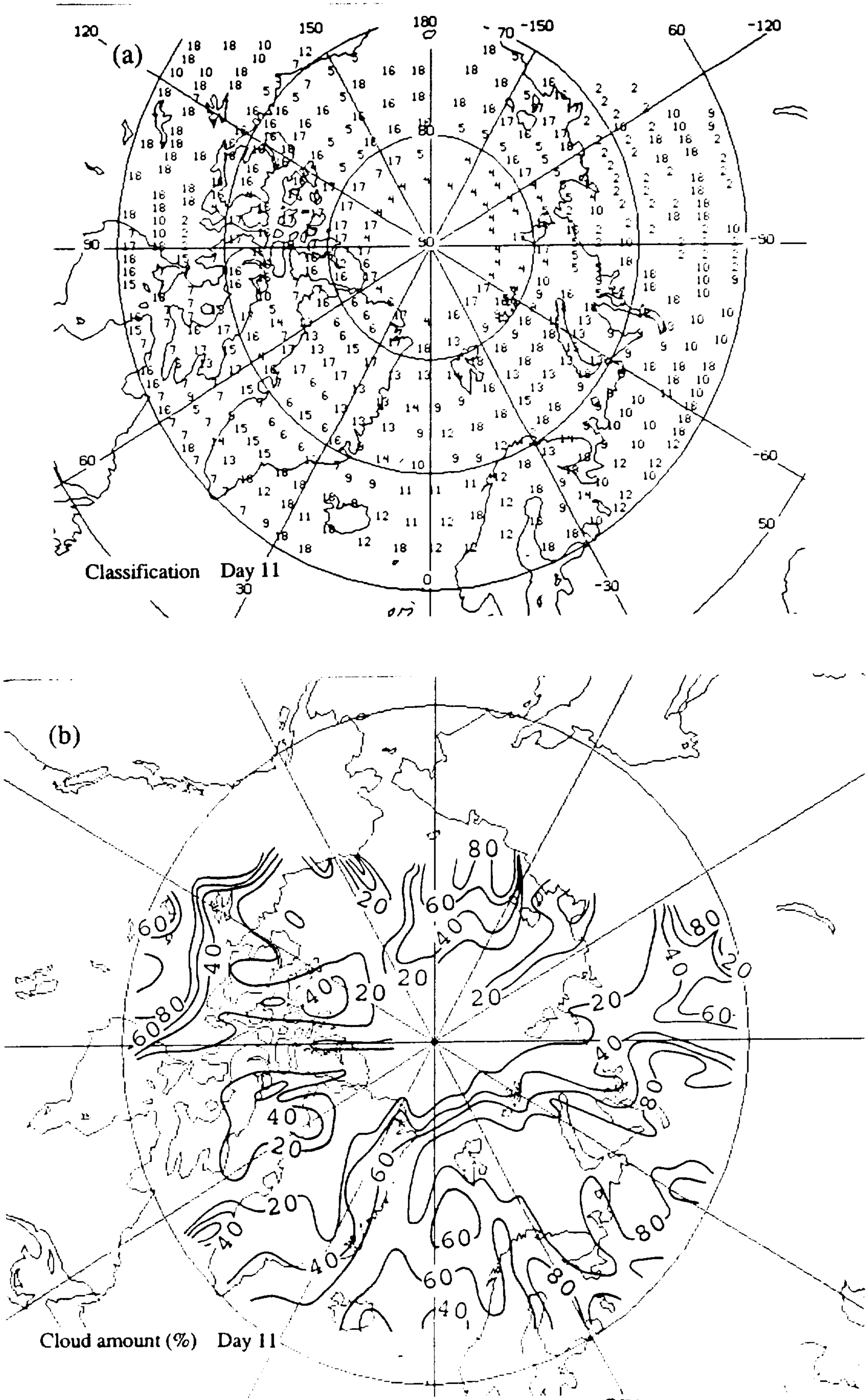
(a)
120
150
180
70
-150
60
-120
90
-90
80
60
-60
50
30
0
-30
Classification Day 11
(b)
80
60
40
20
0
Cloud amount (%) Day 11

Figure 15

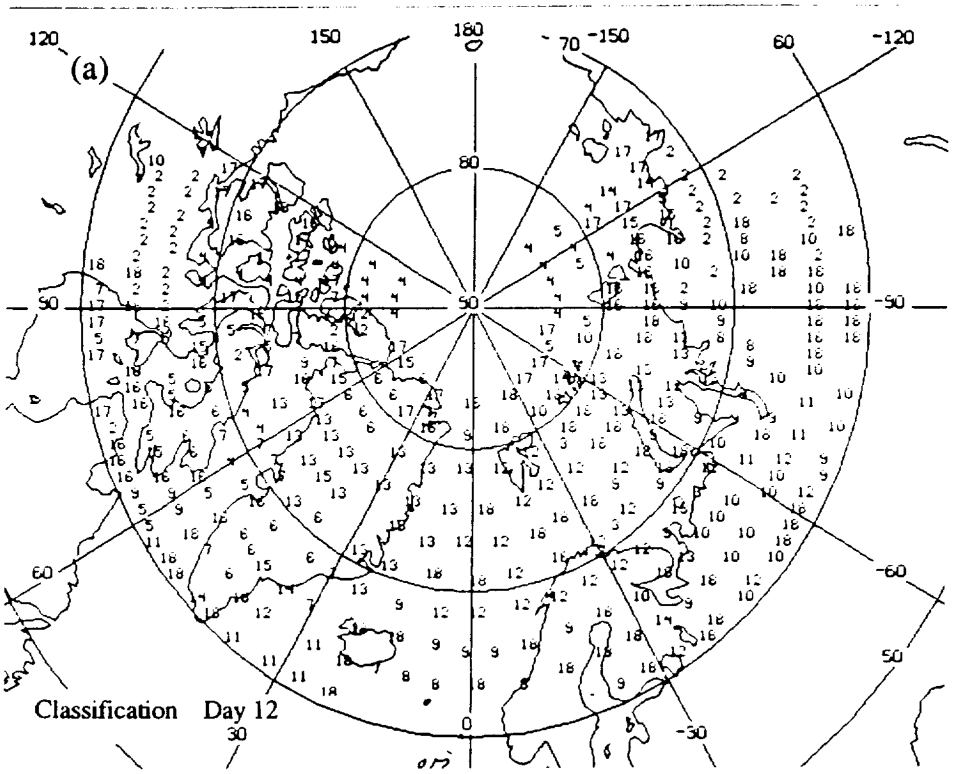

Classification Day 12

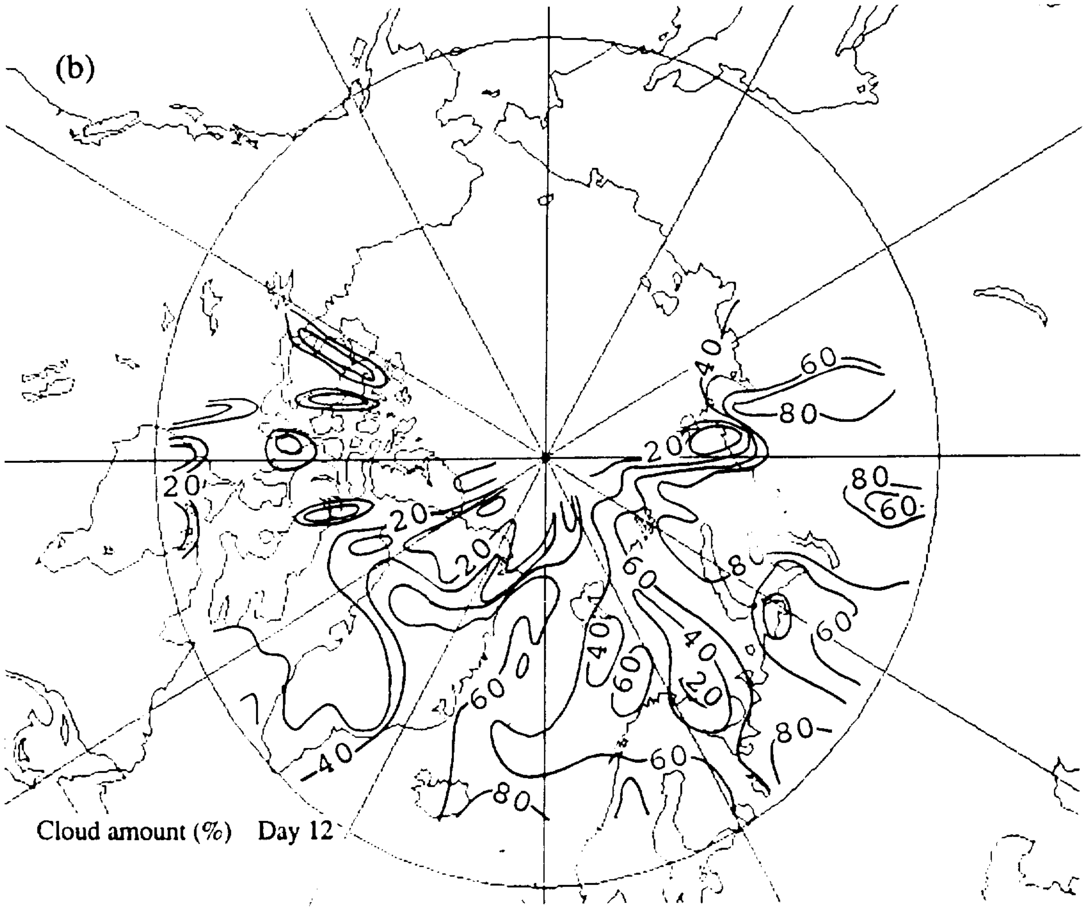

Cloud amount (%) Day 12

Figure 16

ORIGINAL PAGE IS
OF POOR QUALITY

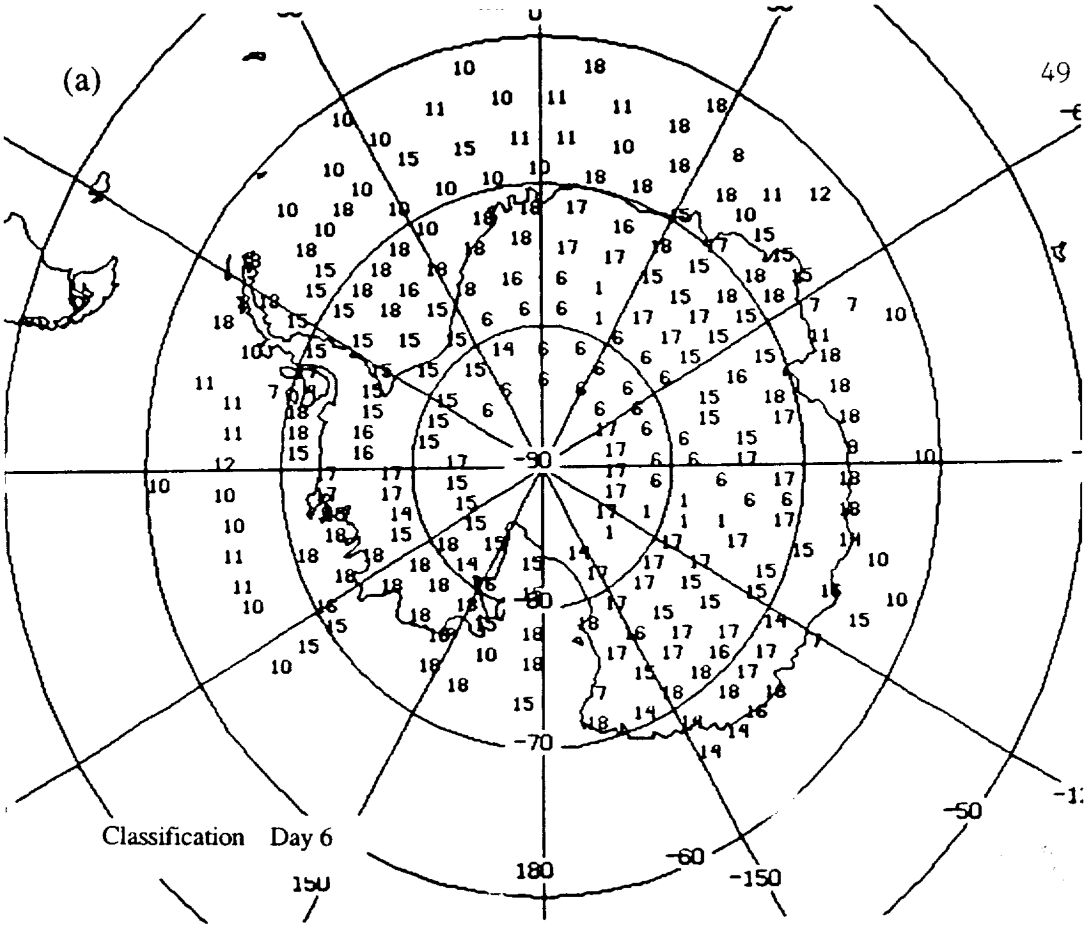

Classification Day 6

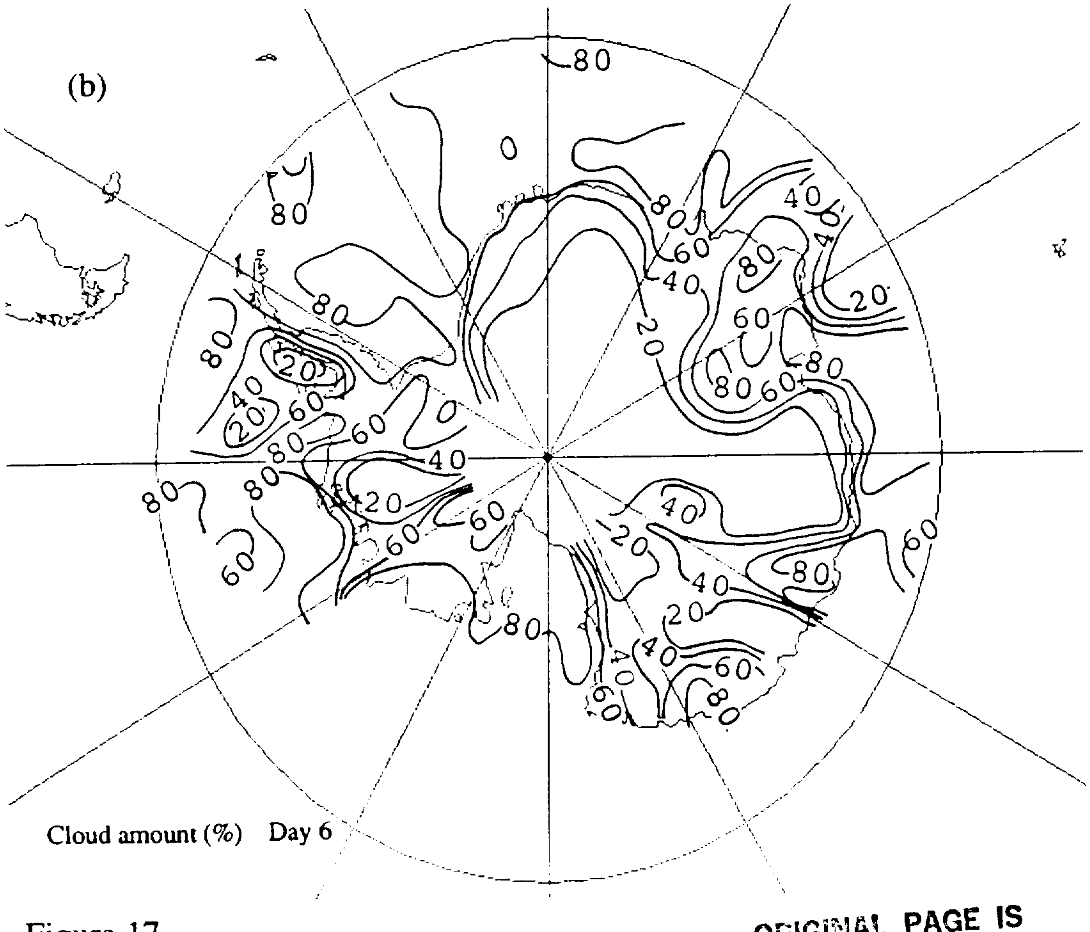

Cloud amount (%) Day 6

Figure 17

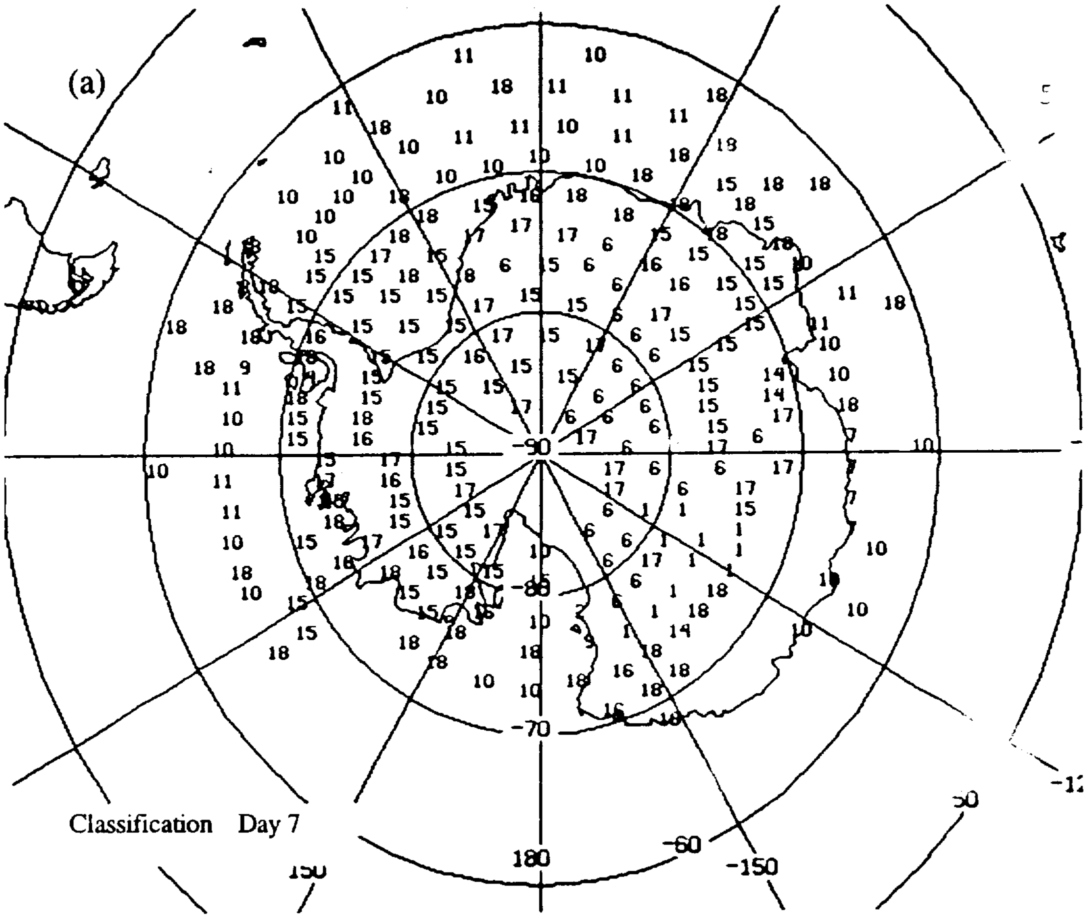

Classification Day 7

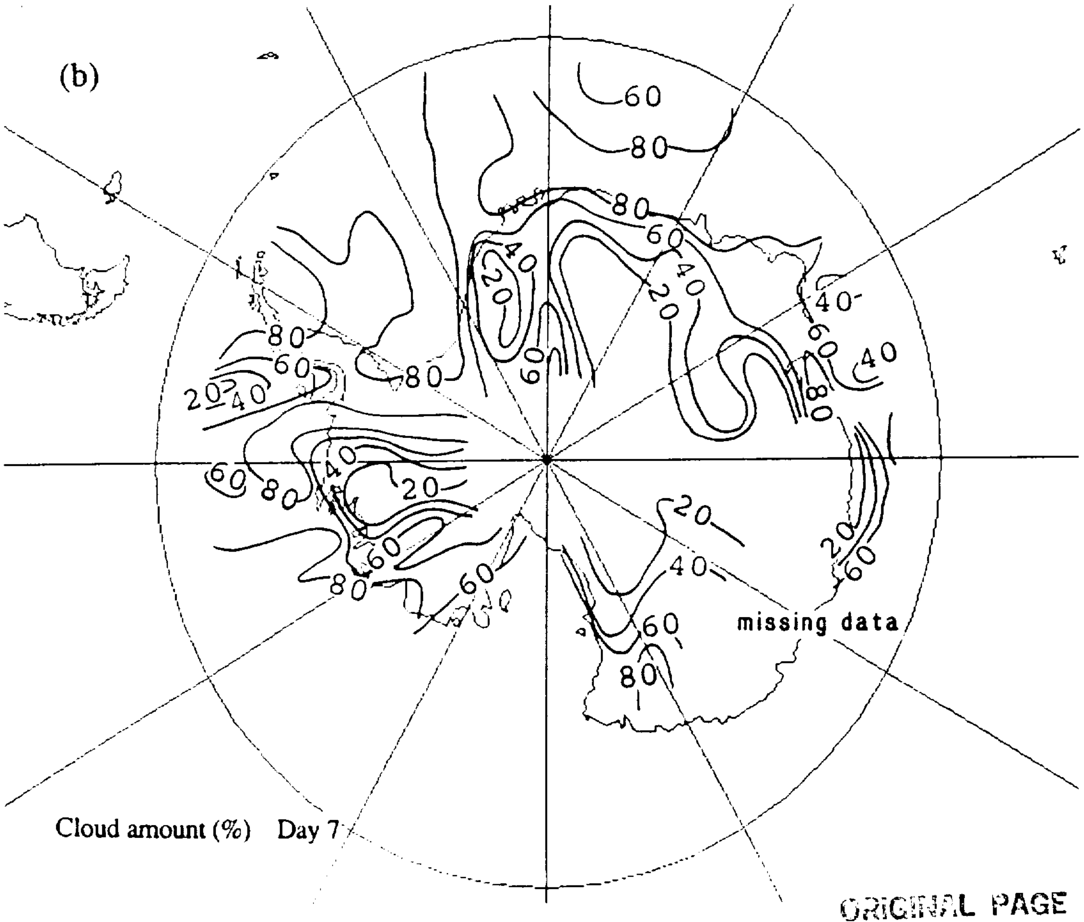

Cloud amount (%) Day 7

Figure 18

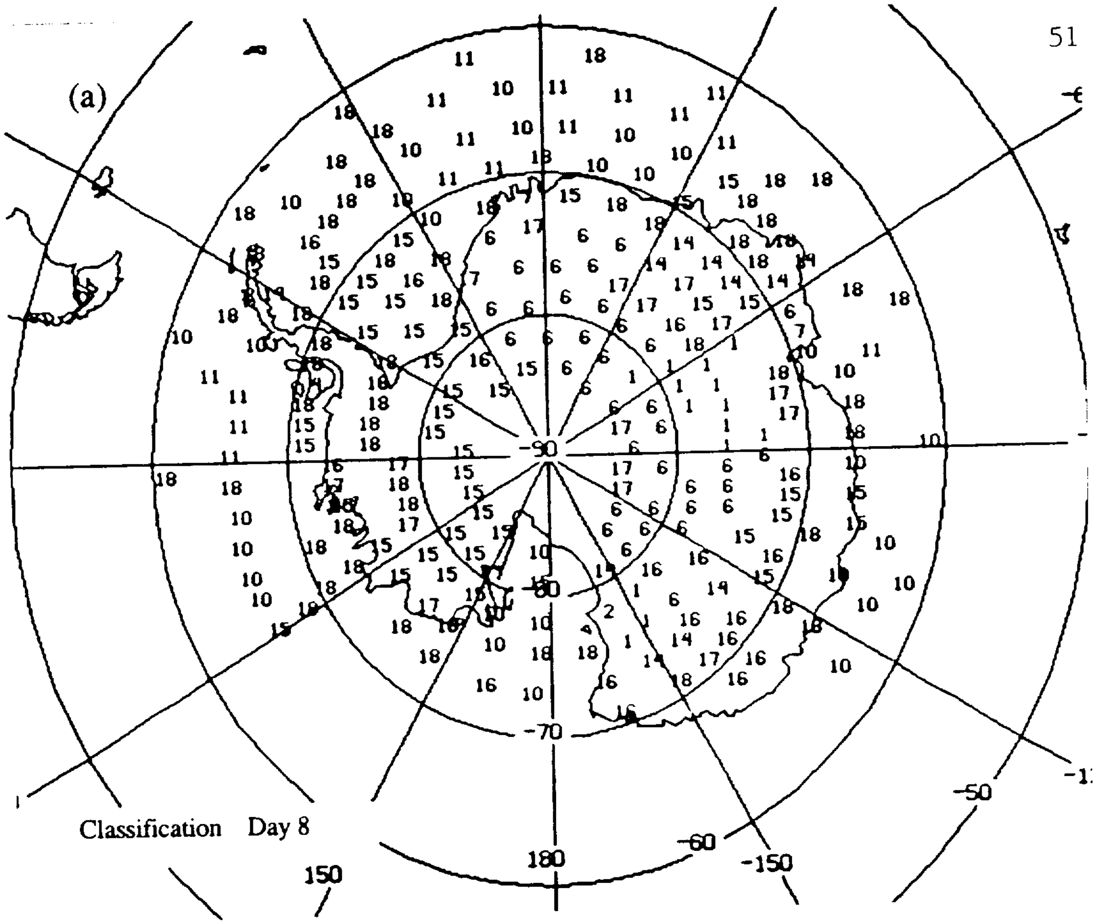

Classification Day 8

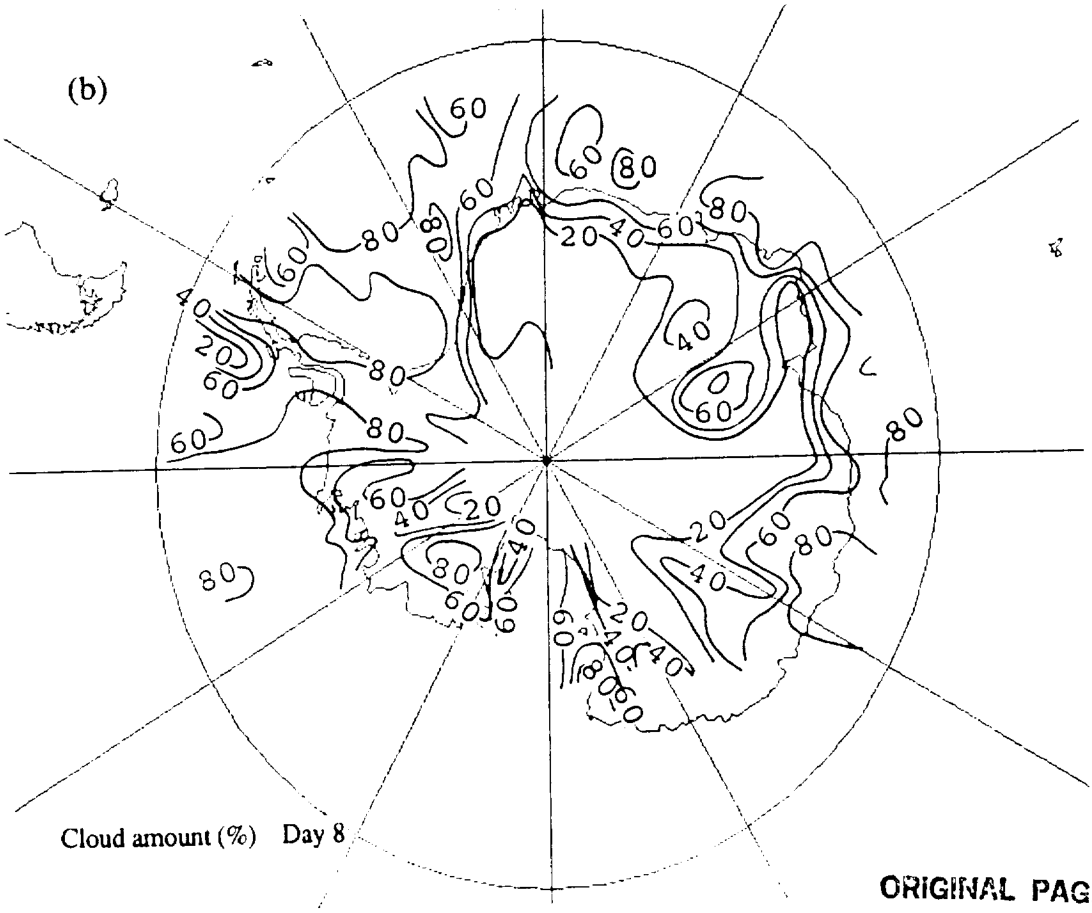

Cloud amount (%) Day 8

Figure 19

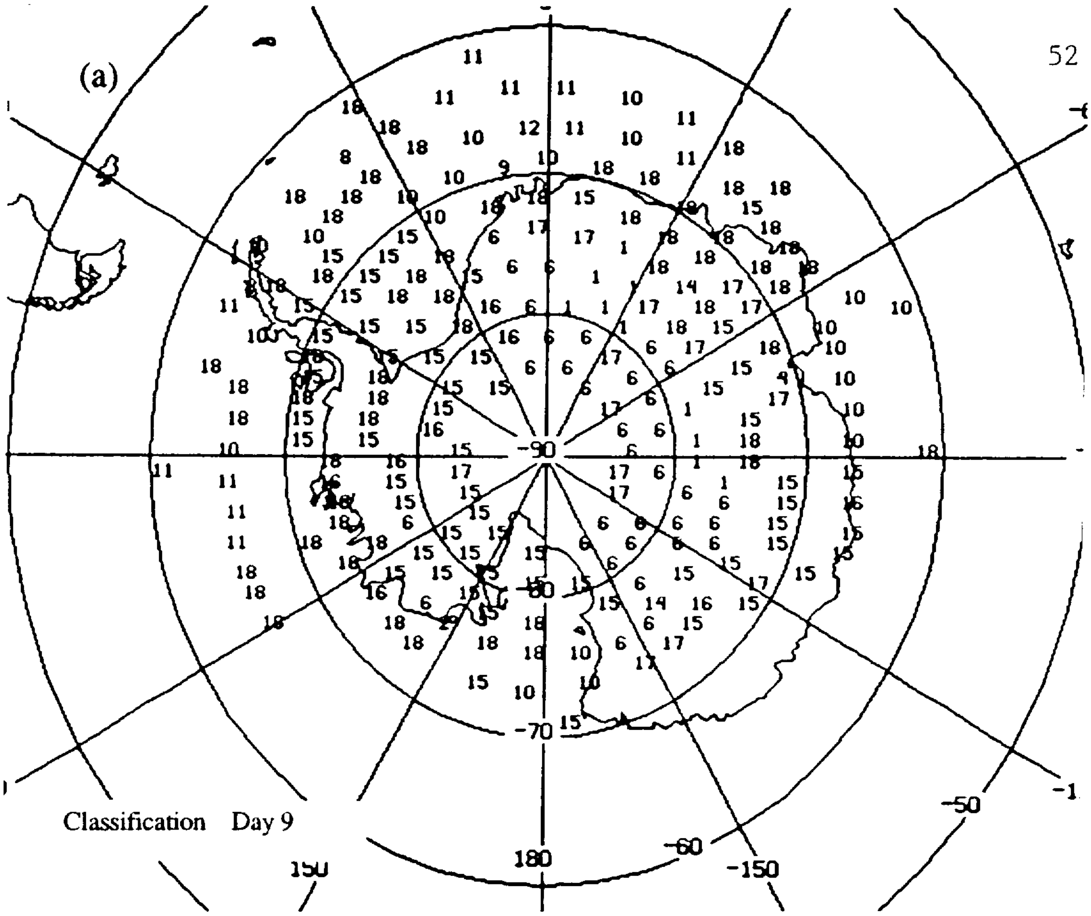

Classification Day 9

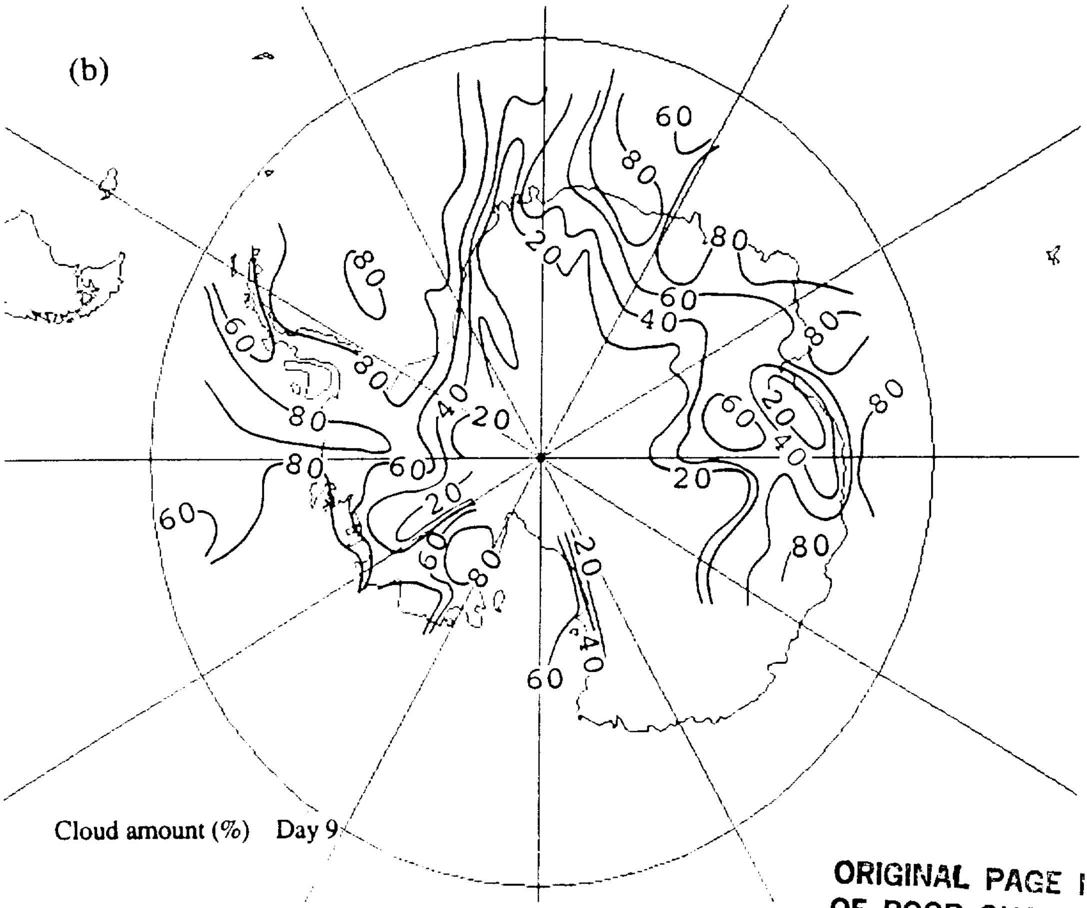

Cloud amount (%) Day 9

Figure 20

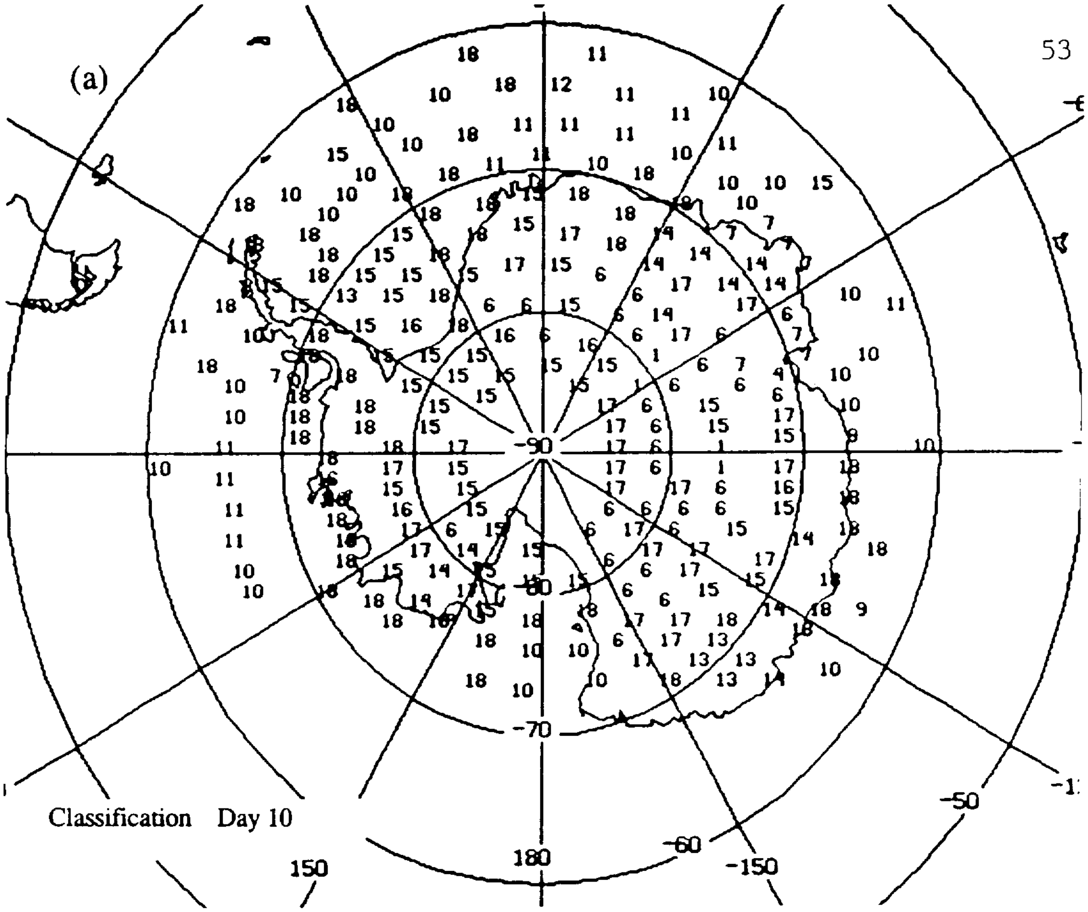

Classification Day 10

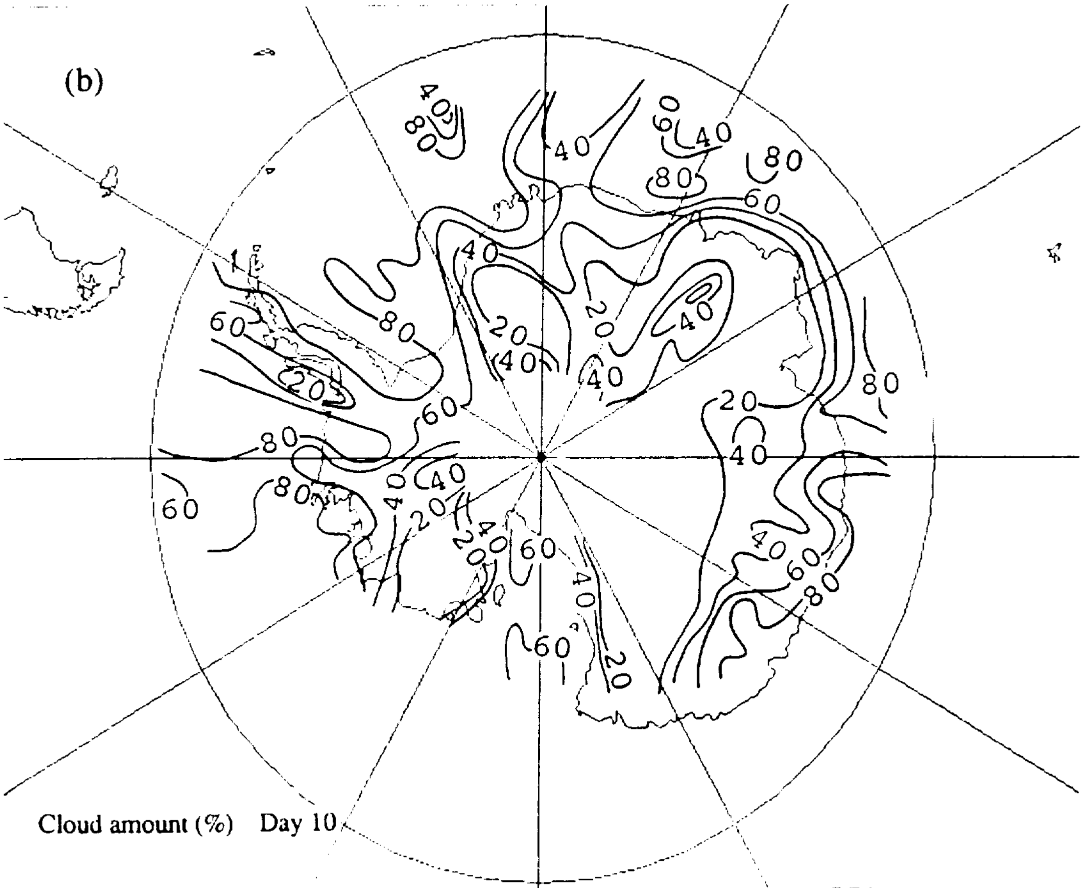

Cloud amount (%) Day 10

Figure 21

ORIGINAL PAGE IS OF POOR QUALITY

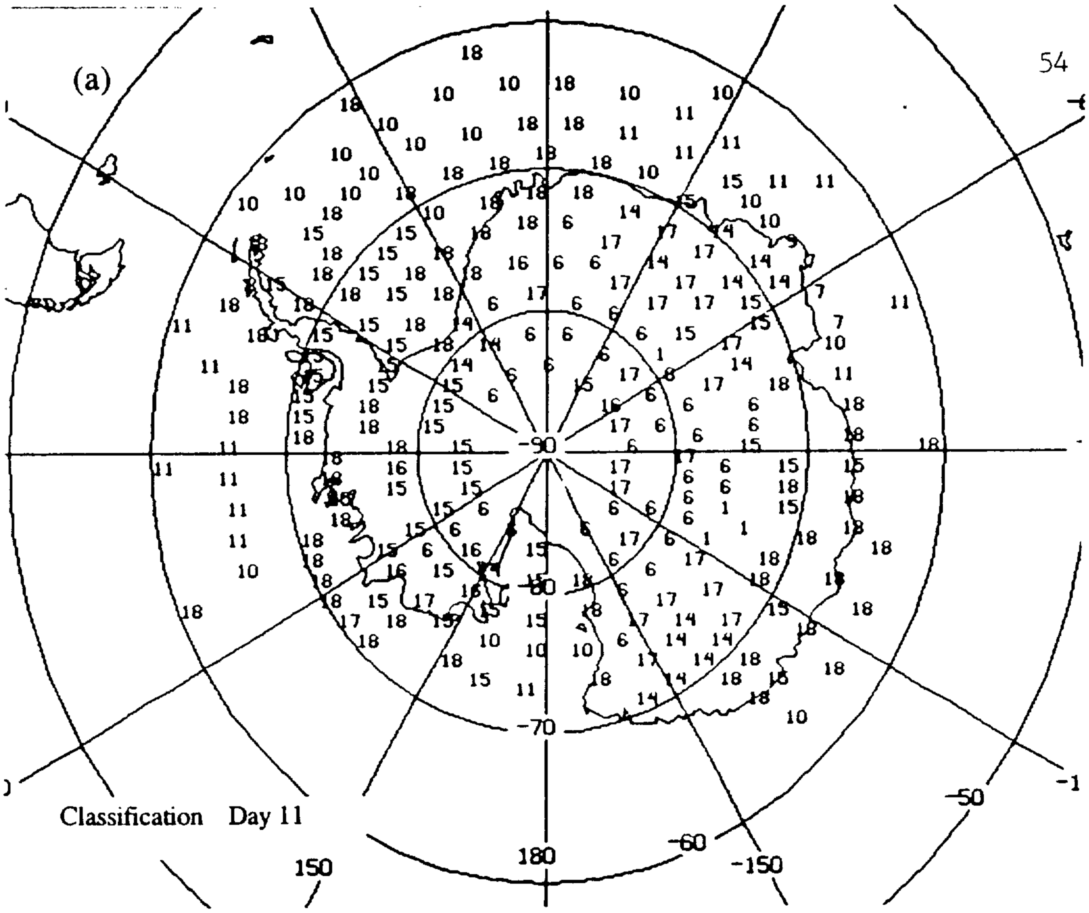

Classification Day 11

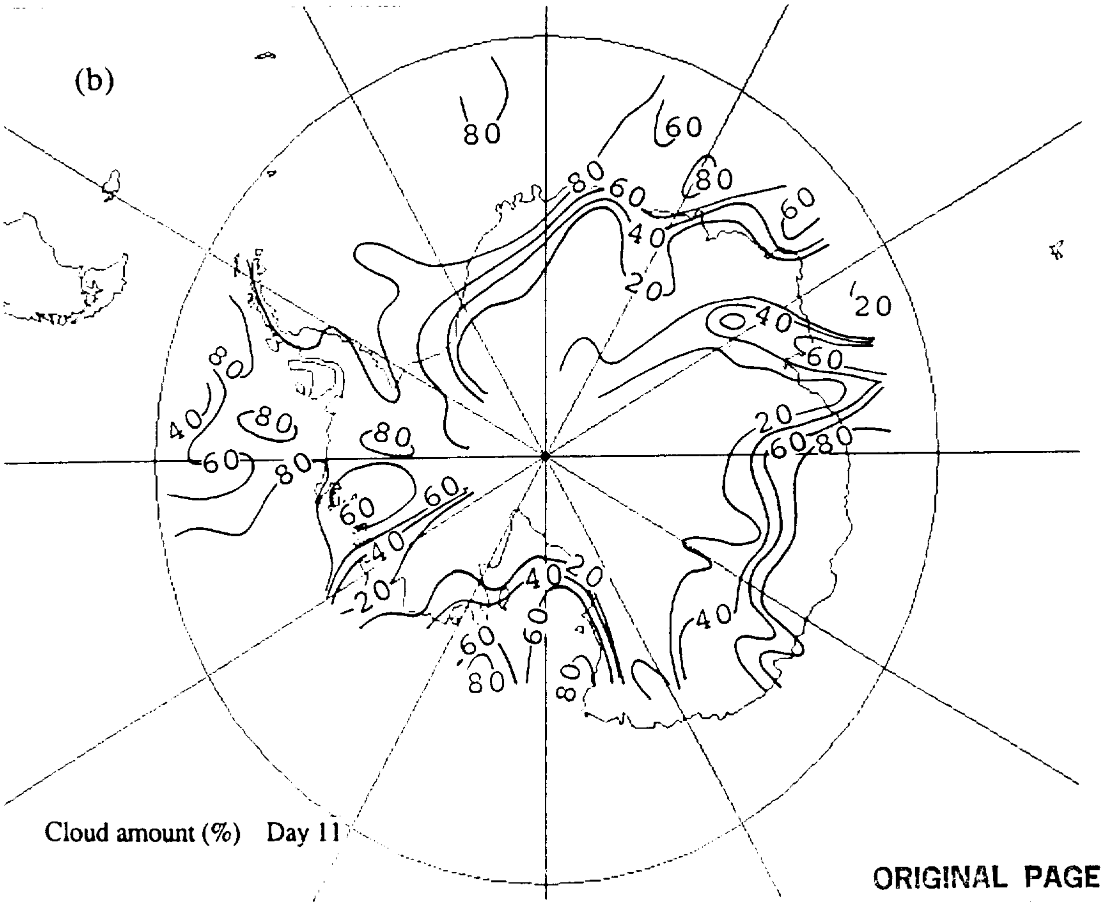

Cloud amount (%) Day 11

ORIGINAL PAGE IS OF POOR QUALITY

Figure 22

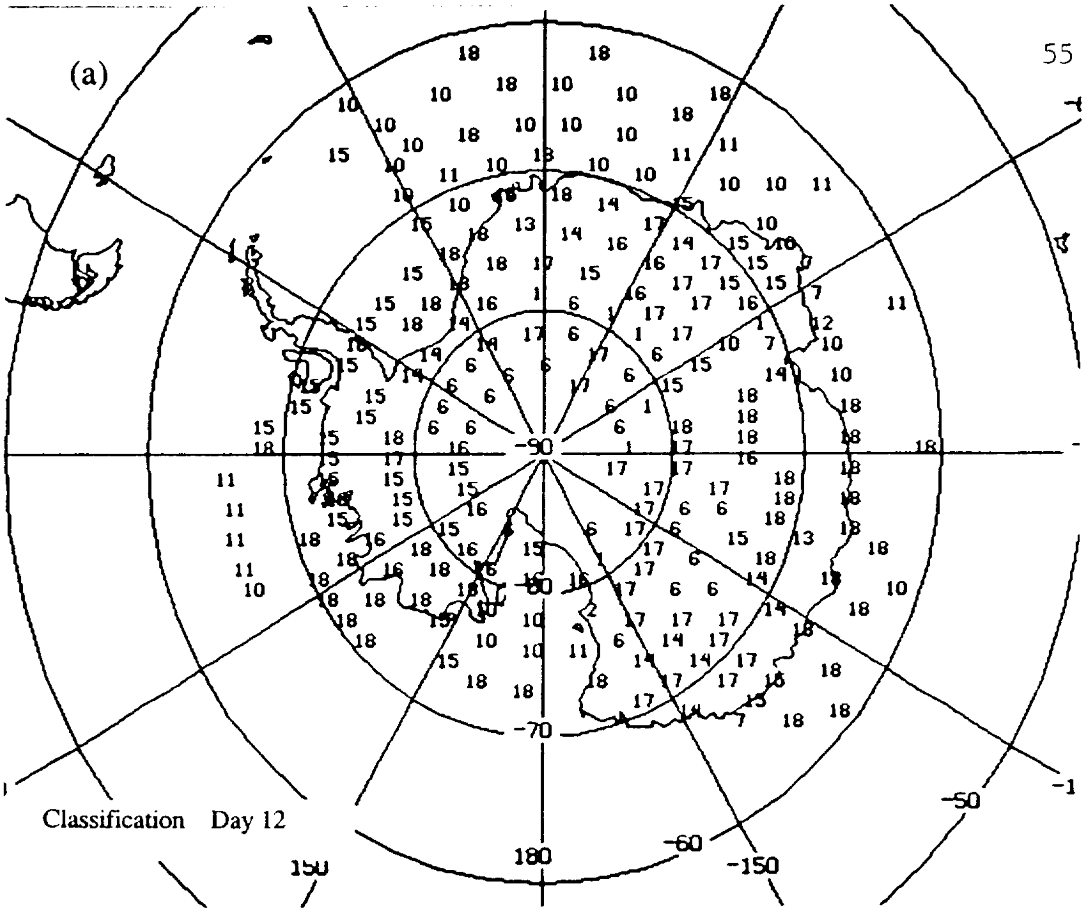

Classification Day 12

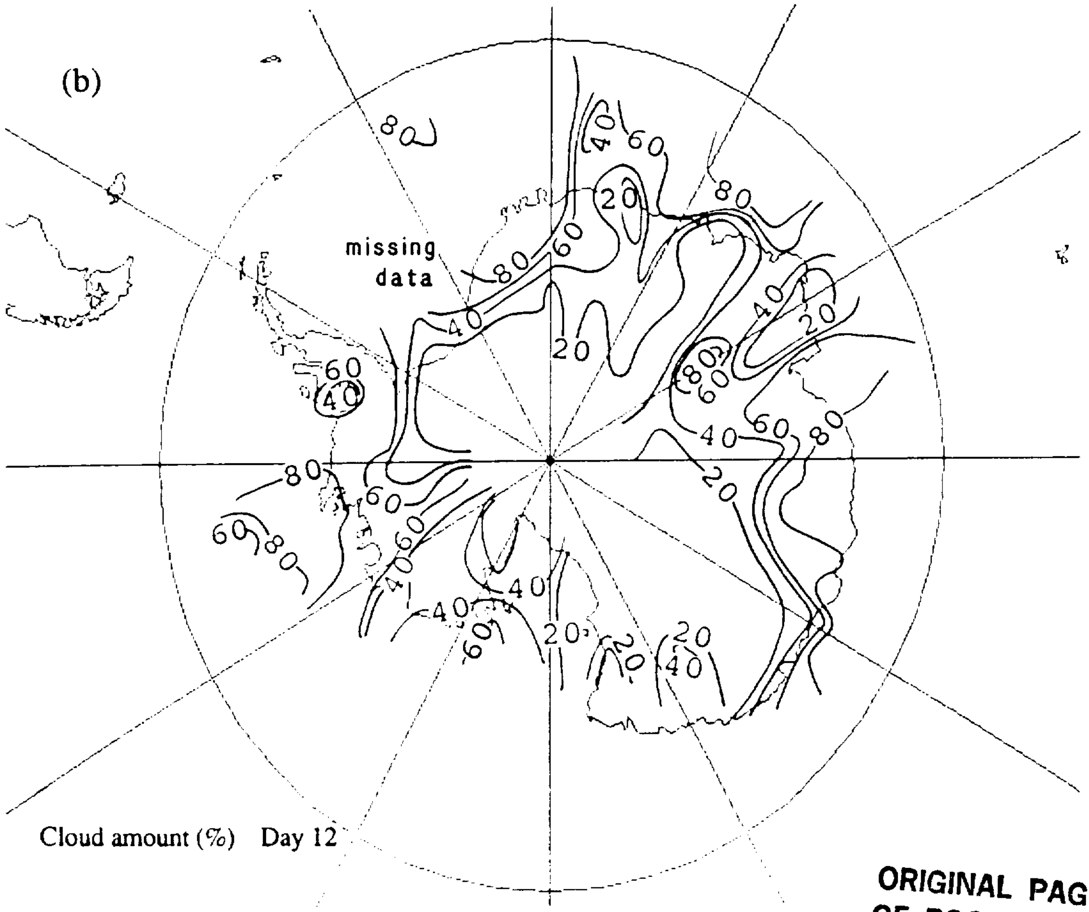

Cloud amount (%) Day 12

Figure 23

ORIGINAL PAGE IS OF POOR QUALITY

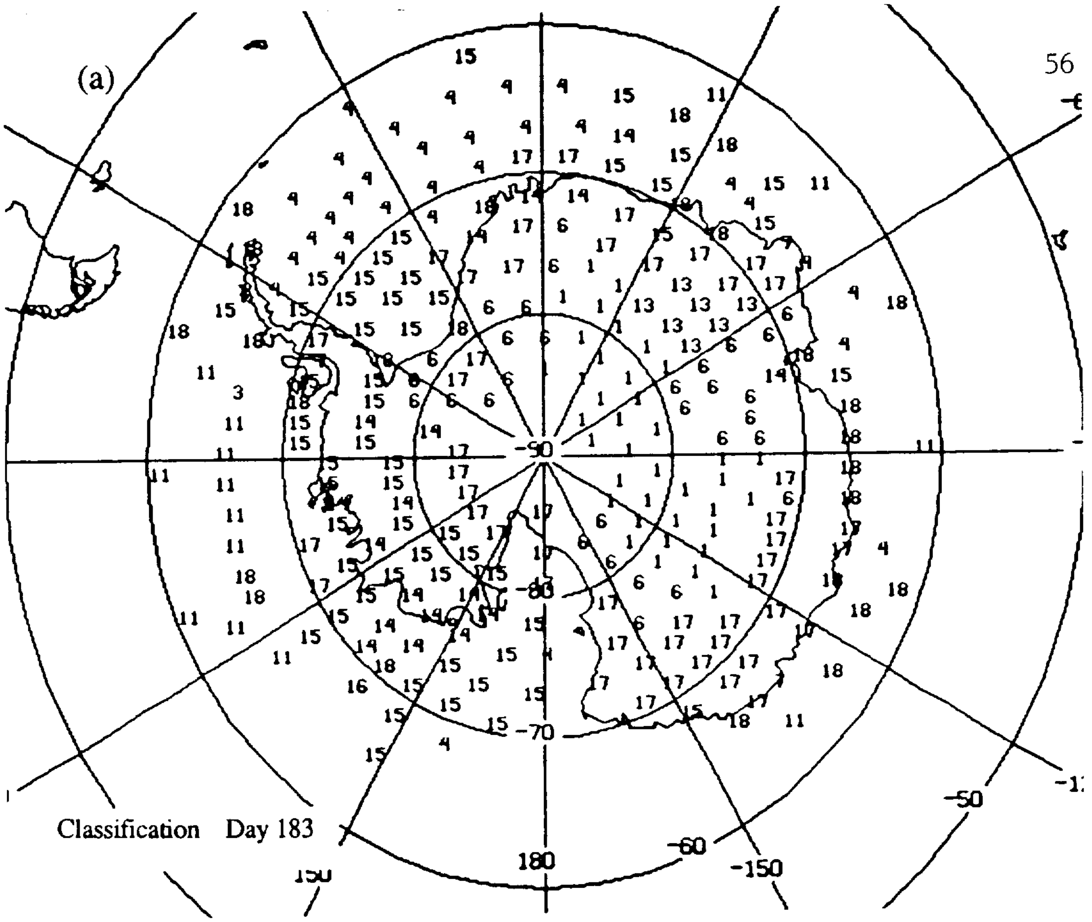

Classification Day 183

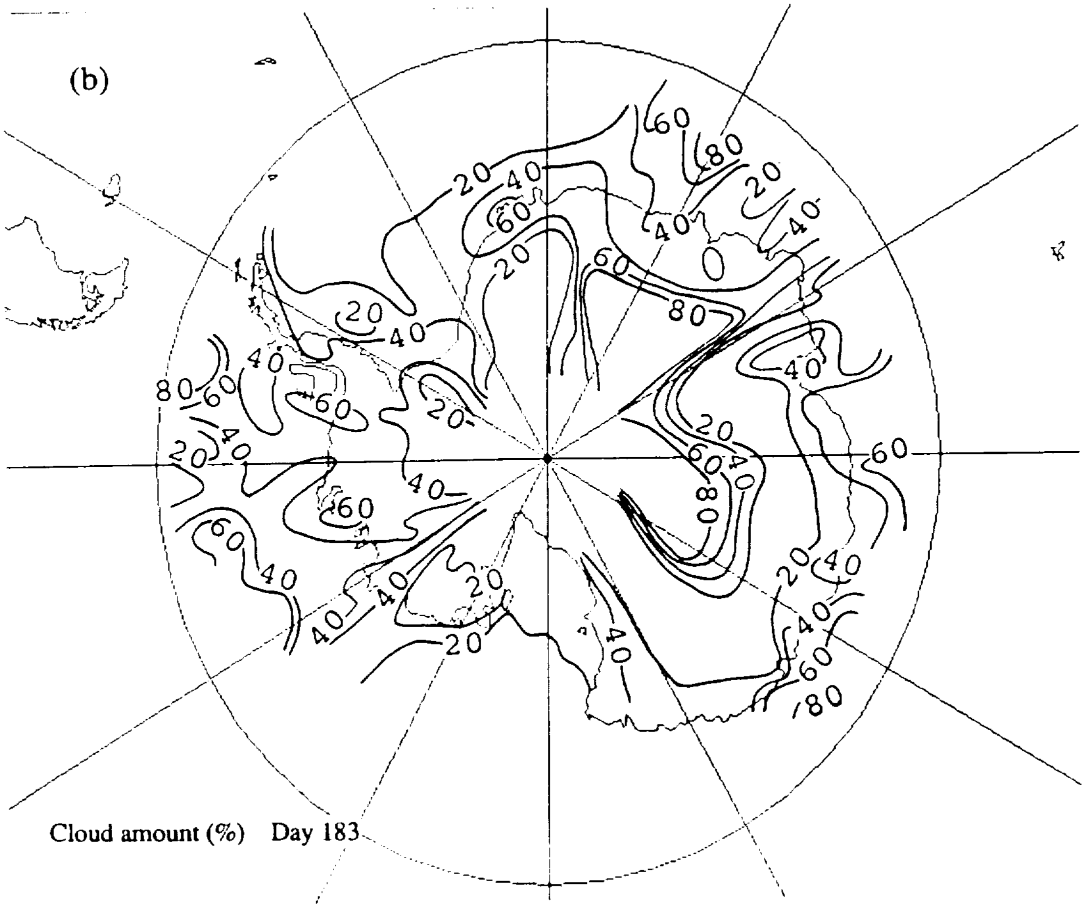

Cloud amount (%) Day 183

Figure 24

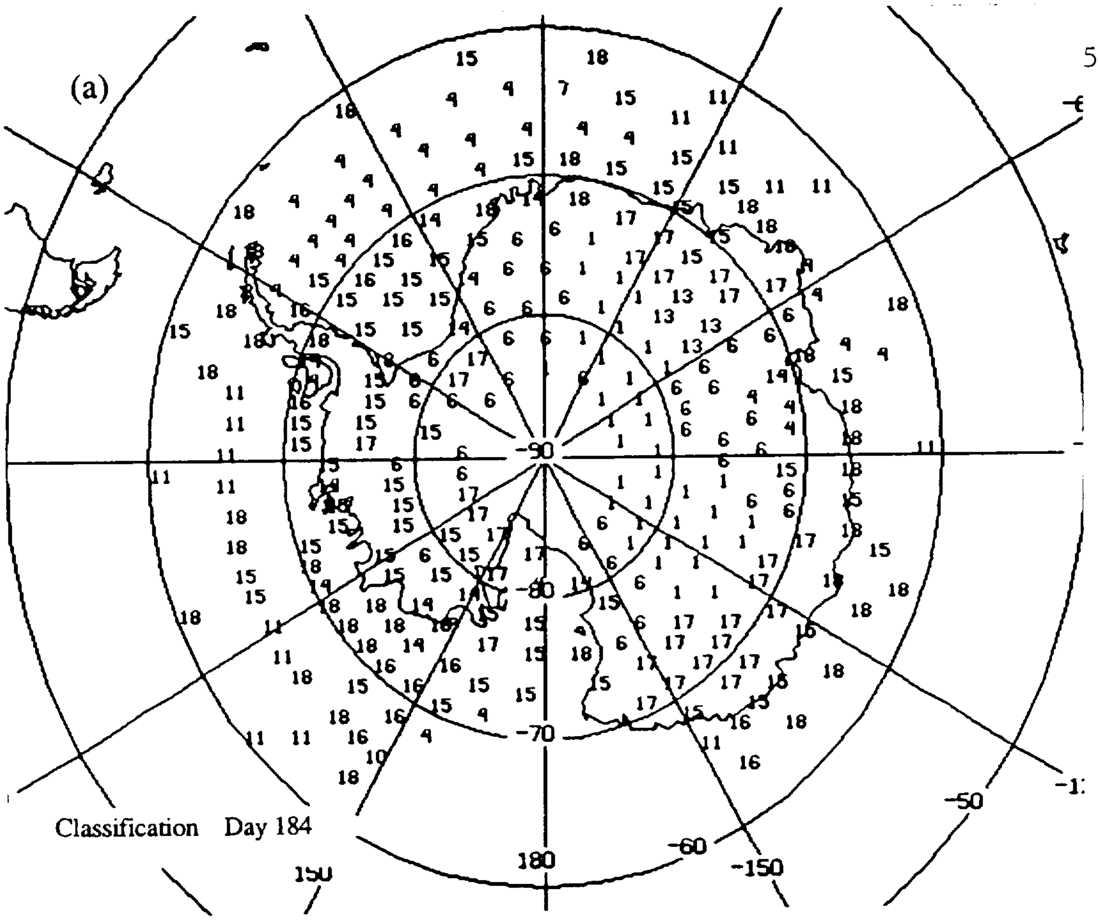

Classification Day 184

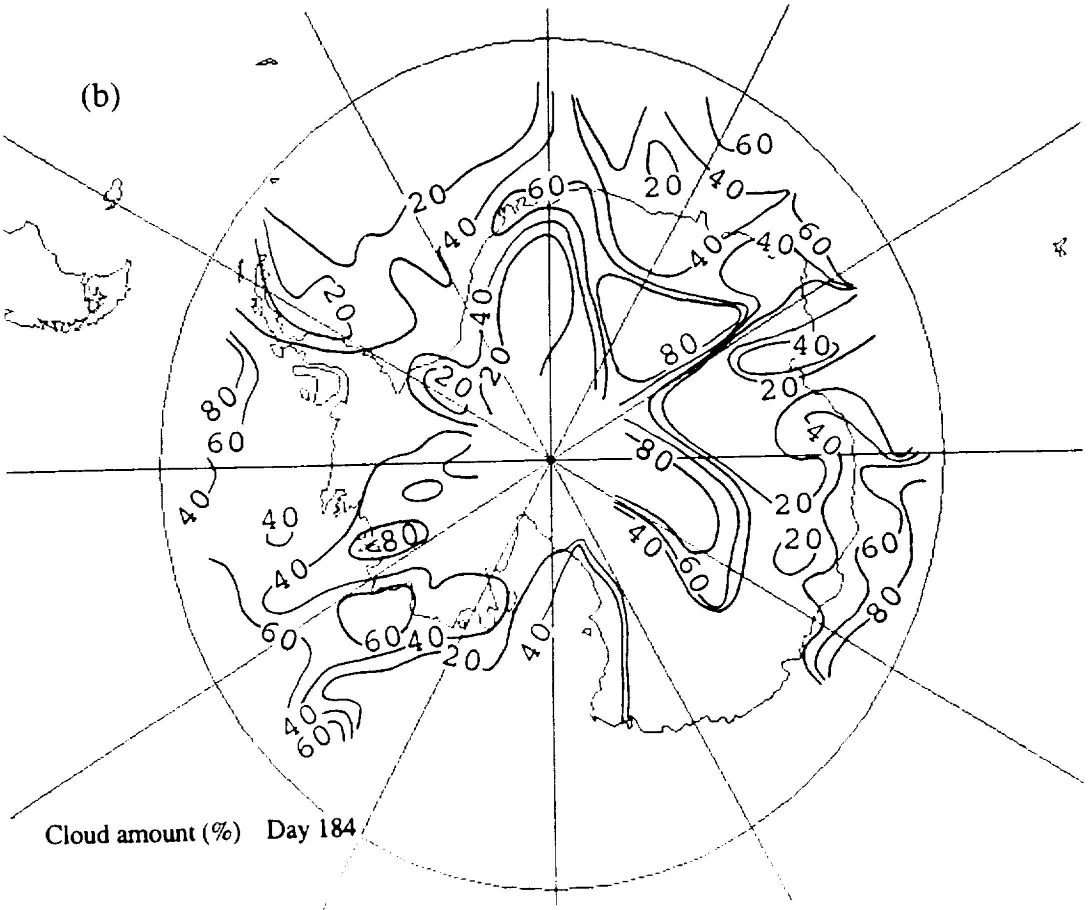

Cloud amount (%) Day 184

Figure 25

(a)

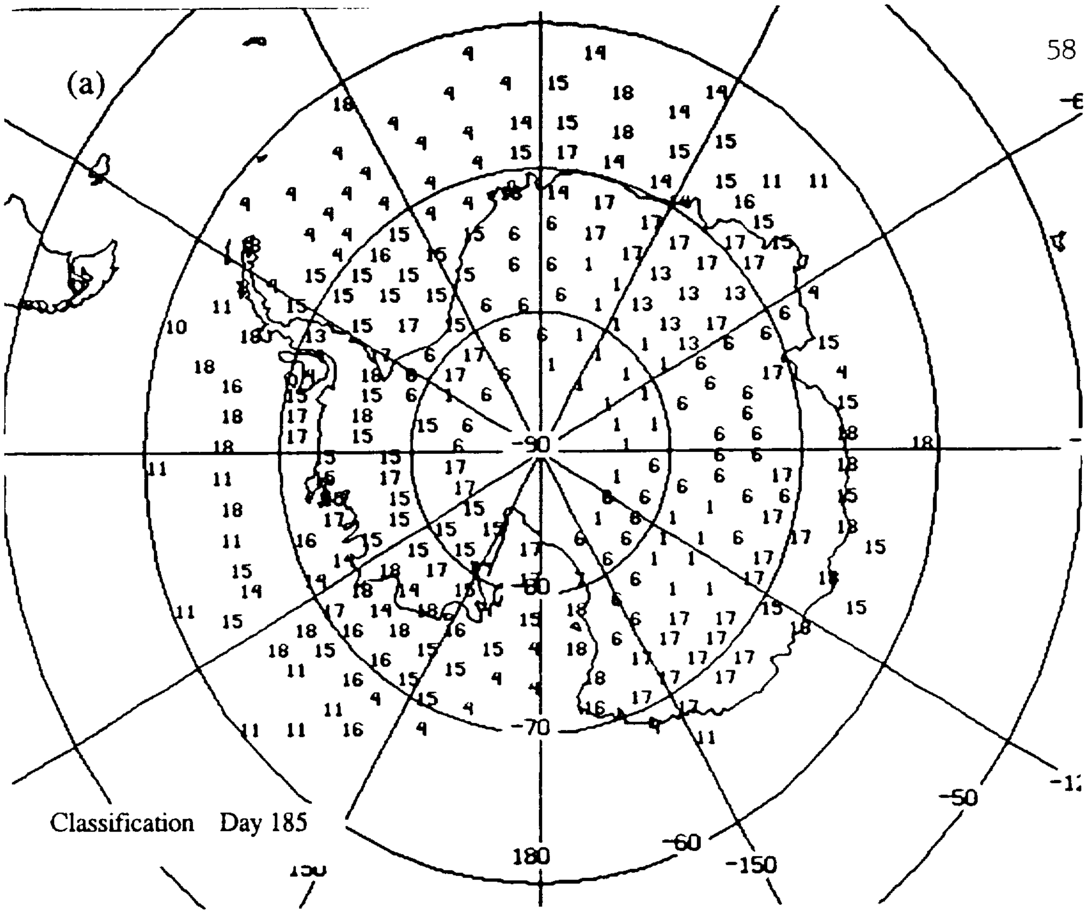

Classification Day 185

(b)

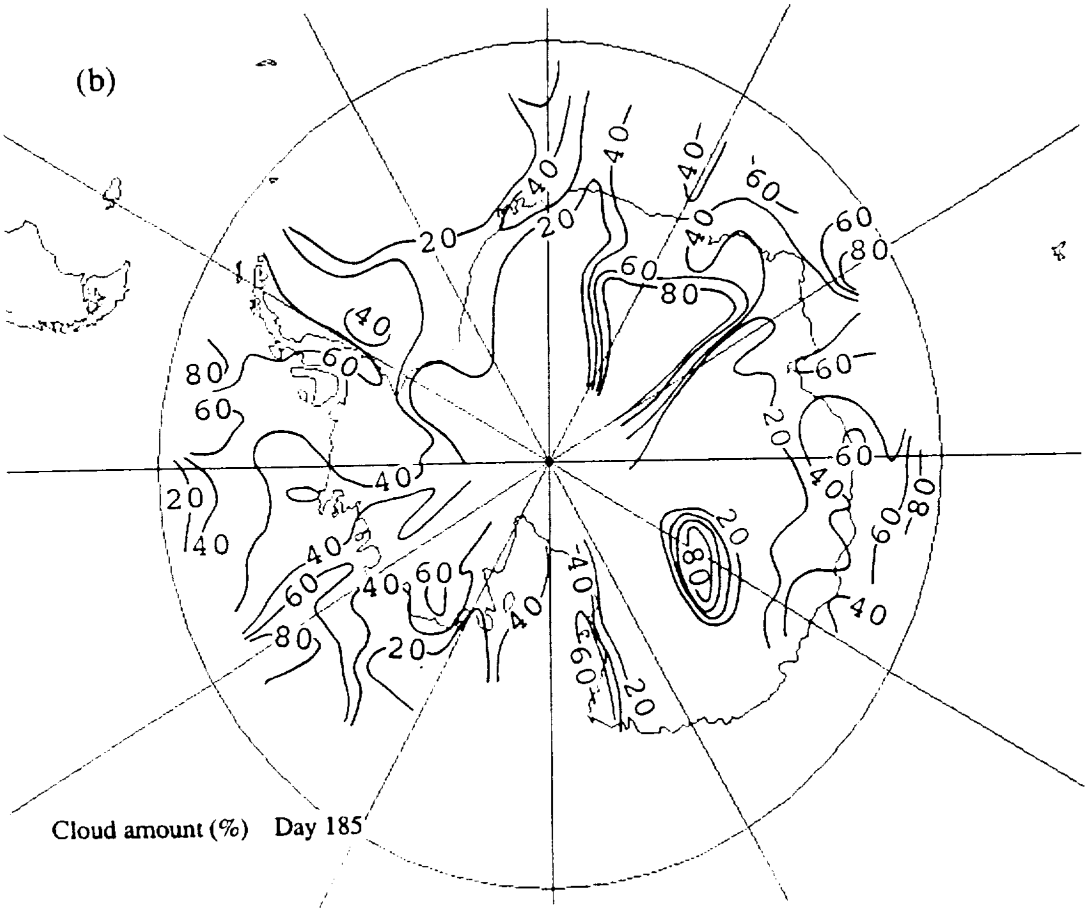

Cloud amount (%) Day 185

Figure 26

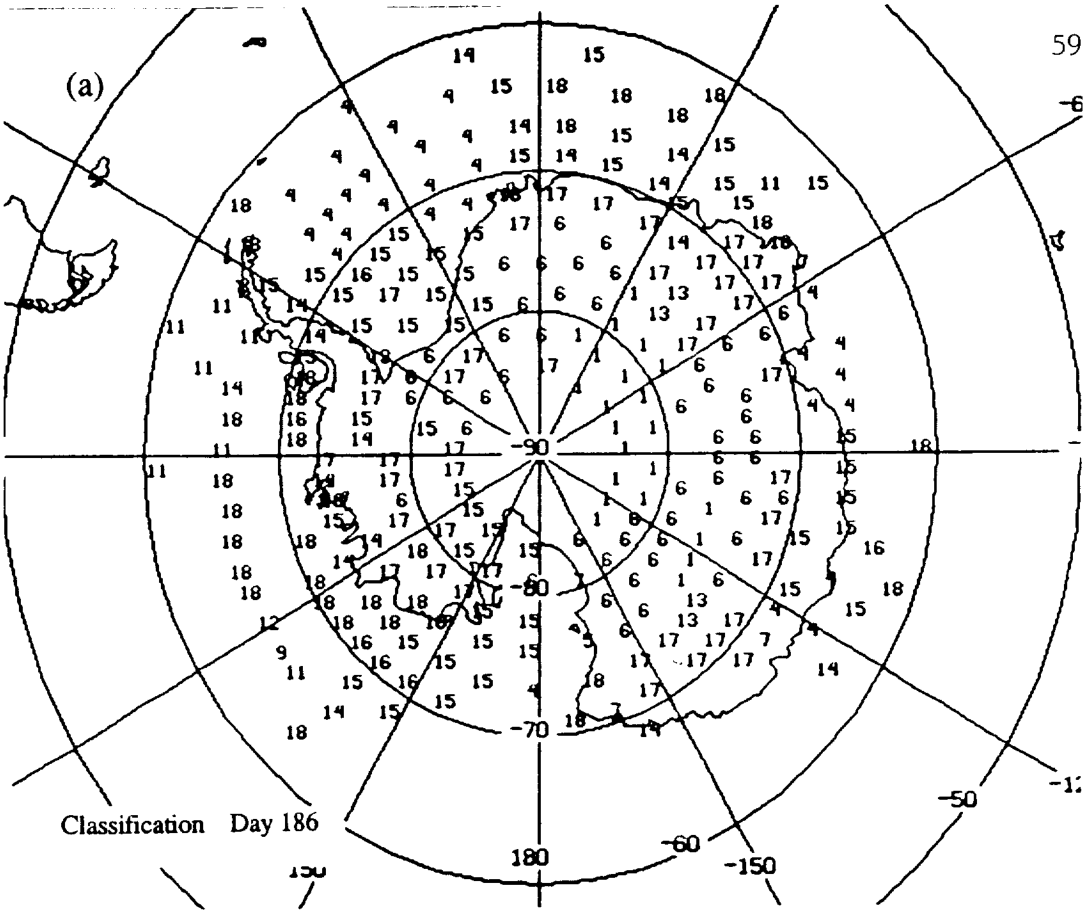

Classification Day 186

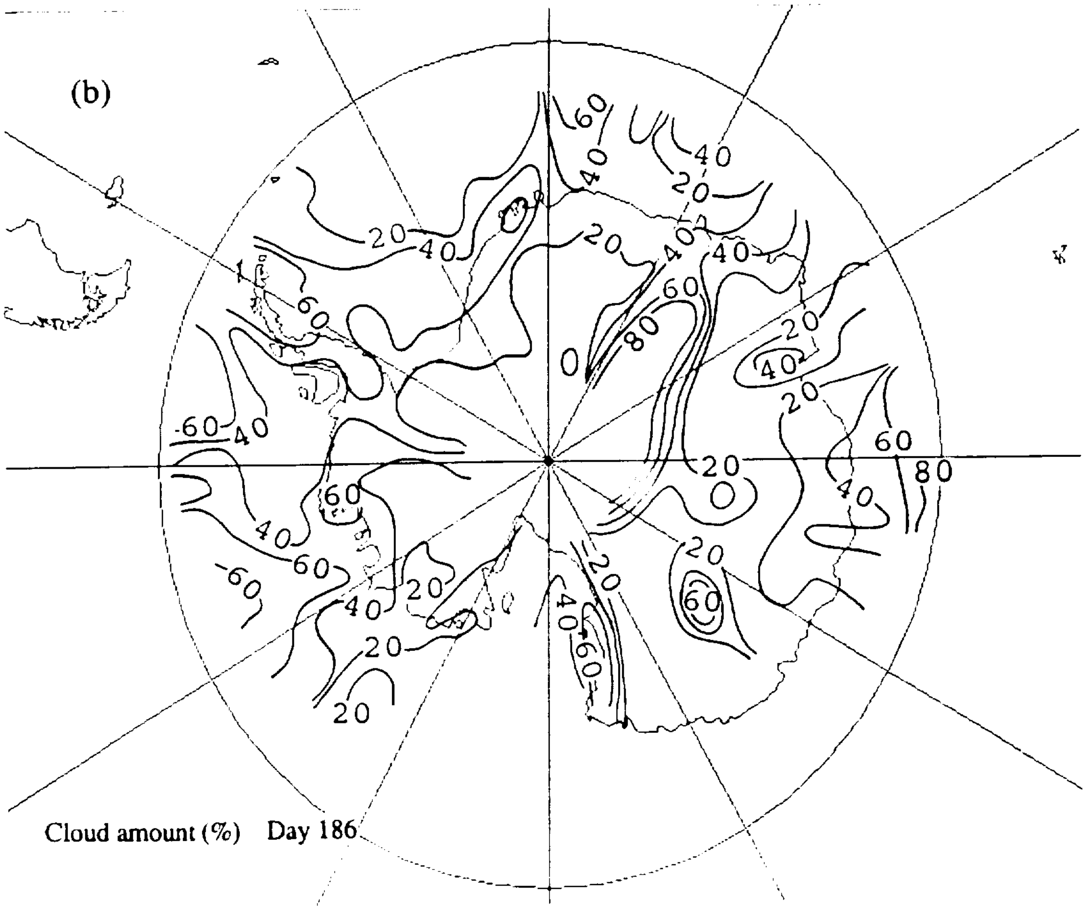

Cloud amount (%) Day 186

Figure 27

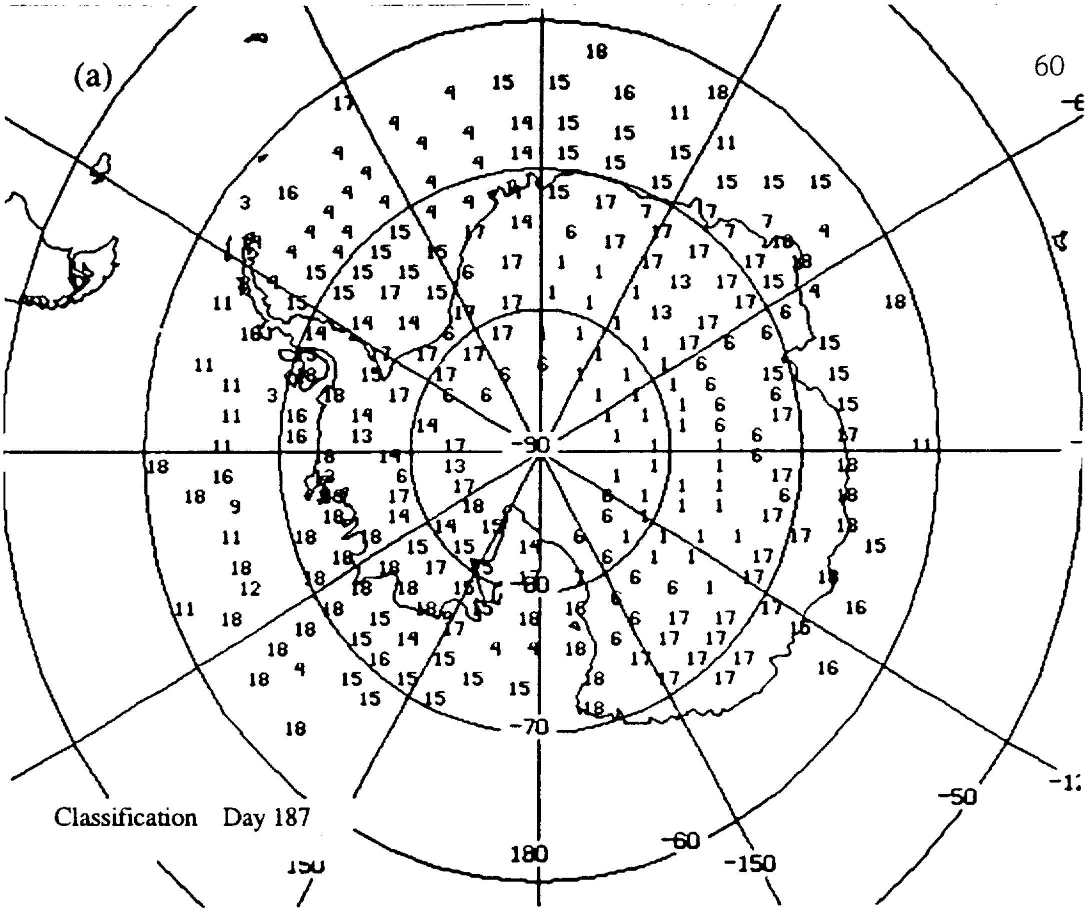

Classification Day 187

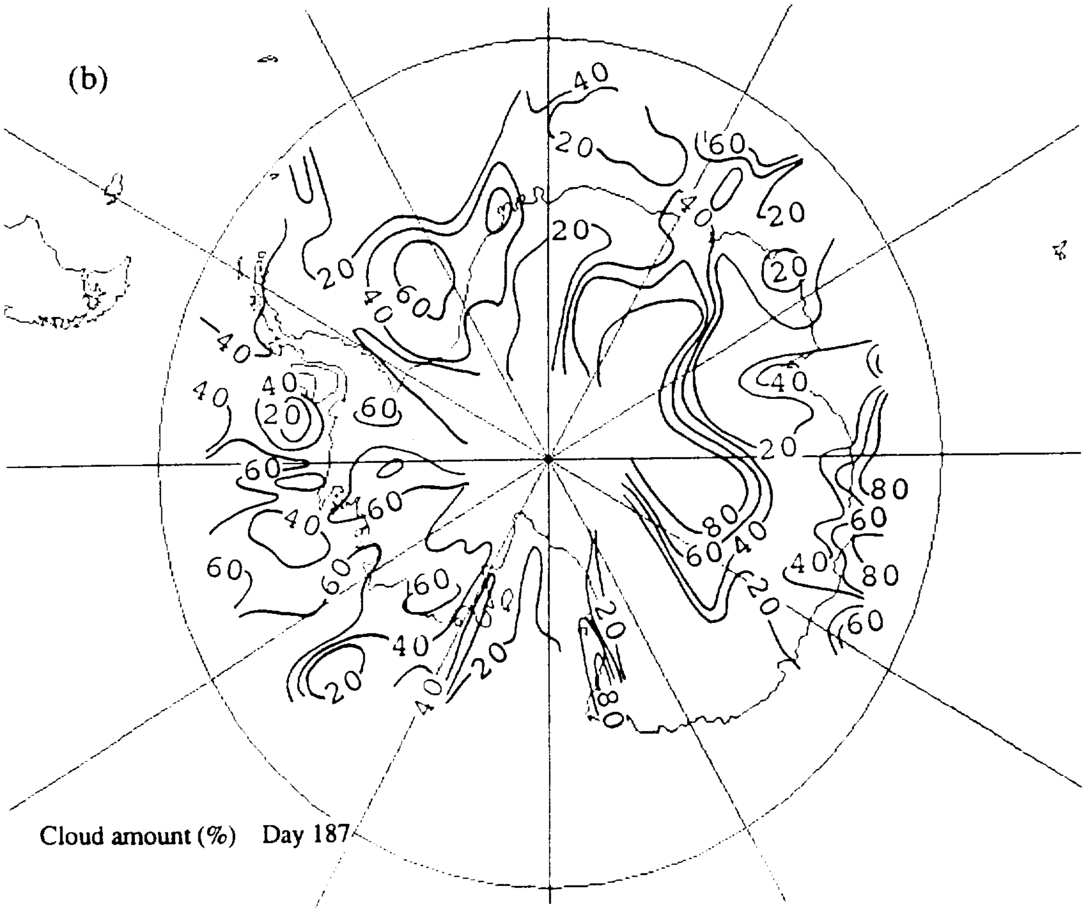

Cloud amount (%) Day 187

Figure 28

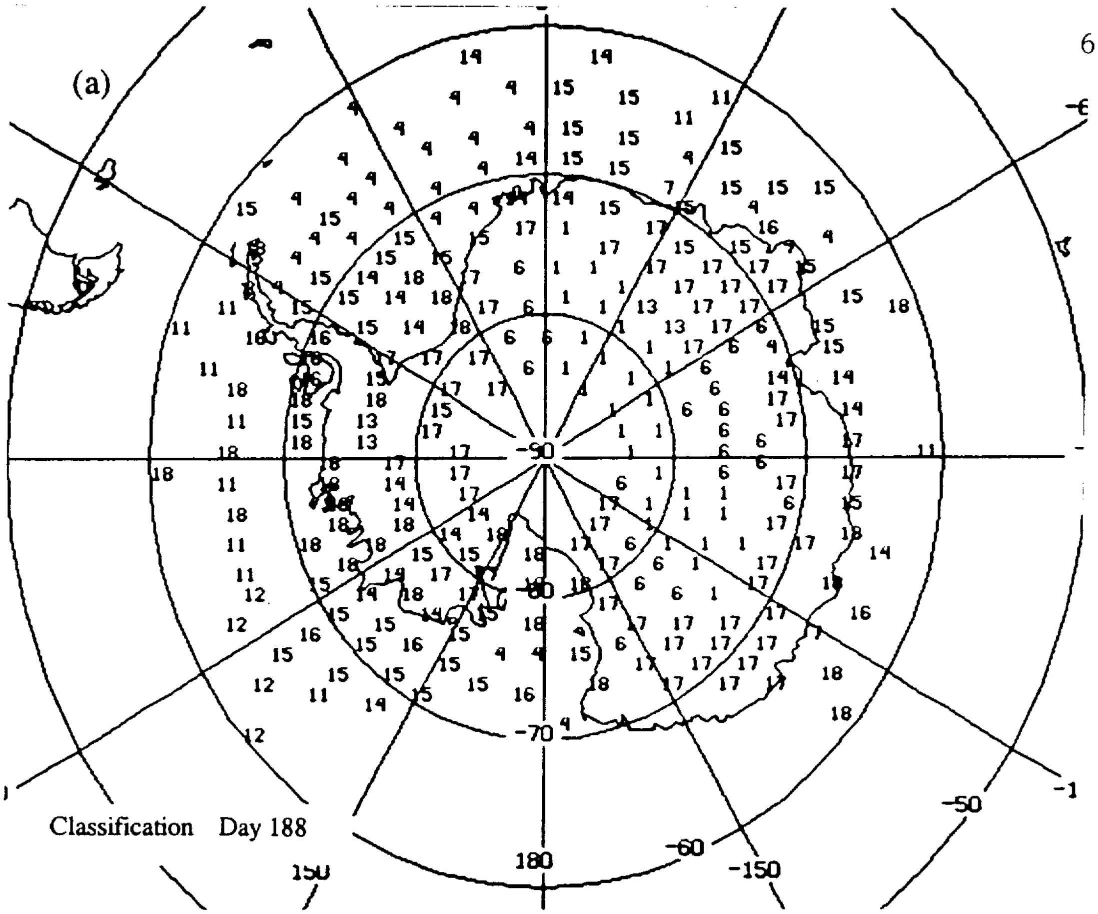

Classification Day 188

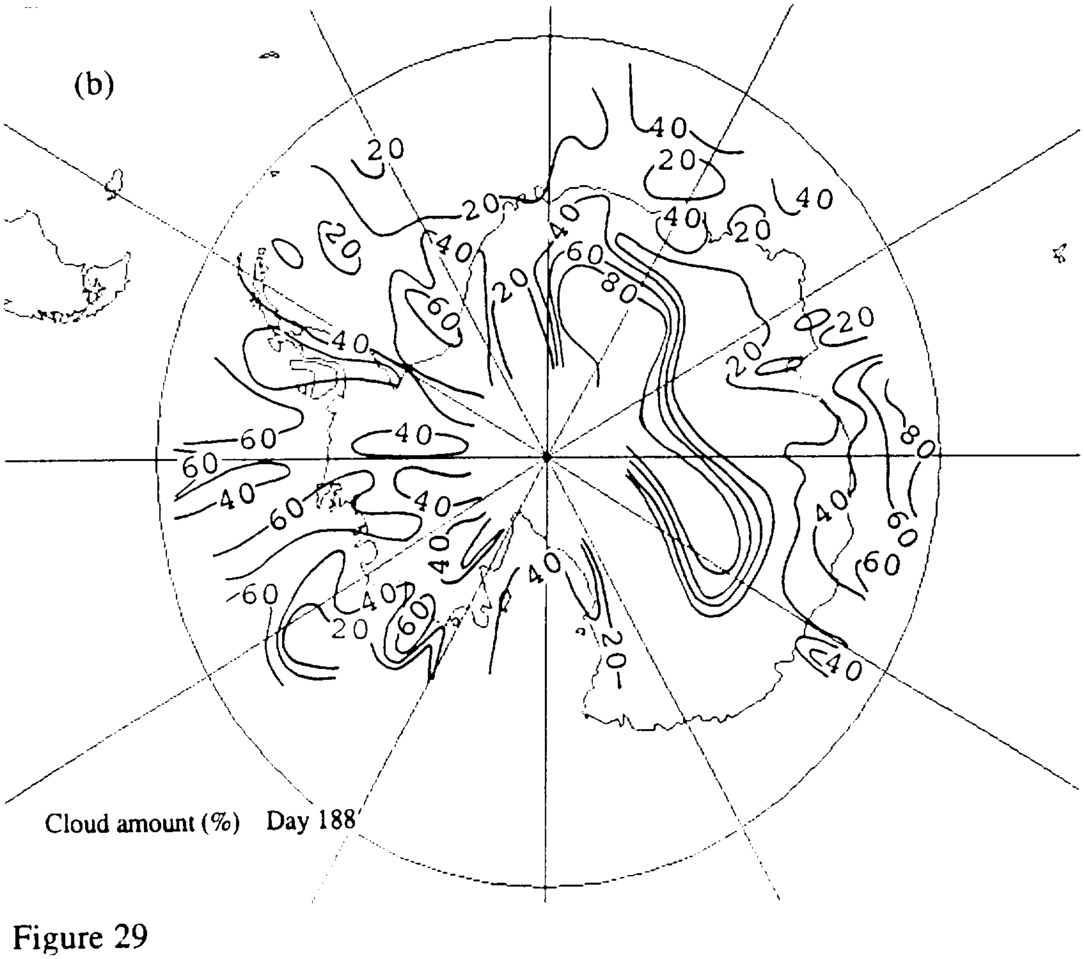

Cloud amount (%) Day 188

Figure 29

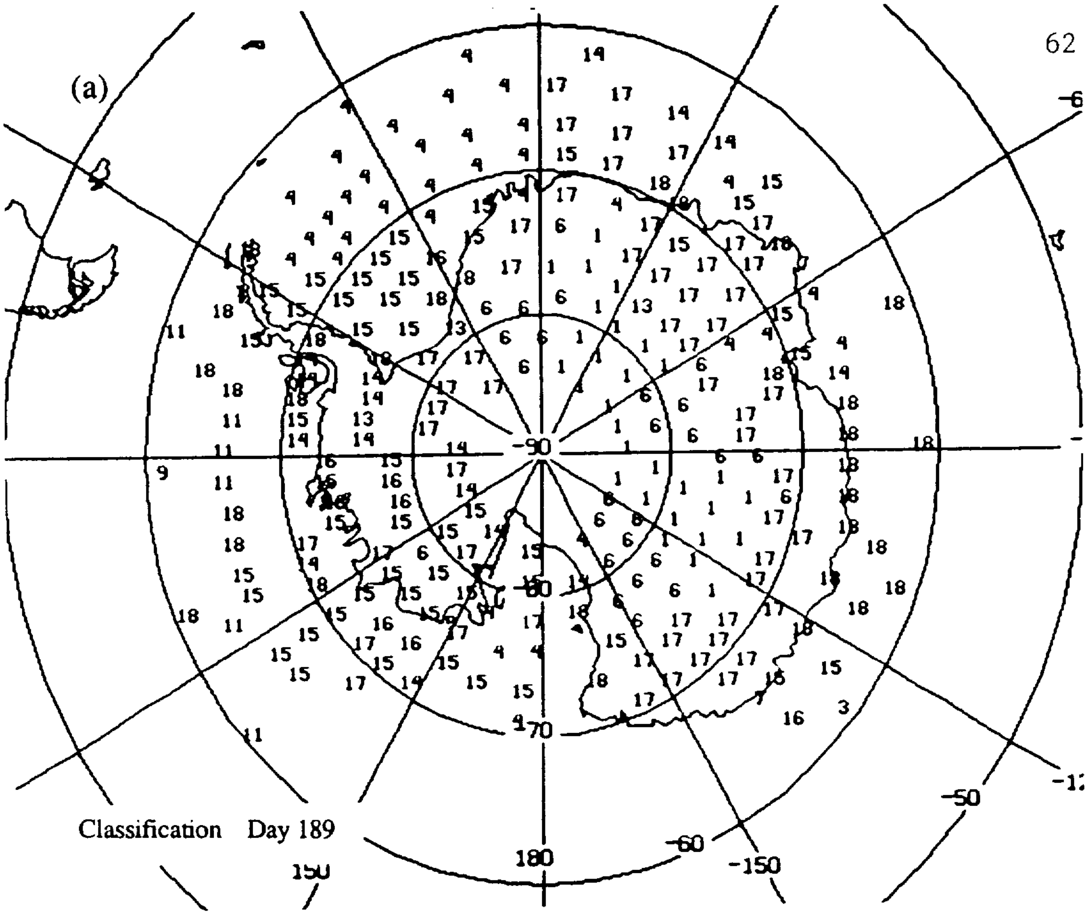

Classification Day 189

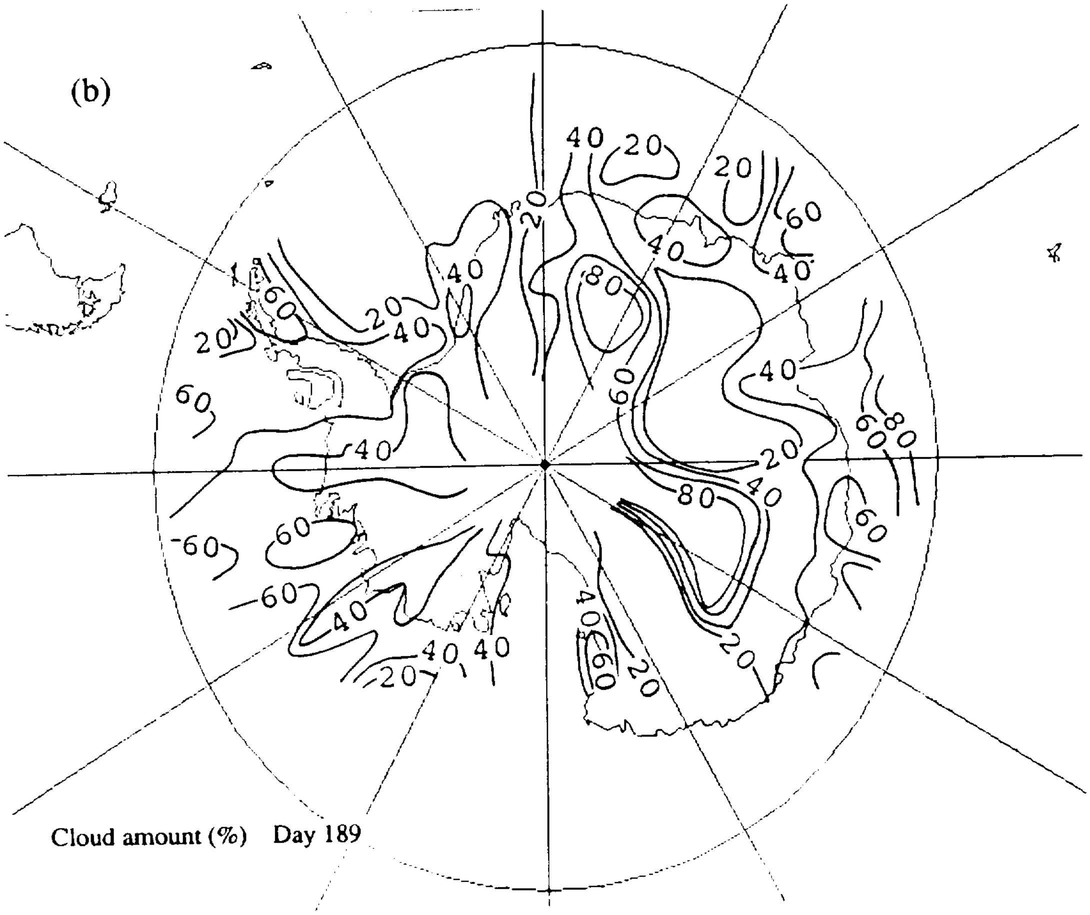

Cloud amount (%) Day 189

Figure 30

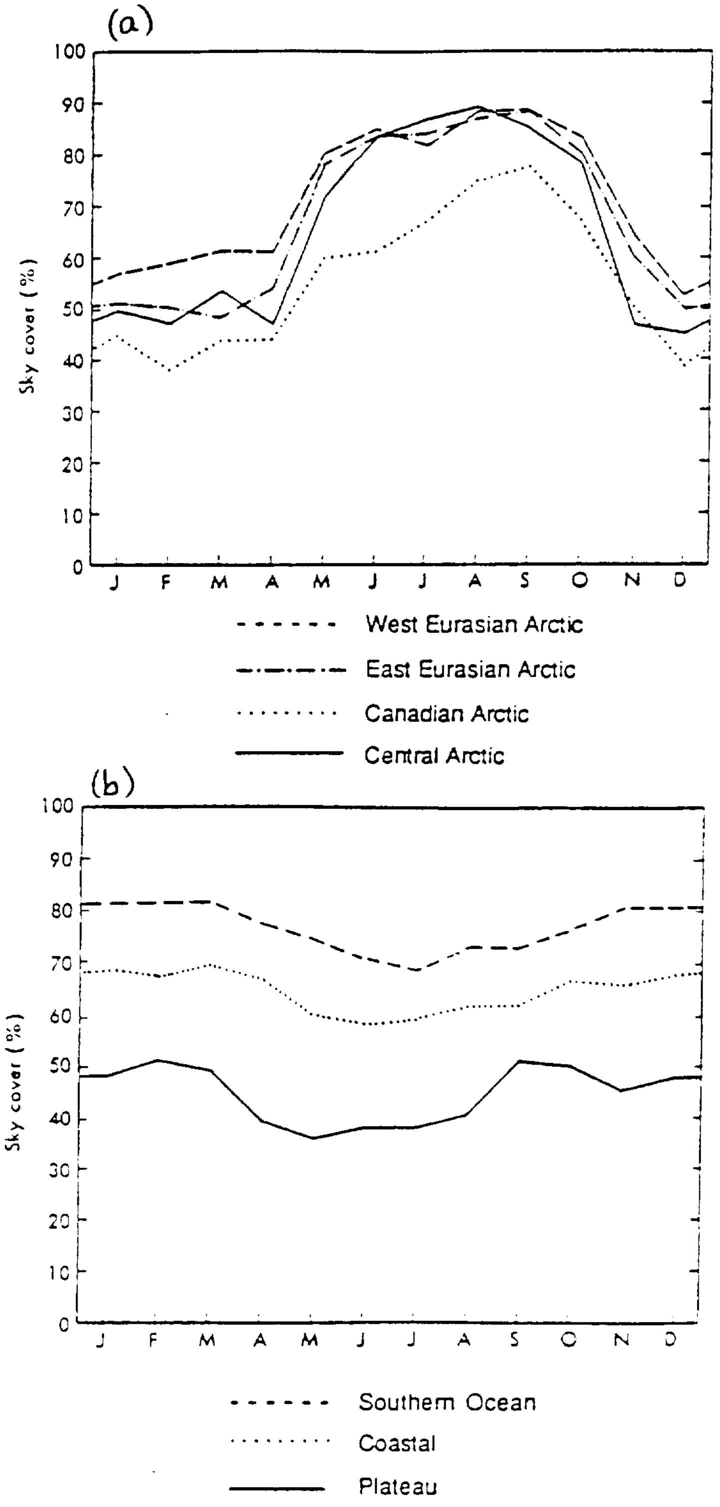

Figure 31. Annual variation of cloud fraction with region in (a) the Arctic (Huschke, 1969), and (b) the Antarctic (from the climatic tables of Schwerdtfeger, 1970).

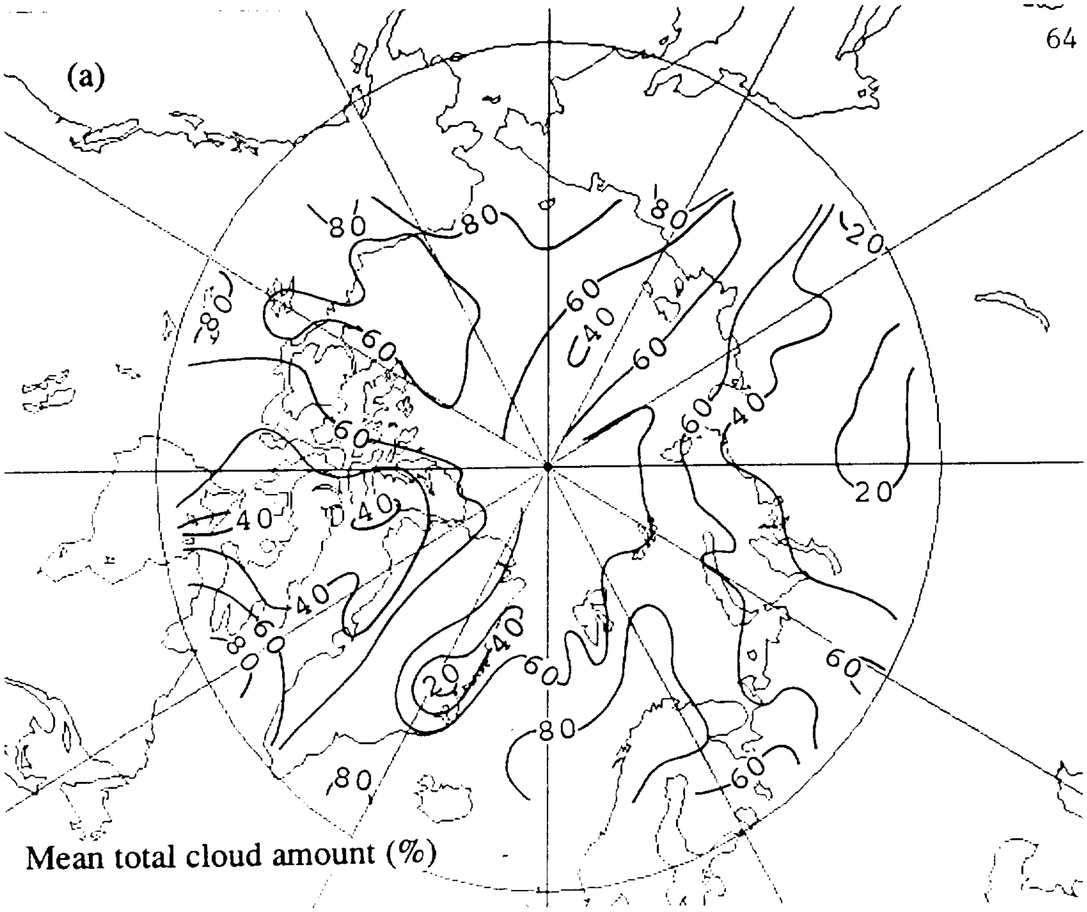

Mean total cloud amount (%)

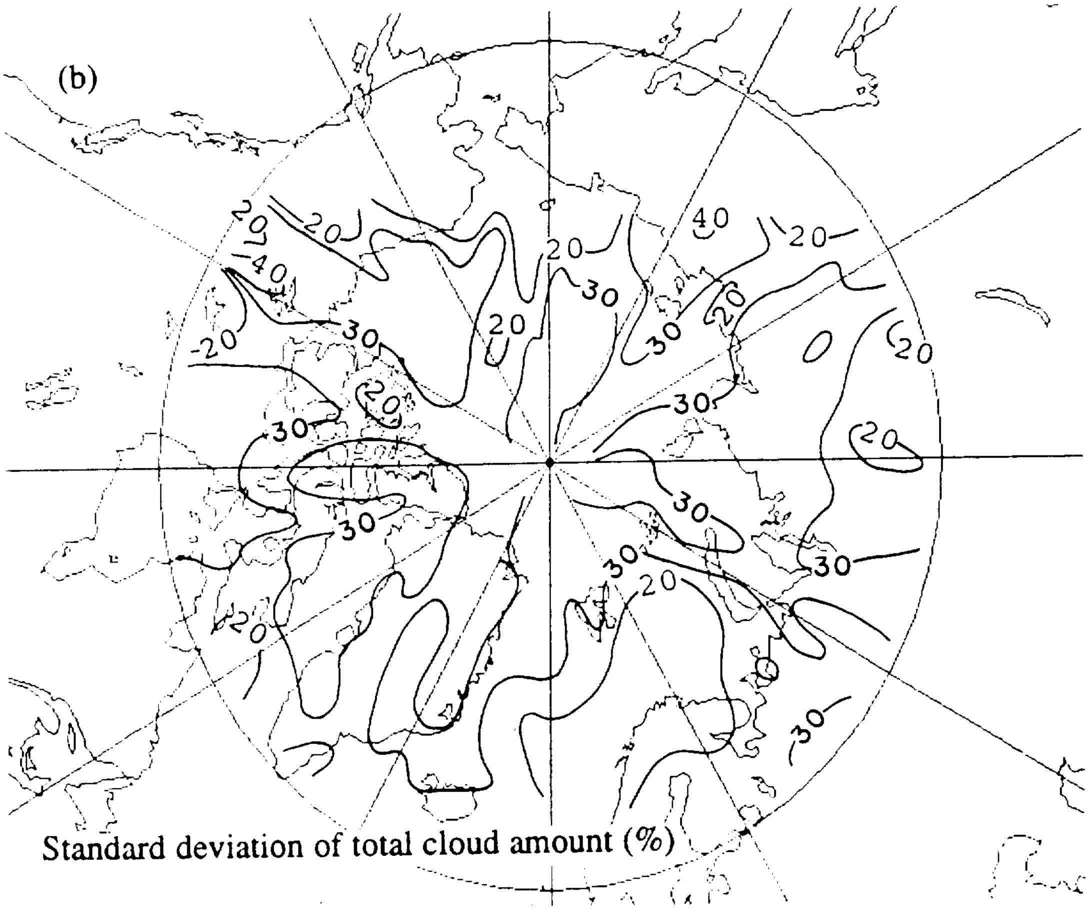

Standard deviation of total cloud amount (%)

Figure 32

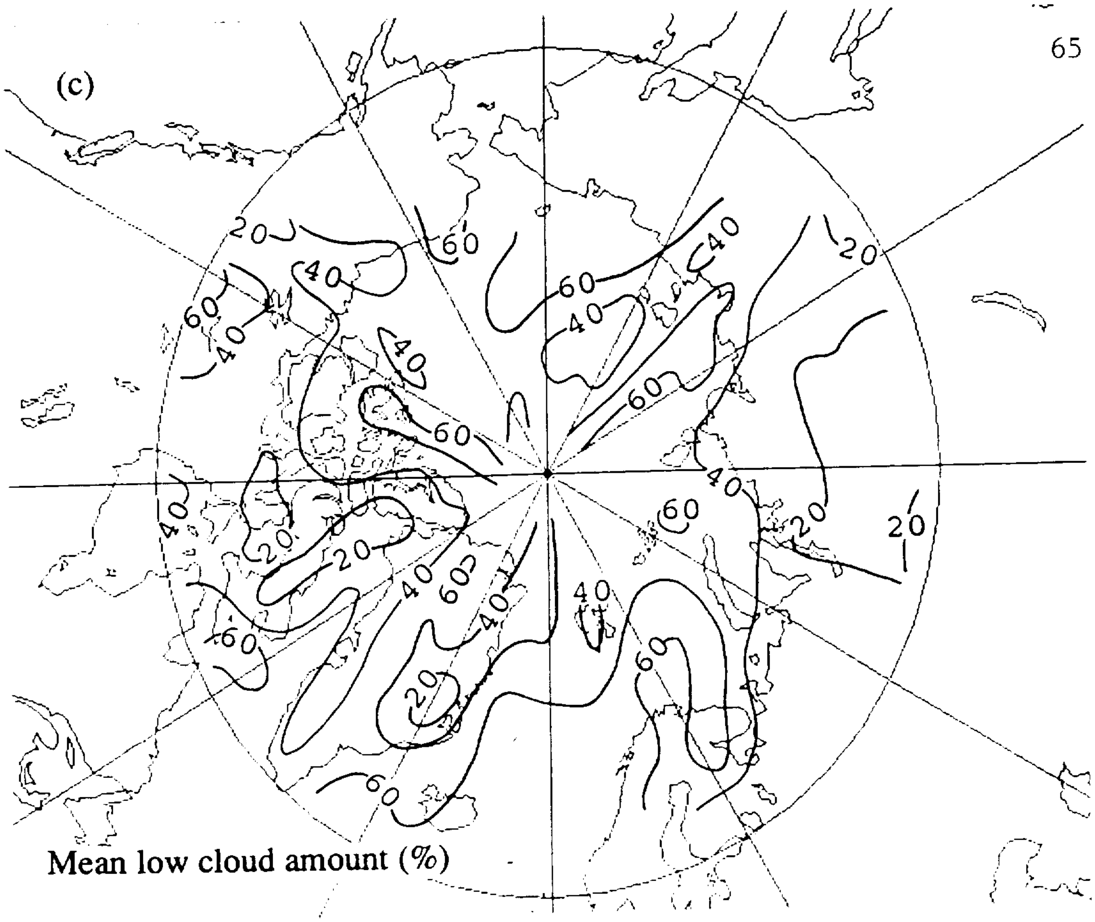

Mean low cloud amount (%)

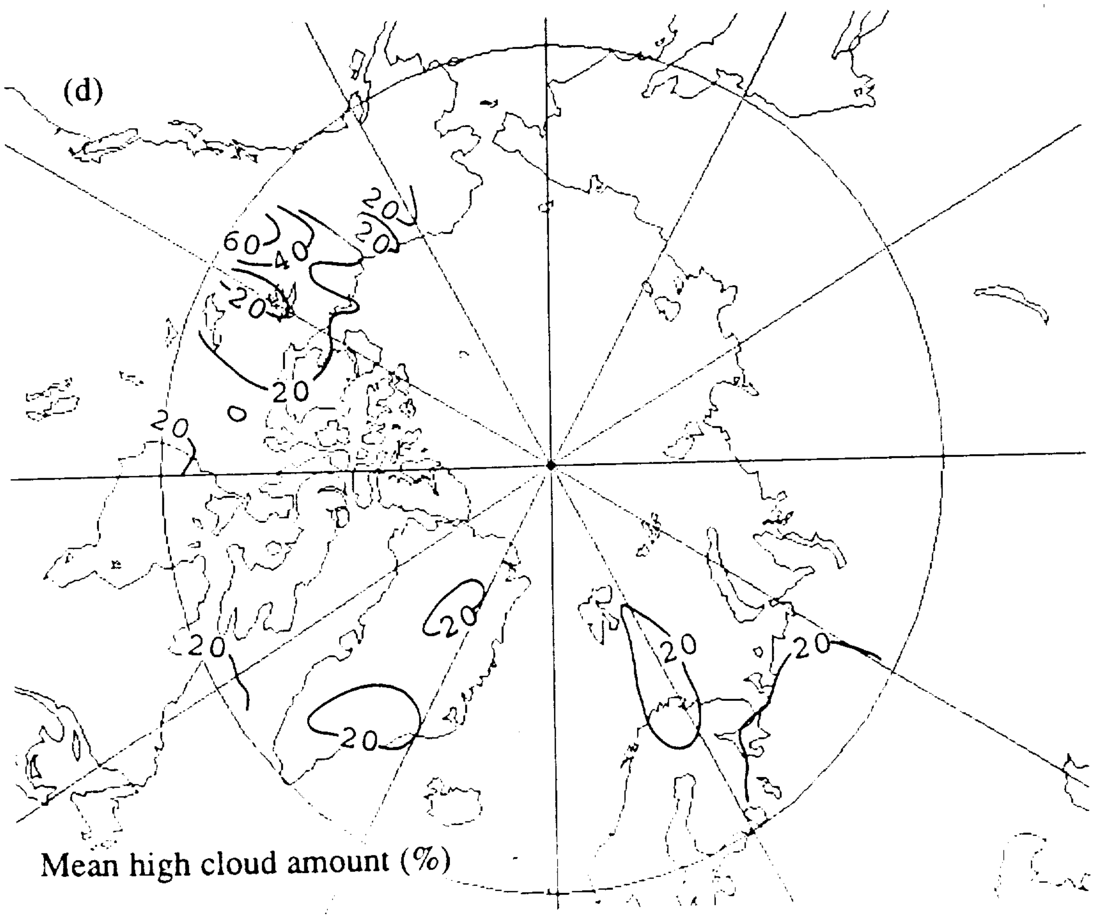

Mean high cloud amount (%)

Figure 32

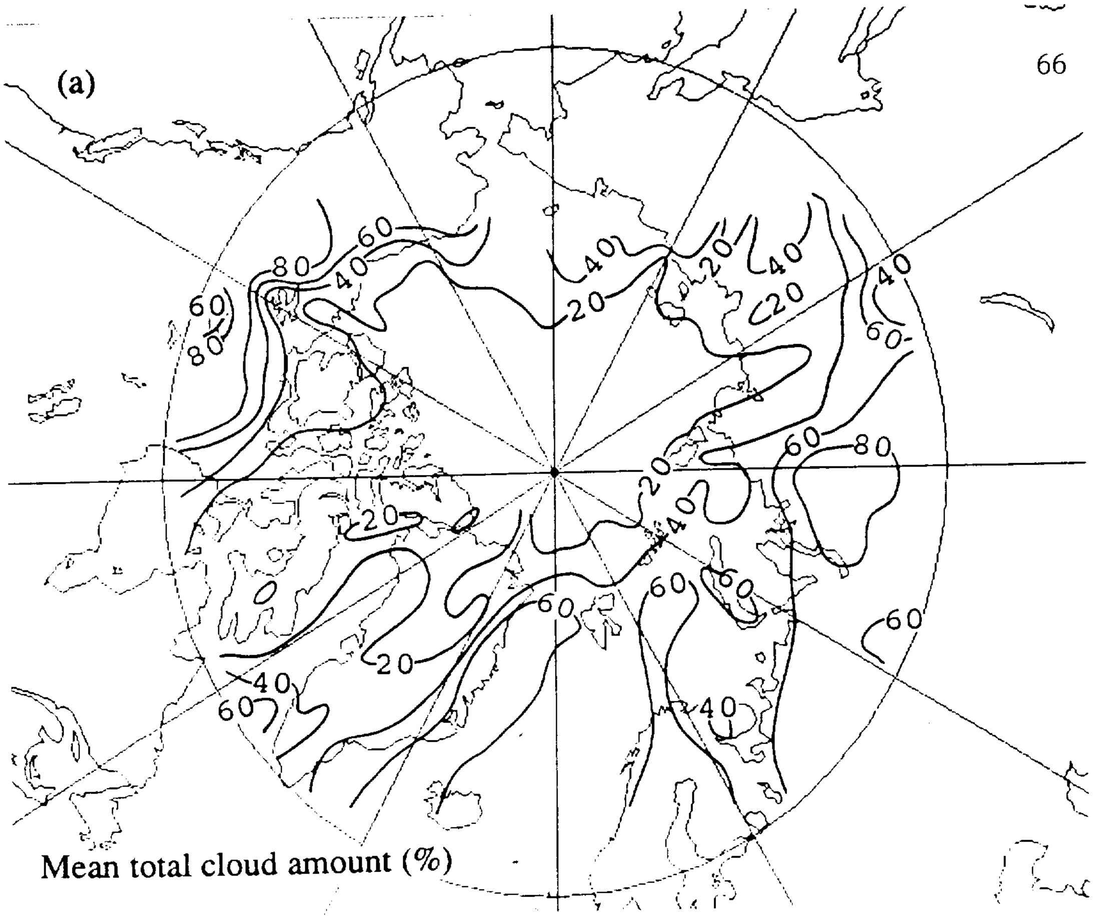

Mean total cloud amount (%)

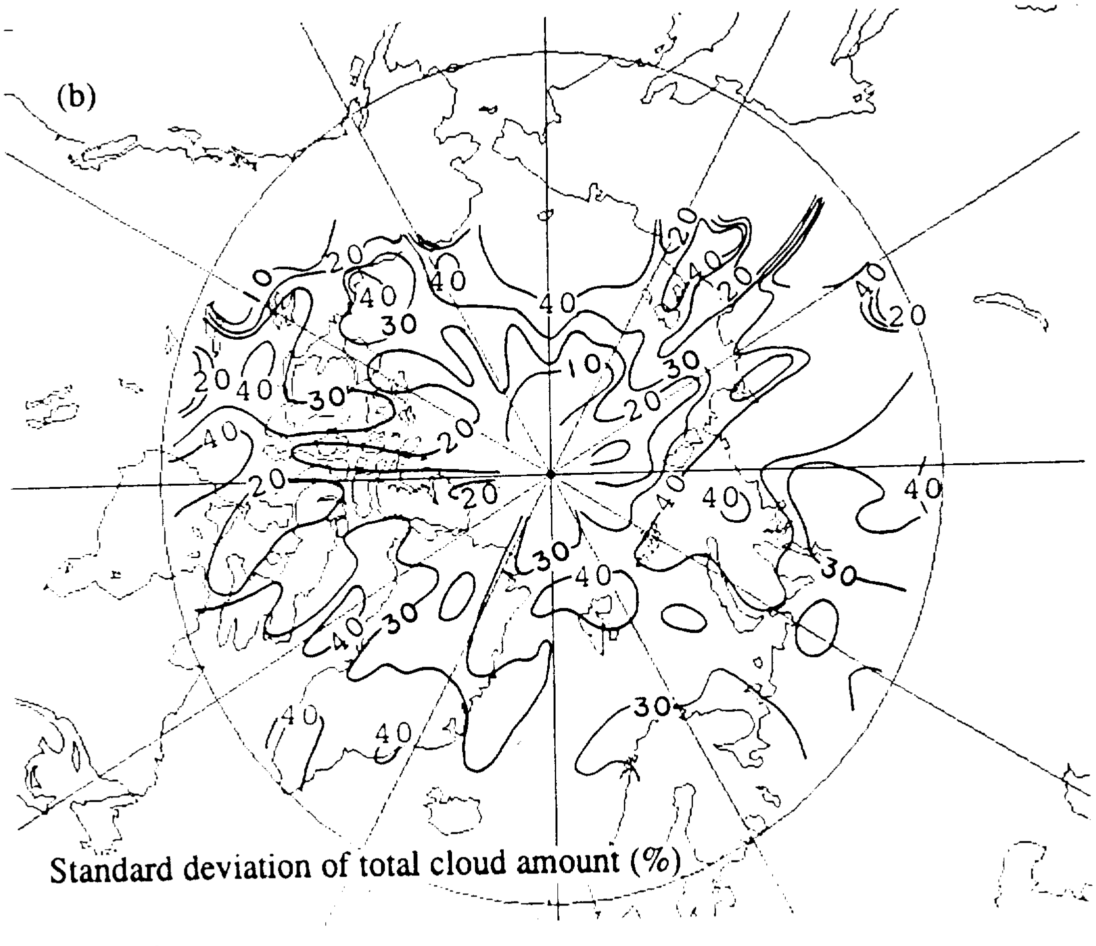

Standard deviation of total cloud amount (%)

Figure 33

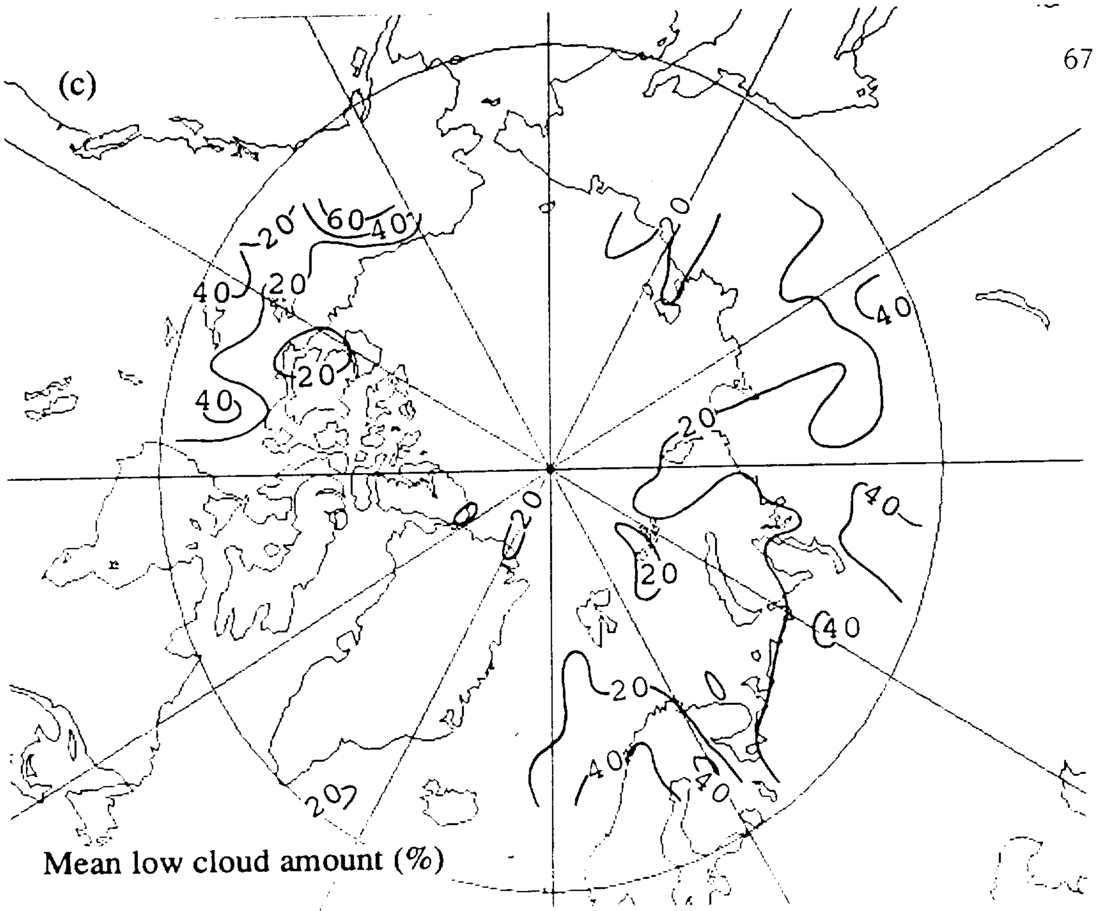

Mean low cloud amount (%)

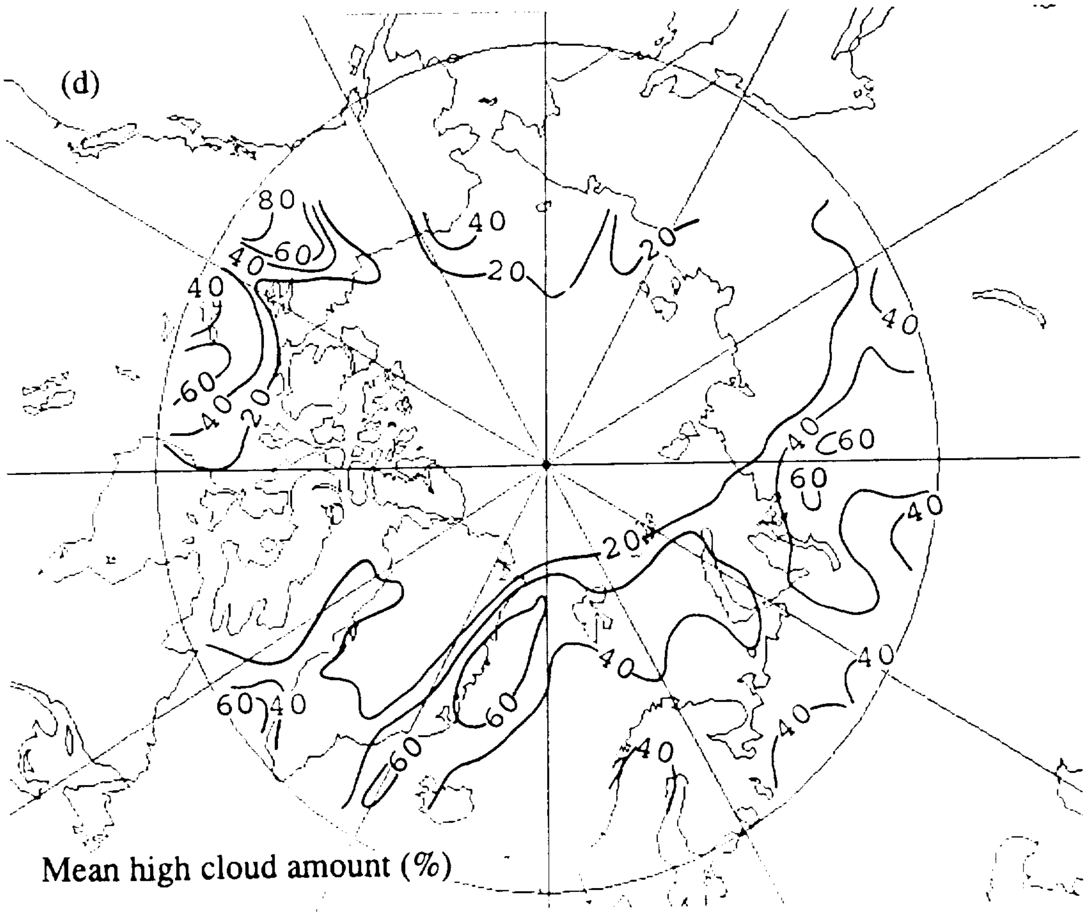

Mean high cloud amount (%)

Figure 33

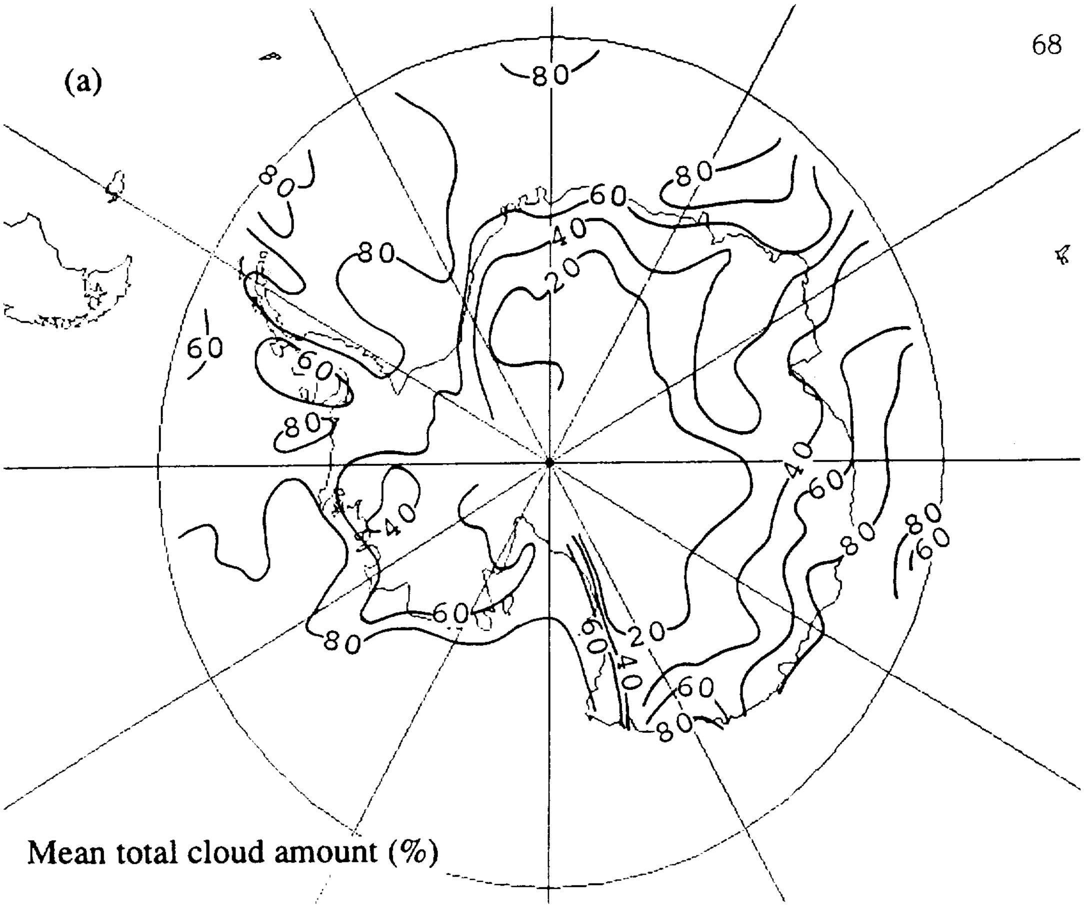

Mean total cloud amount (%)

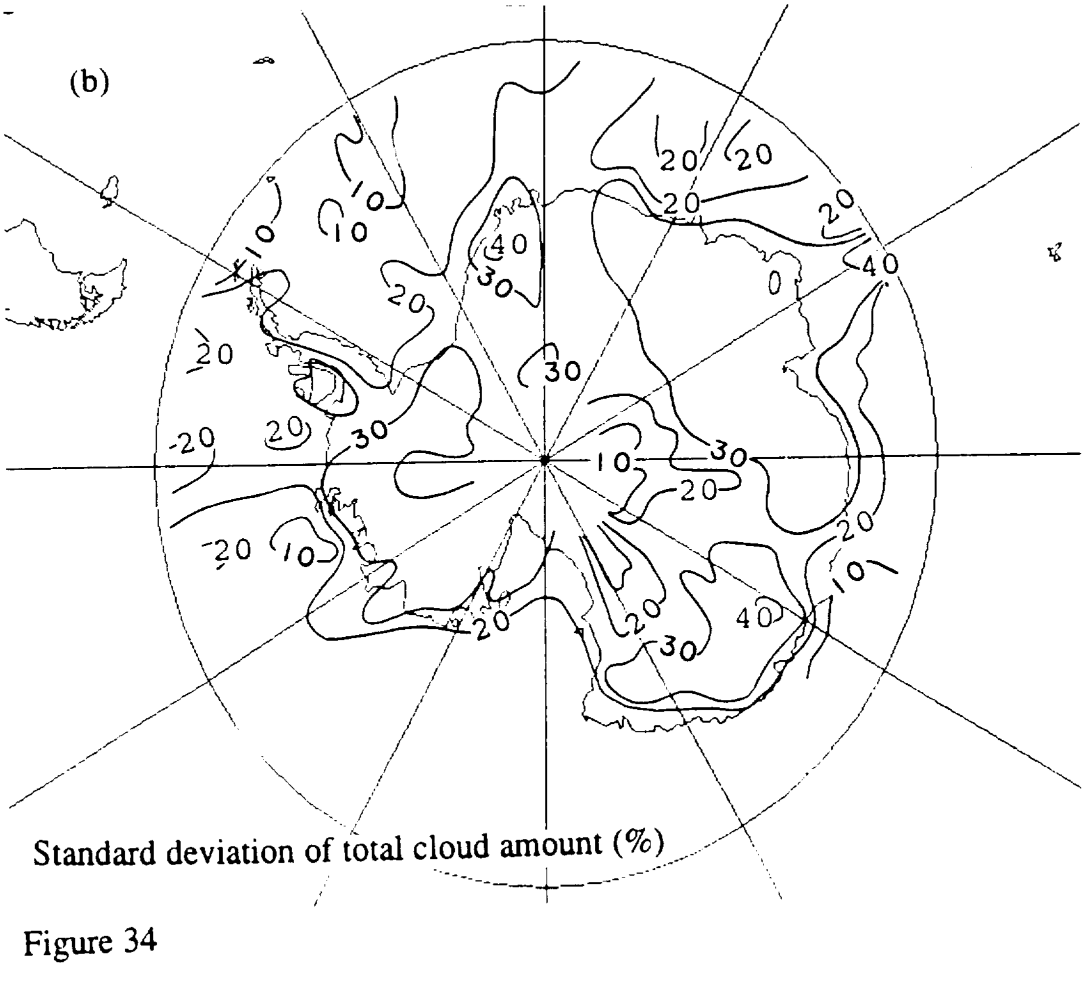

Standard deviation of total cloud amount (%)

Figure 34

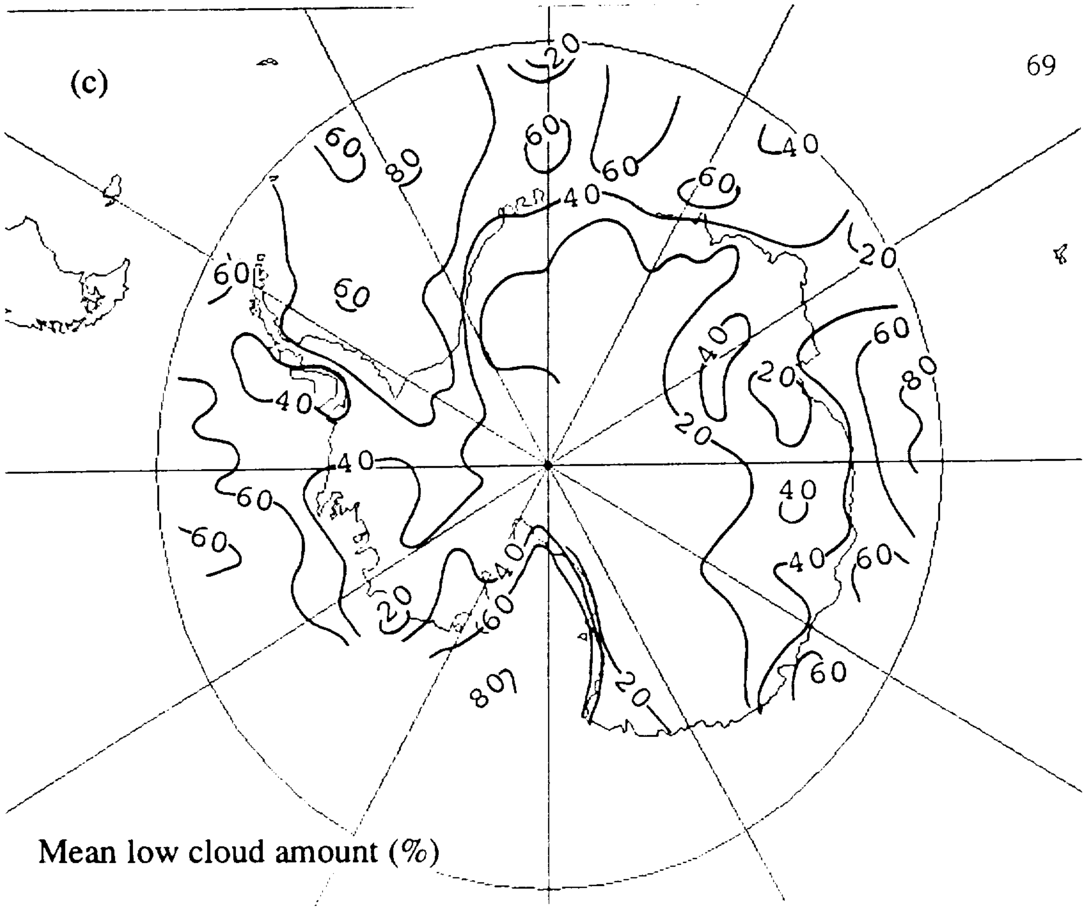

Mean low cloud amount (%)

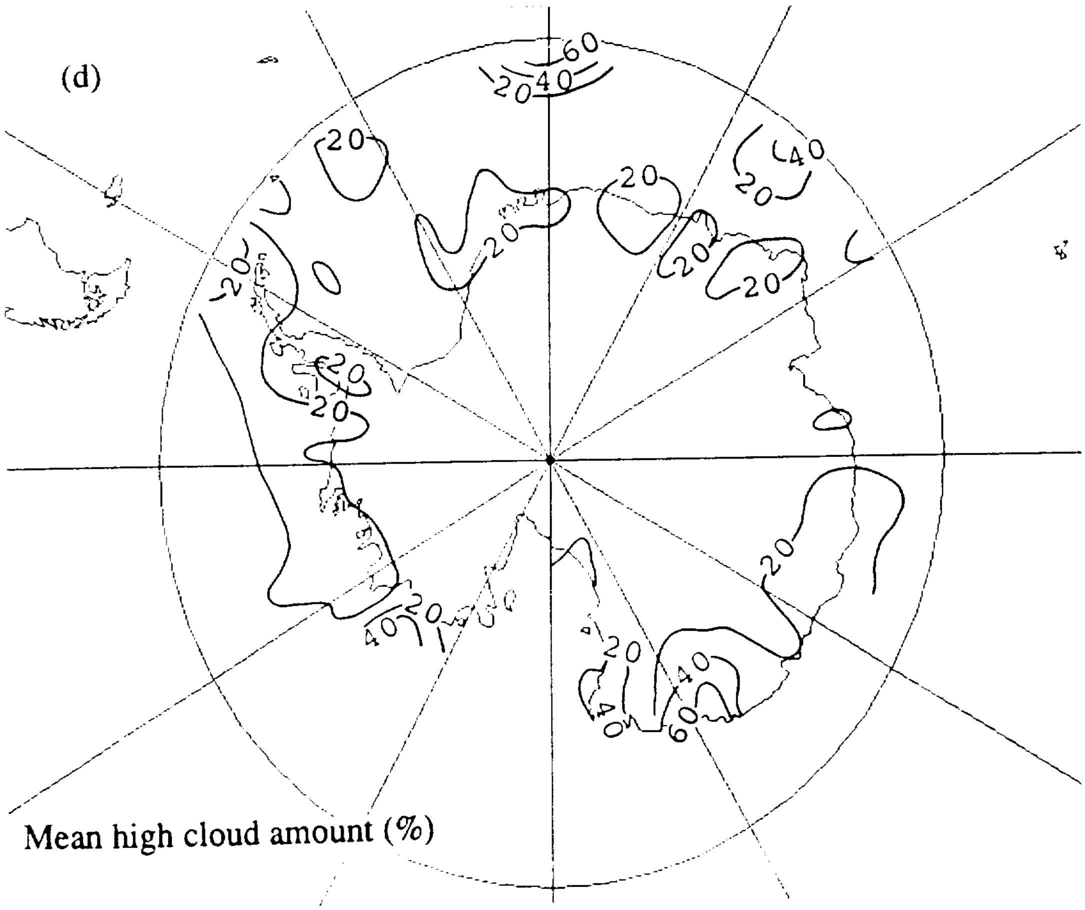

Mean high cloud amount (%)

Figure 34

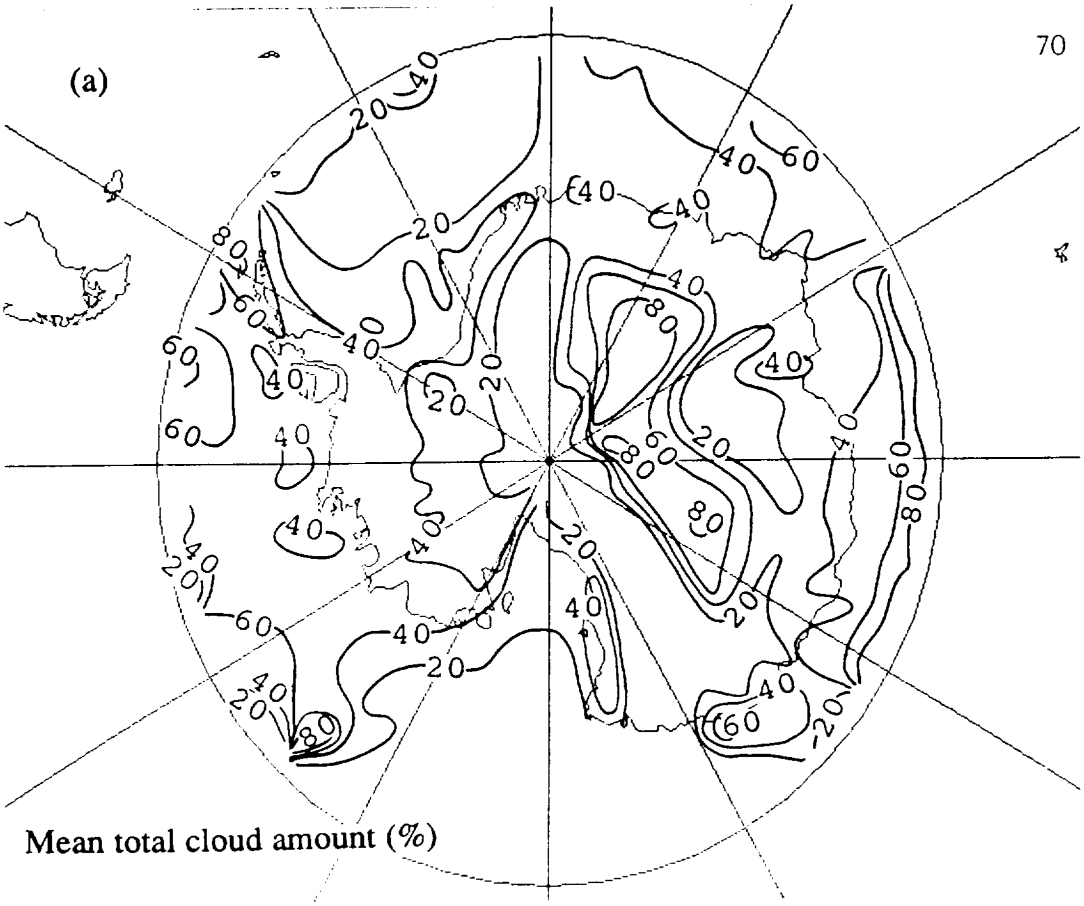

Mean total cloud amount (%)

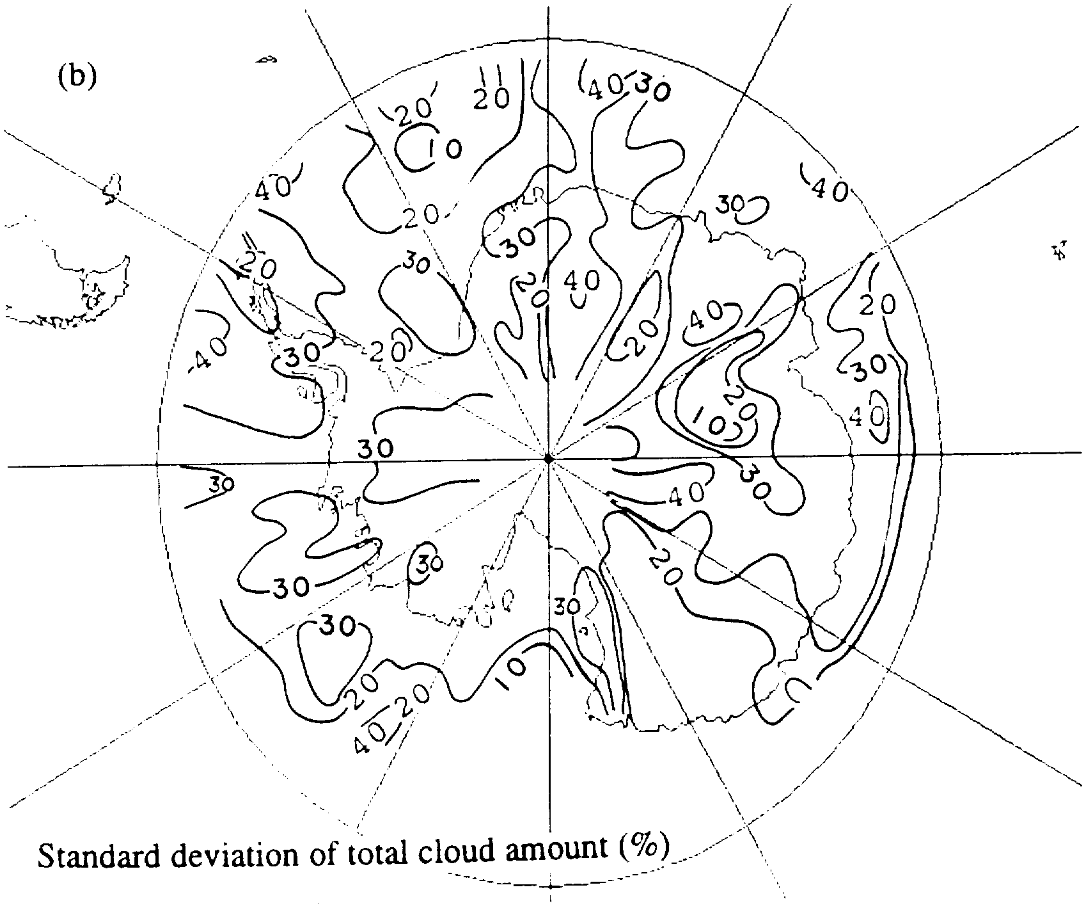

Standard deviation of total cloud amount (%)

Figure 35

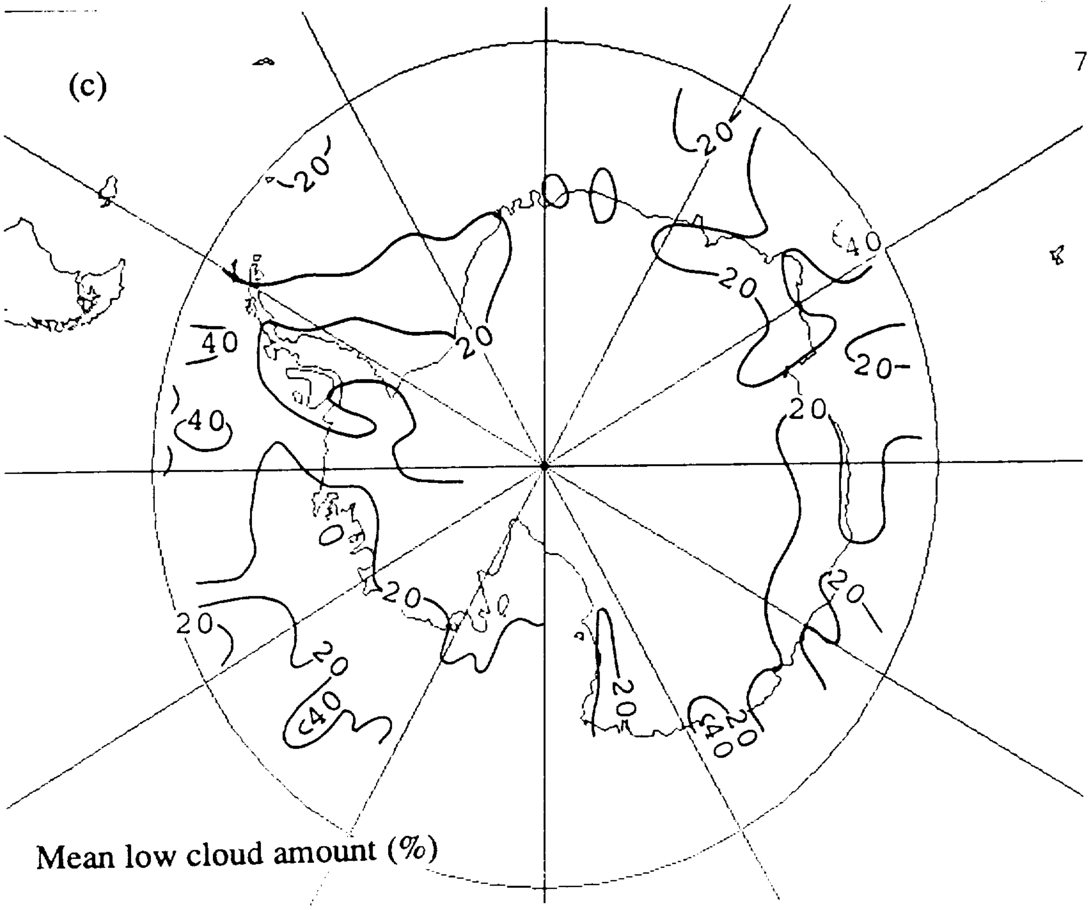

Mean low cloud amount (%)

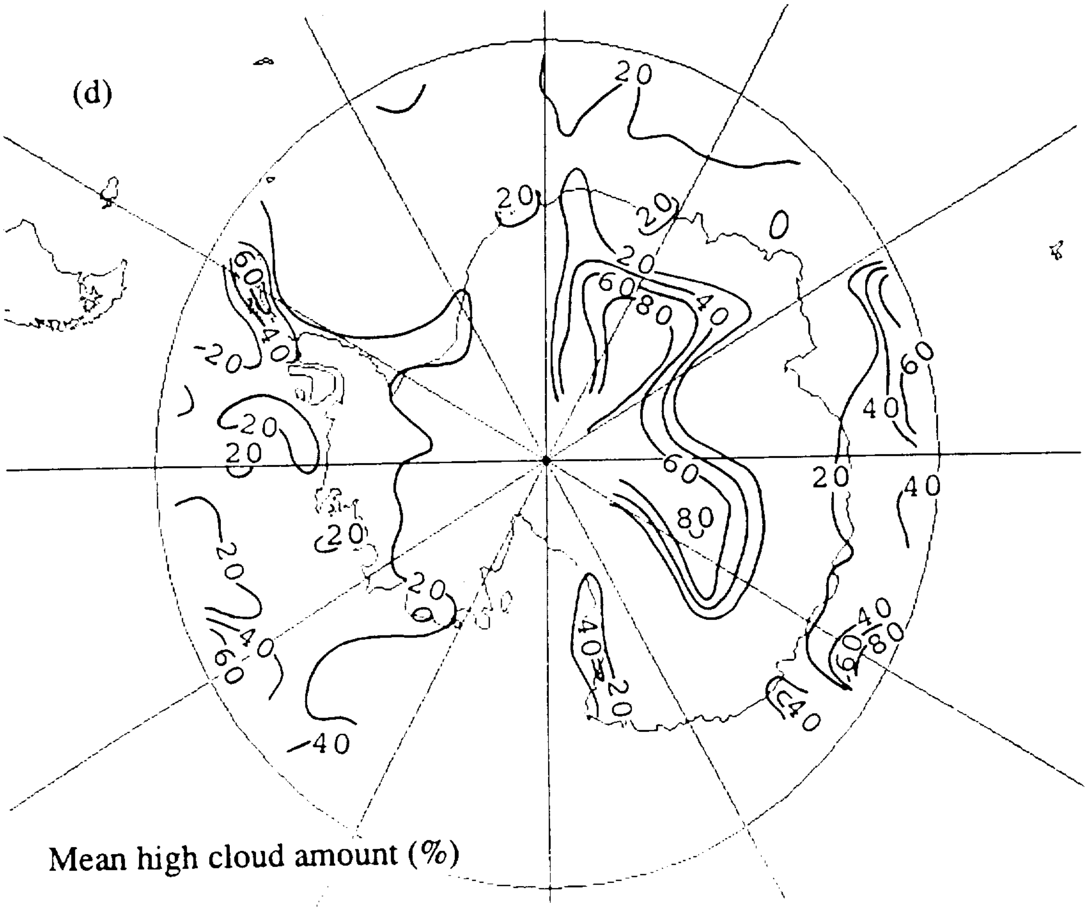

Mean high cloud amount (%)

Figure 35

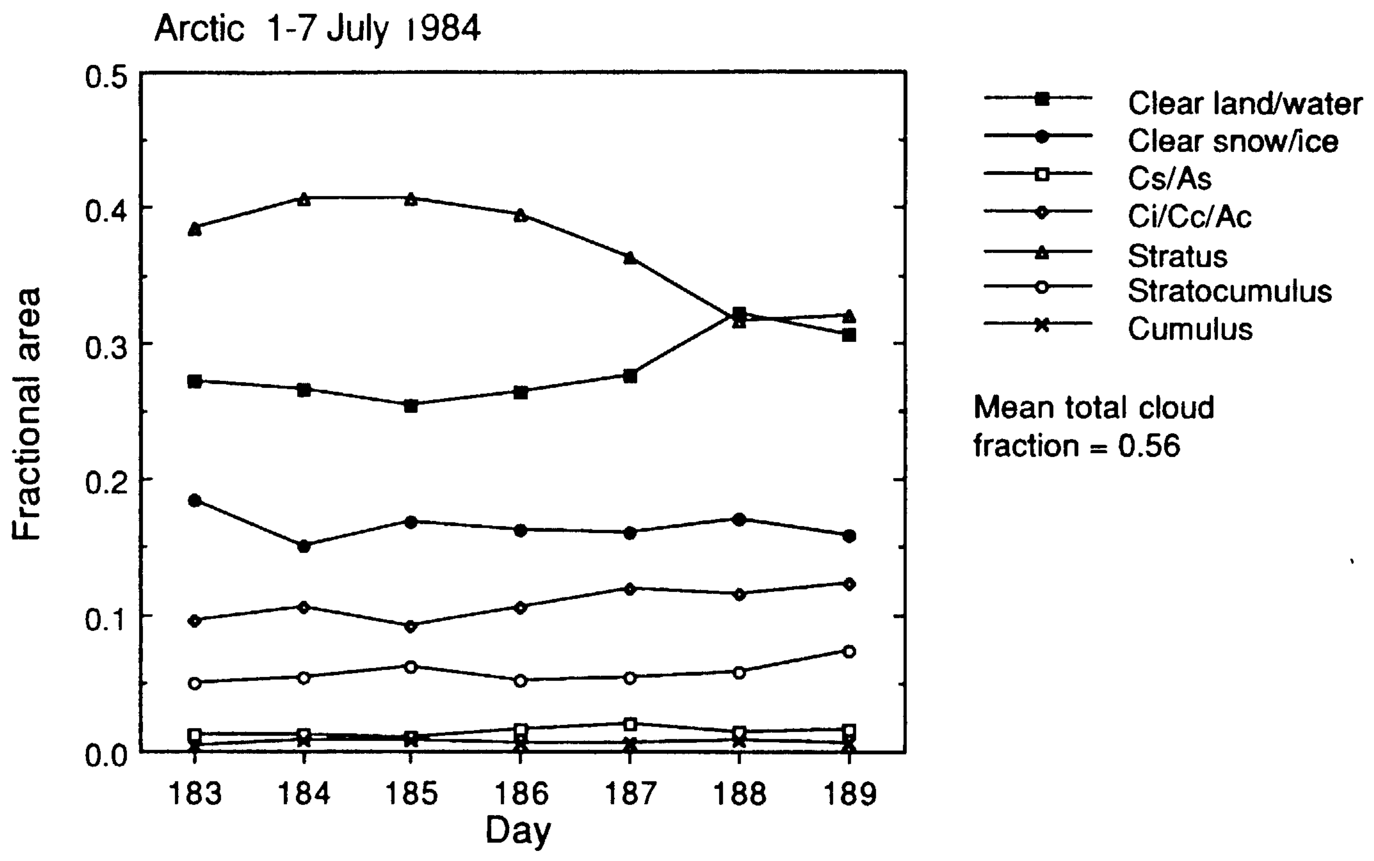

Fig. 36. Fractional area covered by each surface and cloud type during the week of 1-7 July 1984 in the Arctic.

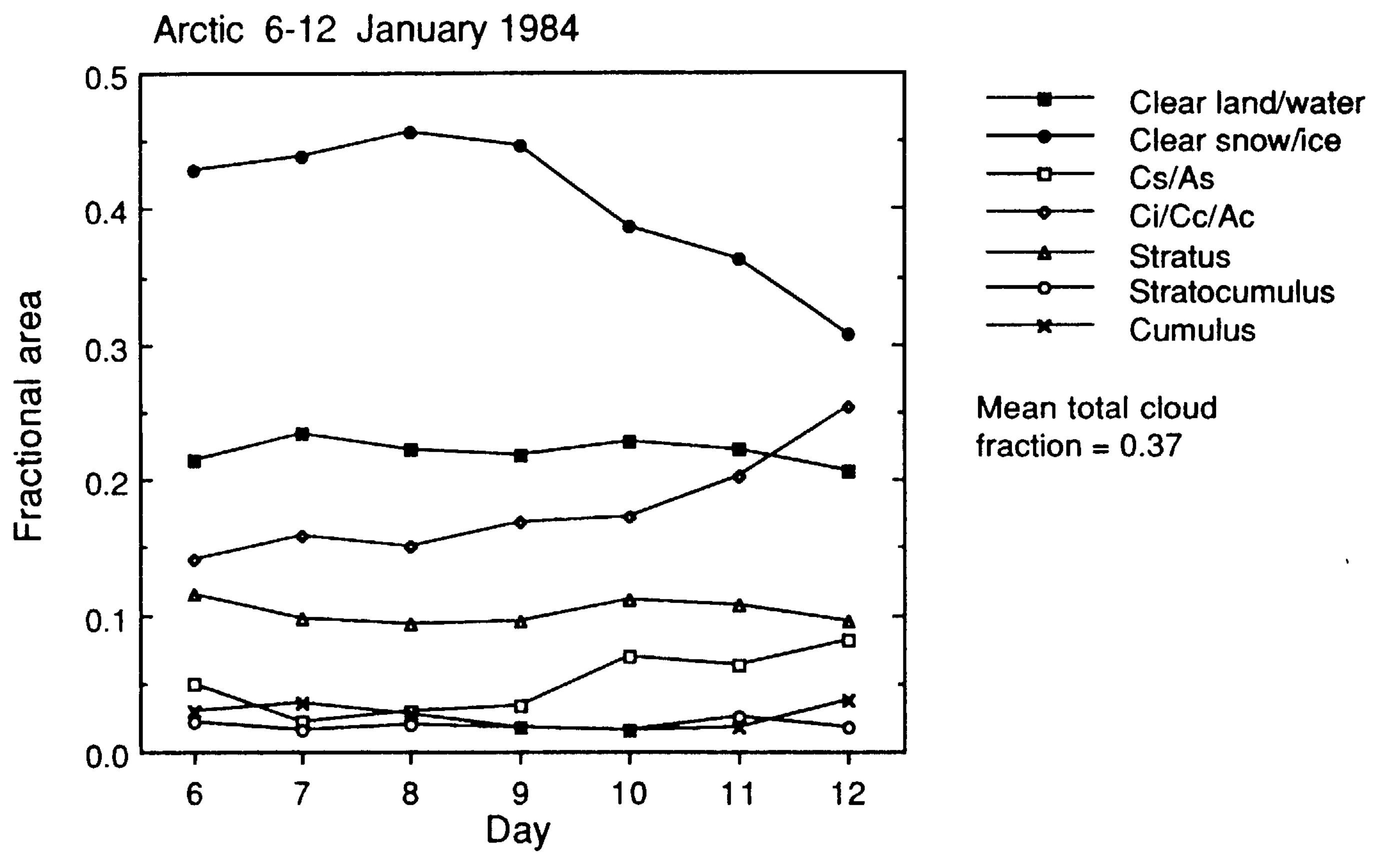

Fig. 37. Fractional area covered by each surface and cloud type during the week of 6-12 January 1984 in the Arctic.

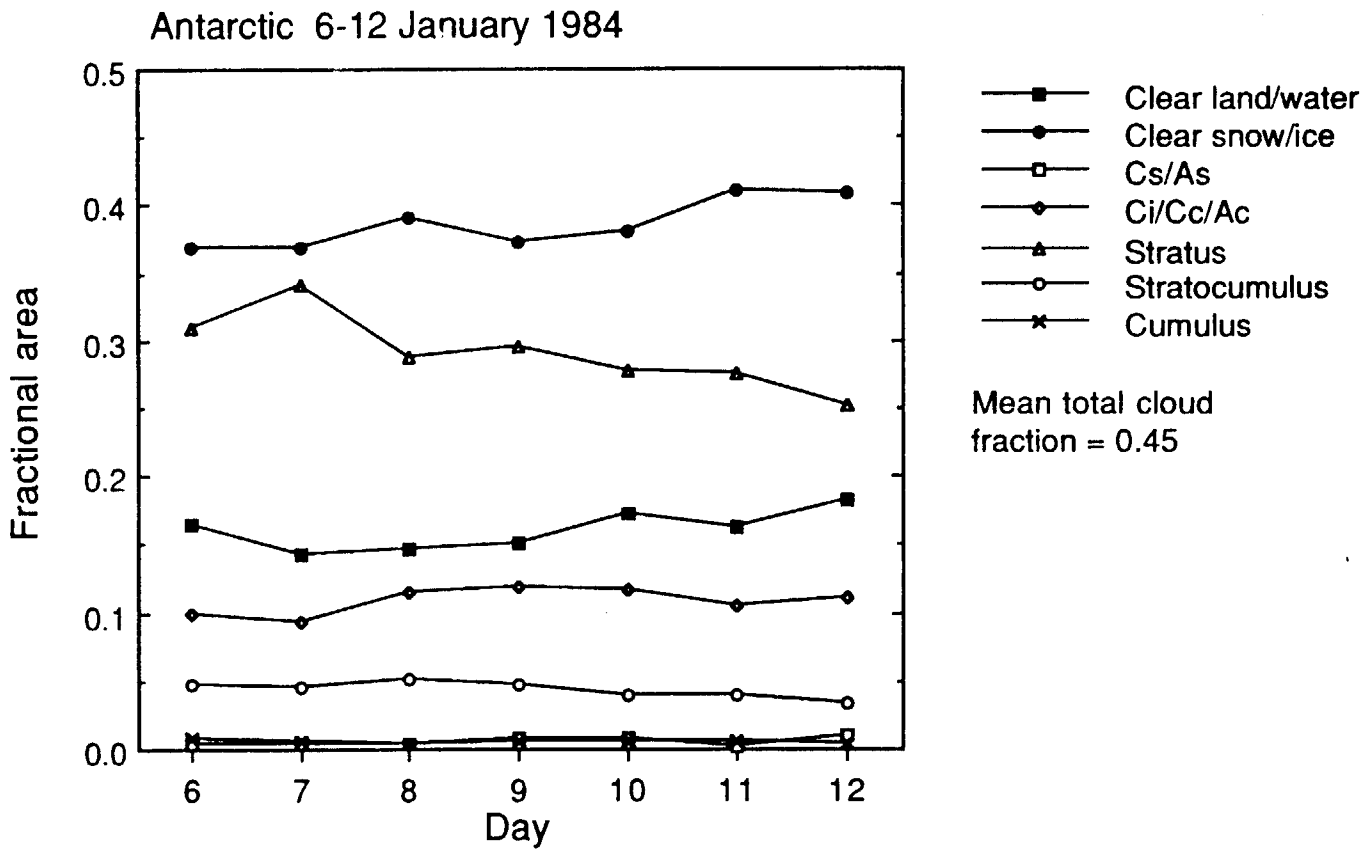

Fig. 38. Fractional area covered by each surface and cloud type during the week of 6-12 January 1984 in the Antarctic.

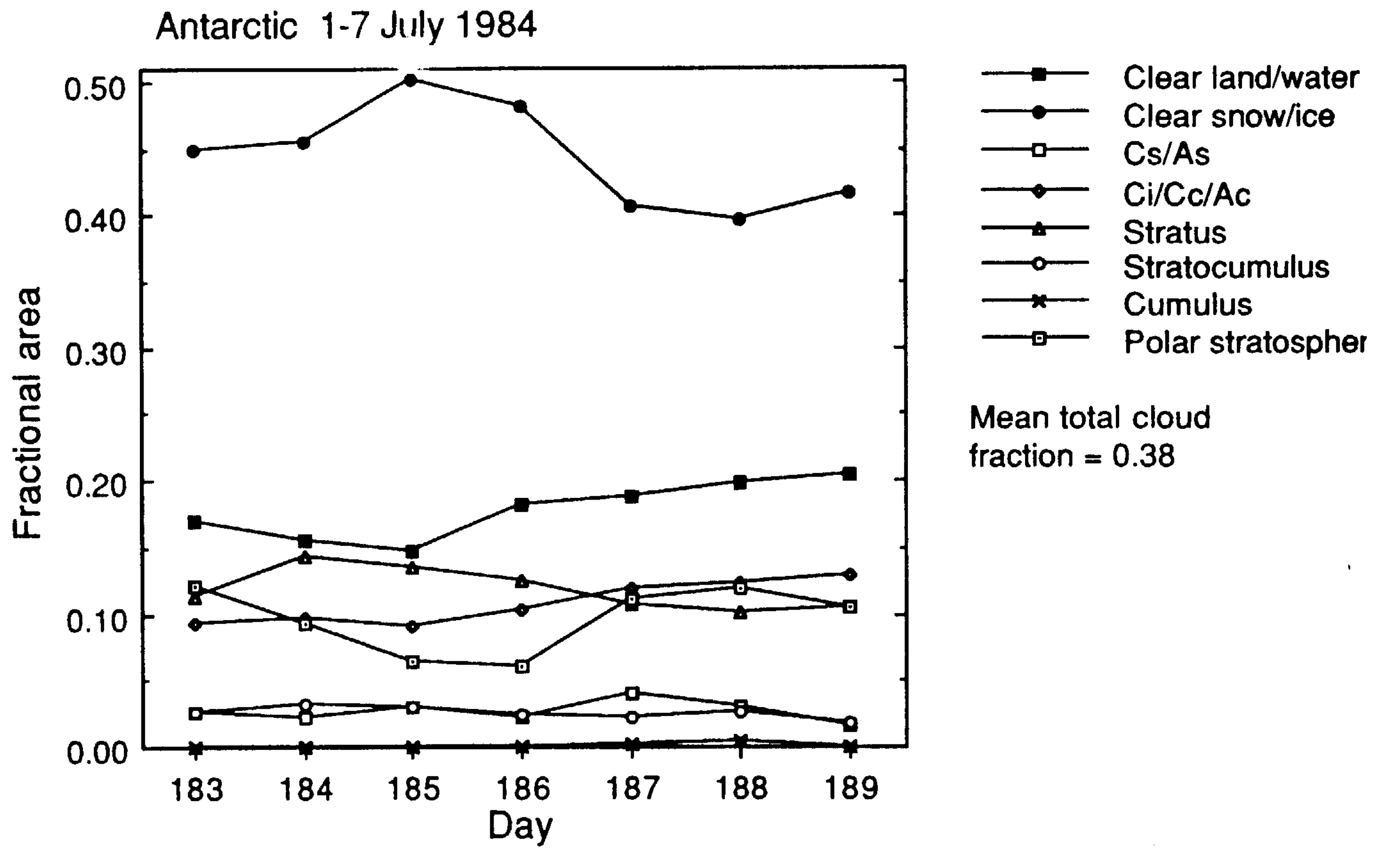

Fig. 39. Fractional area covered by each surface and cloud type during the week of 1-7 July 1984 in the Antarctic.

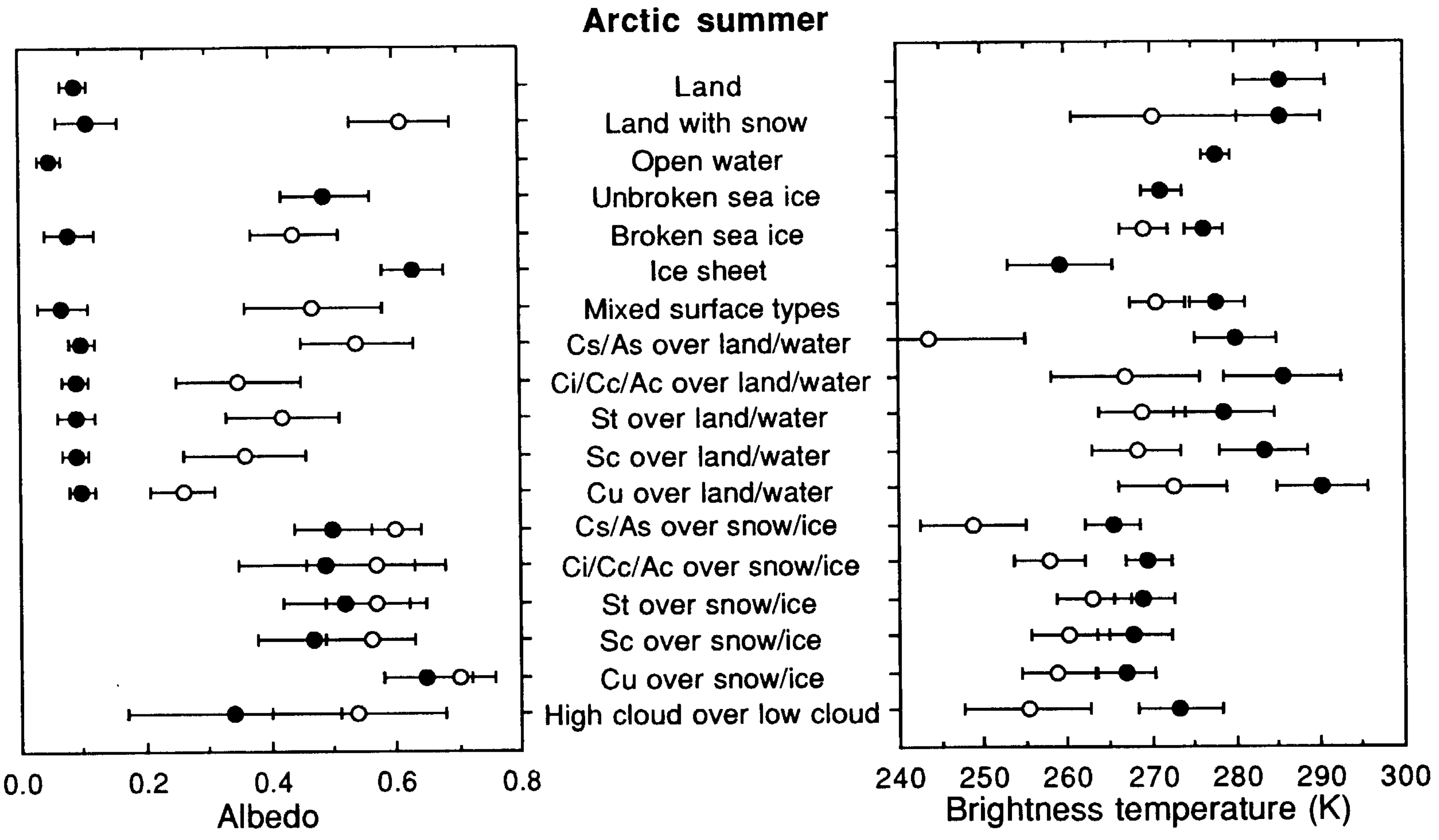

Fig. 40. Mean and standard deviation of channel 1 albedo and channel 4 brightness temperature for the Arctic during 1-7 July 1984. Closed circles denote the surface values, open circles denote the cloud values, and error bars indicate one standard deviation on each side of the mean. For the interpretation of "cloud" in classes 2, 5, and 7, refer to the footnote in Table 3.

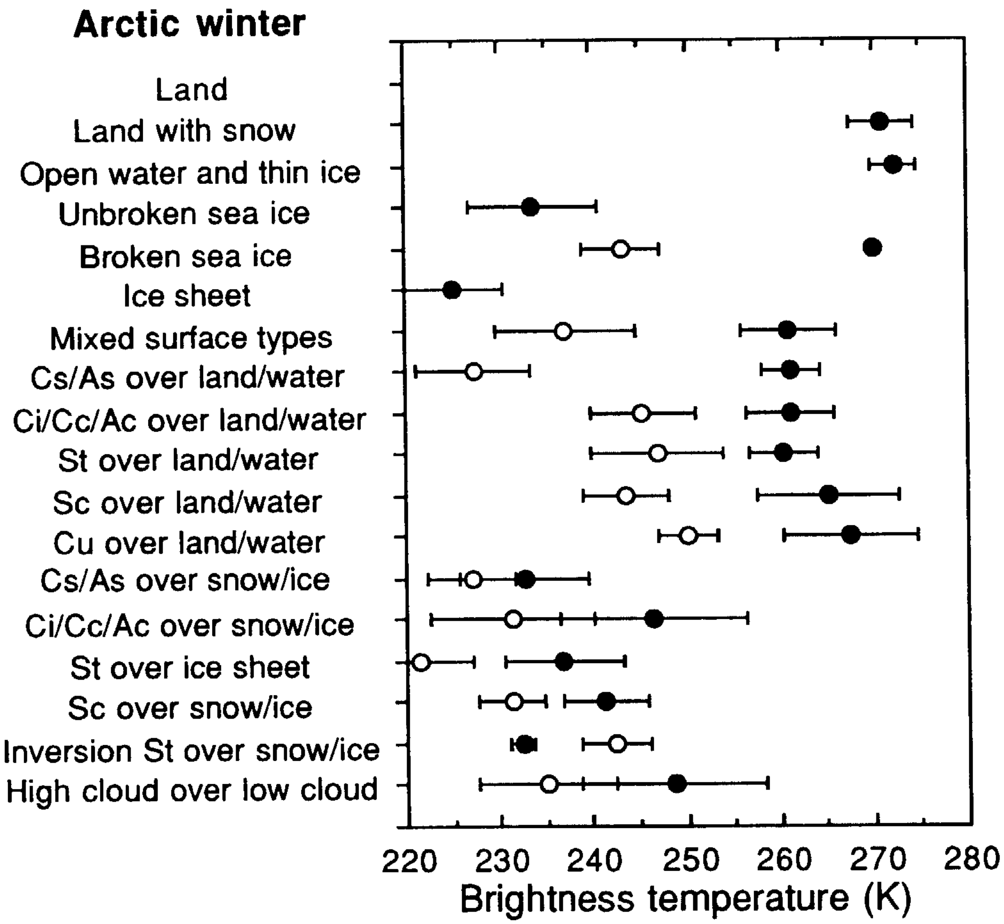

Fig. 41. Mean and standard deviation of channel 4 brightness temperature for the Arctic during 6-12 January 1984. For the interpretation of "cloud" in classes 5 and 7, refer to the footnote in Table 4.

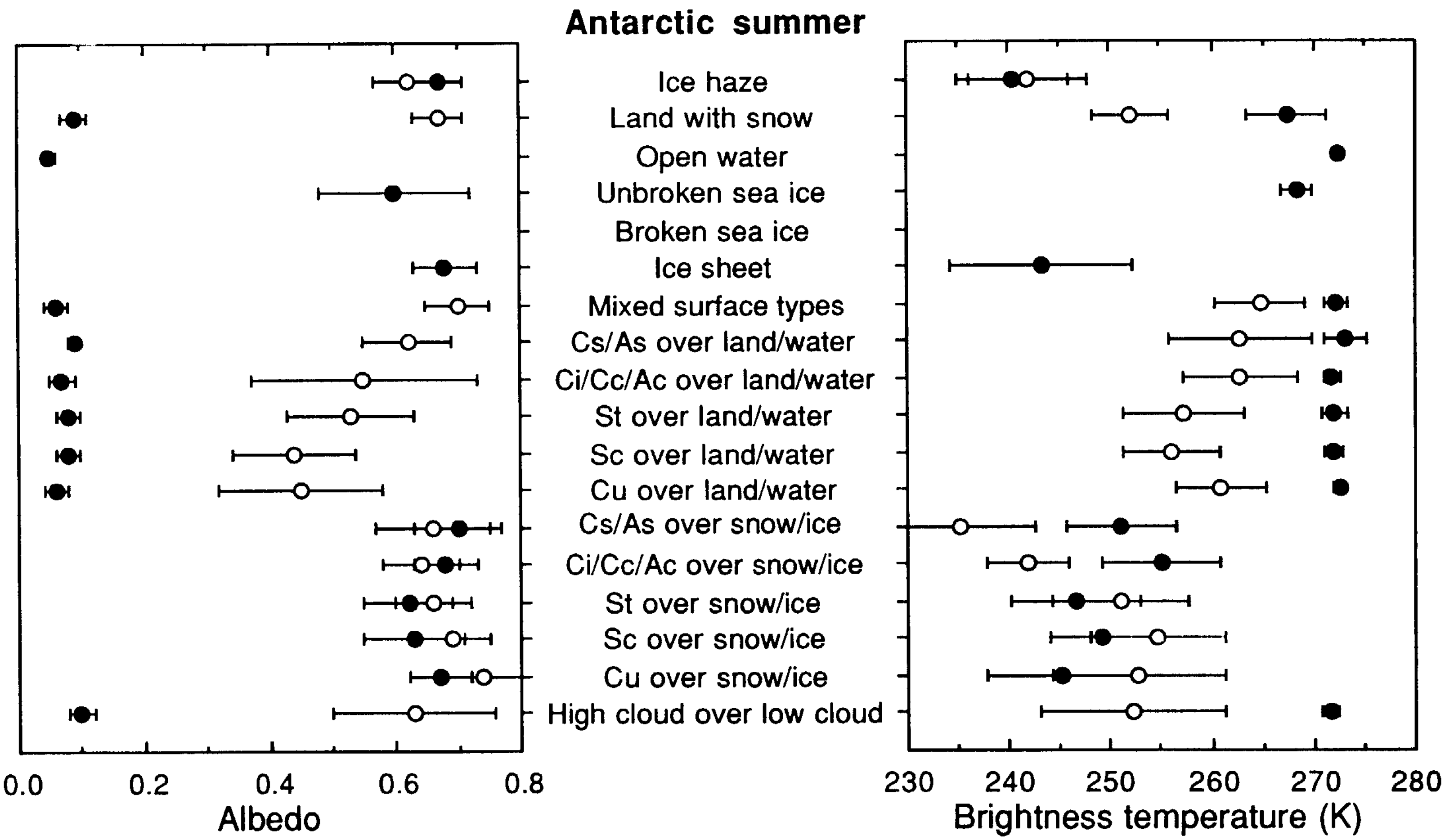

Fig. 42. Mean and standard deviation of channel 1 albedo and channel 4 brightness temperature for the Antarctic during 6-13 January 1984. For the interpretation of "cloud" in classes 2, 5, and 7, refer to the footnote in Table 5.

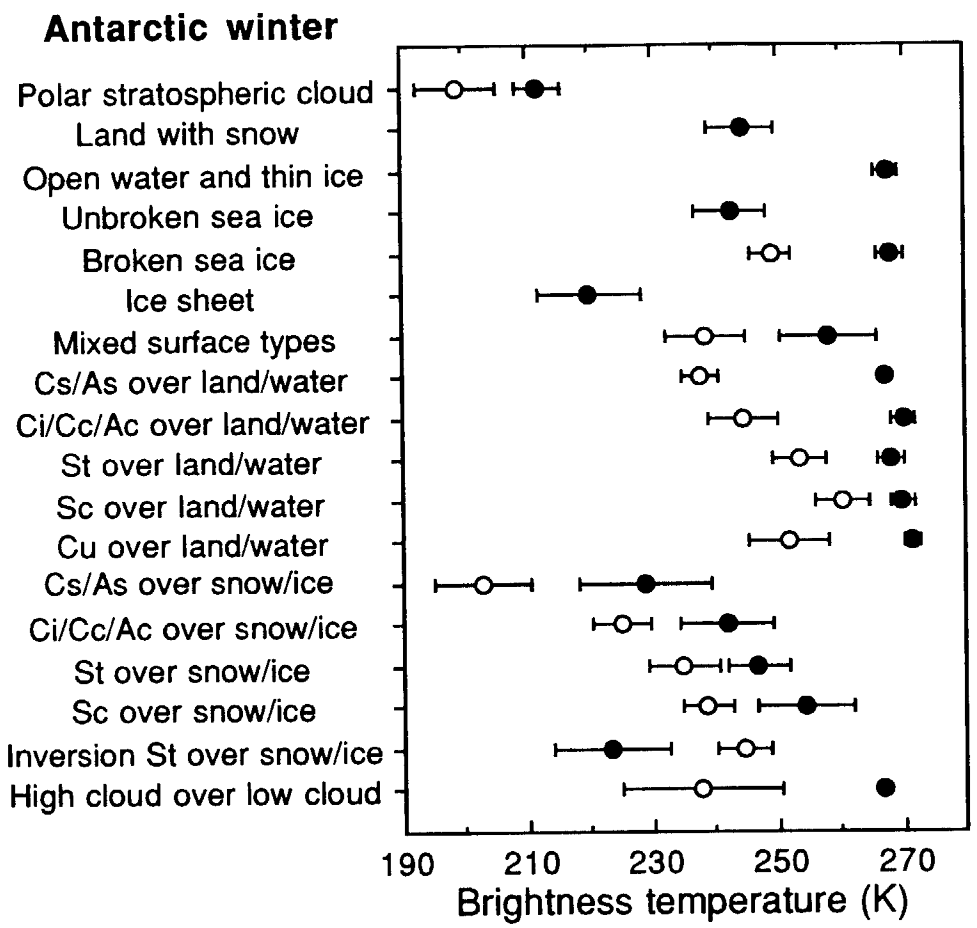

Fig. 43. Mean and standard deviation of channel 4 brightness temperature for the Antarctic during 1-7 July 1984. For the interpretation of "cloud" in classes 5 and 7, refer to the footnote in Table 6.

Appendix. Papers published and submitted

Two papers based on the analysis of the Polar Cloud Pilot Data Set are included in this appendix:

Ebert, E.E., 1989: Analysis of polar clouds from satellite imagery using pattern recognition with a statistical cloud analysis scheme. *J. Appl. Meteor.*, **28**, 382-399.

Ebert, E.E., 1990: Pattern recognition analysis of polar cloud during summer and winter. *Int. J. Remote Sensing*, in press.

The first was funded by a NASA grant issued to another PI and was submitted before the start of this grant period. However, it contains the full details of the statistical cloud analysis scheme and is included here for completeness. The second paper is an expansion of a presentation given at the IAMAP Symposium for Remote Sensing in the Polar Regions in Reading, England, in August 1989. It has been accepted for publication in a special issue of the International Journal of Remote Sensing devoted to the topic of remote sensing of the polar regions.

Reprinted from JOURNAL OF APPLIED METEOROLOGY, Vol. 28, No. 5, May 1989
American Meteorological Society

Analysis of Polar Clouds from Satellite Imagery Using Pattern Recognition and a Statistical Cloud Analysis Scheme

ELIZABETH E. EBERT

Analysis of Polar Clouds from Satellite Imagery Using Pattern Recognition and a Statistical Cloud Analysis Scheme

ELIZABETH E. EBERT

Department of Meteorology, University of Wisconsin, Madison, Wisconsin

(Manuscript received 18 June 1988, in final form 26 November 1988)

ABSTRACT

The analysis of cloud cover in the polar regions from satellite data is more difficult than at other latitudes because the visible and thermal contrasts between the cloud cover and the underlying surface are frequently quite small. Pattern recognition has proven to be a useful tool in detecting and identifying several cloud types over snow and ice. Here a pattern recognition algorithm is combined with a hybrid histogram-spatial coherence (HHSC) scheme to derive cloud classification and fractional coverage, surface and cloud visible albedos and infrared brightness temperatures from multispectral AVHRR satellite imagery. The accuracy of the cloud fraction estimates were between 0.05 and 0.26, based on the mean absolute difference between the automated and manual nephanalyses of nearly 1000 training samples. The HHSC demonstrated greater accuracy at estimating cloud fraction than three different threshold methods. An important result is that the prior classification of a sample may significantly improve the accuracy of the analysis of cloud fraction, albedos and brightness temperatures over that of an unclassified sample.

The algorithm is demonstrated for a set of AVHRR imagery from the summertime Arctic. The automated classification and analysis are in good agreement with manual interpretation of the satellite imagery and with surface observations.

1. Introduction

Understanding the nature and distribution of global cloud cover is a key element in improving our ability to understand and model the global climate. Indeed, the improved knowledge of global cloud fraction, height and thickness has been identified as a critical factor for improving weather and climate forecasts using general circulation models (WMO 1978; ECMWF 1981). To this end, the first project of the World Climate Research Programme is the International Satellite Cloud Climatology Project (ISCCP) (WMO 1982), which began collecting global satellite radiance data in 1983 and will continue until 1990 (Rossow personal communication). The goal of the ISCCP is to assemble a set of global radiance data over an interval of several years, from which 3-hourly cloud cover statistics may be derived and made available to the modeling community. One phase of the ISCCP was the development of a general procedure for estimating cloud cover from visible and infrared radiances; this procedure is detailed by Rossow et al. (1985).

In the polar regions the climate is especially sensitive to the presence of clouds because of their strong radiative influence on the surface energy balance. The analysis of cloudiness in polar high latitudes presents some potential problems for the ISCCP algorithm, as well as many other cloud algorithms developed for use in lower latitudes. The absence of sunlight during winter renders the visible radiances useless during much of the year. During the summer the albedos of the clouds and underlying snow and ice surface are similar, again restricting the usefulness of the visible information. The infrared radiances contain useful information during all seasons, but the distinction between cloud and surface is often unclear due to the frequent isothermal or inversion structure of the tropospheric temperature profile. Even the definition of cloudy and clear skies can be ambiguous. Cold season ice crystal precipitation ("diamond dust") from clear skies also have strong radiative effects in the lower troposphere (Curry 1987), and might justifiably be considered as cloudiness.

Because the geostationary satellites do not adequately view the polar regions, polar orbiting satellites are the only source of remotely sensed data for these regions. These data are less convenient to use than the geostationary satellite data because of the moving frame of reference and reduced temporal coverage, but this is offset by the increased spatial coverage and, on the TIROS-N and NOAA satellites, the increased spectral resolution of the Advanced Very High Resolution Radiometer (AVHRR). Results from an ISCCP workshop on polar clouds (WMO 1987) suggest that the additional spectral channels, beyond the visible and infrared channels common with the geostationary satellites, do

---

Corresponding author address: Elizabeth E. Ebert, Bureau of Meteorology, GPO Box 1289K, Melbourne, Vic. 3001, Australia.

indeed allow clouds to be distinguished from snow and ice. In particular, information from the near-infrared portion of the spectrum can be used to differentiate clouds of liquid phase from clouds of ice phase and the snow and ice surface (Knottenberg and Raschke 1982; Kidder and Wu 1984; Raschke et al. 1986; Mölders 1987), and to detect low clouds over land or ocean at night (Eyre et al. 1984; d'Entremont and Thomason 1987). Solar radiation at 3.7 μm (AVHRR channel 3) is reflected well by cloud water droplets but not by the larger ice crystals found in cirrus clouds or by the surface (Arking and Childs 1985).

The textural appearance of the imagery can be used to help identify surface and cloud types. Cirrus, cumulus, and stratocumulus clouds have significantly different macro- and microtextural characteristics which can be quantitatively measured (Welch et al. 1988; Kuo et al. 1988). Features such as cold, bumpy cloud tops, cloud shadows on the snow, illumination of cloud sides, and cracks and leads in the sea ice can aid the human observer in distinguishing cloud cover from sea ice and snow in satellite imagery (Kukla 1984; Welch et al. 1989). Ebert (1987) used several spectral and textural features in an automated pattern recognition algorithm to classify 18 surface and cloud types with a skill of approximately 84% from Arctic summertime AVHRR imagery. Pattern recognition is yet a relatively new approach to analyzing meteorological satellite imagery, and has been used successfully to measure cloud cover in other parts of the globe (e.g., Harris and Barrett 1978; Bunting and Fournier 1980; Wu et al. 1985; Burfiend et al. 1987; Seze and Desbois 1987; Garand 1988).

It is likely that the a priori knowledge of a cloud type can provide information which would aid in the analysis of its radiative properties, and possibly also the radiative properties of the underlying surface. In this study the pattern recognition algorithm of Ebert (1987) is used to classify high latitude surface and cloud types from AVHRR imagery. The classification is then input to a hybrid histogram-spatial coherence analysis scheme which determines the cloud fraction, surface properties, and cloud albedo and brightness temperature. Comparisons against threshold methods with and without classification reveal the extent to which classification can improve the cloud analysis. The combined algorithm is demonstrated for one day of summertime satellite imagery from the Arctic. This data is part of a Polar Cloud Pilot Data Set being analyzed simultaneously by several research groups in an effort to develop an improved scheme for detecting cloud in the polar regions for the ISCCP (WMO 1987).

The satellite data and auxiliary data for verifying the analyses are described in section 2. Section 3 describes the combined classification and analysis algorithm, as well as its ability to correctly diagnose the cloud type and fraction for a set of training samples. The classification and analysis of imagery from the Polar Cloud Pilot Data Set are presented and discussed in section 4. The sensitivity of the results to underlying assumptions in the algorithm, the propagation of error, and comparisons to threshold methods are made in section 5. Section 6 presents a summary and discussion.

2. Data

a. Satellite data

The algorithm was trained and tested using NOAA-7 AVHRR satellite imagery collected over the polar regions at the lower resolution Global Area Coverage (approximately 3 × 5 km field of view at nadir). The spectral data include AVHRR channels 1 (0.55–0.68 μm), 2 (0.725–1.1 μm), 3 (3.55–3.93 μm), and 4 (10.5–11.5 μm), representing visible, near-infrared and infrared radiances. [The data from AVHRR channel 5 (11.5 μm–12.5 μm) were not included because the AVHRR instruments on many polar orbitting satellites (TIROS-N, NOAA-6, and NOAA-8) do not measure radiances in this spectral band.] These data are read and processed from tape using the Man-computer Interactive Data Access System (McIDAS) at the University of Wisconsin. Calibration of the pixel brightnesses to albedos, ρ (channels 1, 2, and 3), and brightness temperature T_B (channel 4) is made according to Kidwell (1984). The albedo in channel 3, which contains both reflected solar and emitted thermal radiation, is estimated by subtracting the thermal radiance that would be emitted between 3.55–3.93 μm from a blackbody radiating at the brightness temperature measured in channel 4. Since the composition of the scene is not known a priori, this is only a rough approximation to the true channel 3 albedo. It will tend to slightly underestimate the 3.7 μm albedo of overcase low clouds, but overestimate the 3.7 μm albedo of broken cirrus clouds. In general, however, these errors are not large enougn to cause confusion between water and ice clouds.

Each image is divided into an array of cells of dimension 2.5° latitude by 2.5° longitude, in accordance with the ISCCP Polar Cloud Pilot Study (WMO 1987). Near 60°N, this comprises about 2400 pixels, while at the pole a 2.5° × 2.5° cell has only 112 pixels. In order to make the cell areas more nearly equal and provide enough pixels (i.e., data points) for the classification and histogram analysis, the cells nearest the pole are combined for those steps. The cloud fraction, however, is still analyzed for 2.5° × 2.5° cells everywhere.) Between 80°N and 85°N the cell width increases to 5° longitude, between 85°N and 87.5°N the cell width again doubles to 10° longitude, and between 87.5°N and the pole the cell width again doubles to 20° longitude. The 45 pixels at the extreme left and right of each satellite image are discarded because of significant distortion due to the earth's curvature.

The temporal coverage of the satellite imagery spanned the dates from 1–7 July 1984. Complete cov-

TABLE 1. Auxiliary data for verifying the Arctic cloud analyses.

Data type	Location	Source
Surface synoptic observations*	North American Arctic	National Atmospheric and Oceanic Administration
Surface synoptic observations	European Arctic	Berliner Wetterkarte (publ. Free University of Berlin)
Surface synoptic observations	Fram Strait (approx. 80°N, 0°E)	Lindsay (1985)
Hemispheric analyses of sea level pressure and 500 mb geopotential height	Northern Hemisphere	European Centre for Medium Range Weather Forecasting
Weekly sea ice concentration	Northern Hemisphere	Navy-NOAA Joint Ice Center, Suitland, Maryland

* Surface synoptic observations include sea level pressure, surface temperature and dewpoint, wind velocity, surface weather, cloud fraction, and frequently cloud type.

erage of the Arctic from 60° to 90° latitude and 90°W to 90°E longitude, plus additional incomplete coverage between 90°E and 90°W, were included. A subset of this data representing a variety of surface and cloud types was selected for training and testing the algorithm. The training sample dimensions were 32 × 32 pixels, which were chosen to simplify the testing of certain textural features while providing an area compatible with that used for the cloud analysis.

b. Auxiliary data

While the classification and analysis algorithm employs satellite data alone, supplementary data are needed to verify the algorithm's analyses. There is no extensive network of surface observing stations in the Arctic, so additional comparisons must be made against the scattered data which are available, including surface observations from isolated stations, Navy sea ice estimates, and special observations made during the 1984 Marginal Ice Zone Experiment (MIZEX 84). Table 1 summarizes the auxiliary data used to verify the cloud analyses.

3. Cloud analysis algorithm

The algorithm comprises two steps for each 2.5° × 2.5° box. First, a classification algorithm identifies the surface and cloud type within the box. This information is then used in a hybrid histogram-spatial coherence analysis procedure which estimates cloud fraction, and clear and cloudy albedos and brightness temperatures.

a. Classification of the scene

The classification algorithm is based on the pattern recognition algorithm described by Ebert (1987) and shown schematically in Fig. 1. A summary of this classification algorithm is presented here.

Spectral and textural features characterizing each cell are extracted from the radiance data. Spectral features describe the characteristics of the sample as a whole, such as its mean albedo or its brightness temperature range. The textural features describe aspects of the variability, or "bumpiness," of a scene, and are computed from the albedo or brightness temperature differences between each individual pixel and its neighbors.

The classification algorithm employs the following numerical features, in order of importance: 1) Mean channel 1 albedo, 2) Mean channel 4 brightness temperature, 3) Channel 1 albedo − channel 2 albedo, 4) Percentage of pixels with $\rho_3 < 0.08$, 5) Percentage of pixels with $T_B > 273$, 6) Ratio of channel 3 and channel 1 albedos, 7) Percentage of pixels with $\rho_1 < 0.15$, 8) Mean channel 4 angular second moment, 9) Maximum channel 3 entropy, 10) Maximum channel 1 entropy. At least one spectral and one textural feature were chosen in each channel.[1] The first seven features describe the warm, dark characteristics of land and water surfaces, and the cooler, brighter nature of the clouds and the snow and ice surface. The fourth and sixth features, which make use of the channel 3 albedo, aid in distinguishing the highly reflective water-phase clouds from the poorly reflecting ice crystal clouds and the snow and ice surface. The last three features are textural features, and generally discriminate between smooth and variable fields.

The classification of a sample is made using the maximum likelihood decision rule, a statistical technique which is widely employed in classification problems. The maximum likelihood decision rule assumes the existence of distinct classes, $C_1, C_2, \ldots, C_J$, which may be represented by clusters in the 10-dimensional feature space. In essence, a sample or observation which is characterized by a 10-dimensional feature vector, $\mathbf{v} = [v_1, v_2, \ldots, v_{10}]^T$, where each feature, v_i, describes some aspect of the sample (mean channel 1 albedo, etc.), will be assigned to that class, C_k, to which its feature vector is closest in the feature space.

Eighteen surface and cloud categories were differentiated in the training data: 1) Land without snow, 2) Land with snow, 3) Open water, 4) Unbroken sea

---

[1] This feature list differs slightly from that of the Ebert (1987) algorithm due to improved calibration procedures used in the more recent version.

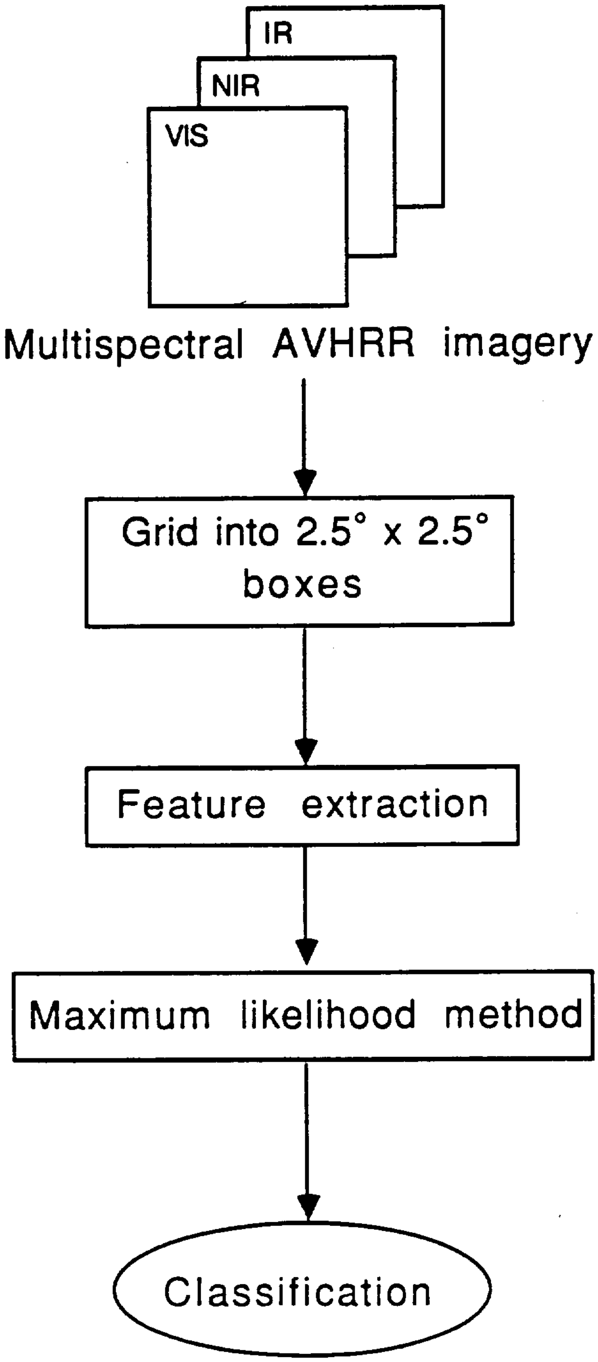

FIG. 1. Flowchart of the automated classification algorithm.

ice. 5) Broken sea ice. 6) Ice sheet. 7) Mixed surface types. 8) Cs/As over land/water. 9) Ci/Ci/Ac over land/water. 10) St over land/water. 11) Sc over land/water. 12) Cu over land/water. 13) Cs/As over snow/ice. 14) Ci/Cc/Ac over snow/ice. 15) St over snow/ice. 16) Sc over snow/ice. 17) Cu over snow/ice. 18) High cloud over low cloud. This selection of categories is somewhat subjective, and different investigators might opt for different categories. In fact, many classification schemes use unsupervised clustering techniques to allow the data to fall into "natural" categories. The danger there, however, is that the classes may not necessarily represent logical physical groupings, and the clustering is highly dependent on the distribution of samples.

Here the classes are specified as certain surface and cloud types which have geophysical significance. The clouds are separated according to whether they are stratiform or broken, ice or water phase, and are over a land/ocean or snow/ice surface. The distinction between surface types underlying the cloud classes is made because the differing visible and thermal properties of the warm, dark land and water surfaces, and cold, bright snow and ice can influence both the albedo of partially transparent clouds due to multiple reflections, and the cloud brightness temperature due to transmission of thermal radiation from the surface. Cirriform and alto clouds are defined here to be composed primarily of ice crystals, and stratus, stratocumulus and cumulus are defined to be composed primarily of liquid water droplets. Class 17, cumulus over snow/ice, refers not only to convective cumuliform clouds, but also to small (but not subgrid scale) isolated clouds which may be shallow in depth. Class 18 refers to clouds of ice phase overlying clouds of liquid phase.

An iterative training procedure was used to teach the algorithm the characteristics of the 18 classes, based on the features derived from the training samples. The algorithm's skill, S, at classifying the training samples was 85%, as defined by

$$S = \frac{R - E}{T - E} \times 100\ (\%), \qquad (1)$$

where R is the number of correct classifications, T is the total number of classifications, and E is the number of correct classifications expected due purely to random chance. Aside from layered cloudiness, the most common classes present in the training imagery were stratus and stratocumulus over land/water and snow/ice, typical for the Arctic during summer (Curry and Herman 1985). The algorithm had the most difficulty identifying high cloud over low cloud, misclassifying it as either low cloud or high cloud alone. Cirrus over land/water was sometimes undetected, as was stratus cloud over sea ice on some occasions. The algorithm also failed to find very small amounts of cumulus cloudiness over land. Overall, about 2% of the cloudy regions were misclassified as clear, and less than 1% of the clear regions were misclassified as being cloudy. The estimated skill of the algorithm in classifying independent imagery is comparable to that of the training set when verified against the analyses of independent experts (Ebert 1987).

b. Analysis of the scene

Information from the classification phase is combined with a hybrid histogram-spatial coherence

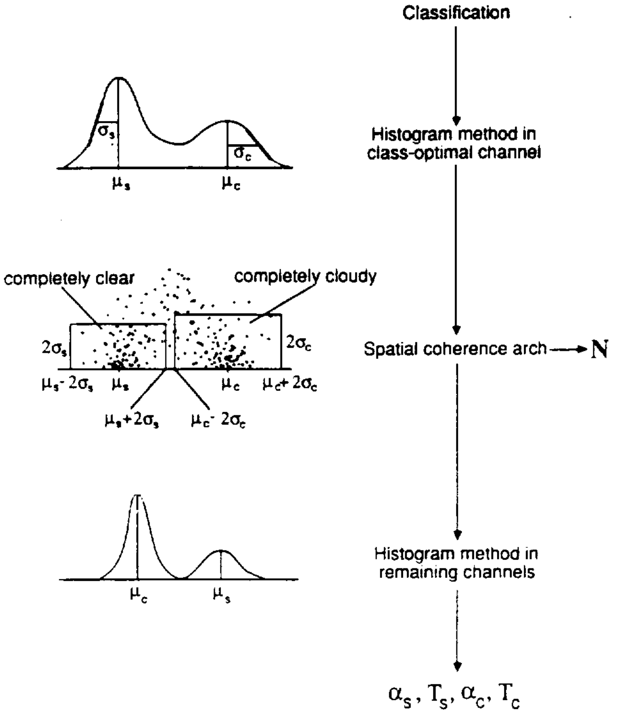

FIG. 2. Schematic diagram of the hybrid histogram-spatial coherence method.

method adapted from Liu et al. (1988) to determine the fractional cloudiness of the scene. This scheme is ideally suited for analyzing ensembles of pixels. The cloud fraction, N, is defined here to represent the fraction of an area covered by cloud when viewed from directly above. For clear classes with two types of surfaces, such as snow on land, broken sea ice, and mixed surface types, the fractional amount of each surface type is computed. The channel 1 albedo and channel 4 brightness temperature of the clear and cloudy portions of the scene (denoted α_s, T_s, α_c, and T_c) are determined as part of the analysis. These represent satellite observed values (i.e., uncorrected for atmospheric effects), which may differ from the true surface and cloud albedos and temperatures.

1) DETERMINATION OF CLOUD FRACTION

The hybrid histogram-spatial coherence method (HHSC) is shown schematically in Fig. 2. The object of the scheme is to identify clear, partly cloudy, and completely cloudy pixels within a scene and to determine the mean albedos or brightness temperatures associated with the completely clear and completely cloudy pixels. The cloud fraction is then easily obtained using the spectral channel which shows the greatest contrast between cloud and surface.

The optimal channel for determining cloud (ice) fraction for each class is given in Table 2. Each of the AVHRR channels used was optimal for at least one class. Channel 2 was employed for mixed surface types because land, water, and snow/ice each have a distinctive signature in this spectral region. For "high cloud over low cloud," channel 3 is used to estimate the low cloud fraction, and channel 4 is used to determine the high cloud fraction.

First we use a histogram technique in the class-optimal channel to find the albedos or brightness temperatures representing completely clear and completely cloudy pixels in the scene. The histogram technique is based on the assumption that, due to random instrument noise and natural variance, the values of ρ or T_B in an ensemble of clear or cloud filled pixels are distributed normally, with the peak of the distribution representing the mean value. (We note that, except for channel 3, the AVHRR data is nearly noise-free, so that the observed variation is due almost entirely to natural variance. In this case the distribution of the pixel values is not necessarily Gaussian; nevertheless, we find that, in practice, this technique can quite adequately determine a representative value of ρ or T_B corresponding to the ensemble of pixels.) For a sample containing both clear and cloudy regions, we expect to find two peaks in the histogram, corresponding to the clear and cloudy albedos or brightness temperatures. The use of the class-optimal channel in this step maximizes the separation of these peaks. Partly cloudy pixels obscure the shape of the distribution curve between the clear and cloudy peaks. Therefore the geometry of the outer portions of the distribution is used to infer

TABLE 2. Class optimal AVHRR channel for Arctic summer cloud fraction analysis.

Class	Optimal channel	Class	Optimal channel
1. Land	1	10. St over land/water	1
2. Snow on land	1	11. Sc over land/water	1
3. Open water	1	12. Cu over land/water	1
4. Unbroken sea ice	1	13. Cs/As over snow/ice	4
5. Broken sea ice	1	14. Ci/Cc/Ac over snow/ice	4
6. Ice sheet	1	15. St over snow/ice	3
7. Mixed surface types	2	16. Sc over snow/ice	3
8. Cs/As over land/water	4	17. Cu over snow/ice	3
9. Ci/Cc/Ac over land/water	4	18. High cloud over low cloud	3, 4

the means of the clear and cloudy peaks. In the visible channel this would correspond to the dark side of the surface albedo distribution and the bright side of the cloud albedo distribution.

Each peak in the histogram is analyzed using the 3-point method (Brower et al. 1976). For a normal probability density function for albedo or brightness temperature, x, the frequency of occurrence of x is given by

$$f(x) = f_0 \exp\{-(x - \mu_0)^2/2\sigma^2\}, \quad (2)$$

where the peak frequency, mean and standard deviation (f_0, μ_0 and σ, respectively) are unknown. By taking three points (x_i, f_i), (x_j, f_j) and (x_k, f_k) from the outside of the distribution curve (see Fig. 2), three equations in three unknowns.

$$\begin{aligned} f_i &= f_0 \exp\{-(x_i - \mu_0)^2/2\sigma^2\} \\ f_j &= f_0 \exp\{-(x_j - \mu_0)^2/2\sigma^2\} \\ f_k &= f_0 \exp\{-(x_k - \mu_0)^2/2\sigma^2\}, \end{aligned} \quad (3)$$

can be solved using Gaussian elimination to obtain the peak value

$$\mu_0 = \frac{x_i^2 \log(f_j/f_k) - x_j^2 \log(f_i/f_k) + x_k^2 \log(f_i/f_j)}{2[x_i \log(f_j/f_k) - x_j \log(f_i/f_k) + x_k \log(f_i/f_j)]} \quad (4)$$

and the standard deviation

$$\sigma = \frac{-[(x_i - x_j)^2 - 2\mu_0(x_i - x_j)]}{2 \log(f_i/f_j)}. \quad (5)$$

For each peak, values of μ_0 and σ are calculated from many different 3-point combinations, then plotted against each other on a two-dimensional histogram. The combination of (μ_0, σ) with the greatest frequency of occurrence in the 2-D histogram is taken to be representative of the mean clear (cloudy) value, μ_s (μ_c), and its standard deviation, σ_s (σ_c), for the cell.

It is necessary to specify reasonable characteristic values and bounds on pixel albedos and brightness temperatures in order to avoid misidentification of clear or cloudy peaks. These bounds are initially estimated from the characteristic mean, maximum and minimum values for the classes in the training set, and continuously updated during the analysis procedure. Initial class/channel characteristic values for the cloud analysis algorithm are given in Table 3, along with bounds (thresholds) on pixel values which can be considered completely clear or completely cloudy.

If only one peak is clearly defined in the histogram, as would be the case for a cloud fraction near 0.0 or 1.0, then its definition as either "surface" or "cloud" is dependent on whether it more nearly matches the characteristic clear or cloudy value for that channel and class. In that case, the most likely type (surface or cloud) is assigned the peak value, while the other type is assigned its characteristic value for the class. If no peaks are definable, as for clouds of varying temperature or optical thickness covering the scene, the class characteristic values for both the surface and cloud values are used.

Next, the spatial coherence method (Coakley and Bretherton 1982) is used to isolate completely clear

TABLE 3. Initial class characteristic values for surface and cloud for the Arctic summer cloud analysis algorithm. The values in parentheses are the bounds on clear and cloudy albedos and brightness temperatures which separate the two. For classes 2, 5, and 7, the "cloud" values refer to a second surface type, generally snow/ice.

	Ch. 1		Ch. 3		Ch. 4	
	Clear	Cloud	Clear	Cloud	Clear	Cloud
	(albedo × 100)		(albedo × 100)		(K)	
1. Land	11 (17)				285 (293)	
2. Snow on land	11 (17)	64 (54)			285 (276)	273 (276)
3. Open water	8 (15)				279 (287)	
4. Unbroken sea ice	49 (64)				271 (274)	
5. Broken sea ice	8 (15)	49 (32)			279 (271)	271 (275)
6. Ice sheet	64 (74)				259 (270)	
7. Mixed surface types*	10 (17)	56 (32)	11 (21)	27 (10)	282 (271)	265 (275)
8. Cs/As over land/water	10 (17)	56 (31)			282 (271)	248 (275)
9. Ci/Cc/Ac over land/water	10 (17)	45 (21)			282 (271)	248 (275)
10. St over land/water	10 (17)	45 (26)			282 (271)	269 (282)
11. Sc over land/water	10 (17)	55 (20)			282 (271)	266 (282)
12. Cu over land/water	10 (17)	53 (20)			282 (271)	265 (282)
13. Cs/As over snow/ice	56 (74)	69 (35)			265 (255)	251 (270)
14. Ci/Cc/Ac over snow/ice	56 (74)	69 (22)			265 (255)	251 (273)
15. St over snow/ice	56 (74)	61 (39)	2 (5)	17 (5)	265 (255)	262 (274)
16. Sc over snow/ice	56 (74)	71 (31)	2 (5)	28 (10)	265 (255)	255 (279)
17. Cu over snow/ice	56 (74)	71 (31)	2 (5)	23 (10)	265 (255)	255 (273)
18. High cloud over low cloud (low)	56 (74)**	55 (21)	2 (5)	22 (5)	265 (255)**	263 (282)
(high)		60 (21)				252 (275)

* For class 7, the class characteristic values listed under Ch. 3 are actually for Ch. 2.

** Equatorward of 75°N, the surface characteristic values are initialized to those of classes 8–12.

and completely cloudy pixels. This corresponds to Liu et al.'s (1988) "improved two-threshold method." Local means and standard deviations of ρ or T_B in 4-pixel squares within a cell are plotted against each other to form an arch-like structure. The feet of the arch represent completely clear and completely cloudy regions, while the central portion of the arch contains partly cloudy pixels. An arch "foot" is defined here as the region containing local mean values within two standard deviations (2σ) of μ_0 as determined from the histogram procedure, and whose local standard deviations are also less than 2σ. In cases where the feet overlap, a threshold is set which separates the two regions in proportion to their relative values of σ. In addition, the thresholds separating completely clear and completely cloudy pixels (i.e., $\mu \pm 2\sigma$) were constrained not to go beyond their respective bounds given in Table 3.

Pixels identified as completely clear or completely cloudy are tagged and given weights of $w = 0$ or $w = 1$, respectively, where the weights represent pixel cloud fraction. Those pixels outside the arch feet are given weights

$$w = \frac{x - \mu_s}{\mu_c - \mu_s}, \tag{6}$$

subject to the constraint that $0 \leqslant w < 1$. The weights are then summed over the entire scene and divided by the total number of 4-pixel squares to obtain the cloud fraction, N.

Although the selection of 2σ to define the arch feet may seem rather lax, it is necessary to guarantee enough pixels for the subsequent histogram analysis of the remaining surface and cloud properties, described in the next subsection. Moreover, we have found that the derived cloud fraction is not very sensitive to the choice of 2σ when compared to the results obtained using 1σ or 0 (i.e., no arch feet).

2) DETERMINATION OF REMAINING SURFACE AND CLOUD PROPERTIES

Once the completely clear and completely cloudy pixels have been tagged using the HHSC in the class-optimal channel, these pixels are used to generate "clean" histograms in the remaining spectral channels. The three-point histogram analysis is performed on the "clean" histograms to obtain α_s, α_c, T_s and T_c. There is an advantage to combining the histogram method with the spatial coherence method, rather than using the histogram method alone or the spatial coherence method alone in each spectral channel. The natural variability of the GAC pixels over the 2.5° × 2.5° region causes the feet of the spatial coherence arch to be poorly defined. The histogram method is able to find mean values for the clear and cloudy peaks in most cases. This is used to define the regions of the feet for the spatial coherence method, which sorts the clear and cloudy pixels. This sorting better defines the peaks in the remaining channels, yielding a more accurate estimate of the mean surface and cloud properties in those channels.

Often one peak dominates the histogram. This results when the clear and cloudy values are nearly equal, as for clouds overlying snow and ice, or when only a small amount of surface or cloud is present. To resolve this problem, the pixels in the "clean" histogram are split according to the cloud fraction determined in the optimal channel, and each side of the histogram is analyzed independently. In this way, a minor peak representing a small number of cloudy pixels will not be ignored in favor of a larger surface peak. Again, if a clear or cloudy peak cannot be found, its class characteristic value is used.

The characteristic values are updated after each cell is analyzed by keeping a running mean of clear and cloudy values for each channel and class. This ensures that the characteristic values are representative of the surface and cloud values already encountered in the scene. Only at the beginning of each satellite image are these characteristic values reinitialized to prespecified values determined from the training set.

c. Testing the cloud analysis algorithm

An objective test of the HHSC was conducted by creating and analyzing synthetic cloud samples. These samples were generated from the 4-channel class characteristic means and standard deviations using a Gaussian random number generator, and arranged in the six test patterns shown in Fig. 3: (a) checkerboard, (b) overcast, (c) cloud edge, (d) complete gradient, (e) partial gradient, and (f) sine wave. The test patterns approximate cloudy situations which occur in the imagery. Ten simulations were run for each cloud type and test pattern.

Table 4 shows the means of the simulations for three cloud classes, each with a different class-optimal channel. The analyzed cloud fraction is generally correct to within 0.10, and always within 0.20. The analyzed surface and cloud albedos and brightness temperatures are usually accurate to within about 0.05 and 4 K, respectively. The most difficult scenes to analyze accurately were the overcast and complete gradient patterns. The underestimation of the overcast cloud fraction occurred because the pixels at the dark or warm end of the histogram were analyzed as being partly cloudy instead of completely cloudy. The scene composed entirely of a horizontal gradient, (d), was problematic because the histogram contains no obvious surface or cloud peaks. The clear and cloudy albedos and brightness temperatures analyzed by the algorithm tend to be closer to the center of the histogram than the true values are. The overall performance of the HHSC on the artificial cloud fields is summarized in Table 5 for all of the classes. Except for the second test, the algorithm slightly overestimated cloud fraction, typically by about 0.05–0.10.

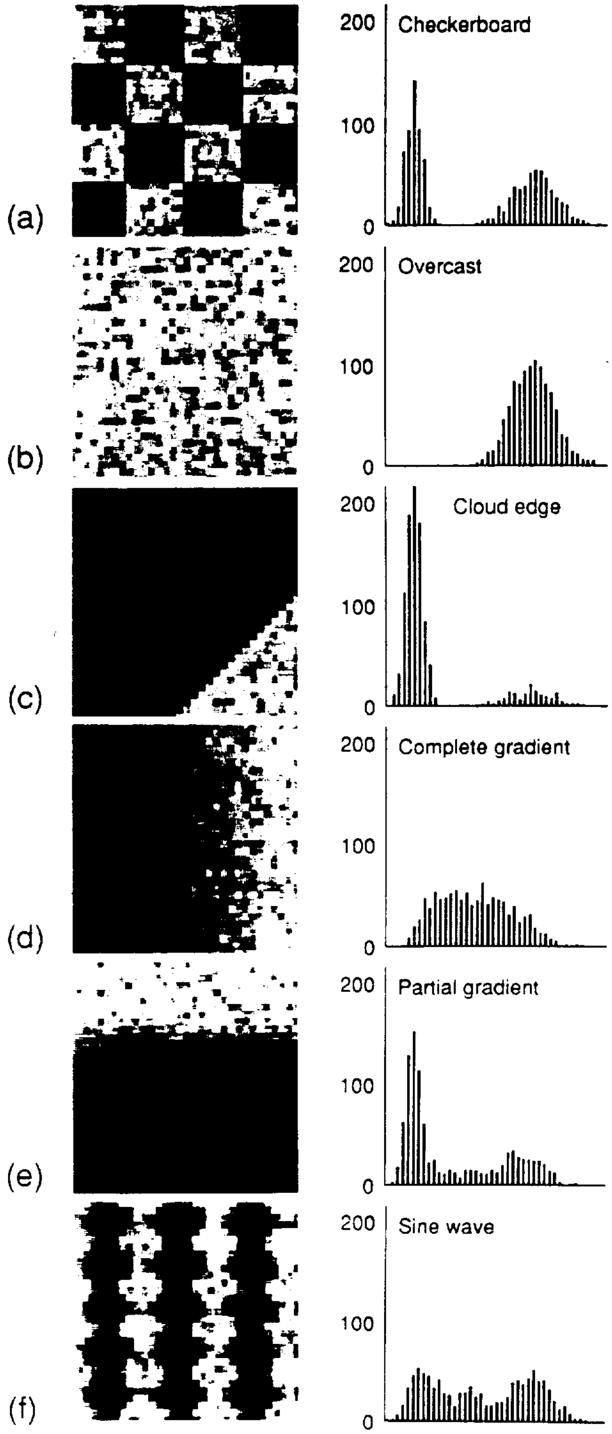

FIG. 3. Test patterns and associated histograms for six synthetic cloud samples.

The HHSC was also tested against a manual nephanalysis of the training samples. Figure 4 shows the manual and automated analyses of cloud fraction for the three training images. (These correspond to Fig. 2 of Ebert 1987.) There is generally good qualitative agreement between the two analyses. The clear and cloudy regions are well diagnosed, especially in the second and third images. Table 6a quantitatively compares the manual and automated analyses for all of the cloud samples, including those which were misclassified. Assuming the manual analyses to be accurate, the algorithm underestimated fractional cloud cover for five of the classes, and overestimated it for six classes. The largest errors occurred in the analysis of high cloud fraction as measured by the root-mean-square (RMS) error, and the cumulus cloud fractions were analyzed most accurately. The mean absolute error averaged about 0.13 for low clouds and 0.23 for high clouds.

By comparing the manual nephanalysis to the automated nephanalysis for only those cloud samples which were correctly classified, one can determine the accuracy of the cloud algorithm under the best of circumstances. The error statistics for the correctly classified samples are presented in Table 6b. The RMS errors do not differ greatly from those obtained using all the samples. Less than 3% of the cloudy samples were misclassified as clear, while the remaining misclassifications were between various cloud types. The HHSC does not appear to be extremely sensitive to these misclassifications. (A more thorough discussion of algorithm sensitivity to classification errors appears in section 5.)

The tendency of the hybrid histogram-spatial coherence method to predict low cloud fraction more accurately than high cloud fraction is in contrast to the performance of the U.S. Air Force three-dimensional nephanalysis (3DNEPH), which relies on satellite, surface and aircraft observations (Fye 1978). In a comparison of the 3DNEPH cloud fraction estimates to manual estimates using high resolution DMSP imagery over the Beaufort Sea in June 1980, Curry and Herman (1985) found a mean absolute difference of 0.43 for low clouds, 0.12 for middle clouds, and 0.06 for high clouds. This indicates the difficulties associated with using an infrared threshold technique to detect low clouds at polar latitudes.

4. Analysis of Polar Cloud Pilot Data

In this section, the surface and cloud cover are analyzed and discussed for 1 July 1984, the first day of the Arctic summer imagery in the Polar Cloud Pilot Data Set. Fourteen satellite images cover the region between 60° and 90° north latitude. At least one satellite overpass was used for all regions of the Arctic except the Alaskan and far eastern portions, and a small region immediately surrounding the pole, where the pixels were too close to the edge of the image and were discarded due to distortion (see section 2). Each image was analyzed individually, then the analyses combined and averaged to form a hemispheric mosaic.

TABLE 4. Results of the cloud analysis simulations for three cloud classes, each with a different class optimal channel: α_s = ch. 1 surface albedo; ρ_{3s} = ch. 3 surface albedo; T_s = surface brightness temperature; α_c = ch. 1 cloudy albedo; ρ_{3c} = ch. 3 cloudy albedo; T_c = cloudy brightness temperature.

(a) Class 11: Sc over land/water ($\alpha_s = 0.10$; $\alpha_c = 0.55$; $T_s = 282$; $T_c = 266$; Class optimal channel = 1)

Test	Actual N	Algorithm N	α_s	α_c	T_s	T_c
(a) Checkerboard	0.55	0.45	0.09	0.60	282	271
(b) Overcast	1.00	0.88	0.10	0.61	282	264
(c) Cloud edge	0.15	0.14	0.09	0.55	282	266
(d) Complete gradient	0.52	0.62	0.14	0.43	279	268
(e) Partial gradient	0.36	0.36	0.09	0.56	282	267
(f) Sine wave	0.58	0.59	0.09	0.51	281	265

(b) Class 15: St over snow/ice ($\alpha_s = 0.56$; $\alpha_c = 0.61$; $\rho_{3s} = 0.015$; $\rho_{3c} = 0.165$; $T_s = 265$; $T_c = 262$; Class optimal channel = 3)

Test	Actual N	Algorithm N	α_s	α_c	ρ_{3s}	ρ_{3c}	T_s	T_c
(a) Checkerboard	0.50	0.52	0.56	0.61	0.014	0.187	265	262
(b) Overcast	1.00	0.86	0.58	0.63	0.015	0.182	264	261
(c) Cloud edge	0.15	0.21	0.54	0.61	0.015	0.166	265	262
(d) Complete gradient	0.52	0.68	0.55	0.59	0.032	0.101	265	262
(e) Partial gradient	0.36	0.47	0.55	0.61	0.013	0.148	264	261
(f) Sine wave	0.58	0.63	0.55	0.60	0.017	0.138	265	262

(c) Class 9: Ci/Cc/Ac over land/water ($\alpha_s = 0.10$; $\alpha_c = 0.45$; $T_s = 282$; $T_c = 259$; Class optimal channel = 4)

Test	Actual N	Algorithm N	α_s	α_c	T_s	T_c
(a) Checkerboard	0.50	0.51	0.10	0.47	285	256
(b) Overcast	1.00	0.95	0.10	0.48	281	255
(c) Cloud edge	0.15	0.23	0.10	0.45	285	266
(d) Complete gradient	0.52	0.66	0.14	0.37	278	267
(e) Partial gradient	0.36	0.43	0.10	0.47	285	260
(f) Sine wave	0.58	0.61	0.11	0.46	283	262

Mosaics of visible and thermal infrared imagery for the 1 July 1984 Arctic are shown in Fig. 5. The imagery shows a large cyclone in the western Canadian Arctic and low cloud cover in the Canadian Archipelago and northwestern Greenland. The Greenland Sea contains broken sea ice, and further south a large region of stratus and stratocumulus blankets the ocean. Layered and cumulus clouds are present over Scandinavia, while a large region in Siberia is clear. The Arctic Basin contains multiyear sea ice with large areas of cloud cover.

The image classification, presented in Fig. 6, and the analyzed cloud fraction, presented in Fig. 7, together describe the cloud cover analyzed by the algorithm. Overall, for the 1 July 1984 Arctic, the estimated fractional area covered by low clouds alone was 0.26, the estimated fractional area covered by high cloudiness alone was 0.05, and the fractional area covered by layered cloudiness was estimated at 0.24. The most common cloud types analyzed were stratus, both over water and over ice, and layered cloudiness. This matches with the findings of many previous studies (Vowinckel 1962; Gavrilova 1963; Huschke 1969).

Many of the cloud features are related to the synoptic conditions, shown as analyses of sea level pressure and 500 millibar geopotential height for the 1 July Arctic in Fig. 8. The comma cloud in the Northwest Territories is part of an occluded cyclone. The line of cirrus clouds running to the northeast of Novaya Zemlya is

TABLE 5. Summary of the results of the cloud analysis simulations.

Test	Number of samples	Actual fraction	Mean algorithm fraction	RMS error	Mean absolute difference
(a) Checkerboard	10	0.50	0.52	0.07	0.05
(b) Overcast	10	1.00	0.88	0.13	0.12
(c) Cloud edge	10	0.15	0.21	0.09	0.06
(d) Complete gradient	10	0.52	0.64	0.13	0.12
(e) Partial gradient	10	0.36	0.44	0.10	0.08
(f) Sine wave	10	0.58	0.61	0.06	0.05

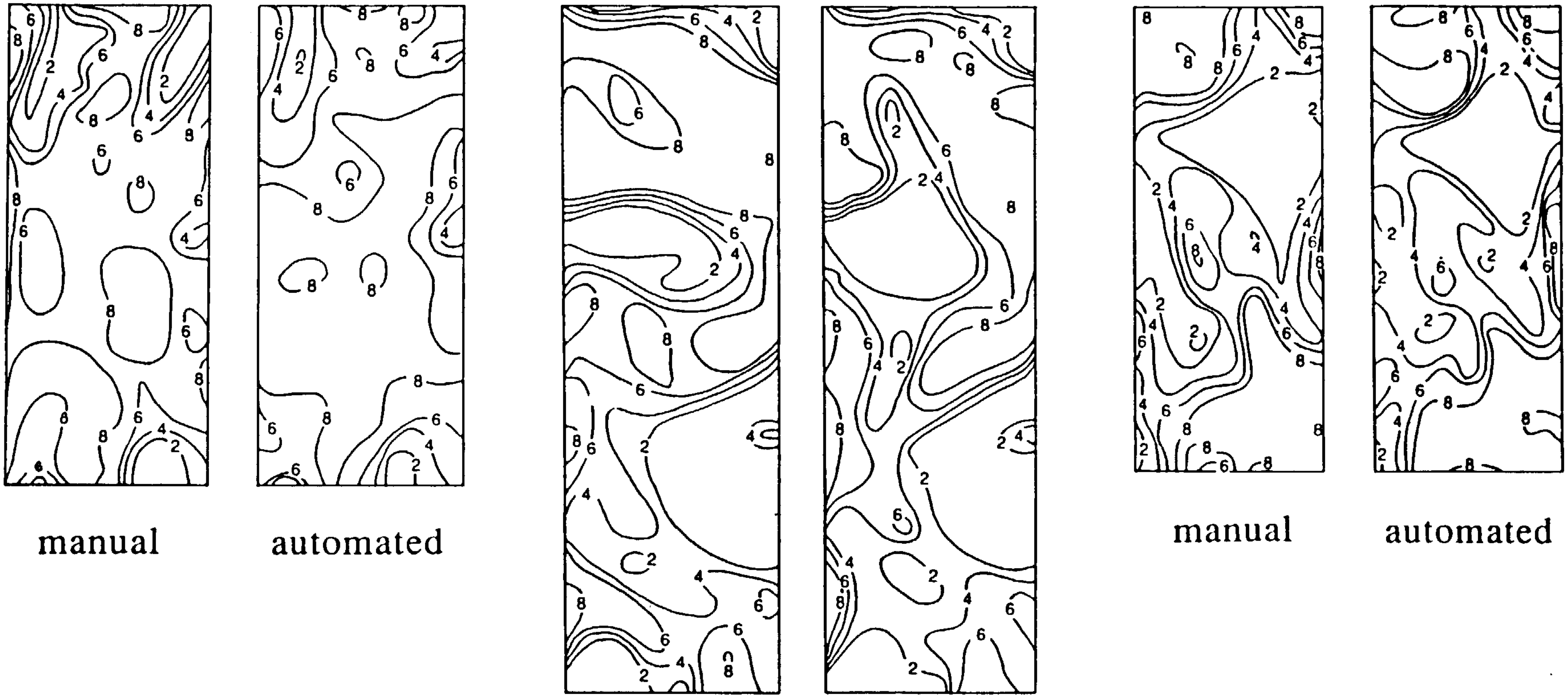

manual automated manual automated manual automated

FIG. 4. Manual and automated cloud fraction analyses of the three Arctic summer training images. Cloud fraction is expressed in units of tenths.

TABLE 6. Statistics for the manual and automated nephanalyses for the Arctic summer cloudy training samples: (a) all samples; (b) correctly classified samples only. Refer to text for category numbers.

(a) All training samples.

Class	Number of samples	Mean manual fraction	Mean algorithm fraction	RMS error	Mean absolute difference
8	17	0.85	0.68	0.34	0.24
9	34	0.35	0.47	0.26	0.22
10	129	0.79	0.75	0.15	0.11
11	60	0.55	0.60	0.15	0.11
12	45	0.21	0.22	0.11	0.09
13	12	0.78	0.83	0.24	0.18
14	51	0.49	0.40	0.35	0.26
15	98	0.74	0.63	0.28	0.19
16	48	0.76	0.66	0.18	0.14
17	14	0.18	0.21	0.06	0.05
18	178	0.79	0.80	0.23	0.17

(b) Correctly classified training samples.

Class	Number of samples	Mean manual fraction	Mean algorithm fraction	RMS error	Mean absolute difference
8	13	0.89	0.66	0.37	0.26
9	30	0.35	0.48	0.27	0.22
10	114	0.82	0.88	0.15	0.11
11	44	0.55	0.61	0.14	0.11
12	34	0.22	0.25	0.09	0.07
13	12	0.78	0.83	0.24	0.18
14	49	0.49	0.40	0.36	0.27
15	87	0.77	0.70	0.24	0.16
16	44	0.79	0.67	0.18	0.14
17	13	0.18	0.21	0.06	0.04
18	130	0.80	0.88	0.21	0.15

associated with the flow of the jet stream around an omega high, which produces subsidence and clearing near 90°E. In the analysis, the Norwegian Sea and North Atlantic are covered by dense stratus cloud cover ($N > 0.80$), with a small clear region over Iceland associated with a surface high pressure center. Greenland is analyzed as mostly cloudy, and stratus and layered clouds are analyzed over much of the Canadian Archipelago. Northern Siberia is analyzed as mostly clear, with scattered cumulus and cirrus clouds. The Arctic Ocean has primarily cloud-free pack ice in the European sector, with stratus and layered cloudiness analyzed in the Soviet and western regions. Much of this cloudiness may be associated with the southeasterly flow of warm moist air near 90°W (Jayaweera 1982; Curry and Herman 1985).

The automated analysis can be compared to the surface and weather conditions observed on 1 July 1984, plotted in Fig. 9 for several stations. These observations consist of station reports from the Canadian and European Arctic, special observations from the MIZEX study area, and the Navy-NOAA Joint Ice Center sea ice analysis from 3 July 1984. Before using these observations to validate the satellite automated analyses, some limitations related to differences in temporal and spatial sampling must be addressed. The surface weather reports plotted in Fig. 9 were made at 3 UTC, 6 UTC, 9 UTC and 15 UTC (depending on the data source) and may not necessarily represent conditions for the entire day, although the diurnal variation in surface and cloud conditions is small in the Arctic at this time of year. Even comparisons between nearly concurrent measurements are impaired by the fact that the surface report is a point measurement, influenced by local topography and a limited sky view, while the satellite analysis covers a 2.5° × 2.5° region. In addition, most stations in the polar regions are located on coastlines, transition zones between maritime, continental, pack ice, and ice sheet regimes, and may thus experience unique weather conditions. Considering these limitations there appears to be good agreement between the analyzed and observed surface and cloud types in the 1 July Arctic. In particular, the cirrus cloudiness near 90°E is well analyzed, as are the layered clouds over Scandinavia and the partly cloudy conditions over much of the Canadian Archipelago. The analyzed cloud cover over Greenland and the pack ice cannot be verified due to the lack of surface observations.

The correct diagnosis of surface type is important in correctly estimating the surface radiation budget. This is particularly true during summer, as the amount

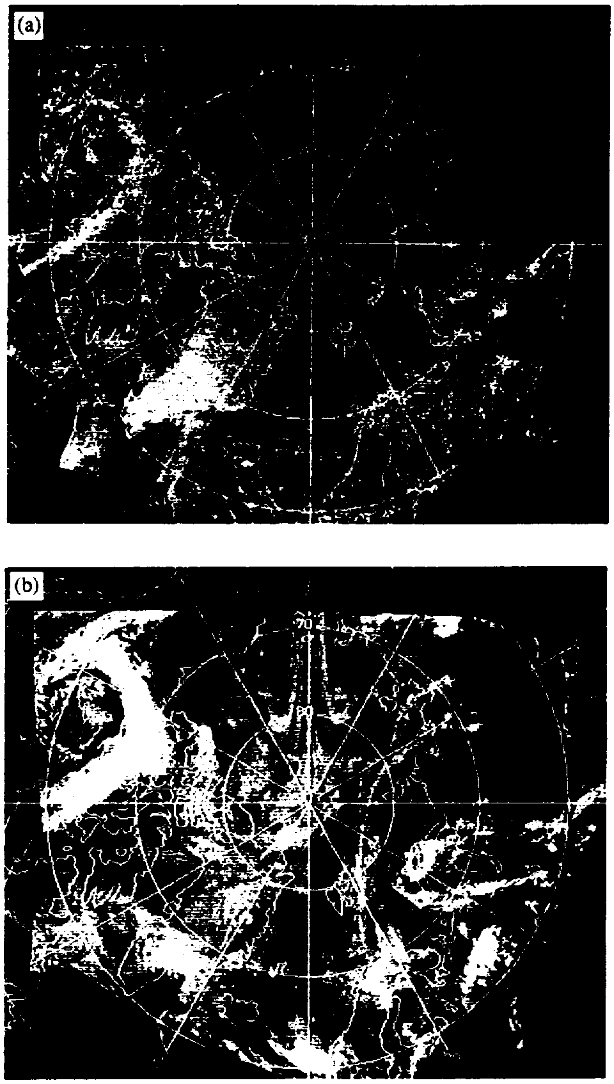

FIG. 5. Mosaic of visible (a) and infrared (b) imagery over the Arctic on 1 July 1984. (It should be noted that *for display purposes only* the mosaics of the visible and thermal imagery were constructed using a maximum brightness criterion, and thus appear colder and cloudier than the individual images, due primarily to cloud motion between consecutive satellite overpasses.)

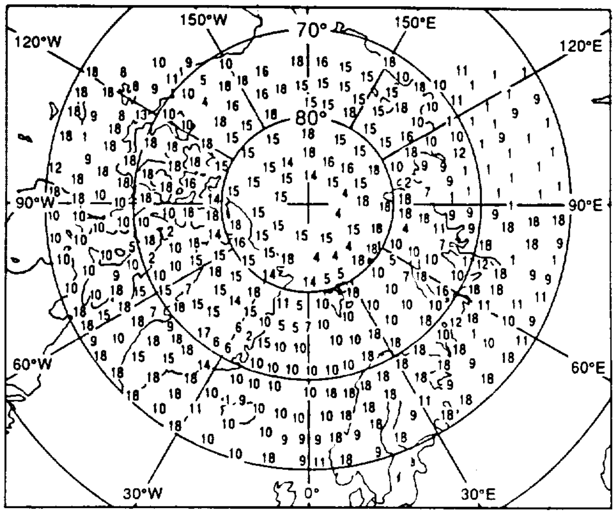

FIG. 6. Automated classification of the Arctic 1 July 1984 imagery.

of absorbed solar radiation is much larger for water and land, which have low albedos, than for the highly reflective snow and ice surface. The sea ice concentration and position of the ice margin can be estimated by combining the results from the classification and analysis steps. Class 4 (unbroken sea ice), class 6 (ice sheet), and classes 13–17 (clouds over snow/ice) are assumed to have an ice fraction of 10/10. For regions identified as class 5 (broken sea ice) and class 7 (mixed surface types) the HHSC is used to estimate the fractional ice coverage from the visible data. Classes 1–3 and 8–12 are assumed to contain exclusively land and water. The surface type beneath layered clouds is unknown in the algorithm and is treated as missing data for this purpose. Figure 10 shows the analyzed sea ice cover for the 1 July Arctic. The automated analysis shows a small amount of sea ice in the Kara Sea, while west of Novaya Zemlya the ocean is analyzed as ice free. The sea ice edge curves over the northern side of Svalbard and becomes quite broken in the Greenland Sea. Broken sea ice is also found in Baffin Bay. Unbroken sea ice is analyzed throughout the polar basin.

The algorithm's analyzed sea ice fraction was verified against the Navy-NOAA sea ice concentration estimated for each 2.5° × 2.5° box from the 3 July ice chart. The expected change in sea ice extent during the two days separating the 1 July Polar Cloud Pilot Data and the Navy-NOAA observations is small, not exceeding 15 km. When compared to the Navy-NOAA analysis, the algorithm accurately diagnosed the sea ice

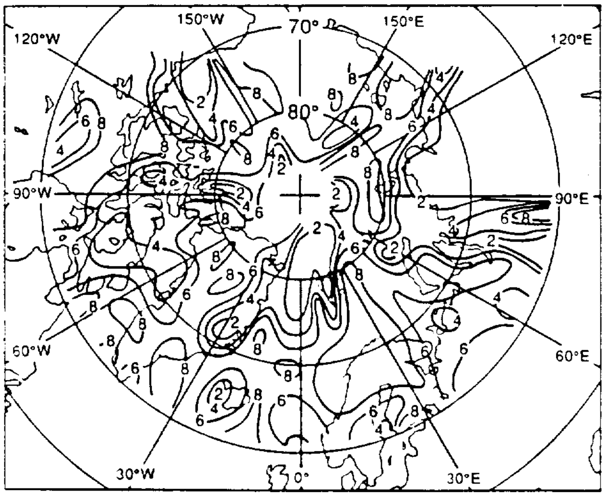

FIG. 7. Automated cloud fraction analysis of the Arctic 1 July 1984 imagery. Cloud fraction is given in tenths.

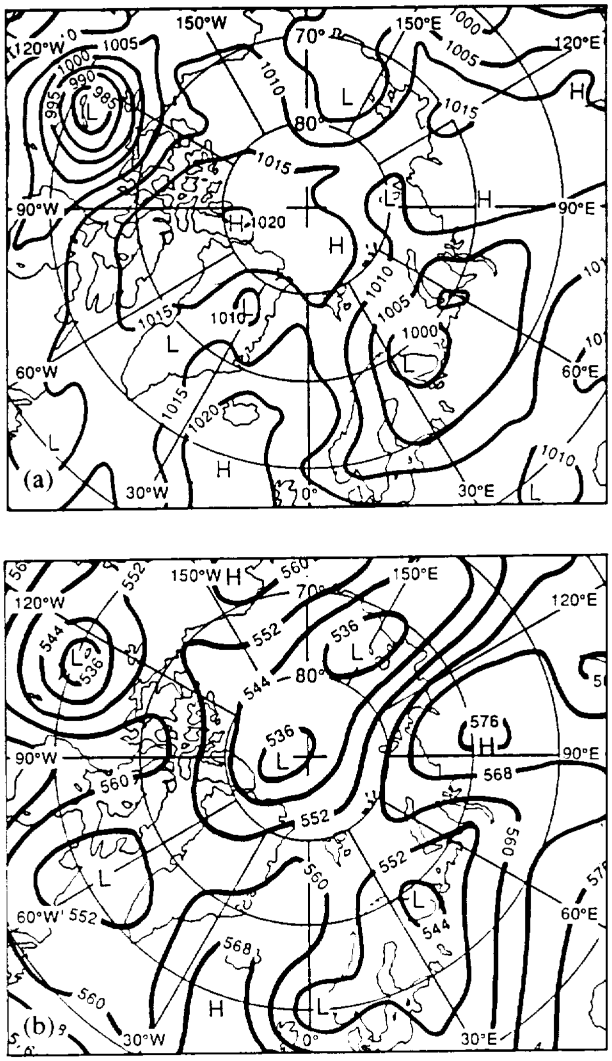

FIG. 8. Analyses of Northern Hemisphere (a) sea level pressure, and (b) 500 mb geopotential height at 12 UTC on 1 July 1984 (ECMWF 1984).

concentration throughout most of the region, with a mean absolute error of 0.10.

5. Algorithm characteristics

This section examines the characteristics of the classification and analysis algorithm. The assumptions used in the algorithm formulation are discussed, an analysis of the propagation of error is performed, and the hybrid histogram-spatial coherence method is compared to existing threshold methods.

a. Discussion of assumptions

The fundamental assumption underlying the entire approach is that an analysis cell is homogeneous with respect to surface and cloud type. Examination of the training imagery reveals that this assumption is generally valid except in the presence of layered clouds or near coastlines. The former situation is ameliorated by the use of a category specifically meant for high clouds overlying low clouds. Class 7, mixed surface types, is intended to account for an inhomogeneous surface, but when clouds are present the classification is ambiguous. This is especially true when one surface is snow or ice and the other is land or water. In training, such a situation is classified as the appropriate cloud type over that surface type which appears to cover the most area in the cell. This problem is encountered often in the area of the Canadian Arctic Archipelago during summer.

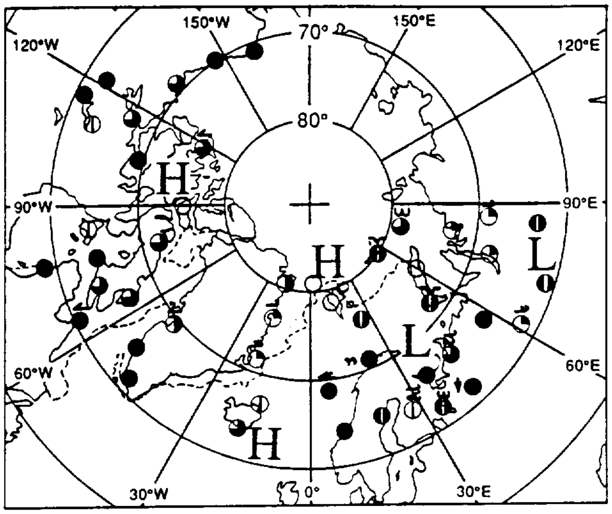

FIG. 9. Arctic surface weather and sky conditions observed on 1 July 1984. The dashed line represents the 1/10 isopleth of sea ice concentration as analyzed by the NOAA-Navy Joint Ice Center for 3 July 1984.

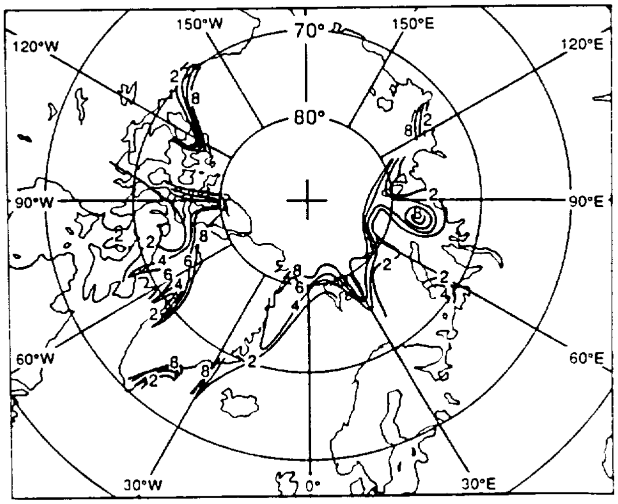

FIG. 10. Automated analysis of Arctic sea ice concentration for 1 July 1984. Values all given in tenths.

Clouds, when present, are assumed to exist in a single layer. This is related to the previous assumption, and is one that is common to many, if not most, cloud analysis algorithms. The single layer assumption is frequently violated in the Arctic (Herman and Goody 1976), and most severely near the core of cyclones. When two cloud layers are visible and well separated in the vertical domain, then class 18 (high cloud over low cloud) is the appropriate category. When one cloud layer completely covers a lower cloud layer, however, only the upper layer can be classified and analyzed. Situations of three or more layers of cloud also cannot be correctly analyzed by the algorithm.

The algorithm assumes that the atmospheric longwave contribution to upwelling radiances received by the satellite is negligible compared to the surface and cloud contributions. The water vapor content of the lower troposphere in the polar regions is typically quite low. The neglect of atmospheric water vapor absorption on the measurement of surface and cloud temperature results in an error of less than 0.5 K at 3.7 μm and less than 2 K at 11 μm (Duggin and Saunders 1984). Arctic haze, an aerosol attributed to anthropogenic sources, has its minimum concentration during the summer months (Rahn 1981). Over new snow, the presence of haze decreases the albedo measured from space, while over old snow and other darker surfaces, the albedo is slightly increased (Shine et al. 1984). These effects are not explicitly increased in the analysis algorithm.

b. *Error analysis*

In this section we examine the effects of classification errors. The magnitudes of the errors in cloud fraction, and surface and cloud albedo and brightness temperature resulting from cell misclassification are largely dependent on the nature of the misclassification. Table 7 illustrates the effect of several types of contrived classification errors on the subsequent analysis. In these examples, incorrect classes were assigned to samples from the training set which were originally classified correctly by the algorithm.

Certain classification errors may have little or no effect on the HHSC analysis if the confusion occurs between clouds with similar heights and underlying surface (type S). In this case the class-optimal channel does not change and the analyzed cloud fraction, clear and cloudy albedos and brightness temperatures are not significantly affected.

When the misclassification involves a cloud of the wrong height (type H), the algorithm chooses an inappropriate channel for the histogram analysis which may not show enough separation between the surface and cloud peaks. If the class characteristic value for the incorrect cloud type is used, as it was in the third example shown in Table 7, then the cloud fraction can be greatly under- or overestimated.

A related error is the incorrect diagnosis of surface type underlying a cloud (type U). The analyzed surface albedo and brightness temperature are likely to be in error because the algorithm looks for a surface peak in the histogram within a reasonable distance of the (incorrect) class characteristic value. Finding none, it assigns the albedo or brightness temperature to be that of the class characteristic value. Again, this can lead to large under- or overestimates in the fractional cloud cover.

TABLE 7. Some examples of contrived classification errors and the resulting errors in the surface and cloud analysis. (T = true classification; F = false classification)

Error type	Class	N	α_s	T_s	α_c	T_c
S	T = St over snow/ice	0.54	0.56	269	0.62	267
	F = Sc over snow/ice	0.54	0.56	269	0.62	267
	T = Ci/Cc/Ac over land/water	0.30	0.10	282	0.42	272
	F = Cs/As over land/water	0.30	0.10	282	0.42	272
H	T = St over snow/ice	0.54	0.56	269	0.62	267
	F = Cs/As over snow/ice	0.03	0.62	269	0.69	251
	T = Ci/Cc/Ac over land/water	0.30	0.10	282	0.42	272
	F = Sc over land/water	0.55	0.09	282	0.25	275
U	T = St over snow/ice	0.54	0.56	269	0.62	267
	F = St over land/water	0.98	0.10	271	0.61	268
	T = Ci/Cc/Ac over land/water	0.30	0.10	282	0.42	272
	F = Ci/Cc/Ac over snow/ice	0.09	0.10	282	0.22	251
L	T = St over snow/ice	0.70	0.61	267	0.64	257
	F = High cloud over low cloud	0.88	0.56	267	0.63	253
	T = High cloud over low cloud	0.93	0.10	267	0.46	263
	F = Cs over snow/ice	0.59	0.27	265	0.39	258
N	T = St over snow/ice	0.70	0.61	267	0.64	257
	F = Unbroken sea ice	0.00	0.62	254		
	T = Cu over land/water	0.39	0.10	287	0.23	279
	F = Land	0.00	0.10	286		

C-2

The majority of misclassifications involved the confusion of "high cloud over low cloud" with single cloud types (type L). For clouds over snow and ice, errors associated with type L misclassifications result from the misinterpretation of the underlying surface as a lower cloud layer, thus overestimating the total cloud fraction, or from the misinterpretation of a lower cloud layer as snow or ice, in which case the cloud fraction is underestimated. If the region is south of 75° latitude, a misclassification of "high cloud over low cloud" may produce greatly erroneous estimates of surface albedo and brightness temperature if the class characteristic values are used (refer to the second type L example in Table 7). Over land and water, type L errors may be associated with multiple layers of the same cloud type. The total cloud fraction is not greatly affected in this case, but the partitioning of cloud fraction between low and high clouds will be in error.

The most serious errors resulting from misclassification can occur when clouds in a cell are not detected at all (type N). Over land or water, the contrast between cloud and surface is usually great enough that only small amounts of cloudiness go undetected, but over snow and ice larger amounts of thin stratus or cirrus may be incorrectly analyzed as cloud-free sea ice or ice sheet. (This is problematic not only for satellite cloud observations, but also for surface observations of cloudiness during the polar night.)

Of the 15% of the training samples which were misclassified, 17% were of type S, 11% were type H, 2% were type U, 52% were type L, and 18% were type N. For the contrived examples in Table 7, the errors in cloud fraction, surface and cloud albedo and brightness temperature associated with misclassifications were frequently quite large. These examples probably overestimate the actual effects of misclassifications when they occur, however, because these scenes do not necessarily resemble the (incorrect) classes to which they were assigned. In section 3 it was shown that the sensitivity of the analysis to actual classification errors was not great, at least for the analysis of total cloud fraction.

c. Comparison to threshold methods

The hybrid histogram-spatial coherence method of analyzing cloud fraction was chosen for two reasons. It takes advantage of the surface-cloud contrast in a class-optimal channel, and it accounts for partially cloudy fields of view. This method is more complicated than the simpler threshold approach, and takes 25% more computing time per cell. It is worthwhile to compare the cloud fraction estimated using the HHSC to the threshold-estimated cloud fraction to evaluate whether the increased complexity is warranted.

Three types of threshold algorithms are tested. The first, (A), uses a VIS-IR threshold *without classification*. This is the most elementary type of threshold method. A pixel must be both darker than the visible threshold and warmer than the infrared threshold to be labeled as surface; otherwise it is labeled as cloudy. This is the reverse of the usual logic, but yields better results at these latitudes than assuming a cell is clear unless proven cloudy. A step change in the threshold value is specified at 75° latitude to account for the surface transition between an ocean and a sea ice regime. The second threshold algorithm, (B), classifies the cell first, then applies a VIS-IR threshold as before, with the values of the thresholds now dependent on the class. In the third threshold algorithm, (C), the classification is followed by a threshold analysis of cloud fraction in the class-optimal channel only. In all three threshold algorithms, the values of the thresholds were computed from the class characteristic values and bounds (Table 3).

Table 8 compares the results of the threshold analyses and the HHSC for the training set. The HHSC estimated the cloud fraction more accurately than the threshold methods in nine out of eleven cloud classes. The cirrostratus (classes 8 and 13) fraction was most accurately computed using (B), the VIS-IR threshold algorithm with classification. The HHSC was noticeably more accurate than the threshold methods when analyzing low cloudiness, particularly over snow and ice. The greater success of the HHSC is due in part to its flexibility. It does not use a fixed threshold, but instead partitions the clear and cloudy pixels according to the statistical distribution of albedos or brightness temperatures in that particular scene. Classification improved the skill of the threshold algorithm in all cases. The one-channel class-optimal threshold method, (C), was more accurate than the VIS-IR threshold method, (B), for cirrus, stratus and stratocumulus cloudiness.

The improvement in cloud analysis achieved by first classifying a scene is exemplified by comparing the cloud fraction estimated by the HHSC and threshold (A) algorithm for the clear samples in Table 8. The threshold algorithm predicted cloud cover in a majority of the clear samples. Some of the clear samples actually do contain a very small amount of cloud (less than 5%), but the contribution to the threshold RMS error is small compared to the gross errors incurred by mistaking surface for cloud. Large overpredictions occurred for the snow on land, sea ice, and ice sheet classes, which tended to be cold and bright in the imagery. In contrast, the HHSC predicted cloud cover in less than 1% of the clear samples, the result of misclassifications. The associated RMS errors are much smaller than those produced by the threshold algorithm without classification.

6. Summary and discussion

This study has demonstrated the detection and classification of clouds in the polar regions from multispectral satellite data using pattern recognition techniques. The algorithm is applied to 2.5° × 2.5° latitude-

TABLE 8. Comparison of the RMS errors for the hybrid histogram-spatial coherence method (HHSC) and threshold methods for the analysis of cloud fraction in the training set. Refer to Table 2 for category numbers.

			RMS error Threshold methods		
Class	Number of samples	HHSC	(A) VIS-IR without classification	(B) VIS-IR with classification	(C) Class-optimal channel
Surface					
1	42	0.00	0.55	0.00	0.00
2	18	0.08	0.85	0.25	0.08
3	7	0.00	0.11	0.00	0.00
4	21	0.16	0.36	0.15	0.22
5	23	0.16	0.79	0.03	0.21
6	36	0.09	0.93	0.15	0.11
7	37	0.00	0.79	0.00	0.00
Cloud					
8	17	0.34	0.17	0.11	0.45
9	34	0.25	0.60	0.42	0.34
10	129	0.16	0.39	0.24	0.24
11	60	0.15	0.34	0.35	0.32
12	45	0.11	0.27	0.25	0.24
13	12	0.24	0.24	0.23	0.23
14	51	0.35	0.56	0.49	0.48
15	98	0.26	0.61	0.59	0.32
16	48	0.18	0.43	0.44	0.21
17	14	0.06	0.52	0.35	0.46
18	178	0.23	0.42	0.39	0.49

longitude boxes of multispectral AVHRR GAC-resolution data. Following the classification, the scene is analyzed to estimate cloud fraction, surface temperature and albedo, and cloudy albedo and brightness temperature using a hybrid histogram-spatial coherence technique. When tested against manual estimates of cloud fraction, the mean absolute error was between 0.05 and 0.26 for the training samples. The HHSC performed well when tested on sixty artificial scenes which had known values of fractional cloudiness and surface and cloud properties.

One day of summertime satellite imagery from the Arctic was analyzed in detail. Large amounts of low and layered cloudiness were seen in the 1 July 1984 analysis. The analyzed cloud types and fractions qualitatively agree with manual interpretation of the satellite imagery and with surface weather observations on the same day. Good correspondence between the algorithm's sea ice fraction estimates and the Navy-NOAA sea ice observations further validates the classification and analysis scheme.

The sensitivity of the classification and analysis to underlying assumptions and the propagation of error were explored in order to assess the abilities and limitations of the algorithm. Errors in classification can lead to large errors in the analyzed cloud fraction if the cloud height is incorrect, the incorrect surface type is diagnosed beneath the cloud, or if the cloud is not detected at all. Overall, the HHSC analyzes the fractional cloudiness more accurately than threshold methods using visible and infrared radiances or even one using the class-optimal channel. Comparisons between threshold methods with and without scene classification clearly show how the prior classification of surface and cloud type can greatly improve the accuracy of the cloud fraction analysis.

This work demonstrates the ability of pattern recognition techniques to successfully identify and analyze clouds in the polar regions, an area of the globe which confounds other cloud detection schemes. An algorithm such as this can be used to gather a data base of cloud observations in the polar regions, from which a cloud climatology can be constructed or numerical models can be validated. This is the goal of the International Satellite Cloud Climatology Project on a global scale.

Several improvements may be made to the classification and analysis algorithm. This study was merely a demonstration of the use of pattern recognition techniques to aid in the analysis of cloud cover in a particular region of the globe. Before such a scheme could be used operationally, more thorough training and testing would be required, including the use of a more extensive training set and a team of experts to train and evaluate the classification algorithm. The class characteristic albedos and brightness temperatures would be further refined in the process.

The algorithm can be used to analyze regions which are smaller than the 2.5° × 2.5° chosen by the ISCCP. Smaller samples would better satisfy the homogeneity and single cloud layer assumptions discussed in section 5. Tests with the classification algorithm indicate that its skill is not greatly reduced for training samples with dimensions of 16 × 16 pixels or even 8 × 8 pixels. The histogram analysis, however, requires at least 500–1000 data points for accurate determination of the peak values and widths. At 60° latitude, 500 GAC pixels would correspond to a sample with dimensions 1.0° latitude by 1.25° longitude; at 80° latitude the sample dimensions would need to be at least 2° × 4°.

Currently the higher resolution AVHRR data (1.1 km field of view) is not saved over most of the polar regions, except by prior request. Use of this higher resolution imagery would not only allow the minimum sample size to be reduced by a factor of 15, but the increased spatial detail in this imagery would almost certainly lead to more accurate classifications and cloud analyses using the pattern recognition and HHSC techniques. Tests are needed to determine the improvement gained by using this higher resolution data, as well as the increase in computing resources that would be needed to perform the analysis.

Temporal and spatial information could be utilized more effectively to improve both the classification and analysis. For example, the classifications of the nearest neighbors in both time and space might serve as use useful features for the classification of a cell, thus including some contextual information. The analyzed surface albedos and brightness temperatures of the nearest neighbors could also be used to filter out inaccurate analyses, at least over homogeneous regions such as open water, pack ice, or ice sheet. In cloud-free regions, cells classified as broken sea ice might be analyzed in more detail by subdividing the cell and employing a simple analysis algorithm (such as a threshold method) which does not require a large number of pixels. The higher resolution AVHRR data would be especially appropriate in this regard.

Finally, additional data from the MSU[2] and HIRS instruments on the TOVS package could provide information about the atmospheric temperature structure, which would aid in cloud detection and height assignment. Microwave sea ice concentration measurements from the DMSP, SMMR, or SSM/I would be extremely useful for specifying surface characteristics.

The next task, after analyzing the cloud type and amount, and surface and cloud albedos and brightness temperatures, should be the estimation of the cloud altitude and optical thickness and surface radiative fluxes using radiative transfer models. The incorporation of vertical temperature profiles would aid in the estimation of the atmospheric radiative fluxes. Class-dependent microphysical models could be used to create a look-up table of cloud optical properties as a function of solar zenith angle, viewing angle, and cloud optical thickness. Before this can be done, however, much more needs to be learned about the microstructure of clouds at high latitudes. Ideally this would include both field measurements of cloud liquid and ice water content, drop size distribution, and crystal habit, as well as the development of improved methods to sense cloud microphysical properties remotely from satellites (e.g., Twomey and Seton 1980; Wu 1987; Platt et al. 1987).

Acknowledgments. The author would like to thank Dr. Gin-Rong Liu for providing the fundamental "improved two-threshold" algorithm from which the HHSC was developed. Many helpful comments and suggestions from Professors Jim Weinman, Gerald Herman, and Judy Curry, as well as two anonymous reviewers, are gratefully acknowledged. This work was supported by a graduate fellowship from the University of Wisconsin and by the National Science Foundation under Grant ATM-8505027.

REFERENCES

Arking, A., and J. D. Childs, 1985: Retrieval of cloud cover parameters from multispectral satellite measurements. *J. Climate Appl. Meteor.*, **24**, 322–333.

Brower, R. L., H. S. Gohrband, W. G. Pichel, T. L. Signore and C. C. Walton, 1976: Satellite derived sea surface temperatures from NOAA spacecraft. Natl. Environ. Satellite Service, Washington, D.C., NOAA Tech. Mem. NESS 78, 74 pp.

Bunting, J. T., and R. F. Fournier, 1980: Tests of spectral cloud classification using DMSP fine mode satellite data. Air Force Geophysics Laboratory, AFGL-TR-80-0181, Environmental Research Papers No. 704, 42 pp.

Burfeind, C. R., J. A. Weinman and B. R. Barkstrom, 1987: A preliminary computer pattern analysis of satellite images of mature extratropical cyclones. *Mon. Wea. Rev.*, **115**, 556–563.

Coakley, J. A., and F. P. Bretherton, 1982: Cloud cover from high-resolution scanner data: Detecting and allowing for partially filled fields of view. *J. Geophys. Res.*, **87**(C7), 4917–4932.

Curry, J. A., 1987: On the contribution of radiative cooling to the formation of cold-core anticyclones. *J. Atmos. Sci.*, **44**, 2575–2592.

——, and G. F. Herman, 1985: Relationships between large-scale heat and moisture budgets and the occurrence of Arctic stratus clouds. *Mon. Wea. Rev.*, **113**, 1441–1457.

d'Entremont, R. P., and L. W. Thomason, 1987: Interpreting meteorological satellite images using a color-composite technique. *Bull. Amer. Meteor. Soc.*, **68**, 762–768.

Duggin, M. J., and R. W. Saunders, 1984: Problems encountered in remote sensing of land and ocean surface features. *Satellite Sensing of a Cloudy Atmosphere: Observing the Third Planet.* A. Henderson-Sellers, Eds., Taylor and Francis, 241–288.

Ebert, E. E., 1987: A pattern recognition algorithm for distinguishing surface and cloud types in the polar regions. *J. Climate Appl. Meteor.*, **26**, 1412–1427.

European Centre for Medium Range Forecasting, 1981: *Workshop on radiation and cloudradiation interactions in numerical modelling.* 209 pp.

——, 1984: Daily global analyses.

Eyre, J. R., J. L. Brownscombe and R. J. Allam, 1984: Detection of fog at night using Advanced Very High Resolution Radiometer (AVHRR) imagery. *Meteor. Mag.*, **113**, 266–271.

---

[2] Key to acronyms: DMSP, Defense Meteorological Satellite Program; HIRS, High Resolution Infrared Radiation Sounder; MSU, Microwave Sounding Unit; SMM/I, Special Sensor Microwave/Imager; SMMR, Scanning Multichannel Microwave Radiometer; TOVS, TIROS Operational Vertical Sounder.

Fye, F. K., 1978: The AFGWC automated cloud analysis model. AFGWC Tech. Memo. 78-002, 97 pp.

Garand, L., 1988: Automated recognition of oceanic cloud patterns. Part I: Methodology and application to cloud climatology. *J. Climate*, **1**, 20–39.

Gavrilova, M. K., 1963: *Radiation Climate of the Arctic*. Gidrometeorologicheskoe Izdatel'stvo, 178 pp.

Harris, R., and E. C. Barrett, 1978: Toward an objective cloud analysis. *J. Appl. Meteor.*, **17**, 1258–1266.

Herman, G. F., and R. Goody, 1976: Formation and persistance of summertime Arctic stratus clouds. *J. Atmos. Sci.*, **33**, 1537–1553.

Huschke, R. E., 1969: Arctic cloud statistics from "air-calibrated" surface weather observations. The RAND Corporation, RM-6173-PR, Santa Monica, Calif., 79 pp.

Jayaweera, K., 1982: Meteorological conditions conducive to the formation of stratus clouds in the Beaufort Sea. *Natl. Wea. Dig.*, **7**, 25–32.

Kidder, S. Q., and H.-T. Wu, 1984: Dramatic contrast between low clouds and snow cover in daytime 3.7 mm imagery. *Mon. Wea. Rev.*, **112**, 2345–2346.

Kidwell, K. B., 1984: *NOAA Polar Orbiter Data (TIROS-N, NOAA-6, NOAA-7 and NOAA-8) Users Guide*. Environmental Data and Information Service, NOAA, U.S. Dept. Commerce.

Knottenberg, H., and E. Raschke, 1982: On the discrimination of water and ice clouds in multispectral AVHRR data. *Annellen der Meteor.*, **18**, 145–147.

Kukla, G. J., 1984: Variation of Arctic cloud cover during summer 1979. Tech. Rep. LDGO-84-2, Lamont-Doherty Geological Observatory, Palisades, N.Y., 67 pp.

Kuo, K. S., R. M. Welch and S. K. Sengupta, 1988: Structural and textural characteristics of cirrus clouds observed using high spatial resolution LANDSAT imagery. *J. Appl. Meteor.*, **27**, 1242–1260.

Lindsay, R. W., 1985: Hourly cloud observations and six-hourly synoptic observations from the *Polar Queen*. Polar Science Center, University of Washington.

Liu, G.-R., W. L. Smith and T. H. Achtor, 1988: The use of visible data in VAS temperature soundings. *J. Appl. Meteor.*, **27**, 1309–1321.

Mölders, N., 1987: Wolkenerkennung in AVHRR-Daten mit besonderer Berücksichtigung der Gebiete über der Arktis. Diplomarbeit, University of Cologne, West Germany, 80 pp.

Platt, C. M. R., J. C. Scott and A. C. Dilley, 1987: Remote sounding of high clouds. Part VI: Optical properties of midlatitude and tropical cirrus. *J. Atmos. Sci.*, **44**, 729–747.

Rahn, K. A., 1981: Arctic air sampling network in 1980. *Atmos. Environ.*, **15**, 1349–1362.

Raschke, E., H. Jacobs, H.-J. Lutz and U. Steffens, 1986: Wolkenerkennung über der Antarktis in Satellitenbildern. *Polarforschung*, **56**, 69–78.

Rossow, W. B., F. Mosher, E. Kinsella, A. Arking, M. Desbois, E. Harrison, P. Minnis, E. Ruprecht, G. Seze, C. Simmer and E. Smith, 1985: ISCCP cloud algorithm intercomparison. *J. Climate Appl. Meteor.*, **24**, 877–903.

Seze, G., and M. Desbois, 1987: Cloud cover analysis from satellite imagery using spatial and temporal characteristics of the data. *J. Climate Appl. Meteor.*, **26**, 287–303.

Shine, K. P., D. A. Robinson, A. Henderson-Sellers and G. Kukla, 1984: Evidence of Arctic-wide atmospheric aerosols from DMSP visible imagery. *J. Climate Appl. Meteor.*, **23**, 1459–1464.

Twomey, S., and K. J. Seton, 1980: Influences of gross micro-physical properties of clouds from spectral reflectance measurements. *J. Atmos. Sci.*, **37**, 1065–1069.

Vowinckel, E., 1962: Cloud amount and type over the Arctic. *Meteorology*, **51**,

Welch, R. M., S. K. Sengupta and K. S. Kuo, 1988: Marine stratocumulus cloud fields off the coast of Southern California observed using LANDSAT imagery. Part II: Textural analysis. *J. Appl. Meteor.*, **27**, 363–378.

——, K. S. Kuo and S. K. Sengupta, 1989: Cloud field classification based on high spacial textual features. Part 3. Discrimination of cloud and surface features in polar regions from digitized imagery. Submitted to *J. Geophys. Res.*

WMO, 1978: *JOC study conference on parameterization of extended cloudiness and radiation for climate models*. Oxford, GARP Climate Dynamics Subprogramme.

——, 1982: The International Satellite Cloud Climatology Project (ISCCP) preliminary implementation plan (Revision 1, November 1982). World Climate Research Programme, WCP-35.

——, 1987: *Report of the International Satellite Cloud Climatology Project (ISCCP) workshop on cloud algorithms in the polar regions* Tokyo, Japan, World Climate Research Programme, WCP-131.

Wu, M.-L. C., 1987: Determination of cloud ice water content and geometrical thickness using microwave and infrared radiometric measurements. *J. Climate Appl. Meteor.*, **26**, 878–884.

Wu, R., J. A. Weinman and R. T. Chin, 1985: Determination of rainfall rates from GOES satellite imagery by a pattern recognition technique. *J. Atmos. Oceanic Tech.*, **2**, 314–330.

PATTERN RECOGNITION ANALYSIS OF POLAR CLOUDS DURING SUMMER AND WINTER

Elizabeth E. Ebert[1]

University of Wisconsin,
Madison, Wisconsin, USA

revised version submitted to

The International Journal of Remote Sensing

6 December 1989

---

[1] Current address: Bureau of Meteorology Research Centre, Melbourne, Vic., Australia

Abstract

A pattern recognition algorithm is demonstrated which classifies eighteen surface and cloud types in high latitude AVHRR imagery based on several spectral and textural features, then estimates the cloud properties (fractional coverage, albedo, and brightness temperature) using a hybrid histogram-spatial coherence technique. The summertime version of the algorithm uses both visible and infrared data (AVHRR channels 1-4), while the wintertime version uses only infrared data (AVHRR channels 3-5).

Three days of low resolution AVHRR imagery from the Arctic and Antarctic during January and July 1984 were analyzed for cloud type and fractional coverage. The analysis showed significant amounts of high cloudiness in the Arctic during one day in winter. The Antarctic summer scene was characterized by heavy cloud cover in the southern ocean and relatively clear conditions in the continental interior. A large region of extremely low brightness temperatures in East Antarctica during winter suggests the presence of polar stratospheric cloud.

1. Introduction and background

The distribution of cloudiness in the polar regions is currently poorly known. This is largely due to the paucity of surface observing stations in the Arctic and Antarctic, but also due to the inherent difficulties in interpreting the much larger volume of satellite data collected in those regions. Certain characteristics of the polar regions make the analysis of cloud cover from satellite data more difficult than at lower latitudes, including low radiance contrasts between clouds and the underlying surface, the frequent inversion structure of the lower troposphere, and the lack of visible data during the winter. The key to improving our understanding of cloud cover, particularly in sparsely observed areas like the Arctic and Antarctic, lies in improving and increasing the use of satellite data for measuring standard quantities such as fractional coverage, cloud height and temperature, and if possible, cloud radiative and microphysical properties. At high latitudes, sensors aboard the NOAA series and Defense Meteorological Satellite Program (DMSP) polar orbiting satellites collect high resolution imagery which can be analyzed to estimate some of the above mentioned cloud parameters.

Knowledge of polar cloud distribution is important for real-time applications such as weather analysis and forecasting, and is potentially valuable in initializing the moisture fields of numerical weather prediction models. Clouds control the hydrological and radiative processes linking the surface and atmosphere (Crane and Barry 1984). Sensitivity tests conducted using general circulation models suggest that the warming produced by an increase in atmospheric CO_2 (the "greenhouse" effect) might be experienced most strongly in the polar regions (e.g. Hansen et al. 1984). Changes in the polar cloud distribution would likely accompany such a warming trend. Regular monitoring of polar cloud cover might be able to detect this trend and its influence on the radiation balance via modifications in cloud conditions (WMO, 1988).

In 1986 the International Satellite Cloud Climatology Project (ISCCP) launched a pilot study to investigate whether the information contained in the NOAA Advanced Very High Resolution Radiometer (AVHRR) channels could be effectively used in cloud algorithms to resolve some of the cloud detection problems encountered in the polar regions. The AVHRR measures radiances in five spectral regions: two in the visible region (ch.1: 0.55-0.68 μm; ch.2: 0.725-1.1 μm), one in the 3.7 μm window region which is particularly useful for identifying low clouds over snow and ice during daylight (ch.3: 3.55-3.93 μm), and two thermal infrared window channels (ch.4: 10.5-11.3 μm; ch.5: 11.5-12.5 μm). A pilot data set comprising fourteen days of Global Area Coverage (~4 km resolution) AVHRR imagery from January and July 1984 was analyzed by various research groups using a variety of schemes, and the preliminary results were presented in a workshop report (WMO, 1987).

Trained observers of satellite imagery identify surface and cloud types at high latitudes by recognizing such features as cracks in the sea ice, the smooth homogeneity of ice sheets, partial obscuring of surface details by thin clouds, cloud shadows and illumination of cloud sides, and the bumpy or wispy appearance, as well as the usually cooler brightness temperatures of certain cloud types (McGuffie et al. 1988). Automated pattern recognition uses the same textural and spectral (radiance) features to objectively classify the components of a scene. The textural features in particular are extremely useful in distinguishing clouds from sea ice and ice sheet in a low contrast scene. Ebert (1987a) used ten spectral and textural features in low-resolution visible, near-infrared, and infrared AVHRR imagery to classify eighteen surface and cloud types in Arctic summertime data using the maximum likelihood method. Welch et al. (1989) found that textural measures in a single visible channel of very high resolution LANDSAT imagery were sufficient to classify four surface and cloud types in the Arctic, again using the maximum likelihood method. Key (1989) used several spectral and textural features to identify cloud patterns in Arctic AVHRR imagery. Yamanouchi et al. (1987) used brightness temperature differences in AVHRR channels 3, 4, and 5 to detect, but not classify, clouds over Antarctica.

Other schemes have been developed to identify clouds over snow and ice from spectral data alone (Bolle 1985, Mölders 1987, Gesell 1989, Key et al. 1989a,b). Spectral methods classify each pixel individually, producing a classification image with the same resolution as the original imagery, while methods employing textural measures operate on clusters of pixels and generally produce a lower resolution classification image.

The majority of polar cloud schemes have been developed and tested on daytime data, where cloud identification relies largely on reflectance contrasts in the visible and particularly in the near-infrared portions of the solar spectrum. During the dark half of the year, only thermal radiances are available for use in cloud analysis. Of the methods mentioned above, only Yamanouchi's algorithm is not affected by the loss of visible data.

This paper presents some results from a pattern recognition analysis of a portion of the ISCCP polar cloud pilot data set. The pattern recognition algorithm of Ebert (1987a) is adapted for wintertime data using AVHRR channels 3, 4, and 5. The cloud types and fractional coverage in 2.5° latitude x 2.5° longitude regions (corresponding to the ISCCP grid) are analyzed in three days of imagery from Arctic winter, Antarctic summer, and Antarctic winter. The results are discussed in the context of concurrent synoptic weather observations.

2. Method

The classification and analysis scheme will be only summarized here; a full description is given in Ebert (1987a,b, 1989). The algorithm consists of two parts: (1) the classification of surface and cloud type in each 2.5° x 2.5° scene using pattern recognition, and (2) the analysis of cloud fraction, clear and cloudy visible albedos and infrared brightness temperatures using a hybrid histogram-spatial coherence technique.

The purpose of the classification step is to determine whether a scene contains clouds, and if so, to identify the general physical nature of the clouds. It does this by computing several spectral and textural features from the calibrated multispectral AVHRR data, then using these feature values in the maximum likelihood method to classify the scene into one of eighteen surface and cloud categories. A different combination of AVHRR channels and classes is necessary for each season and hemisphere. The Arctic summer and Antarctic summer versions of the algorithm use AVHRR visible and infrared channels 1, 2, 3, and 4, while the Arctic winter and Antarctic winter versions use the infrared channels 3, 4, and 5. For the Arctic winter algorithm the categories are:

1. Land without snow
2. Land with snow
3. Open water and thin ice
4. Unbroken sea ice
5. Broken sea ice
6. Ice sheet
7. Mixed surface types
8. Cs/As over land/water
9. Ci/Ci/Ac over land/water
10. St over land/water
11. Sc over land/water
12. Cu over land/water
13. Cs/As over snow/ice
14. Ci/Cc/Ac over snow/ice
15. St over snow/ice
16. Sc over snow/ice
17. Inversion St over snow/ice
18. High cloud over low cloud

(The standard abbreviations for cloud type are from the International Cloud Atlas, WMO 1956) In the two summertime algorithms class 3 was restricted to "open water" and class 17 was assigned to "Cu over snow/ice" to represent cumulus and other isolated or small-scale low cloudiness. No large areas of snow-free land exist south of 60°S, so class 1 was reassigned to "ice haze" in the Antarctic summer algorithm and "polar stratospheric cloud" in the Antarctic winter algorithm.

An iterative training procedure was used to teach each classification algorithm the characteristics of the surface and cloud categories, based on knowledge of the correct classification of a training set of image data. Approximately 1000 samples were included in each training set. The algorithm's classification ability was evaluated using the skill score, S, defined by

$$S = \frac{\#\text{ correct classifications } - \#\text{ expected by chance}}{\#\text{ total classifications } - \#\text{ expected by chance}} \text{ X } 100 \quad (\%)$$

The classification skills achieved on the training data are shown in Table 1. The greatest skill was achieved for the two summertime versions, reflecting the usefulness of visible imagery. The Arctic winter algorithm had the least skill, due mainly to the difficulty in detecting low clouds over snow and ice from thermal data alone. All of the versions had some problems separating layered cloudiness from single layer clouds. Tests suggest that the classification skill on independent data is a few percent less than that achieved on the training data (Ebert, 1987a).

Overall the presence of cloud in a scene was correctly detected 97% of the time during summer and 89% of the time during winter. Figure 1 shows a confusion matrix of predicted versus actual presence of cloudiness for each of the four versions of the pattern recognition algorithm. The majority of clear/cloudy errors resulted from cloudy regions being mistaken for clear surface, especially in winter.

The classification of a scene specifies the optimal AVHRR channel for separating clear and cloudy pixels in the hybrid histogram-spatial coherence technique. For example, channel 4 separates clear and cloudy pixels best for "Ci/Cc/Ac over land/water," while channel 1 is optimal for "Cu over land/water" and channel 3 is optimal for "St over snow/ice" during summer. The surface and cloud classifications are also used to specify initial guesses for the clear and cloudy radiances. The incorporation of the classification information is an extremely important step in the cloud analysis process. Ebert (1989) showed that the prior classification of a scene can greatly improve the determination of cloud fraction in the polar regions where the surface-cloud contrast may be extremely small in the visible and/or infrared imagery.

The hybrid histogram-spatial coherence technique estimates the total cloud fraction, and the clear and cloudy channel 1 albedos and channel 4 brightness temperatures. Briefly, a histogram analysis is first performed in the class-optimal channel to estimate the mean clear (μ_s) and cloudy (μ_c) albedos or brightness temperatures. Next, the spatial coherence method (Coakley and Bretherton, 1982) isolates completely clear and completely cloudy arrays of 2x2 pixels, which are tagged and given weights of w=0 or w=1, respectively, with the weights representing pixel cloud fraction. Partly cloudy arrays are given weights $w = (x-\mu_s)/(\mu_c-\mu_s)$, subject to the constraint that $0 \leq w \leq 1$. The average of all the weights is an estimate for the total cloud fraction. The partly cloudy pixels are then removed, and the completely clear and completely cloudy pixels are used to generate "clean" histograms in the remaining spectral channels, from which the clear and cloudy albedos and brightness temperatures can be estimated.

When verified against manual nephanalyses of the training imagery, the overall root-mean-square (RMS) error in the estimated cloud fraction was 0.18 for the Arctic summer samples and 0.24 for the Arctic winter samples. The classification step ensured that most of the clear scenes were correctly identified. The summertime algorithm analyzed the low cloud cover well with a RMS error of 0.18, but had more difficulty analyzing the high cloud cover, with a RMS error of 0.31. The Arctic wintertime algorithm performed better on the high cloudiness (RMS error of 0.23), but underestimated the low cloud cover (RMS error of 0.35) because some low level clouds were not detected. The Antarctic summer and winter algorithms were not tested against manual analyses. However, Fig. 1 suggests that the accuracy of the cloud fraction estimated by the Antarctic algorithms do not differ greatly from those of their Arctic counterparts.

3. Analyses

Each day's satellite data comprises fourteen images covering most of the region between 60° and 90° latitude. The images were analyzed individually, then the analyses combined and averaged to form a hemispheric mosaic. The region immediately surrounding the pole was not analyzed because those pixels, found at the edges of the imagery, were distorted due to the earth's curvature. In this section the analyses are compared to manual interpretation of the imagery and to the cloud cover observed at the surface.

3.1 6 January 1984 Arctic

Figure 2a shows a mosaic of thermal (channel 4) imagery for the Arctic on 6 January 1984. The European Centre for Medium Range Weather Forecasting (ECMWF) analysis of sea level pressure at 12 UTC, as well as surface synoptic observations of cloud cover from the European and Canadian Arctic (Free University of Berlin 1984; NOAA 3-hourly surface weather analyses) at 7 UTC and 15 UTC, respectively, are plotted in Fig. 2b. In using the surface observations to validate the automated analysis, it should be noted that these observations are point measurements made at a specific time, and may not represent the daily mean conditions over a larger area which is portrayed by the automated analysis.

The imagery shows an extended region of cumulus cloudiness over the Norwegian Sea, with thick low clouds over northern Sweden and Norway. Finland and western Russia are partially clear under the influence of a ridge. Layered and high clouds are found in Siberia between 60°N and 65°N. The Barents Sea between Svalbard and Novaya Zemlya contains clouds at all levels, over open water in the south and sea ice in the north. The Canadian Archipelago and Baffin Bay are mostly clear, with broken and unbroken sea ice and some regions of warm stratus. The textural variability indicates the presence of some cloud cover over Greenland, but it is difficult to tell whether there is cold high cloudiness over a warmer surface, or warm stratus over a colder surface. The Arctic Basin appears to be mostly clear with some warmer inversion stratus in the eastern region.

The classification and cloud fraction analysis of the image are shown in Figs. 2c and 2d. The algorithm accurately classified the cumulus clouds in the Norwegian Sea, the clear conditions over the Arctic Basin and the Canadian Archipelago, and the high cloudiness in eastern Greenland. The high clouds near 90°E were also well classified. It failed to correctly diagnose the thick low cloud cover over northern Scandinavia, and the presence of sea ice east of Novaya Zemlya. It is difficult to verify the clouds analyzed over central Greenland.

3.2 6 January 1984 Antarctic

A mosaic of visible (channel 1) imagery from 6 January 1984 over Antarctica is shown in Fig. 3a. Only one satellite analysis was made for some regions north of 70°S due to the poor illumination, as the satellite descending orbit passed over during the early morning hours. The homogeneous appearance of the ice sheet suggests clear skies over much of the interior. The ocean surrounding the continent is mostly ice-free and quite cloudy, with particularly bright cloud cover over the western Weddell Sea near 50°W. Figure 3b shows the surface analysis from January 6. The map shows three major cyclones situated at 60° latitude, with the strongest of them located near 10°W longitude. The clouds to the east of the Antarctic Peninsula may be related to convergence at the mountain barrier (Schwerdtfeger 1984). An anticyclone is situated over East Antarctica, with few clouds there.

The classification of the image and analyzed cloud fraction are presented in Figs. 3c and 3d. Stratus and stratocumulus were the most frequent cloud types analyzed over the oceans. Layered cloudiness is located primarily in the eastern sides of the cyclonic systems. The clouds over the ice sheet are mainly of liquid phase, and are found throughout the lower elevation regions of Antarctica. The high plateau is mostly clear, with areas of warm, tenuous ice haze near 20°E and 100°E. A strong gradient in cloudiness is observed at the coast near 90°E, the possible result of cold drainage flow from the ice sheet acquiring moisture over the warm water and condensing to form clouds. The analyzed cloud types do not agree very well with the small number of available surface reports, which indicate alto and cirriform cloudiness where the algorithm analyzes low cloudiness.

3.3 1 July 1984 Antarctic

The infrared imagery for the 1 July 1984 Antarctic is combined into a mosaic in Fig. 4a. The accompanying surface synoptic analysis is given in Fig. 4b. East Antarctica appears homogeneous but the measured 11 μm brightness temperatures (not shown) range from 179-200 K, as much as 19° colder than the surface temperature observed at Vostok. The quality of the AVHRR calibration at temperatures below 200 K is not well known, but the errors in brightness temperature are probably not more than 1-2°C (see Appendix A). These very cold temperatures seem to signal a broad region of polar stratospheric cloud. As in the summertime, several cyclonic disturbances surround the continent, with low and layered cloudiness near their centers and eastern flanks. Cloud-free sea ice is apparent east of the Antarctic Peninsula and again between 60°E and 90°E. High cloudiness covers the coast at the eastern side of the Weddell Sea, and thin cirrus covers much of West Antarctica.

The classification and cloud fraction analysis of the imagery are presented in Figs. 4c and 4d. Unbroken sea ice was analyzed in and east of the Weddell Sea and in the region near 60°E. East Antarctica was mostly clear, except for the two large inland lobes of polar stratospheric cloud near 40°E and 100°E. Small amounts of cirrus and warm inversion stratus were analyzed over West Antarctica. Inversion stratus was analyzed mainly around the margin of the continent. There is fair agreement between the analyzed cloud cover and the surface observations. Unfortunately it is not possible to confirm the presence of the analyzed polar stratospheric cloud using limb scanning measurements, which depend upon the extinction of sunlight (McCormick et al. 1982).

4. Conclusions

The analyzed cloud fields show many of the features which have been recorded in climatologies of the Arctic and Antarctic (e.g. Vowinckel and Orvig 1970; Schwerdtfeger 1984), such as the wintertime cumulus clouds over the Norwegian Sea and high cloudiness over Siberia, the continual presence of multiple levels of clouds accompanying cyclones in the southern ocean, and the predominantly clear interior of the Antarctic continent during summer. No climatology exists for polar stratospheric clouds, whose existence has been known for barely a decade (McCormick et al. 1982). These clouds are found in both hemispheres during winter when the stratospheric temperature falls below about 195 K, and may play a catalytic role in the springtime destruction of Arctic and Antarctic ozone (Hamill et al. 1986).

Automated pattern recognition has been shown to be an effective tool for analyzing cloud cover from satellite data in the polar regions, an area where many conventional techniques encounter difficulty. The pattern recognition algorithm demonstrated here classified 2.5° x 2.5° scenes with a skill of 71-86%, depending on the season and hemisphere, and estimated the cloud fraction to an accuracy of 0.18-0.24 as measured by the RMS error. While these results are encouraging, they fall far short of the accuracy of ±0.03 for 30-day mean cloud fraction required by the ISCCP (Schiffer and Rossow 1983). Some improvements could be made by decreasing the dimensions of the analysis region from 2.5° x 2.5° to a smaller size which would better satisfy the homogeneity assumptions implicit in the algorithm, and by increasing the number and quality of the training samples to improve the classification skill.

Better results would almost certainly be obtained using the higher resolution (1.1 km) AVHRR data in which the finer scale features, particularly of low level clouds, are more evident. Microwave and infrared radiometry and high spectral resolution interferometry (Smith et al. 1988) give additional information on the surface conditions and atmospheric structure which would aid in cloud detection and height assignment. With the improvement of technology to remotely sense and analyze polar clouds, we can continue to increase our knowledge of their distribution and improve our understanding of the role they play in the global climate.

Acknowledgements

I would like to thank Professors Jim Weinman, Judy Curry, and Gerald Herman and Mr. Frank LaFontaine for their help during the course of this work. This research was supported by a graduate fellowship from the University of Wisconsin, the National Science Foundation under Grant ATM-8505027, and the National Aeronautics and Space Administration under Grant NAG 5-1117.

Appendix A. Low temperature calibration of AVHRR thermal sensors

The radiance, R, measured in an AVHRR thermal channel is estimated as a linear function of the raw counts, X:

$$R = S\,X + I.$$

S and I are the slope and intercept values valid for each scan line, determined by a 2-point fit to a set of in-flight calibrations against an internal black body target and outer space.

The radiance is converted to brightness temperature by inverting the Planck function in the appropriate spectral region. The dependence of the Planck function itself on temperature is accounted for by varying the central wavelength, λ, of each band over three temperature ranges. For channel 4 of the NOAA-7 AVHRR these central wavelengths are λ=10.797 μm for T=180-225 K, λ=10.790 μm for T=225-275 K, and λ=10.785 μm for T=275-320 K (Kidwell, 1984).

The 2-point linear calibration does not account for the nonlinearity of the sensor response over the observed range of radiances. This can result in temperature errors of up to 3°C (Brown et al. 1985). A recent NOAA publication (NOAA 1988) lists values of the nonlinear correction term which should be added to the linearly calibrated brightness temperature to obtain a more accurate value of brightness temperature. These corrections, plotted in Fig. 5, were determined from an analysis of the original thermal vacuum data which did not include measurements at temperatures below 205 K. However, the trend clearly favors negative corrections at colder temperatures. A possible source of error is contamination of the scene radiance by internal emission from the radiometer housing (Brown, personal communication).

The AVHRR data in this paper were calibrated and analyzed prior to the publication of the NOAA memorandum using only the linear calibration outlined by Kidwell (1984). Figure 5 suggests that these temperatures may be 1-2°C warmer than the true scene brightness temperatures.

A post-launch calibration of thermal channel radiances against known values of scene temperature (for example, hourly surface temperature measurements made at several Antarctic stations) might be used to test the linearity of the radiometer response at temperature below 205 K. In the future all pre-flight calibrations of radiometers intended for operation on polar orbiting satellites should include some very low temperature measurements, as these are not uncommon at high latitudes during winter.

References

Bolle, H.-J., 1985: Assessment of thin cirrus and low cloud over snow by means of the maximum likelihood method. *Adv. Space Res.*, **5**, 169-175.

Brown, O.B, J.W. Brown and R.H. Evans, 1985: Calibration of Advanced Very High Resolution Radiometer infrared observations. *J. Geophys. Res.*, **90**, C6, 11667-11677.

Coakley, J.A. and F.P. Bretherton, 1982: Cloud cover from high-resolution scanner data: Detecting and allowing for partially filled fields of view. *J. Geophys. Res.*, **87** (C7), 4917-4932.

Crane, R.G. and R.G. Barry, 1984: The influence of clouds in climate with a focus on high latitude interactions. *J. Climatol.*, **4**, 71-93.

Ebert, E.E., 1987a: A pattern recognition algorithm for distinguishing surface and cloud types in the polar regions. *J. Clim. Appl. Meteor.*, **26**, 1412-1427.

Ebert, E.E., 1987b: Classification and analysis of surface and clouds at high latitudes from AVHRR multispectral satellite data. Ph.D. Thesis, University of Wisconsin-Madison.

Ebert, E.E., 1989: Analysis of polar clouds from satellite imagery using pattern recognition with a statistical cloud analysis scheme. *J. Appl. Meteor.*, **28**, 382-399.

Free University of Berlin, 1984: Berliner Wetterkarte, *Meteorologische Abhandlungen, Serie B*, **43**, No.33-6.

Gesell, G., 1989: An algorithm for snow and ice detection using AVHRR data. An extension to the APOLLO software package. *Int. J. Remote Sensing*, **10**, 897-905.

Hamill, P., O.B. Toon and R.P. Turco, 1986: Characteristics of polar stratospheric clouds during the formation of the Antarctic ozone hole. *Geophys. Res. Lett.*, **13**, 1288-1291.

Hansen, J., A. Lacis, D. Rind, G. Russell, P. Stone, I. Fung, R. Reudy and J. Lerner, 1984: Climate sensitivity: Analysis of feedback mechanisms. *Climate Processes and Climate Sensitivity*, Geophysical Monograph 29, Maurice Ewing Vol. 5, Amer. Geophys. Union, 130-163.

Key, J.R., 1989: Cloud analysis with Arctic AVHRR and SMMR data, Part II: Classification of cloud patterns using spectral and textural measures. *J. Geophys. Res.*, in press.

Key, J.R., J.A. Maslanik, and R.G. Barry, 1989a: Cloud classification from satellite data using a fuzzy sets algorithm: A polar example. *Int. J. Remote Sensing*, in press.

Key, J.R., J.A. Maslanik, and A.J. Schweiger, 1989b: Classification of merged AVHRR and SMMR Arctic data with neural networks. *Photogramm. Engin. and Remote Sensing.*, **55**, 1331-1338.

Kidwell, K.B., 1984: NOAA polar orbiter data (TIROS-N, NOAA-6, NOAA-7, and NOAA-8) users guide. NOAA NESDIS, Natl. Climatic Data Center, Satellite Data Services Division.

McCormick, M.P., H.M. Steele, P. Hamill, W.P. Chu and T.J. Swissler, 1982: Polar stratospheric cloud sightings by SAM II. *J. Atmos. Sci.*, **39**, 1387-1397.

McGuffie, K., R.G. Barry, A. Schweiger, D.A. Robinson and J. Newell, 1988: Intercomparison of satellite-derived cloud analyses for the Arctic Ocean in spring and summer. *Int. J. Remote Sensing*, **9**, 447-467.

Mölders, N., 1987: Wolkenerkennung in AVHRR-Daten mit besonderer Berücksichtigung der Gebiete über der Arktis. Diplomarbeit, University of Cologne, West Germany, 80 pp.

NOAA, 1988: Data extraction and calibration of TIROS-N/NOAA radiometers. NOAA Tech. Memo. NESS 107 (Rev. 1).

Schwerdtfeger, W., 1984: *Weather and Climate of the Antarctic* (Elsevier, Amsterdam).

Schiffer, R.A. and W.B. Rossow, 1983: The International Satellite Cloud Climatology Project (ISCCP): The first project of the World Climate Research Programme. *Bull. Amer. Meteor. Soc.*, **64**, 779-784.

Smith, W.L., H.M. Woolf, H.B. Howell, H.E. Revercomb and H.-L. Huang, 1988: High Resolution Interferometer Sounder—the retrieval of atmospheric temperature and water vapor profiles. *AMS Third Conference on Satellite Meteorology and Oceanography, Anaheim, Calif., 1-5 February 1988, Preprint Vol.*, 266-271.

Vowinckel, E. and S. Orvig, 1970: The climate of the North Polar Basin. *Climates of the Polar Regions*, S. Orvig, Ed., World Survey of Climatology, **14** (Elsevier, Amsterdam).

Welch, R.M., K.S. Kuo and S.K. Sengupta, 1989: Cloud field classification based on high spatial resolution textural features. Part 3: Discrimination of cloud and surface features in polar regions from digitized imagery. *J. Geophys. Res.*, in press.

WMO, 1956: *International Cloud Atlas* (WMO, Geneva).

WMO, 1987: Report of the International Satellite Cloud Climatology Project (ISCCP) workshop on cloud algorithms in the polar regions (Tokyo, Japan, 19-21 August 1986).

World Climate Research Programme, WCP-131.

WMO, 1988: Report of the third session of the working group on sea ice and climate (Oslo, Norway, 31 May-3 June 1988). World Climate Research Programme, WCRP-18.

Yamanouchi, T., K. Suzuki and S. Kawaguchi, 1987: Detection of clouds in Antarctica from infrared multispectral data of AVHRR. *J. Meteor. Soc. Japan*, **65**, 949-961.

	Classification skill score	Problem areas
Arctic summer	85.8%	Layered clouds, small amts. of Cu over land
Arctic winter	71.9%	Layered clouds, low clouds over snow/ice, especially inversion St
Antarctic summer	85.1%	Layered clouds, some Ci over ice sheet
Antarctic winter	78.4%	Layered clouds, low clouds over snow/ice, especially inversion St

Table 1. Classification skill scores achieved on four training sets.

Figure captions

Fig. 1. Confusion matrices of clear and cloudy classifications for the (a) Arctic summer, (b) Arctic winter, (c) Antarctic summer, and (d) Antarctic winter training samples.

Fig. 2a. AVHRR channel 4 image mosaic for the 6 January 1984 Arctic. (The routine for producing the image mosaic uses a maximum brightness criterion, and thus the mosaic appears colder and cloudier than the individual images due to cloud motion between the fourteen satellite overpasses.)

Fig. 2b. ECMWF sea level pressure analysis at 12 UTC and observed cloud conditions on 6 January 1984.

Fig. 2c. Automated surface and cloud classification for the 6 January 1984 Arctic. (Key: 1=Land without snow, 2=Land with snow, 3=Open water and thin ice, 4=Unbroken sea ice, 5=Broken sea ice, 6=Ice sheet, 7=Mixed surface types, 8=Cs/As over land/water, 9=Ci/Cc/Ac over land/water, 10=St over land/water, 11=Sc over land/water, 12=Cu over land/water, 13=Cs/As over snow/ice, 14=Ci/Cc/Ac over snow/ice, 15=St over snow/ice, 16=Sc over snow/ice, 17=Inversion St over snow/ice, 18=High cloud over low cloud)

Fig. 2d. Automated cloud fraction analysis for the 6 January 1984 Arctic. Cloud fraction is expressed in units of tenths.

Fig. 3a. AVHRR channel 1 image mosaic for the 6 January 1984 Antarctic.

Fig. 3b. ECMWF sea level pressure analysis at 12 UTC and observed cloud conditions on 6 January 1984.

Fig. 3c. Automated surface and cloud classification for the 6 January 1984 Antarctic. (Key: 1=Ice haze, 2=Land with snow, 3=Open water, 4=Unbroken sea ice, 5=Broken sea ice, 6=Ice sheet, 7=Mixed surface types, 8=Cs/As over land/water, 9=Ci/Cc/Ac over land/water, 10=St over land/water, 11=Sc over land/water, 12=Cu over land/water, 13=Cs/As over snow/ice, 14=Ci/Cc/Ac over snow/ice, 15=St over snow/ice, 16=Sc over snow/ice, 17=Cu over snow/ice, 18=High cloud over low cloud)

Fig. 3d. Automated cloud fraction analysis for the 6 January 1984 Antarctic. Cloud fraction is expressed in units of tenths.

Fig. 4a. AVHRR channel 4 image mosaic for the 1 July 1984 Antarctic.

Fig.4b. ECMWF sea level pressure analysis at 12 UTC and observed cloud conditions on 1 July 1984.

Fig. 4c. Automated surface and cloud classification for the 1 July 1984 Antarctic. (Key: 1=Polar stratospheric cloud, 2=Land with snow, 3=Open water and thin ice, 4=Unbroken sea ice, 5=Broken sea ice, 6=Ice sheet, 7=Mixed surface types, 8=Cs/As over land/water, 9=Ci/Cc/Ac over land/water, 10=St over land/water, 11=Sc over land/water, 12=Cu over land/water, 13=Cs/As over snow/ice, 14=Ci/Cc/Ac over snow/ice, 15=St over snow/ice, 16=Sc over snow/ice, 17=Inversion St over snow/ice, 18=High cloud over low cloud)

Fig. 4d. Automated cloud fraction analysis for the 1 July 1984 Antarctic. Cloud fraction is expressed in units of tenths.

Figure 5. Nonlinear temperature correction as a function of the channel 4 brightness temperature obtained using the 2-point linear calibration for the NOAA-7 AVHRR (from NOAA 1988).

(a) Arctic summer

		Predicted	
		clear	cloudy
Actual	clear	228	6
	cloudy	20	691

(b) Arctic winter

		Predicted	
		clear	cloudy
Actual	clear	358	24
	cloudy	98	616

(c) Antarctic summer

		Predicted	
		clear	cloudy
Actual	clear	340	16
	cloudy	10	739

(d) Antarctic winter

		Predicted	
		clear	cloudy
Actual	clear	601	19
	cloudy	120	600

Fig 1

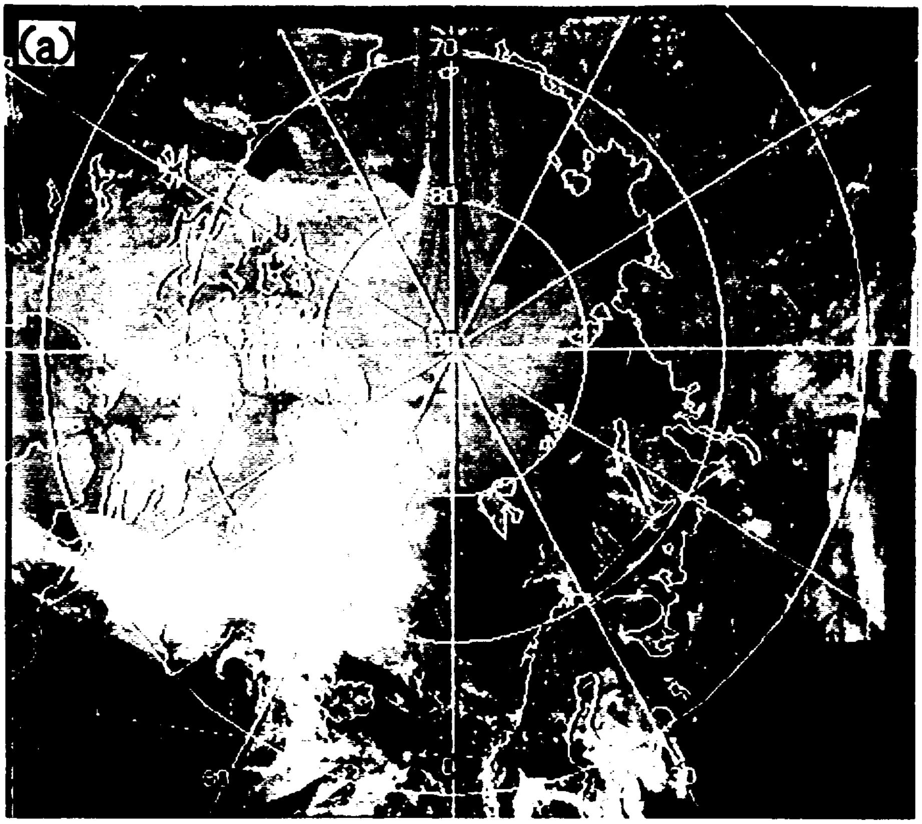

Fig 2a

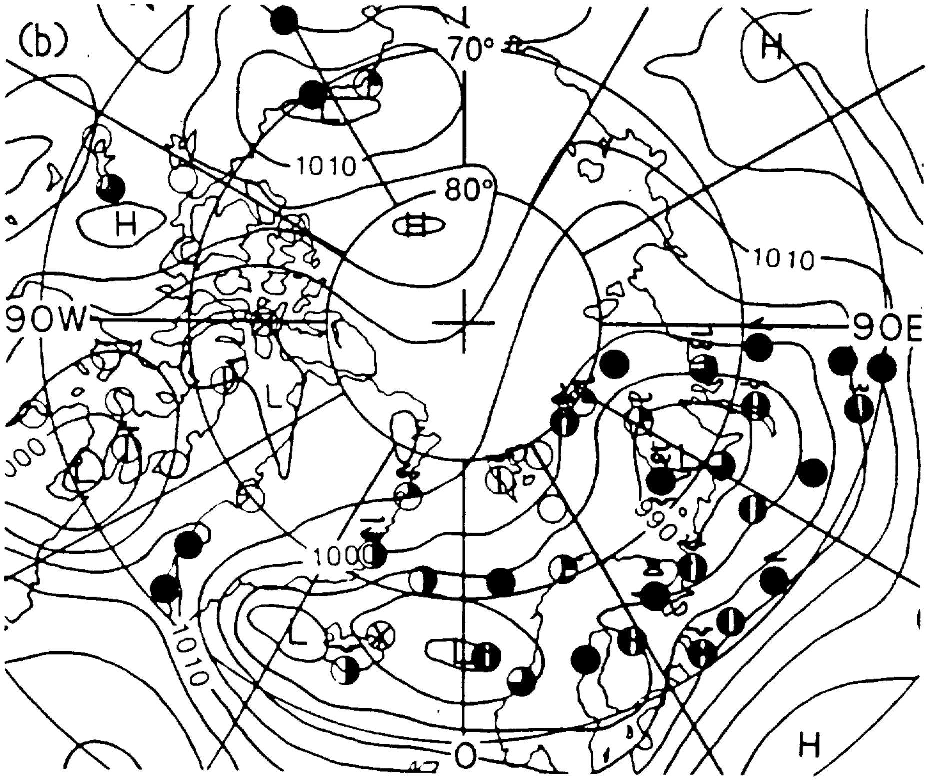

Fig 2b

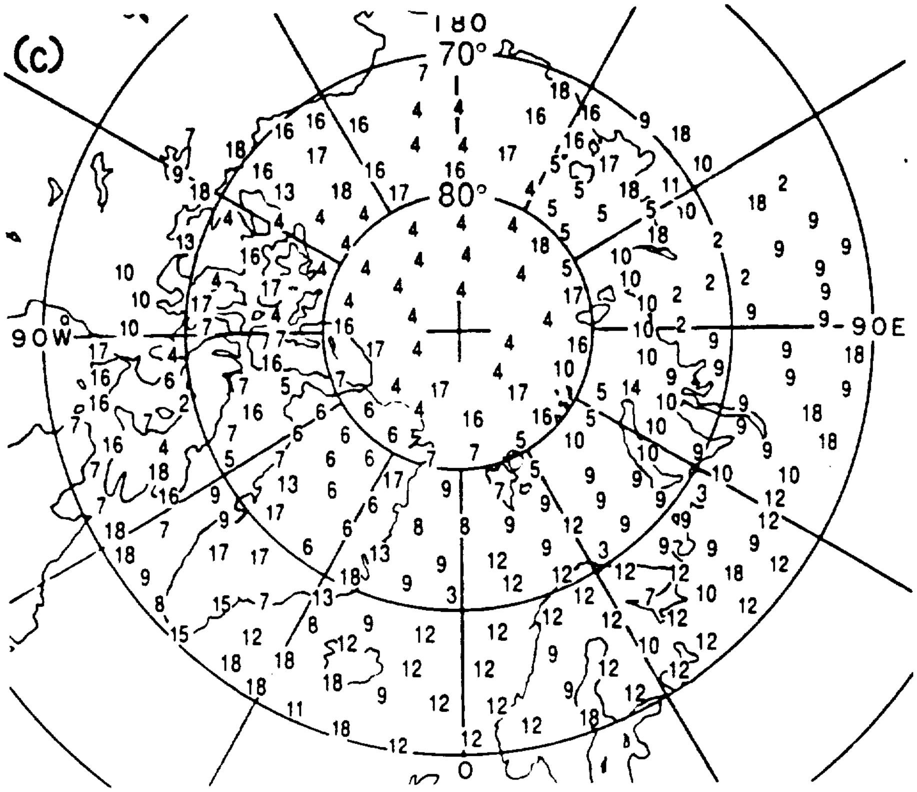

Fig. 2c

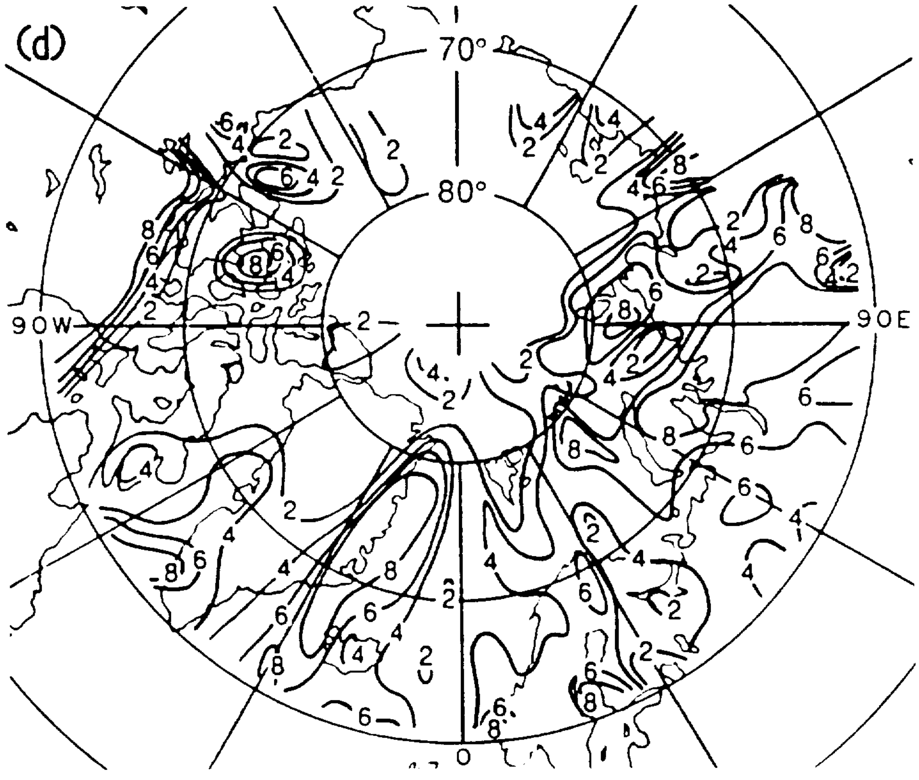

Fig 2d

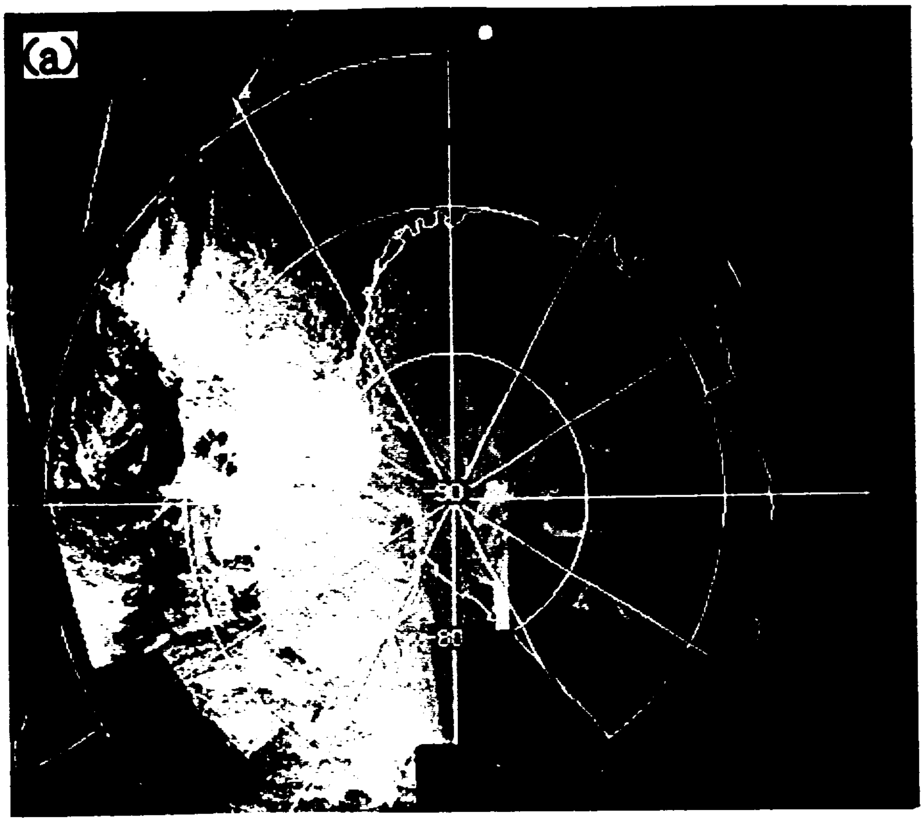
(a)
80
80

Fig. 3a

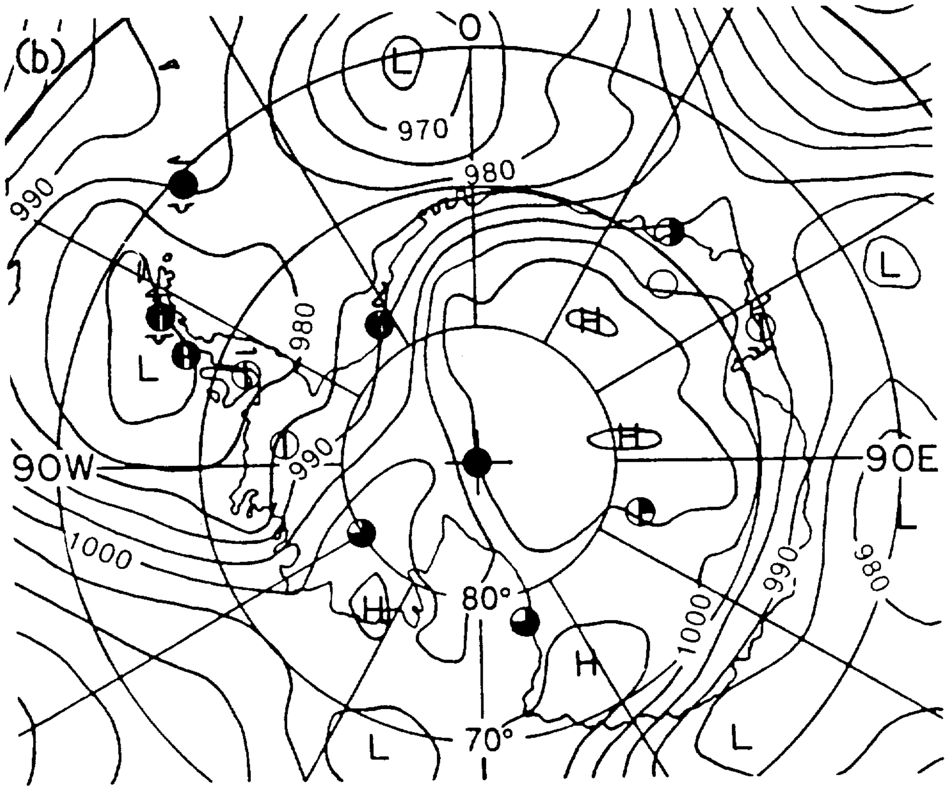
(b)
O
L
970
980
990
980
L
990
90W
90E
L
1000
H
80°
H
1000
990
980
L
70°
L
L

Fig. 3b

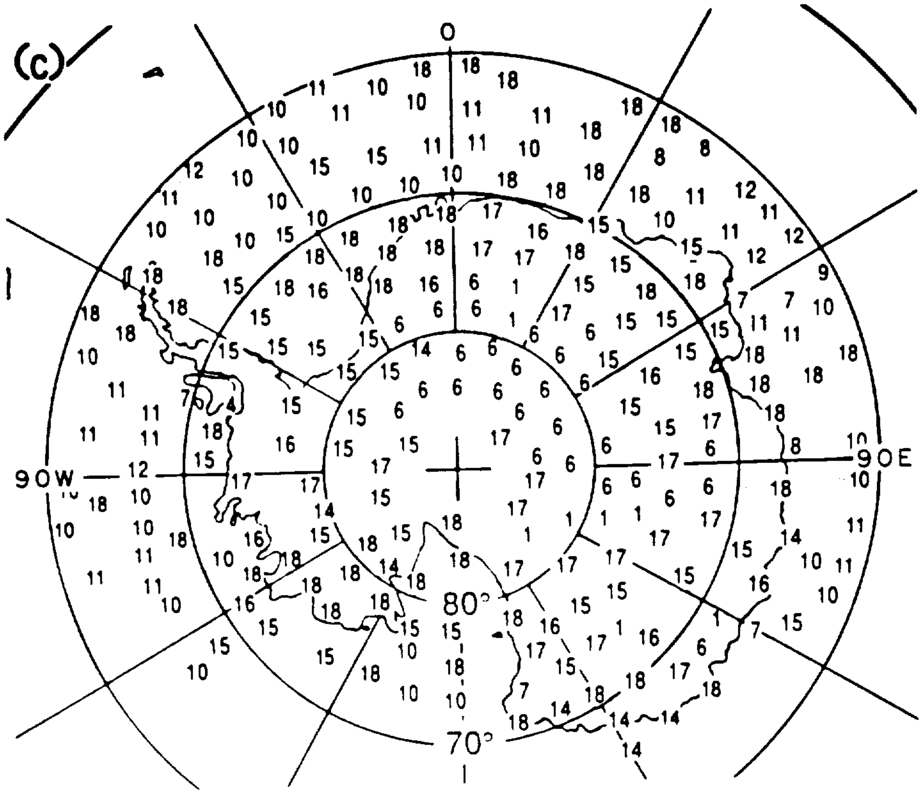

Fig. 3c

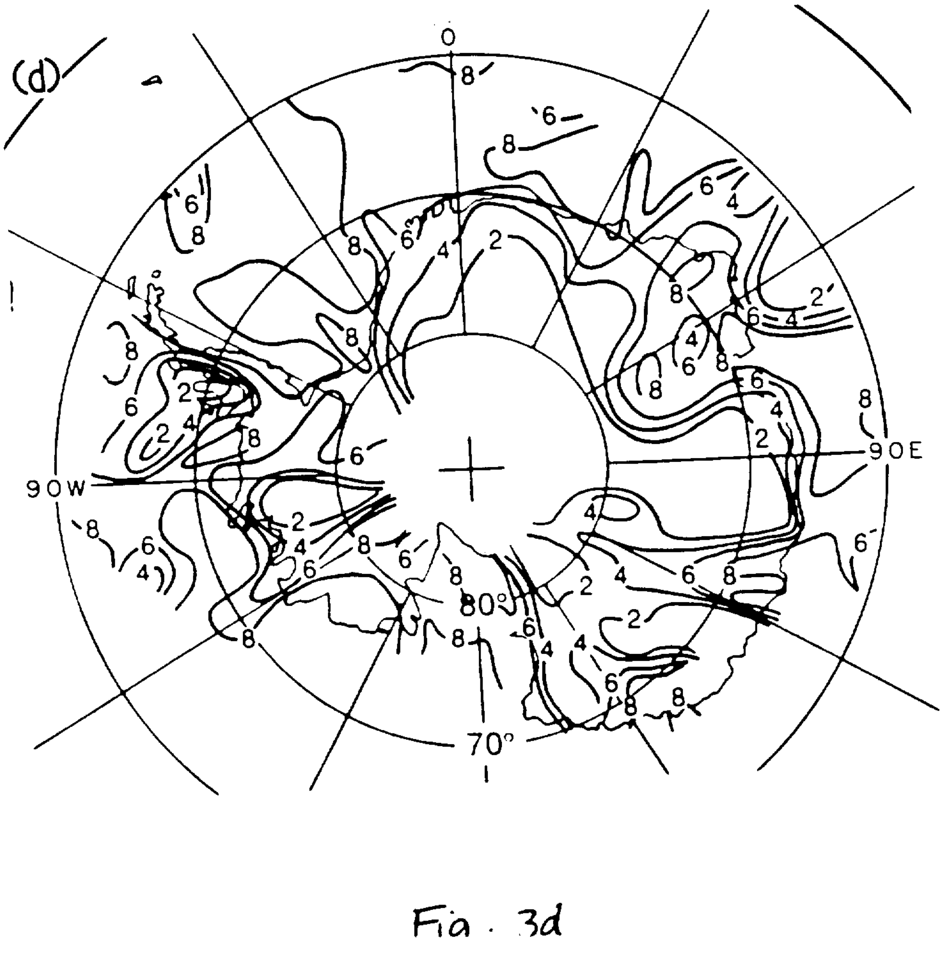

Fig. 3d

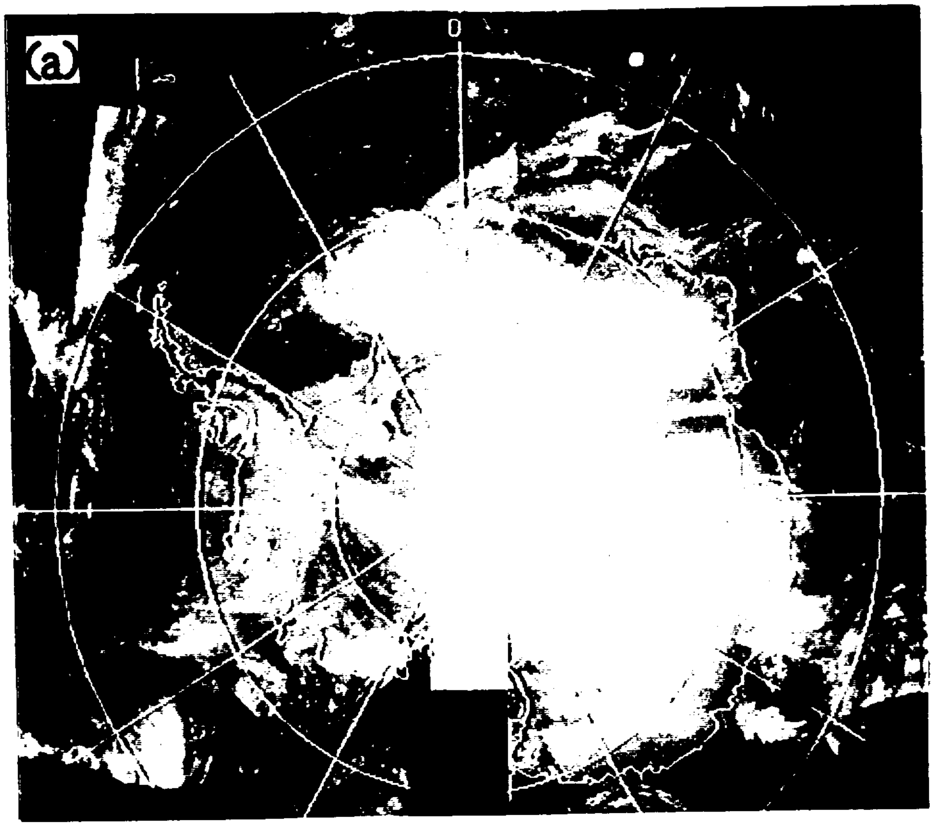
(a)
0

Fig. 4a

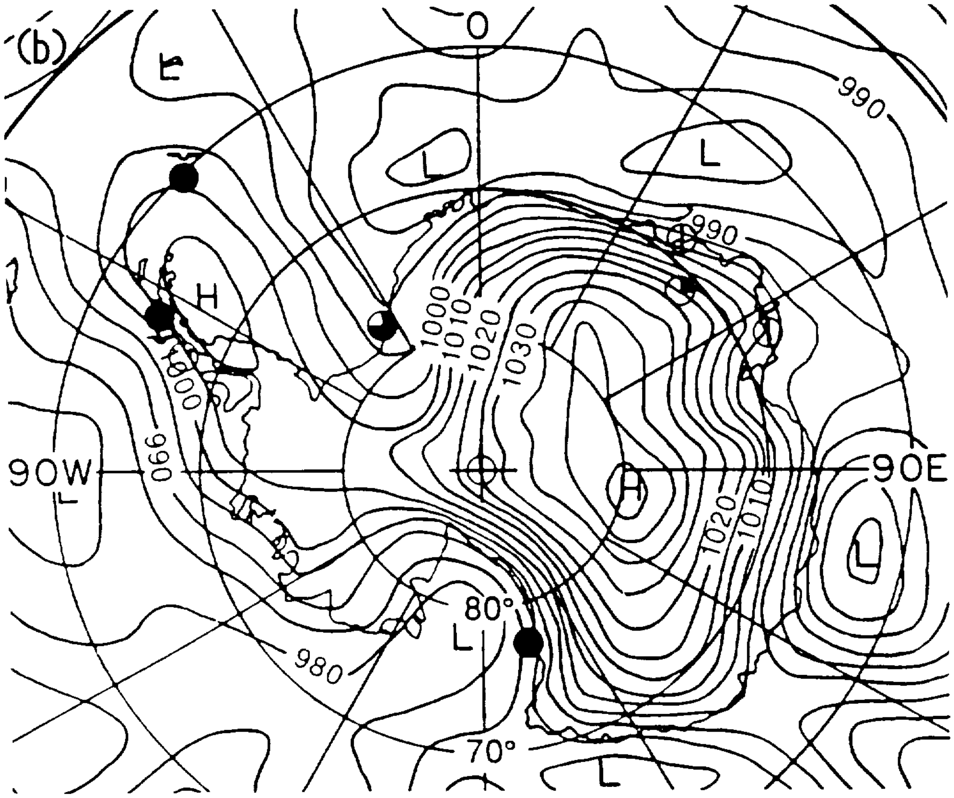
(b)
0
990
L
L
990
H
1000
1010
1020
1030
1000
1000
990
90W
L
90E
H
1020
1010
L
80°
L
980
70°
L

Fig. 4b

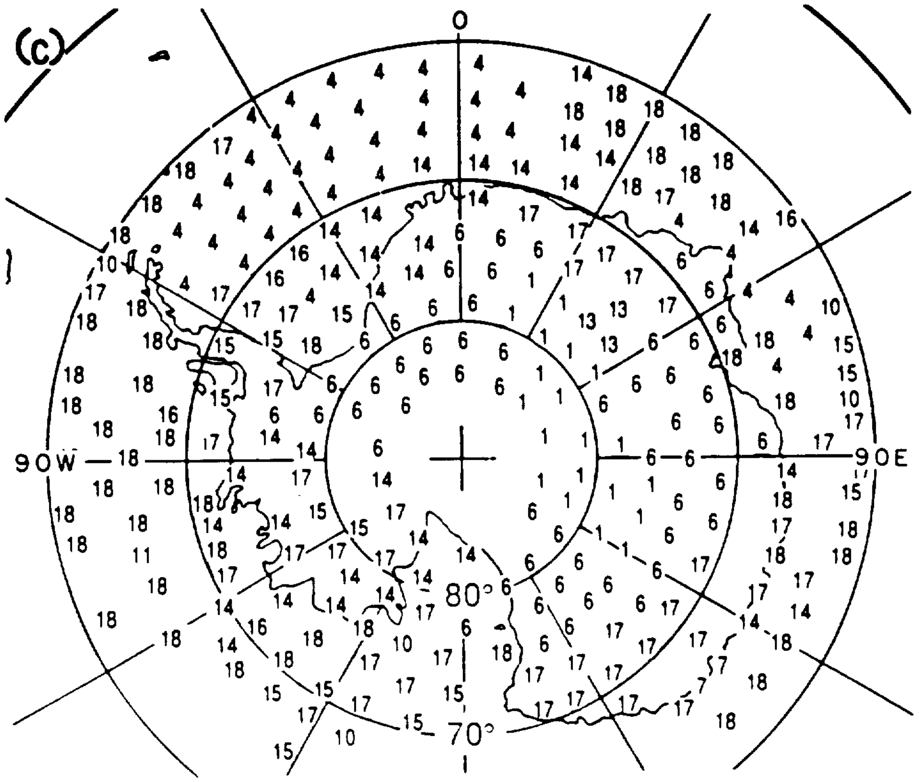

Fig. 4c

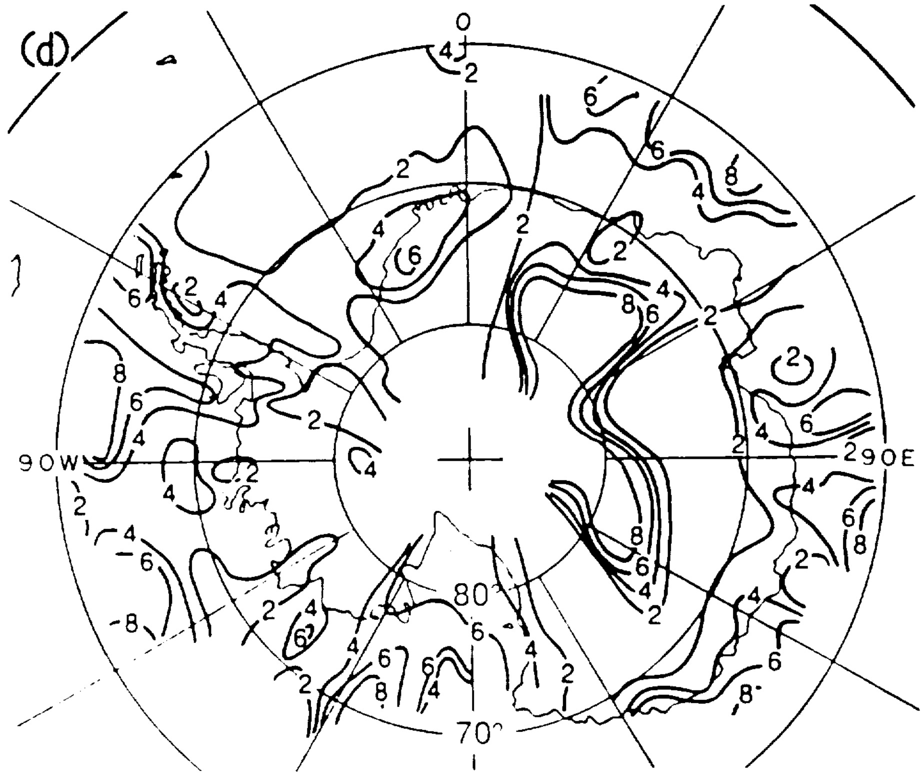

Fig. 4d

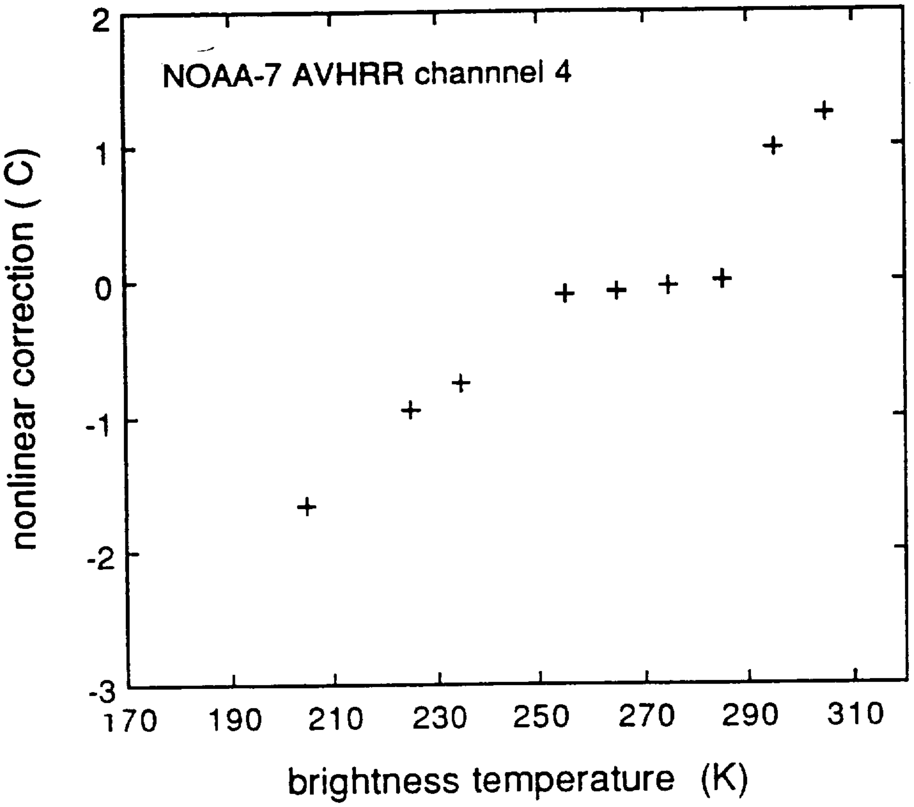
NOAA-7 AVHRR channnel 4
nonlinear correction (C)
2
1
0
-1
-2
-3
170
190
210
230
250
270
290
310
brightness temperature (K)

Fig. 5